Behaviorally Modifying the Rheology of Simulated Nuclear Legacy Waste

Shafeeq Ahmed

School of Chemical and Process Engineering

The University of Leeds

Submitted in accordance with the requirements for the degree of Doctor of Philosophy

January 2021

Intellectual Property and Publication Statements

The candidate confirms that the work submitted is his own and that appropriate credit has been given where reference has been made to the work of others.

Acknowledgements

With great appreciations to my supervisor Associate Professor Dr David Harbottle for his immense support, guidance, expertise and time throughout the duration of this research programme. Without his guidance and support the completion of this programme would have been unsuccessful.

Thank you Juliette Behra for being there and supporting me throughout the project, you have truly been a good friend during good and bad times. Your support has seen me through this project. Your passion for rheology has inspired me and given me the support to further develop the project. I hope our friendship lasts a lifetime.

I would like to specially thank Chris Hodges for all his support and guidance. I have been very fortunate to spend many hours with him discussing my project and receiving his expert knowledge and guidance, lunch breaks have been seriously more enjoyable. I would like to thank the lab technicians for the astounding management of the labs allowing me to undertake my research. Thank you to all the lectures, my colleagues especially Asim, David Austin, Dewi, Huagui, Simeon Adjei-Doku, Stefanos, Suparit Tangparitkul, and all others who have supported me over the years.

I would like to thank Leeds University for providing me with the opportunity to undertake this Ph.D, without which I would have not been able to achieve such academic success.

A huge thanks to my dear friend Dr Kashif Shehzad for believing in me and supporting me throughout the project. Dr Mushtaq Ahmed and family, thank you for all your immense support and counselling over the years, you have encouraged me to persevere when things have been tough.

With great appreciation to my mother and late farther for believing in me and supporting me throughout my life. A big thank you to my wonderful children Zain, Hassan and Aqsa who have made me smile on the darkest of days and given me the reason to continue. They have been the light in my life without whom I would be empty.

Finally and most importantly, I would like to thank my dear wife who has put up with me over the years, a truly remarkable women who has the patience of a saint. She has always been there for me with a huge smile whenever I was down and struggled. She really means the world to me.. Once again thank you very much for be part of my life and soul.

Table of Contents

List of Figures

List of Tables

Chapter 1

Introduction

Significant amounts of radioactive sludge wastes from defence and civil reactors has accumulated at Sellafield, UK (1) and Hanford, USA (2, 3). The nuclear reactors used metallic uranium fuel with either an aluminium or magnesium alloy cladding, which when stored wet for long periods of time has led to the alloy corroding to form the sludge waste (4, 5). Today, this waste is stored in open air ponds and large storage tanks which are highly undesirable for long term storage (6). In the past several years there has been increasing government pressure to address the storage of intermediate level wastes, with a requirement to recover, treat and suitably prepare the waste for long-term interim storage.

In the UK, used Magnox fuel has been stored in open air ponds since the 1950s, and in the 1960s, delays in the reprocessing of Magnox fuel led to the fuel being held in the cooling ponds (Fig. 1.1a-b) for a longer time than desired, thus leading to the corrosion of the fuel cladding (1, 7). In 1964, the Magnox Swarf Storage Silos (MSSS) shown in Fig 1.1c were commissioned and constructed to temporarily store contaminated solid waste, exposed equipment, debris and metallic cladding produced in the decanning process of FGMSP. MSSS has 22 compartments, each with a storage capacity of 600

m^3, and a total amount of material stored between 9700 m^3 (8) and 11000 m^3 (9). In addition to intermediate level waste, high level waste from the reprocessing of the nuclear fuel is stored in the Highly Active Storage Tanks (HAST) (10) (Fig. 1.1d) for cooling prior to vitrification.

Corroded fuel cladding (sludge) has complex chemical and physical properties, with particles of varying size, density, shape, settled and dispersed in an aqueous medium which is maintained at pH 11 but includes many cationic species (7). At Sellafield, approximately 1200-1500 m^3 of radioactive sludge composed of primarily $Mg(OH)_2$ is stored in the First-Generation Magnox Storage Pond (FGMSP) (Fig. 1.1a-b) (1, 7, 11). With limited land availability and FGMSP being located in the centre of the Sellafield site, challenges to empty these ponds and treat the sludge for suitable long term storage have been encountered over several decades. Some of the challenges relate to the remobilization of settled sediment which exhibits very high yield stresses, settled sediments which hide uncorroded disposed items (tools), and overturned skips which may contain hydrogen.

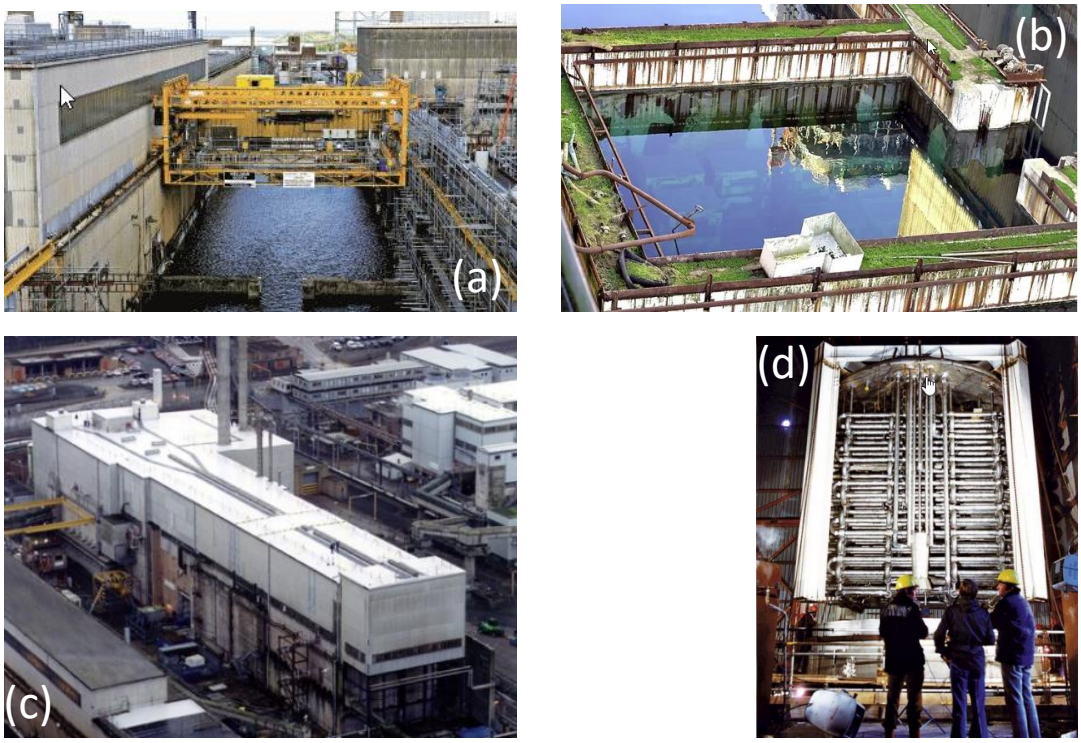

Figure 1-1. The main legacy waste storage buildings at Sellafield UK (1), (a-b)The First Generation Magnox Storage Ponds (FGMSP), (c) Magnox swarf storage silos (MSSS) (12) (d) Highly Active Storage Tank (HAST) (13).

In order to understand the rheology of the settled sludge and determine how the sludge can be processed for long-term interim storage, many attempts to measure the rheology of the sludge have been made, showing a wide range of rheological properties, with sediments exhibiting yield stresses > 1000 Pa (14). The potential to process yield stress fluids is undesirable, along with the potential for high yield stress sludges to re-develop when stored in the interim containers. Therefore, a need to prepare sludges such that the undesirable properties do not develop is highly sought.

The estimated cost to clean up the Sellafield site by 2120 is now $121 billion (15). A substantial proportion of this cost is due to the short-to-medium phase of the legacy waste clean-up that is comprised of three stages: (i) the retrieval of the legacy nuclear wastes from ponds and silos (which has been earmarked to be completed by 2036); (ii) the treatment of the retrieved effluent, and; (iii) the Post Operational Clean Out phase of THORP (the fuel reprocessing facility).

Similar to the UK, the US has challenges with the recovery and long-term storage of legacy waste sludge. Unlike the UK, the sludge is alumina due to the aluminium fuel cladding (Fig. 1-2). The legacy waste is mainly stored in tanks adjacent to K-basins reactors (4, 16), while secondary waste streams from historic reprocessing activities are stored in large underground single and double-shell tanks.

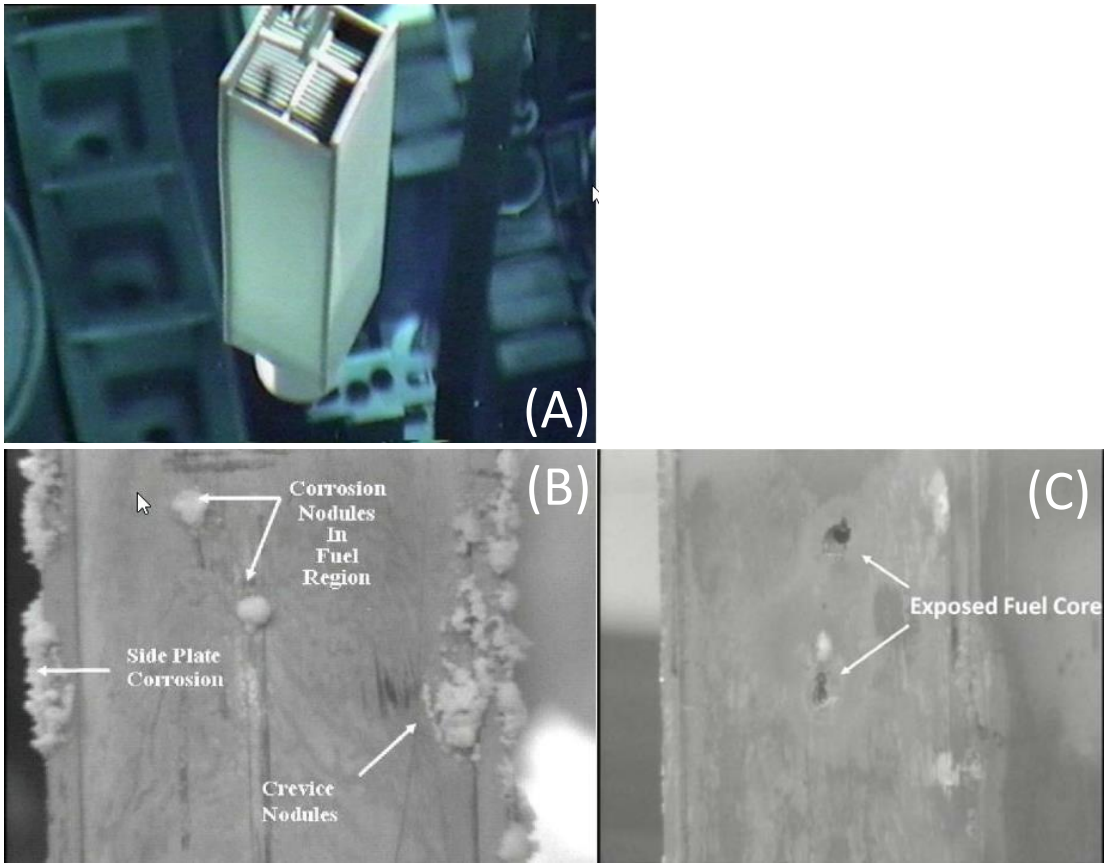

Figure 1-2. Spent nuclear fuel assembly of aluminium-base cladding stored in water (A). Corroded spent nuclear fuel assembly (B and C). Pictures were taken from Vinson et al. (17).

From the two reactors on the Hanford site, 60000 metric tons of spent HLW containing aluminium clad uranium metal fuel was received at the two K-basins (18). The sludge is composed of aluminium base corrosion products accounting for almost 77% of total waste (18), uncorroded uranium, ferrous corrosion products and chromium (~ 3%) products, spalled concrete and windblown sand (19) contaminated with transuranics and fission products (16). In 2007, a significant volume of this sludge was recovered (20) with further treatment of the sludge still on hold at a waste isolation pilot plant (WIPP) in New Mexico (21).

The underground storage tanks at Hanford contain huge quantities of sludge and hydrogen, which is stored at a great safety risk. Within 149 single and 28 double-shell tanks (22), approximately 200000-250000 m^3 (23) of sludge waste is stored. These underground tanks are up to 23 m in diameter with a capacity of 3800 m^3 (22), indicating their much larger size than the MSSS tanks. The contained waste has two distinct phases namely: a sludge of oxides, aluminates, silicates; and a supernatant layer of contaminated water containing soluble caesium, strontium, and technetium (24, 25). Some of the salts in the water have cemented the sludge material through precipitation reactions, and a carbonate rich mineral crust is observed on top of the waste (26).

There exists variation between the contents in the four tank farms which includes uncertainties in concentration and composition of the waste (25). For example, the U-farm contains bismuth, sodium and nitrate rich secondary reprocessing wastes from lanthanum fluoride decontamination (27), the S and SX-farms contain wastes from early REDOX reprocessing operations, with higher activity waste in the SX-farm tanks, and the BY-farms contain metal and caesium scavenging wastes (27). It has been reported that 67 of the single-shell tanks have leaked, causing a radionuclide plume to develop under the site. As such, these wastes have been transferred to the larger double shell tanks (28, 29). Besides the chemical variation, the wastes are also physically diverse, with yield stresses varying from 30 Pa to 6000 Pa (27, 30).

Based on the similar issues encountered in the UK and US, the current study has focused on modifying the rheology of alumina based systems. While being more relevant to the US sludge problem, the study of alumina systems allows for conditions away from the particle iso-electric point to be considered, something which is not easily achieved with $Mg(OH)_2$, due to its buffering potential to the pH iso-electric point.

The research will seek to elucidate the physical and chemical properties that govern the flowability and stability of nuclear waste sludges. The specifics of this study is to better understand the particle-particle interactions that occur in heterogeneous colloidal systems and manipulate those interactions so the sludge properties can be tuned for favourable flow and stability properties. The colloid species used throughout the study are aluminium oxide and silica, with alumina mimicking the main particle species encountered in the US legacy wastes and the silica being the flow modifier. A focus is given to measuring the rheology of the concentrated particulate suspensions and understanding the potential to modify the suspension yield stress.

It is commonly known in a shear flow that the mobility of spheres is much easier (i.e. lower viscosity at an equivalent solids concentration) than that of rods and plates, or irregular-shaped particles, a consequence of the greater apparent volume fraction induced by the rotation of irregular-shaped particles. As such, the research hypothesis relates to the modification of the flow of

irregular-shaped particles by blending with smooth, spherical particles, in principle lowering the yield stress of concentrated solid suspensions. Such flow modification would be beneficial to the transport of legacy waste and the safe storage of waste in long-term interim storage containers. It is worth noting that the flowability of high solids content suspensions is of great practical applicability to many industries such as mining (transport, separation settling, separation flotation), pharmaceutical manufacturing (powder flowability and compaction), paints and pigment manufacturing (flowability and film formation) and water treatment (sludge processing and dewatering).

1.1 Research Hypothesis

The flowability and stability of a suspension of irregular-shaped particles (alumina) can be manipulated by dilute blending with colloidal spherical particles.

1.2 Research Objectives

- Develop a robust experimental test method to measure the yield stress of heterogeneous suspensions;
- Demonstrate behavioral modification of Al_2O_3 sludges by blending with silica nanospheres. Identify critical conditions to remove the sludge yield stress;
- Determine the effect of sample aging on the measured yield stress.

1.3 Thesis layout

- Chapter 2 covers some of the fundamental science underpinning the study, as well as providing a brief overview some of the key literature which has inspired to work.
- Chapter 3 provides a detailed description of the materials and experimental techniques used throughout the study.
- Chapter 4 provides a comprehensive discussion on developing a reproducible an accurate method to measure the yield stress high solids content suspensions.
- Chapter 5 discusses the main findings of the research wherein the rheology of high solids content suspensions is successfully modified by blending a minor component of colloidal silica to a major component of colloidal alumina.
- Chapter 6 highlights the findings of a gelling phenomenon which was observed in a no yield stress blended suspension with a relatively high colloidal silica content.
- Chapter 7 brings together the main findings of the research and provides three options for further work which will provide greater clarity on optimizing the system for industrial application.

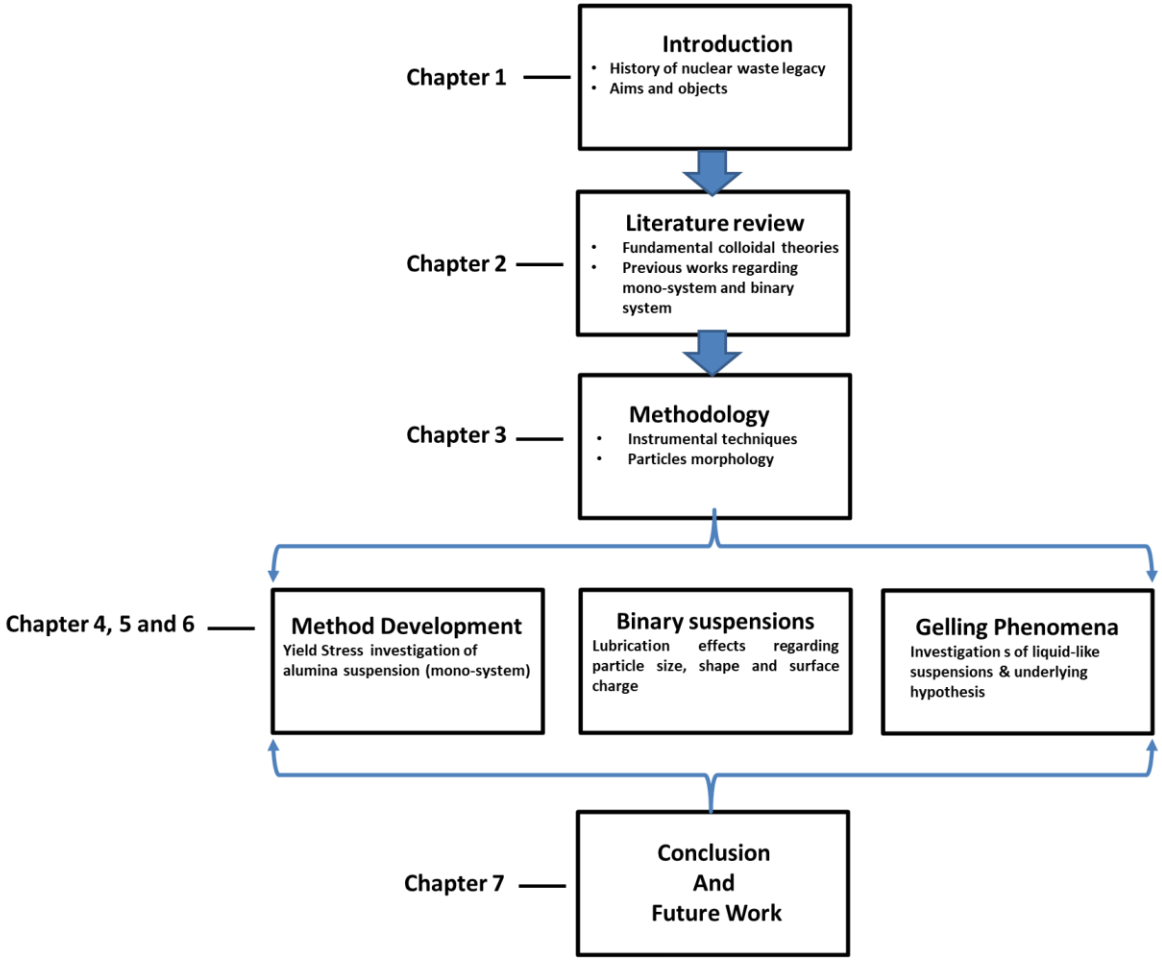

Figure 1-3. Thesis layout.

References

1. Hastings, J.J., Rhodes, D., Fellerman, A.S., McKendrick, D. and Dixon, C. New approaches for sludge management in the nuclear industry. *Powder Technology.* 2007, **174**(1), pp.18-24.
2. Kam, S.I., Gauglitz, P.A. and Rossen, W.R. Effective Compressibility of a Bubbly Slurry: I. Theory of the Behavior of Bubbles Trapped in Porous Media. *Journal of Colloid and Interface Science.* 2001, **241**(1), pp.248-259.
3. Sherwood, D.J. and Eduardo Sáez, A. The start of ebullition in quiescent, yield-stress fluids. *Nuclear Engineering and Design.* 2014, **270**, pp.101-108.
4. Delegard, C.H., Sinkov, S.I., Chenault, J.W., Schmidt, A.J., Welsh, T.L. and Pool, K.N. Determination of uranium metal concentration in irradiated fuel storage basin sludge using selective dissolution. *Journal of Radioanalytical and Nuclear Chemistry.* 2014, **299**(3), pp.1871-1882.
5. Parry, S.A., O'Brien, L., Fellerman, A.S., Eaves, C.J., Milestone, N.B., Bryan, N.D. and Livens, F.R. Plutonium behaviour in nuclear fuel storage pond effluents. *Energy & Environmental Science.* 2011, **4**(4), pp.1457-1464.
6. Watson, J.H.P. and Ellwood, D.C. The removal of the pertechnetate ion and actinides from radioactive waste streams at Hanford, Washington, USA and Sellafield, Cumbria, UK: the role of iron-sulfide-containing adsorbent materials. *Nuclear Engineering and Design.* 2003, **226**(3), pp.375-385.
7. Jackson, S.F., Monk, S.D. and Riaz, Z. An investigation towards real time dose rate monitoring, and fuel rod detection in a First Generation Magnox Storage Pond (FGMSP). *Applied Radiation and Isotopes.* 2014, **94**, pp.254-259.
8. Baldwin, N. Remediating Sellafield: A New Focus for the Site. In: *International Conference on Radioactive Waste Management and Environmental Remediation*, 2003, pp.35-40.

9. Le Clere, S. Magnox Swarf Storage Silo Liquor Effluent Management: Sellafield Site, Cumbria, UK. In: *International Conference on Radioactive Waste Management and Environmental Remediation*, 2011, pp.67-75.
10. Liland, A., Lind, O.C., Bartnicki, J., Brown, J.E., Dyve, J.E., Iosjpe, M., Klein, H., Lin, Y., Simonsen, M., Strand, P., Thørring, H., Ytre-Eide, M.A. and Salbu, B. Using a chain of models to predict health and environmental impacts in Norway from a hypothetical nuclear accident at the Sellafield site. *Journal of Environmental Radioactivity.* 2020, **214-215**, p.106159.
11. Gregson, C.R., Goddard, D.T., Sarsfield, M.J. and Taylor, R.J. Combined electron microscopy and vibrational spectroscopy study of corroded Magnox sludge from a legacy spent nuclear fuel storage pond. *Journal of Nuclear Materials.* 2011, **412**(1), pp.145-156.
12. Le Clere, S. Magnox Swarf Storage Silo Liquor Effluent Management: Sellafield Site, Cumbria, UK. In: *ASME 2011 14th International Conference on Environmental Remediation and Radioactive Waste Management*, 2011, pp.67-75.
13. Dobson, A., Phillips, C. and America, B. High Level Waste Processing in the UK–Hard Won Experience that can Benefit US Nuclear Cleanup Work. *Waste Management.* 2006, **6**.
14. Morgan, S.P. *Review of the processing and characterisation of legacy ponds and silos sludges and test materials.* UK, 2020.
15. NAO. *The Nuclear Decommissioning Authority: progress with reducing risk at Sellafield.* UK, 2018.
16. Knollmeyer, P., Phillips, C. and Townson, P. *Progress with K Basins sludge retrieval stabilization & packaging at the Hanford nuclear site.* Hanford Site (HNF), Richland, WA, 2006.
17. Proceeding, I. Management and storage of research reactor spent nuclear fuel. In: *Proceeding of a technical meeting held in Thurso*, 2009.

18. Snow, L.A., Lumetta, G.J., Fiskum, S. and Peterson, R.A. Boehmite actual waste dissolution studies. *Separation Science and Technology.* 2008, **43**(9-10), pp.2900-2916.
19. Schmidt, A.J. and Zacher, A.H. *Composition and Technical Basis for K Basin Settler Sludge Simulant for Inspection, Retrieval, and Pump Testing.* Pacific Northwest National Lab.(PNNL), Richland, WA (United States), 2007.
20. GERBER, M. Final Frontier at Hanford Tackling The Central Plateau. *Radwaste Solutions.* 2008, **15**(3).
21. Witwer, K. Preliminary Demonstration of GeoMelt Treatment of Hanford's K-Basin Sludge. In: *International Conference on Radioactive Waste Management and Environmental Remediation*, 2011, pp.747-752.
22. Prugue, X. Development of a mechanical based system for dry retrieval of single-shell tank waste at Hanford. In: *International Conference on Radioactive Waste Management and Environmental Remediation*: American Society of Mechanical Engineers, 2013, p.V001T002A032.
23. Gephart, R.E., Lundgren, R.E. and Gephart, R.E. *Hanford tank cleanup: a guide to understanding the technical issues.* Battelle Press Columbus, Ohio, 1998.
24. Lukens, W.W., Shuh, D.K., Schroeder, N.C. and Ashley, K.R. Identification of the non-pertechnetate species in Hanford waste tanks, Tc (I)− carbonyl complexes. *Environmental science technology.* 2004, **38**(1), pp.229-233.
25. Mashal, K., Harsh, J.B., Flury, M., Felmy, A.R. and Zhao, H. Colloid formation in Hanford sediments reacted with simulated tank waste. *Environmental science technology.* 2004, **38**(21), pp.5750-5756.
26. Page, J.S., Reynolds, J.G., Ely, T.M. and Cooke, G.A. Development of a carbonate crust on alkaline nuclear waste sludge at the Hanford site. *Journal of hazardous materials.* 2018, **342**, pp.375-382.
27. Rassat, S.D., Mahoney, L.A., Wells, B.E., Mendoza, D.P. and Caldwell, D.D. *Assessment of Physical Properties of Transuranic Waste in*

Hanford Single-Shell Tanks. Pacific Northwest National Lab.(PNNL), Richland, WA (United States), 2003.

28. Chen, G., Flury, M., Harsh, J.B. and Lichtner, P.C. Colloid-facilitated transport of cesium in variably saturated Hanford sediments. *Environmental science technology.* 2005, **39**(10), pp.3435-3442.
29. Deng, Y., Harsh, J.B., Flury, M., Young, J.S. and Boyle, J.S. Mineral formation during simulated leaks of Hanford waste tanks. *Applied Geochemistry.* 2006, **21**(8), pp.1392-1409.
30. Wells, B.E., Jenks, J.W., Boeringa, G.K., Bauman, N.N., Guzman, A.D., Arduino, P. and Keller, P. *Lateral Earth Pressure at Rest and Shear Modulus Measurements on Hanford Sludge Simulants.* Pacific Northwest National Lab.(PNNL), Richland, WA (United States), 2010.

Chapter 2

Literature Review

Synopsis

The rheology of particle suspensions is strongly governed by several parameters including particle size, particle shape, solids concentration, and for colloidal particles, those of which are influenced by the thermal energy of the system, the strength of the particle-particle interaction energy. This chapter provides an overview of the fundamental theory that describes colloidal particle behavior and how the interaction forces between particles can be tuned by modifying the water chemistry. The interaction strength between colloidal particles is explored in the following chapters to determine if modifying the flow of concentrated particle suspensions critically depends on either weakly attractive or weakly dispersive interactions between the two particle species.

2.1 Introduction to Colloids

A colloidal system is practically defined as a dispersion of small particles in a continuous phase. The dispersed species have at least one dimension in the sub-micron range. Colloids are now used widely in nano-medicines, health care products, food products and even in energy conservation (1, 2). Colloidal dispersions are not only used in industrial processes such as fast moving consumer goods, pharmaceuticals and mineral processing, but colloidal dispersions can also be found in nature.

Interaction between colloidal particles is governed by random collisions caused by (i) intrinsic Brownian motion; (ii) external forces such as shear and hydrodynamic forces as well as thermal energy; and (iii) gravitational forces (3-5). There are only two outcomes from the particle collisions; either the particles simply rebound off one another or the particles aggregate together, with the aggregation being either irreversible or reversible. The formation of aggregates in a colloidal system makes the system unstable, due to an increase in the effective particle diameter (increased mass) (2).

2.2 Brownian Motion

In 1827, Robert Brown observed the random motion of pollen grain dispersed in water under a microscope. This phenomenon of random motion of solid particles is called Brownian motion. The molecules of the liquid medium are subjected to thermal and kinetic motions, and begin to vibrate, which results in the collision between each other as well as the solid particles. The random nature of the collisions initiate the solid particles to move in an arbitrary path (6, 7). Figure 2-1 shows the random walk of a Brownian particle.

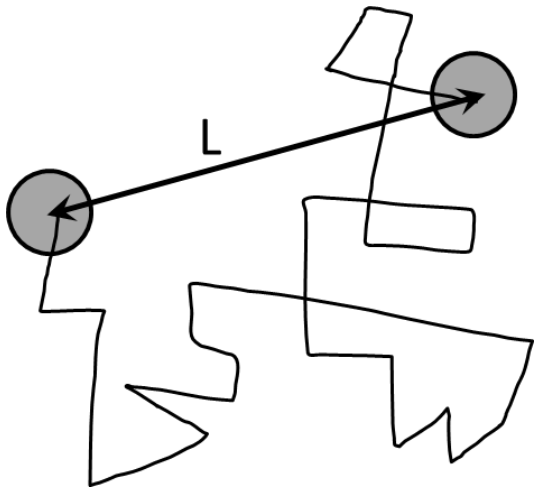

Figure 2-1. Illustrates the random movement of Brownian particle. L is shown as the travel distance of the particle between two points over the time. Redrawn from ref. (6).

Further studies on Brownian motion by Einstein and Smoluchowski proposed the diffusion of particles from a high to a low concentrated region. Einstein describes the mathematical equation to determine the average distance (L) travelled by the Brownian particle over a fixed period of time (t) (8, 9) and is given by:

$$L = \sqrt{\frac{2kT}{3\pi x\mu}t} \qquad \textbf{Eq. 2.1}$$

where k is the Boltzmann constant = 1.381 x 10^{-23} J/K, T is the temperature in K, x is the particle diameter and μ is the viscosity of the fluid. It can be seen from Eq. 2.1 that distance travelled by the colloidal particle is proportional to temperature and inversely proportional to the particle size and viscosity of the fluid.

2.3 Van der Waals Forces

Electrodynamic interactions which include Keesom, Debye and London dispersion forces are often described as van der Waals forces. These forces arise between polar and non-polar molecules.

An atom consists of a positive nucleus and negative electrons evenly distributed in the orbit of an atom. At any moment in time, there can be an uneven distribution of electrons which causes the formation of a temporary dipole. These dipoles can induce temporary dipoles in neighbouring atoms inducing attraction. This attractive force is illustrated in Fig. 2-2. The overall attractive energy between two particles is the sum of all dipoles of all the atoms in each particle (6, 10).

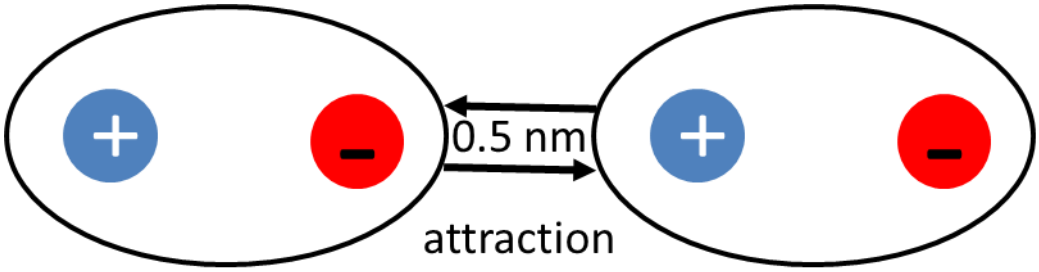

Figure 2-2. Schematic illustration between two atoms of two particles, which are under the influence of instantaneous induce dipole-dipole (Van der Walls) attraction. The blue circle in the atom is shown as a nucleus with a positive charge (+). The red circle in the atom is shown as a cloud density of electrons with obtaining a negative charge(-). A dipole moment forms within an atom as positive charge nucleus and negative charge of electrons do not interact with each other, however when a neighbouring atom approaches then negative and positive charges attract between both atoms due to Coulomb's law.

The total van der Waals interaction energy (V_{vdw}) or force (F_{vdw}) between two spherical particles is described by Eqs. 2.2 and 2.3, respectively

$$V_{vdw} = -\frac{A_H d}{24x} \qquad \textbf{Eq. 2.2}$$

$$F_{vdw} = -\frac{A_H d}{24x^2} \qquad \textbf{Eq. 2.3}$$

where (d) is the separated distance between two particles, x is the particle diameter and (A_H) is the Hamaker constant, which is material specific. The sign and magnitude of the Hamaker strongly influences the nature of the van der Waals forces. If the Hamaker constant is positive then the interaction van der Waals forces are attractive, and repulsive for a negative Hamaker constant. Hamaker constants for alumina and silica with intervening medium of water are shown in Table 2-1.

Table 2-1. Hamaker constant of two material oxides with suspending fluid (6).

Particle 1	Suspending fluid	Particle 2	A_H(J)
Alumina	Water	Alumina	5.0×10^{-20}
Silica	Water	Silica	0.7×10^{-20}

2.4 Surface Charge

Introducing colloidal particles into an aqueous environment causes the formation of surface charges. There are a number of mechanisms by which surface charge can be obtained; (11-14)

1. Ionisation – one of the surface chemical species of the particle dissociates into the aqueous environment;
2. Ion adsorption – the unequal adsorption of cations and anions;
3. Ion dissolution – one of the chemical species on the surface of the particle dissolves into the aqueous environment.

Ion dissolution is the underlying mechanism of surface charge for the particles considered in the current study. The surface ion dissolution mechanism of an oxide material (M) is shown by Eqs. 2.4 and 2.5:

$$\mathbf{M-OH+\ H^{+}\ \overset{K_a}{\rightarrow}\ M-OH_2^{+}} \qquad \textbf{Eq. 2.4}$$

$$\mathbf{M-OH+\ OH^{-}\ \overset{K_b}{\rightarrow} M-O^{-}+\ H_2O} \qquad \textbf{Eq. 2.5}$$

Where $H^+$and OH^- are potential-determining ions and M represents metal oxide particle (11-14).

Alumina (Al_2O_3) is the primary metal oxide particle used throughout the study. When alumina is submerged in water it forms hydroxyl groups as Al-OH. The magnitude of surface ion dissolution depends on the pH of the medium. Alumina surface is highly negative at high pH as it forms $Al\text{-}O^-$ bonds while at low pH, alumina surface is highly positive due to the formation of $Al\text{-}OH_2^+$ (12). Equations 2.4 and 2.5 suggest there is a distinctive pH where a particle surface has equal number of positive and negative charges, and the particle has a net zero charge. This value of pH is called the isoelectric point (IEP) (10, 12, 14).

2.5 Electrostatic Double Layer Forces

In 1853, Helmholtz proposed the electrostatic double layer as a simple capacitor. This model indicates that counter ions are attracted to a charged surface while co-ions are repelled (15, 16). The Gouy-Chapman model introduced a diffuse layer where the electrical charge potential decreases exponentially with distance away from the charged surface (17). Further development by Otto Stern in 1924 (18) suggested that some ions adsorb to the surface, while some ions form the diffuse layer. This was adapted by Grahame who divided the Stern layer into two layers: an inner layer (inner Helmholtz layer) and an outer layer (outer Helmholtz layer). Grahame also introduced the idea of “specifically adsorbed ions”. These ions can enter the

Stern layer and adsorb to the solid surface due dehydration pf the solvation shell (16, 19).

The electrical double layer is shown in Fig. 2-3, where a solid particle is immersed in the aqueous solution to form a negative surface charge.

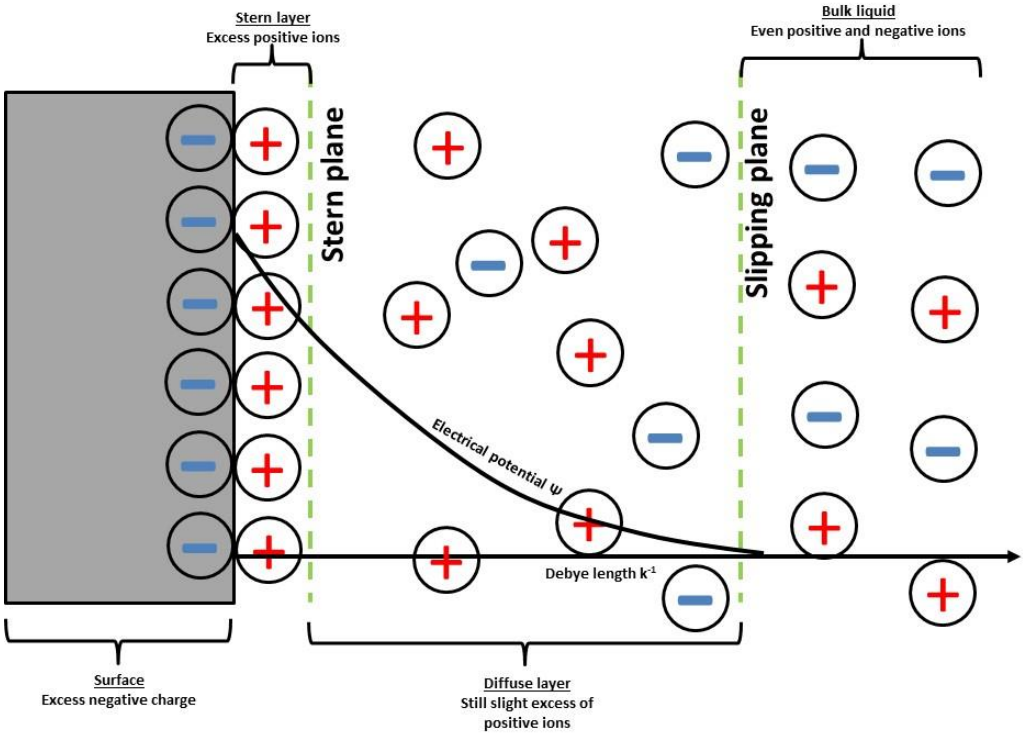

Figure 2-3. Schematic of Gouy-Chapman-Stern model of electrical double layer in a dispersed medium around a negatively charged solid surface. Stern plane occupied with counter positively charge ions. Diffuse layer is having slightly more positive ions than negative ions. Even positive and negative number of ions are showing in the bulk can also be observed.

The zeta potential is the potential at the slipping plane relative to the bulk fluid. Even though the zeta potential cannot be directly measured it can be determined via the electrophoretic mobility. When considering the stability of

colloidal suspensions, the general “rule of thumb” is that when the zeta potential value is less than $\pm$30mV the colloidal system is unstable, and when the zeta potential value is greater than $\pm$30mV then the measured dispersion is stable. The stability can be controlled by manipulating the zeta potential by varying the i) suspension pH and ii) the ionic concentration of the dispersion medium(20).

Johnson et al. added a monovalent salt, KCl, of different concentrations to alumina suspensions (Fig. 2.4) (21), finding that the magnitude of zeta potential decreases with increasing the salt concentration. The electrical double layer is reduced due to a high number of ionic species which increases the Debye length (κ^{-1}).

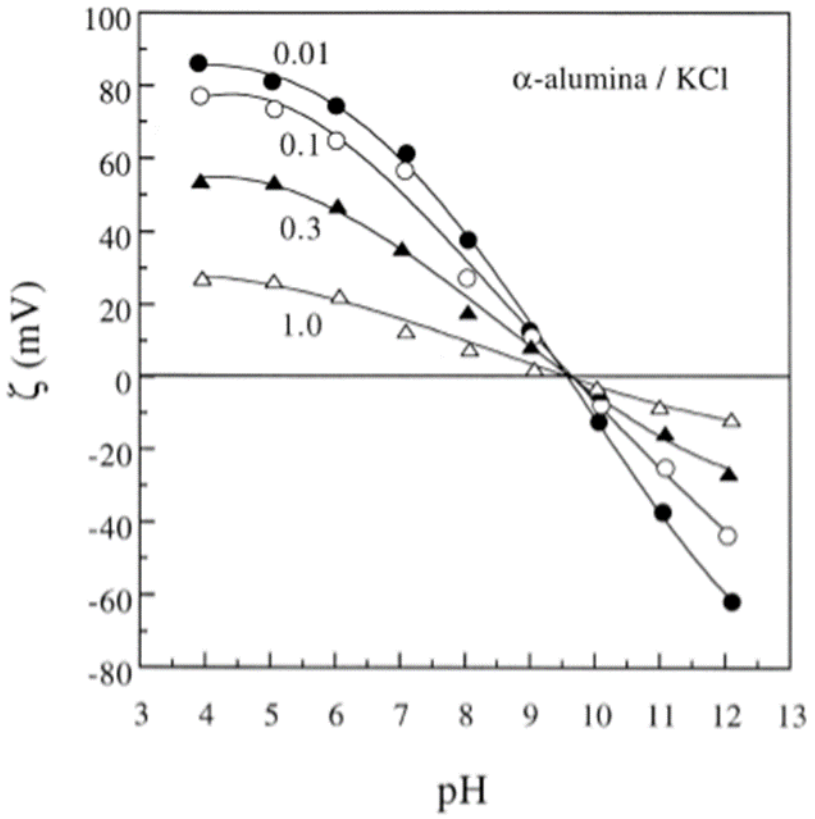

Figure 2-4. Data of zeta potential of α-alumina particles as the function of pH. Monovalent salt, KCl was varied as a background electrolyte. Zeta potential decreased with increasing the salt concentration (M) due to screening or compression of the EDL (taken from ref. (Johnson, Franks et al. 2000))

2.6 DLVO Theory

The DLVO theory as described by Derjaguin and Landau (22) and Verwey and Overbeek (23) describes the total interaction energy (V_T) between two surfaces:

$$\boldsymbol{V_T = V_A + V_R} \qquad \textbf{Eq. 2.6}$$

where (V_A) is the energy associated to the van der Waals forces and (V_R) the energy associated to the electrostatic repulsive forces. Equation 2.7 describes the repulsive energy arising from the electric double layer forces:

$$V_R = 2\pi\varepsilon r\zeta^2 \exp(-\kappa d) \qquad \textbf{Eq. 2.7}$$

where the dielectric constant of the solvent is represented by ε, the particle radius is represented by r, the zeta potential is represented by ζ, Debye-Hückel screening parameter which is related to concentration of electrolyte is represented by κ, which is given by (24, 25)

$$\kappa = \left(\frac{2e^2 N_A c z^2}{\epsilon k T}\right)^{1/2} \qquad \textbf{Eq. 2.8}$$

where e is the elementary charge, N_A the Avogadro's number, c the electrolyte concentration, z the valencey, ϵ the permittivity of a material, k the Boltzmann constant, T the absolute temperature in K, and κ the Debye length. The electrical double layer thickness (m) is given by $1/\kappa$. It can be seen from the above equations that an increase in the electrolyte concentration increases κ and this results in a decrease of the electrical double layer thickness. Vice-versa decreasing the electrolyte concentration decreases κ which then increases the magnitude of the electrical double layer, thus increasing the repulsive forces. Overlapping of the EDLs of two approaching particles causes the repulsive component of inter-particle interaction. The overlap of EDLs

creates localised areas of non-equilibrium counter-ions concentration which is osmotically unfavourable and hence leads to repulsion as the osmotic pressure is greater than the surrounding bulk fluid (26).

The applicability of the classical DLVO theory is governed by five assumptions (10):

- The surfaces involved must be flat and infinite (this is true for colloidal particles);
- The surface charge must be uniform in density;
- The surface charge must not become redistributed which results in the electric potential of the surface remaining constant;
- The electric potential must also remain unchanged such the concentration profile of the ions and counter-ions that determine the surface charge must not change;
- The only influence exerted by the solvent is via a constant dielectric.

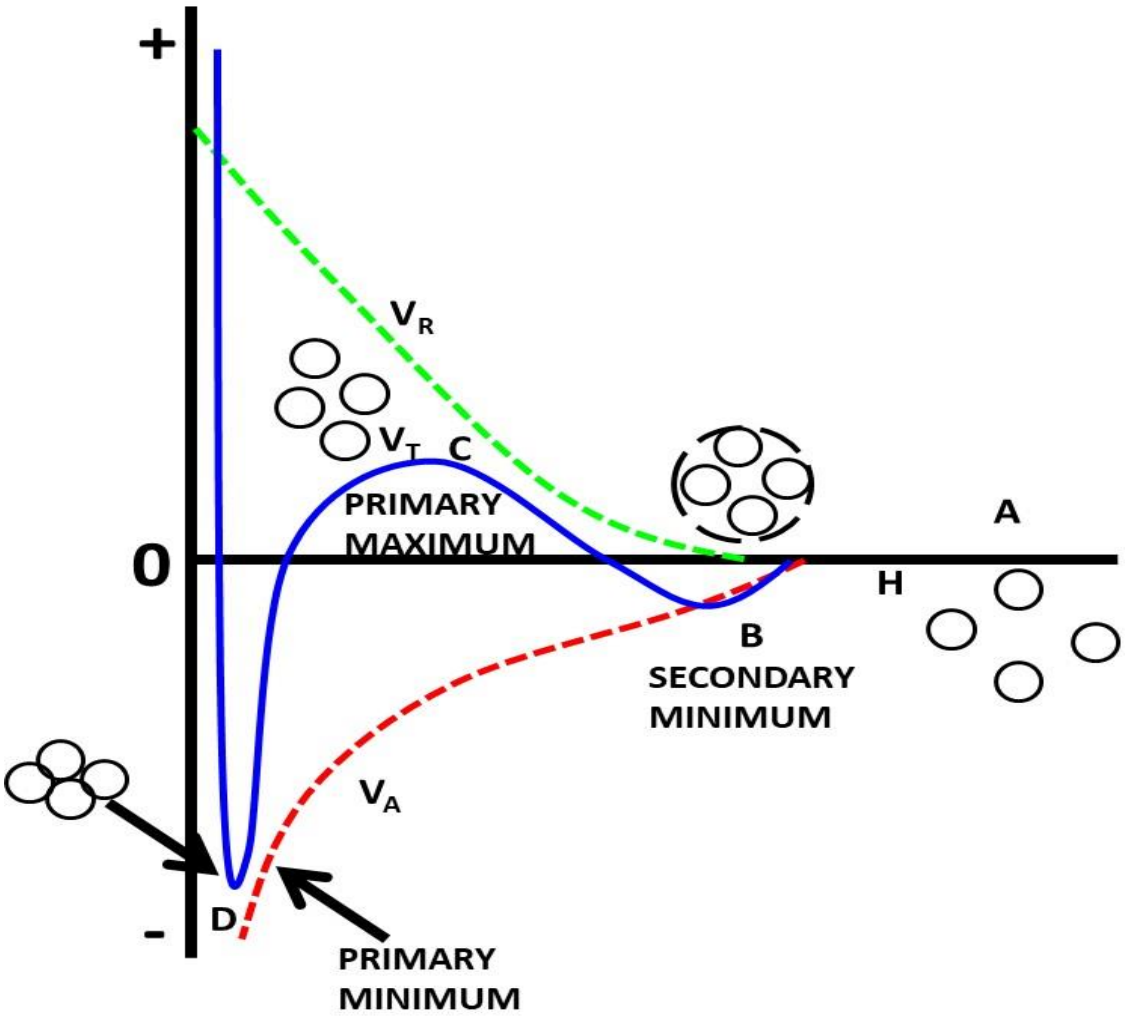

Figure 2-5. A schematic representation of the overall potential energy profile and its contributing parts. V_A (the sum of all energy caused by van der Waals attractive forces); V_R (the sum of all energy from the repulsive interactions due to the EDL) ; V_S is the energy resulting from solvent forces and V_T is the total energy of interactions (adapted from(2)).

Figure 2-5 is a schematic showing of the interaction potential as two particles approach contact. In the region labelled (A) the colloidal system is in a dispersed and stable state, the particles are non-interacting. When particles begin to approach one another both V_A and V_R increase as illustrated by their respective dashed lines in Fig. 2-5. Initially, the increase in V_A is greater than

V_R thus the attractive force dominates at these larger inter-particle separations, which is represented by region (B), and is a weak secondary minimum at the approximate inter-particle separation distance of 60 nm and this is called reversible coagulation (2). When the inter-particle distance has decreased to approximately 20 nm the effects of V_R have now increased to the extent that a large energy barrier has formed to inhibit the continuing approach of the particles towards one another; which is represented by region (C). There is a critical distance that the approaching particles must reach (point D) where the V_A is once again dominating V_R such that irreversible aggregation occurs forming strong aggregates (2). The intrinsic kinetic energy of the approaching particles dictates the behaviour of the particles after they collide. If the resulting kinetic energy of the particle prior to the collusion is greater than that of the energy barrier to aggregate, then point (D) on the graph is attained; the primary minimum due to aggregation. However, if the kinetic energy was not sufficient to overcome the energy barrier then the particles return to the secondary minimum region; where a stable dispersions forms and/or weak particle associations are formed. In such cases the aggregates formed are usually easily redispersed by changing the solvent environment or gentle agitation (2).

2.7 Non-DLVO Forces and Heteroaggregation

Heteroaggregation is a term used to describe aggregation in a colloidal system that has more than one type of particle species (1, 27, 28). The nature of the hetero-aggregate can be influenced by; (i) particle size, (ii) particle

shape, (iii) surface potential (-ve or +ve), (iv) magnitude of surface potential (v) surface composition (non-DLVO forces) (29). In 1965, Hogg et al. (30) derived equations that satisfy the potential energy interactions that occurred when a colloidal system contains dissimilar spherical particles. An approximation for low surface potentials was used. Thus it was possible to define an overall stability ratio that accounts for the interactions between like and unlike particles in the colloidal system.

While the total potential energy is once again defined by the attractive and repulsive terms, the theory had to account for dissimilar particles. Therefore, the attractive force is given by (1, 30);

$$\boldsymbol{V_{vdW} = -\frac{A_{123}}{6H}\frac{a_1 a_2}{(a_1+a_2)}} \qquad \textbf{Eq. 2.9}$$

The electrical double layer force between two dissimilar particles is:

$$\boldsymbol{V_R = -\frac{\pi\varepsilon_0\varepsilon_r a_1 a_2}{(a_1+a_2)}\left(2\psi_1\psi_2 \ln\left[\frac{1+e^{-\varkappa H}}{1-e^{-\varkappa H}}\right] + (\psi_1^2+\psi_2^2)\ln[1-e^{-2\varkappa H}]\right)} \qquad \textbf{Eq. 2.10}$$

where a is the radius of the particle, ε_0 is the permittivity of a vacuum, ε is the relative dieletric constant, κ is the inverse of the Debye length, H is the separation distance and the Hamaker constant is given by A. The subscripts of 1 and 2 represent the two different particle types (1). Summation of the two interaction forces is known as the HHF theory.

2.8 Yield Stress of High Solids Content Suspensions

Many researchers (31-33) have considered the shear yield stress of concentrated particle suspensions. Conventionally, the yield stress is described as ‘the minimum shear stress that must be applied to the material in order to produce a flow’ (34). Liddell and Boger considered shear stress to be the magnitude of stress at which the sludge tends to transform from elastic solid-like state to a viscous liquid-like state (31). As the particle concentration increases the gel point will be attained where the particles in the suspension interact with each other to form a three dimensional network structure (32-36). As such, the yield stress is the stress needed to rupture this network of particles and induce flow (32).

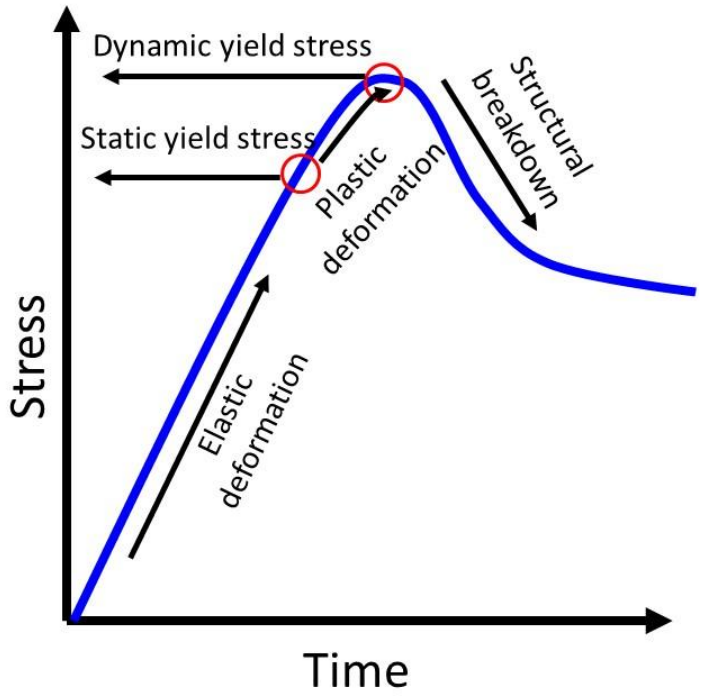

Figure 2-6. Schematic of classic shear stress response of a concentrated suspension against time in a rate controlled mode. Viscometer was used rotationally with vane geometry (adapted from (31)). Material behaves solid-like (elastic deformation) below the static yield stress. Static yield stress can be defined as the required stress to initiate the flow i.e. material does not recover fully once the stress is removed.

Two yield stress categories, static and dynamic yield stress have been suggested by Zukoski et al., see Fig. 2-6 (31, 37). Static yield stress is termed as the stress at which the material deforms up to a fixed finite amount, however on removal of stress the strain in the material is fully recovered, i.e. the material undergoes elastic deformation. Beyond this point a further increase in stress results in the dynamic yield stress where the material is in viscoelastic region. In this region, plastic deformation occurs where the strain in the material continues to increase at a non-steady rate and upon removal

of stress, partial strain recovery is obtained (31, 37). Beyond the dynamic yield stress, i.e. the viscous region, the particle network is destroyed and the suspension behaves like a viscous fluid.

Among the various methods for measuring the yield stress, the vane method is most relevant for sludge rheology. This method was initially developed by Boger, Nguyen and Keentok (32, 34, 38) to measure the shear yield stress of concentrated suspensions. The vane method is used in rate controlled mode which requires a slow and constant rotation of the vane, with the torque adjusted to maintain the rotational speed (Fig. 1-9) (32).

Considering the vane as a cylinder of known diameter, the dynamic yield stress (τy) can be calculated from the maximum torque measured on the rotating vane ($Tmax$) using Eq. 2.11 (21, 31, 38, 39).

$$\boldsymbol{\tau_y = \frac{6T_{max}}{(\pi D^2)(L+D)}} \qquad \textbf{Eq. 2.11}$$

Where L is length of submerged portion of the vane and D represents vane blade diameter. It is assumed that shearing only takes place in the cylindrical volume produced by the vane, where the diameter of the cylinder is the diameter of the vane. Researchers (31, 34, 40) found that this assumption may be inaccurate because the diameter of the sheared cone can be up to 5% larger than that of the vane.

2.9 Influence of Colloidal Forces on the Shear Yield Stress

The effect of modifying the colloidal interaction force to change the rheology concentrated particle suspensions has been studied by many researchers. Yang et al. considered the relationship between zeta potential and yield stress for TiO_2 suspensions, Figs. 2-7A and B (41).

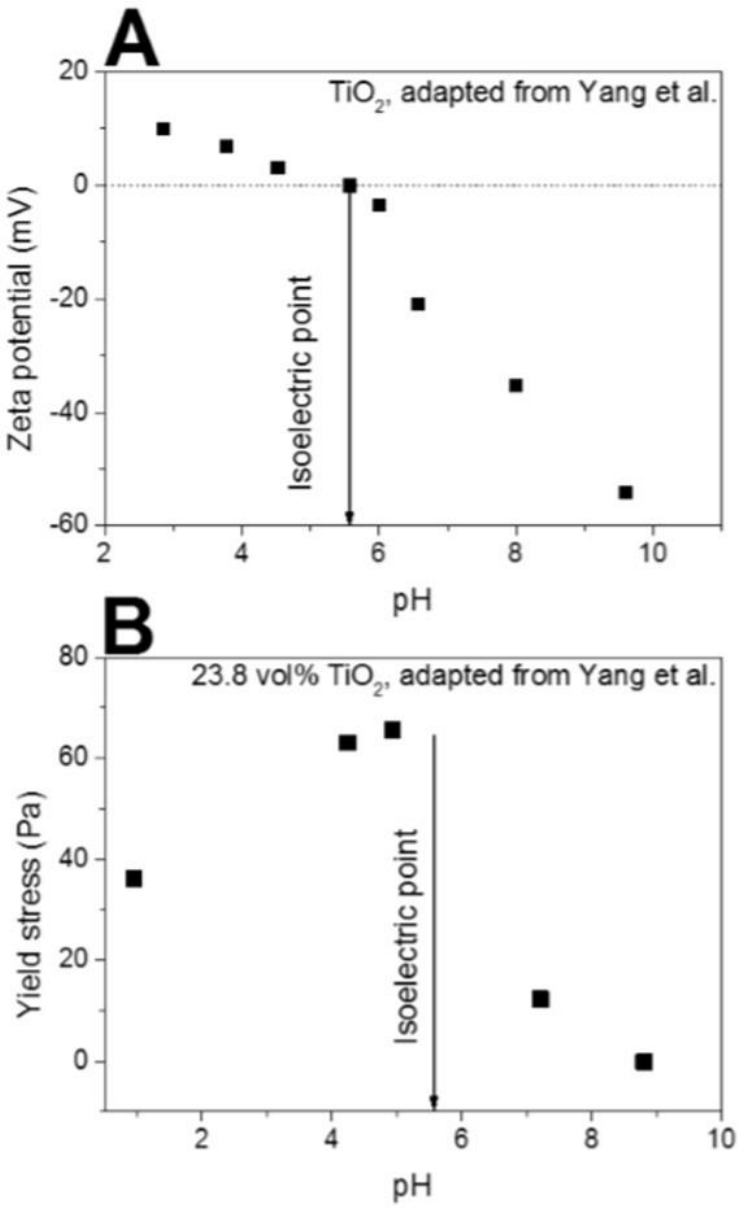

Figure 2-7. The influence of particle zeta potential (A) of TiO_2 on the suspension yield stress (B). The highest shear yield stress of 23.8 vol% of TiO_2 was found at the isoelectric point (B). Figure adapted from Yang et al. (42).

In this study the isoelectric point of TiO_2 was pH 5.7 (Fig. 2-7A) and was similar to the pH at which the maximum yield stress was measured. Similar findings were reported by Mikulášek et al. (43), Leong et al. (44-46), Scales et al. (33), Johnson et al. (21, 47, 48) and Franks et al. (49) for TiO_2, silica, α-alumina and zirconia suspensions. The mechanism responsible for changes in the bulk rheology of these suspensions was explained by the DVLO theory. It was shown that there is a decrease in the electrical double layer repulsive force as the system becomes dominated by the van der Waals forces of attraction, strengthening the overall inter-particle network and increasing the energy required to break the network, hence the increase in yield stress (Fig. 2-7B) (30). In addition to changes in the yield stress with suspension pH, increasing the electrolyte concentration will screen the surface potential of the particle and this again will increase the colloidal interaction strength and thus the yield strength of the concentrated particle suspension. Changes in the particle zeta potential due to altering the electrolyte concentration has been reported by (50, 51).

2.9.1 Effect of Solids Volume Fraction

The suspension yield stress can be increased by increasing the solids concentration due to more particle-particle contacts (21, 33, 44, 46), see Fig. 2-8 showing examples for alumina and zirconia suspensions (33) (44-46).

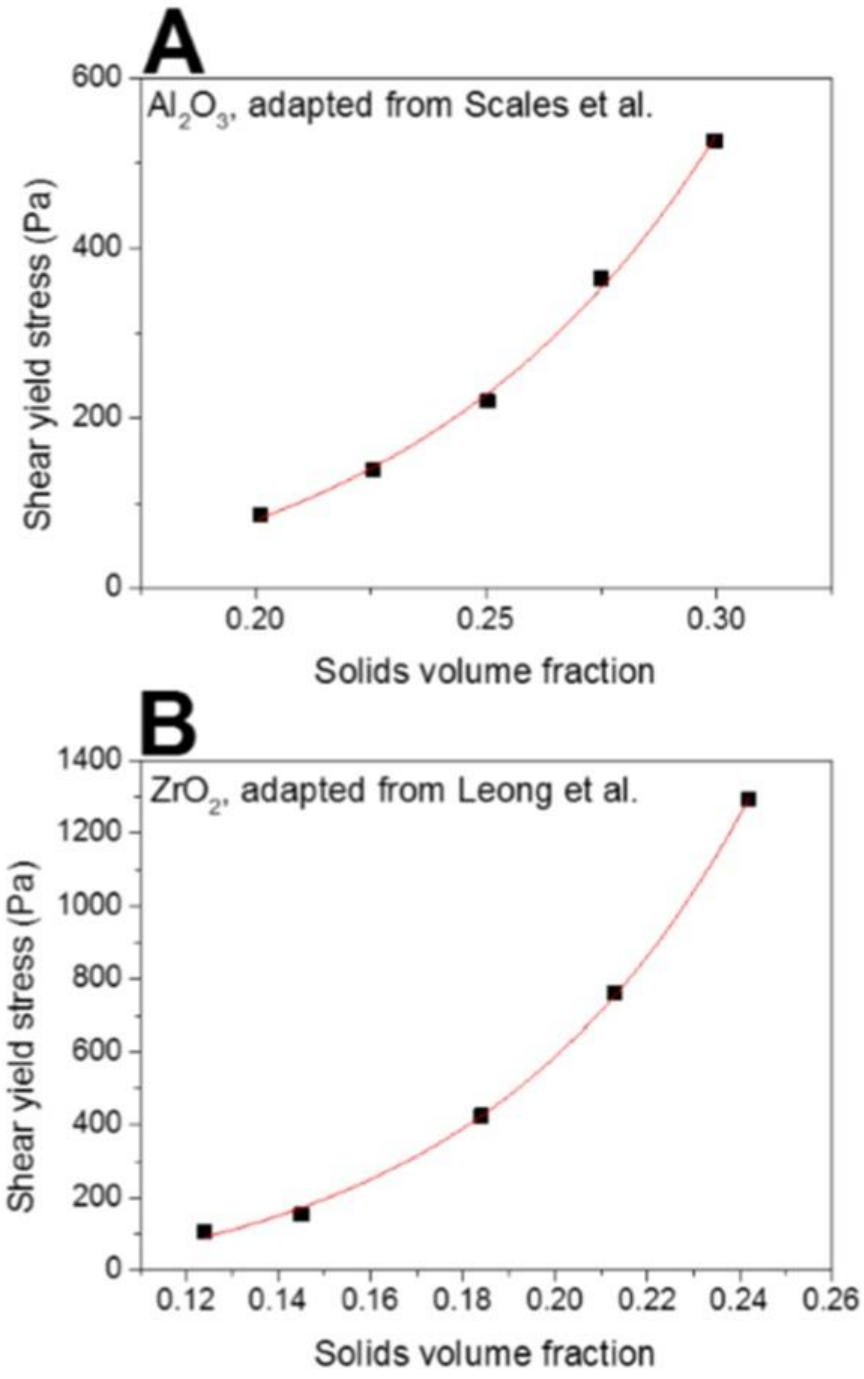

Figure 2-8. The relationship between shear yield stress and solid volume fraction of alumina (A)(adapted from (33)) and zirconia (B) (adapted from (44-46). The maximum yield stress values were found at the isoelectric point for (A) and (B).

The response of the shear yield stress as a function of the solids volume fraction is very similar to the change in relative viscosity as a function of solid volume fraction as explained by the Krieger and Dougherty model. The slight differences in the correlation between yield stress and solids volume fraction as shown in Fig. 2-8 for the alumina and zirconium dioxide particles can be due to a number of factors as will be explained below.

The influence of colloidal interaction strength on the shear yield stress of concentrated particle suspensions was studied by several researchers (52) (33) (48) (47). A good example of this was by (52) who studied the effect of solids volume fraction, particle size, electrolyte concentration, and electrolyte type on the pH dependent yield stress of α-alumina. Figure 2-9A shows the influence of solids volume fraction on the shear yield stress of alumina suspensions as a function of pH. For all suspensions, a bell-shaped curve was observed with the maximum yield stress measured in the region of pH 9.2. Increasing the solids volume fraction increased the yield stress at pH 9.2. The reason for the maximum yield stress is that the alumina particle has an isoelectric point at pH 9.2, hence when the particles are in the most aggregated state, yield strength of the suspension is at a maximum. As the pH is adjusted away from the isoelectric point and the particles become more dispersed (through greater electrostatic repulsive forces), the yield strength of the particle network gradually reduces and eventually when the particles become strongly charged (7.5 > pH > 11.2), the suspension exhibits no yield stress and the suspension is free flowing. This condition relates to the general rule of thumb regarding stable and unstable colloids. The authors also

showed that reducing the particle size increased the magnitude of the shear yield stress, see Fig. 2-9B. For an equivalent volume fraction, reducing the particle size will increase the number of particles in the suspension and thus increase the number of particle-particle contacts which consequently has a great influence on modifying the yield stress of a concentrated particle suspension. The effect of electrolyte concentration was also considered and showed a broadening of the bell-shaped yield stress distribution as a function of pH when the electrolyte concentration was increased from 0.01 M to 1.0 M. Such behavior is associated to the flattening of the zeta potential curve when the electrolyte concentration is increased due to increased charge screening of the particle surface potential. As such, in very high electrolyte concentrations, concentrated colloidal suspensions often exhibit yield stresses over a wide pH range (Fig. 2-9C). For the same electrolyte the particle isoelectric point is not shifted, hence the maximum in yield stress is observed at the same pH. However, if different electrolytes are used there is potential to observe the effect of specific binding of the potential determining ion and shifting the particle isoelectric point, as seen by $LiNO_3$ in Fig. 2-9D. A number of other researchers such as Prestidge (53), Firth (54), Leong et al (45), Hunter et al (55), Friend et al (56) and Avramidis et al (57) have shown similar outcomes for different concentrated suspensions which contain colloidal solid particles.

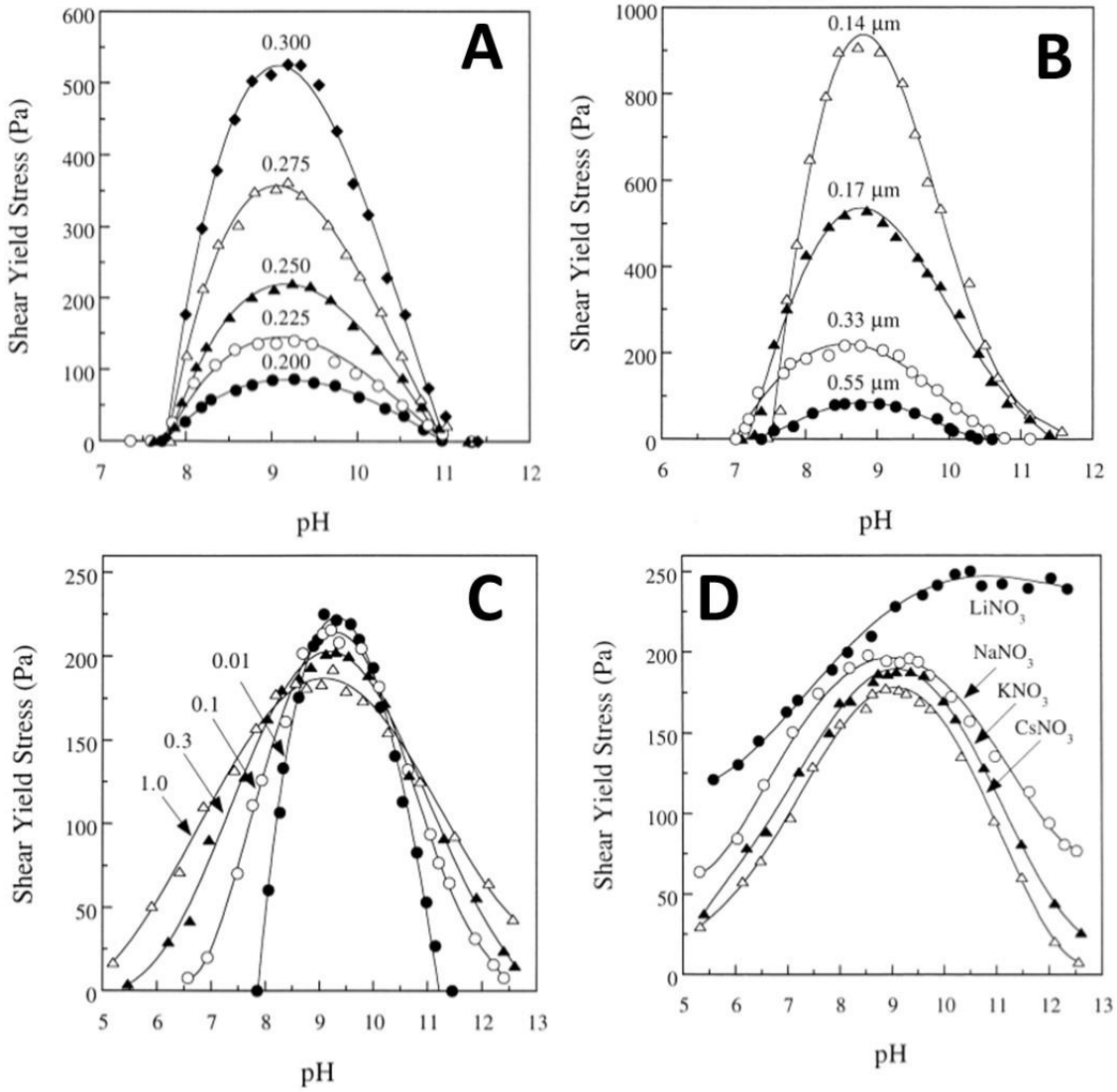

Figure 2-9. (A-D) shows the shear yield stress profiles of α-alumina as a function of pH. (A) increasing the solid volume fraction (Φ) of almost spherical α-alumina (300nm), KCl was used as a back ground electrolyte as 10^{-2} M. (B) varying the size of α-alumina particles (close to spherical shape) and concentration of KCl was fixed at 10^{-2} M. (C) increasing the concentration of KCl, whereas volume fraction of α-alumina (300nm) was fixed as 25 vol%. (D) $LiNO_3$, $NaNO_3$, KNO_3 and $CsNO_3$ were used as monovalent electrolytes, whereas volume fraction of α-alumina (300nm) and concentration of KCl were used as 25 vol% and 1 M, respectively. Figure A and B are taken from ref. (Kapur, Scales et al. 1997) and (33), respectively. Figure C-D are taken from ref. (48) and (47), respectively.

2.9.2 Effect of Particle Shape

Research has shown how particle shape influences the rheology of a suspension (58, 59). Figure 2-10 shows the relative viscosity (against water) for particle suspensions of increasing particle concentrations and as function of the particle aspect ratio (r_e = 5 ~ spheroids, r_e = 25 ~ cylinders).

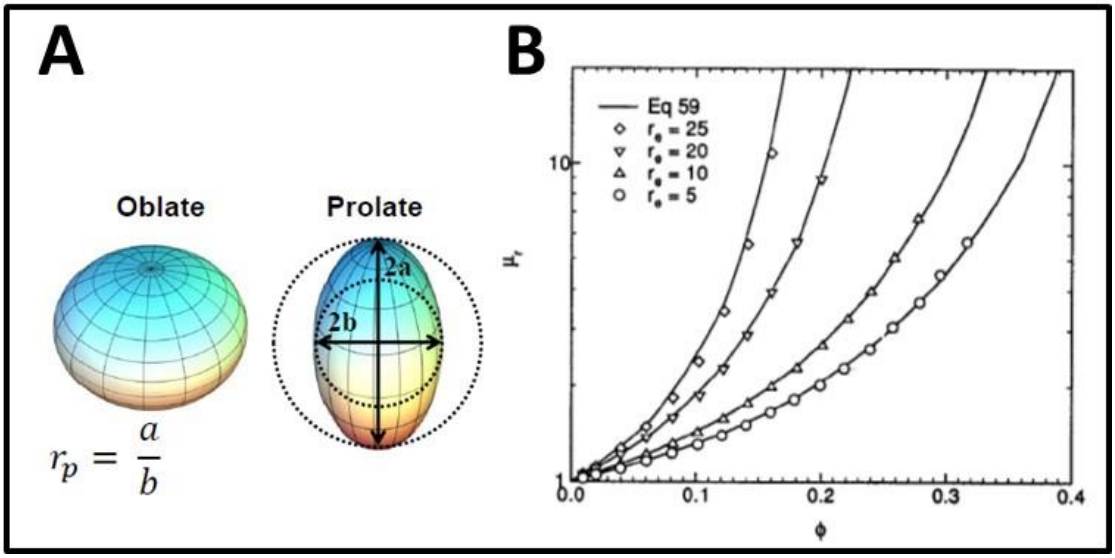

Figure 2-10. a) Aspect ratio (r_p). b) Low shear limit viscosity (μ_r) variation with solid volume fraction (ϕ) and aspect ratio (r_p) for suspensions of spheroids and cylinders (58, 59).

Figure 2-10B shows the effect of particle aspect ratio on the suspension relative viscosity as a function of the solids volume fraction. The particle aspect ratio is defined as the length scales of the major and minor axis (Fig. 1-14A), with a low particle aspect ratio being more spherical and a high particle aspect ratio being more cylindrical or rod-shaped. For an equivalent solids volume fraction, increasing the particle aspect ratio increases the

relative viscosity of the suspension, thus the particle network attains a yield strength condition at a much lower solids volume fraction. Such differences result from the apparent volume occupied by the particle in flow, with the high aspect ratio particle occupying a greater apparent volume due to the volume occupied as the particle rotates, hence the apparent volume of this suspension is much greater than that of a spherical particle suspension. Such behavior underlines the challenge of the current research which is to explore the rheology modification of a suspension of irregular particles through the inclusion smaller spherical particles.

2.10 Heteroaggregation

Heteroaggregation can occur in mixed particle suspensions when the potential for attraction is dominant. The nature of the aggregates depends on the strength of attraction and the sizes of the two interacting particles. If the particles in the mixed particle suspension are of similar size then the dissimilar particles adsorb randomly to one another forming irregular clusters that begin to sediment. Alternatively, if the mixed particles in suspension have a wide range of particle sizes then the smaller particles will adsorb onto the surface of the large particles. In such a situation where the entire surface of the large particle is covered by the smaller particles, the surface become similar to the smaller particles, hence the nature of the interaction gradually changes (Fig. 2-11) (2).

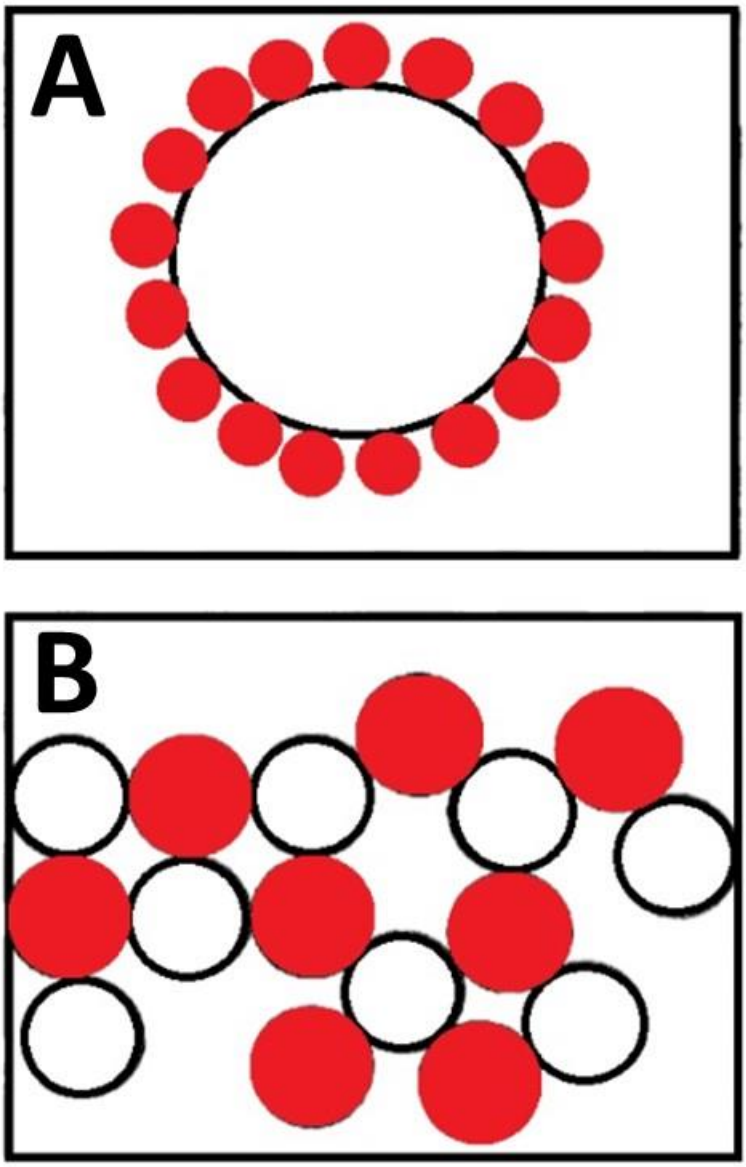

Figure 2-11. A schematic diagram of two different heteroaggregates. (A) shows the arrangement of small particles coated on the surface of large particle (i.e. different size ratios) (B): shows when two different particles with the same size ratio (adapted from ref. (2).

Jones and Pilpel (1965) derived Eq. 2.12 to calculate the “theoretical” maximum number of smaller particles able to deposit onto the surface of a larger particle (60):

$$N_{hex} = \frac{2\pi}{\sqrt{3}}\left(\frac{D}{d} + 1\right)^2 \qquad \textbf{Eq. 2.12}$$

where D and d represent the diameters of the large and small particles, respectively. Eq. 2.12 assumes that the small particles deposit on the surface of the large particle in a hexagonal close packing arrangement (60).

Furusawa and Anzai (1992) studied the fractional surface coverage using latex particles (250nm diameter) to fully coat SiO_2 particles. The particle size ratios (latex to silica) were (*d/D*) 0.157, 0.260, 0.543 and 1.042. The fractional surface coverage was calculated by;

$$\theta = \frac{amount\ adsorbed\ in\ experiment}{calculated\ amount\ for\ total\ coverage} \qquad \textbf{Eq. 2.13}$$

In their study the authors observed the latex particles adsorb onto the SiO_2 particle surface. It was also noted that the theoretical maximum surface coverage was not achievable when the size ratio was more than 0.18. When the particle size ratio was 1:1, the actual measured maximum surface coverage was only 30% of the theoretical coverage. The authors showed that the particle suspension was composed of discrete raspberry shaped hetero-

aggregates at a particle size ratio less than or equal to 0.33, while for size ratios greater than 0.33 the observed result was large irregular aggregates which were caused by inter-particle bridging (61).

Fisher et al. (2001) studied the stability of mixtures of alumina-silica suspensions using different silica particle sizes (5, 15, 25 and 300nm) and a fixed alumina particle size (250nm). The suspension pH was adjusted such that the surface potentials of the alumina and silica particles were opposite; alumina was positive and silica negative (62). It was noted that when the alumina and silica were of similar particle size (alumina 250nm and silica 300nm) there was almost no coating but doublet formation occurred. Whereas when small silica particles were used in the slurry suspension, then at all volume fractions tested the alumina particles were coated.

Silica nanoparticles (15 nm) were added to the alumina slurry at various volume fractions (0.9 vol%, 1.8 vol% and 2.7 vol%). It was observed that the isoelectric point (IEP) shifted from pH 9.1 to pH 3.1; confirming that the silica adsorbed onto the alumina particle surfaces. The maximum IEP shift was found at 1.8 vol%, after which there was no further shift in the IEP (2, 62). A similar effect on the IEP was noted when using the 25 nm silica nanoparticles.

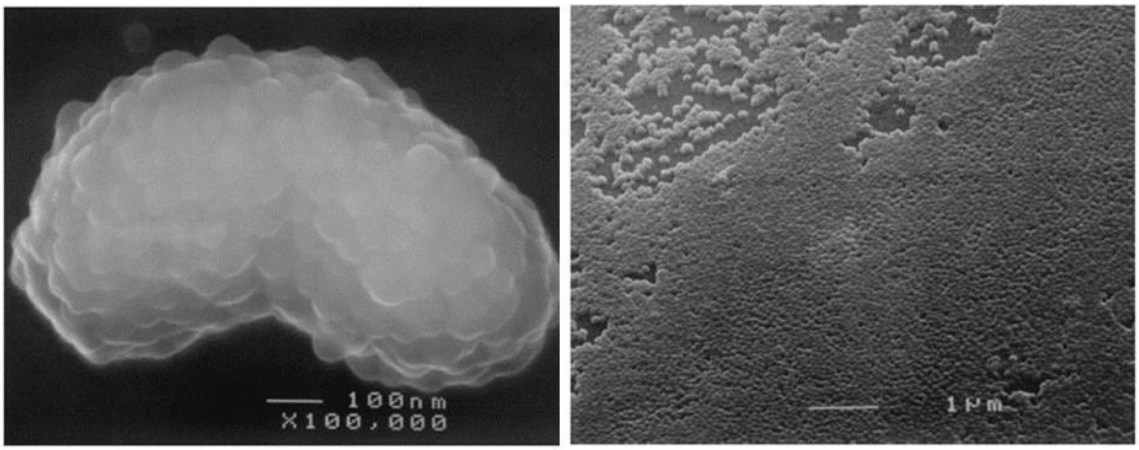

Figure 2-12. SEM micrographs (right) at magnification was used as x 100,000 of a coated alumina particle (or perhaps two particles) from a sample suspension that had 25nm silica at 3.6 vol% (left) length scale 1µm of the surface of a large alumina fibre that has silica particles of 85nm adsorbed onto it. The coverage of the silica particles is almost complete with only small regions uncovered and appears to be a monolayer (one particle thick). Picture taken from ref. (62).

It was noted that by increasing the particle size ratio the viscosity of the particle network also increased. Fisher et al. (2001) used a stress controlled rheometer to measure the suspension viscosity (Fig. 1-17). The slurries containing the smaller sized silica nanoparticles (< 25nm) showed Newtonian behaviour, confirming the adsorption of silica onto the alumina. Whereas for the large silica particles (25 nm and 300nm), the slurry showed non-Newtonian behaviour as the silica particles could not physically cover the alumina particle surfaces. Instead a network of attracted mixed particles of silica and alumina was formed which exhibited higher viscosity (62).

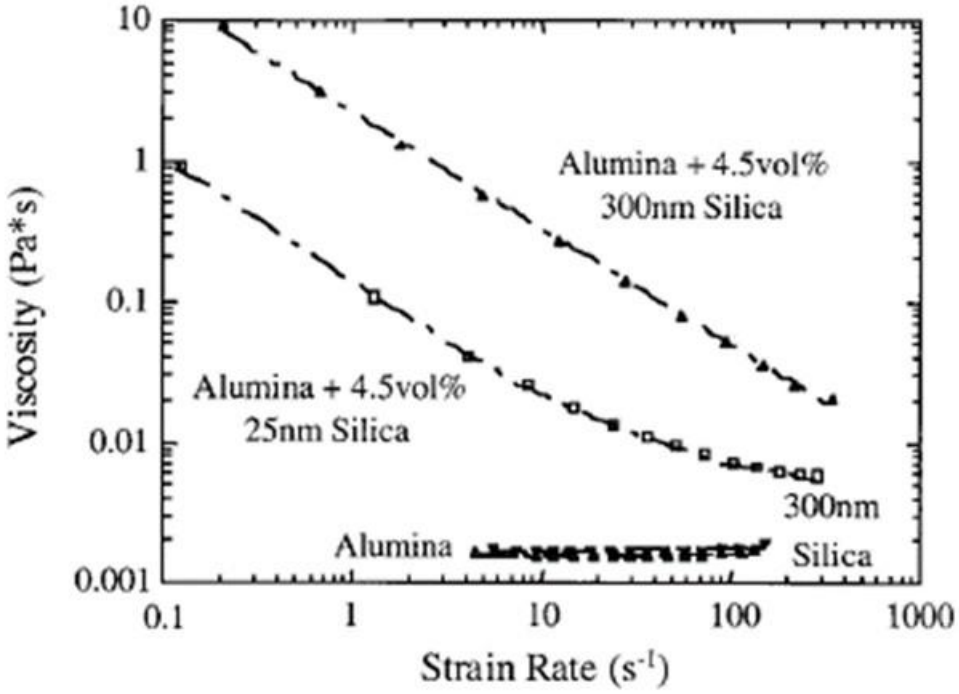

Figure 2-13. A graph of viscosity as a function of shear rate at pH 4 for 10 vol% silica slurries (containing 300nm particles) and for 10 vol% alumina slurries (containing 4.5 vol% of silica powder consisting of particles of different sizes). Figure taken from ref. (62).

2.10.1 Zeta Potential Distribution – Binary Systems

Wu et al. (1) studied the inter-particle interaction of individual particles, binary (alumina–bubble) and tertiary (alumina-bubble-silica) mixtures. A Zetaphoremeter was used to measure the zeta potential distributions. Alumina and silica were used as either micron- or nano-sized, which was for alumina and silica to be 868 nm and 939 nm, respectively, and 15 nm each for the nano-sized particles. Sub-micron sized gas bubbles (350 nm) were generated using a vertical baffled cylindrical high intensity agitation cell (BHIA). KCl was used as the background electrolyte at 1 mM. Dodecylamine hydrochloride (DHA) and sodium dodecyl sulphate (SDS) and DF250 were used as

surfactants to stabilize as well as disperse the nano-sized particles and gas bubbles.

Wu et al. (1) proposed different scenarios to interpret the complex interactions. For example, in a binary system, three different scenarios can occur: 1) if the two different solid particles do not interact then there will be two separate zeta potential distributions; 2) if the particles are strongly attracted to each other, then a single zeta potential distribution would be observed and the position of the peak will depend on the coverage (coating) of one particle to the other; and 3) if the particles are weakly attractive, then three different zeta potential distributions would be observed, indicating some partial coverage, but still dispersed particles.

Figure 2-14 shows typical data which can be collected using this measurement technique. The first three rows represent the individual zeta potential distributions for the three individual species, confirming that the silica particles and the gas bubbles have a negative surface potential while the alumina particles have a positive surface potential. The next three rows represent the results of blending two species together. For the gas bubble and alumina mix, a single zeta potential distribution was measured with a peak at –30 mV, confirming strong interaction between the gas bubbles and alumina particles, with the gas bubbles strongly coating the larger alumina particles. For the gas bubble and silica mix, the two individual species were both negatively charged, and when blended together two distributions were seen, confirming negligible interaction between the two dispersed phases. For the

alumina and silica mix, the resultant zeta potential distribution showed a very broad distribution with two distinct peaks of opposite charge, thus confirming a weak interaction between the two particle species. For the tertiary system, two distinct peaks were once again observed, however the alumina zeta potential distribution was no longer observed and again confirms that the gas bubbles preferentially coated the alumina particles while the silica particles remain dispersed.

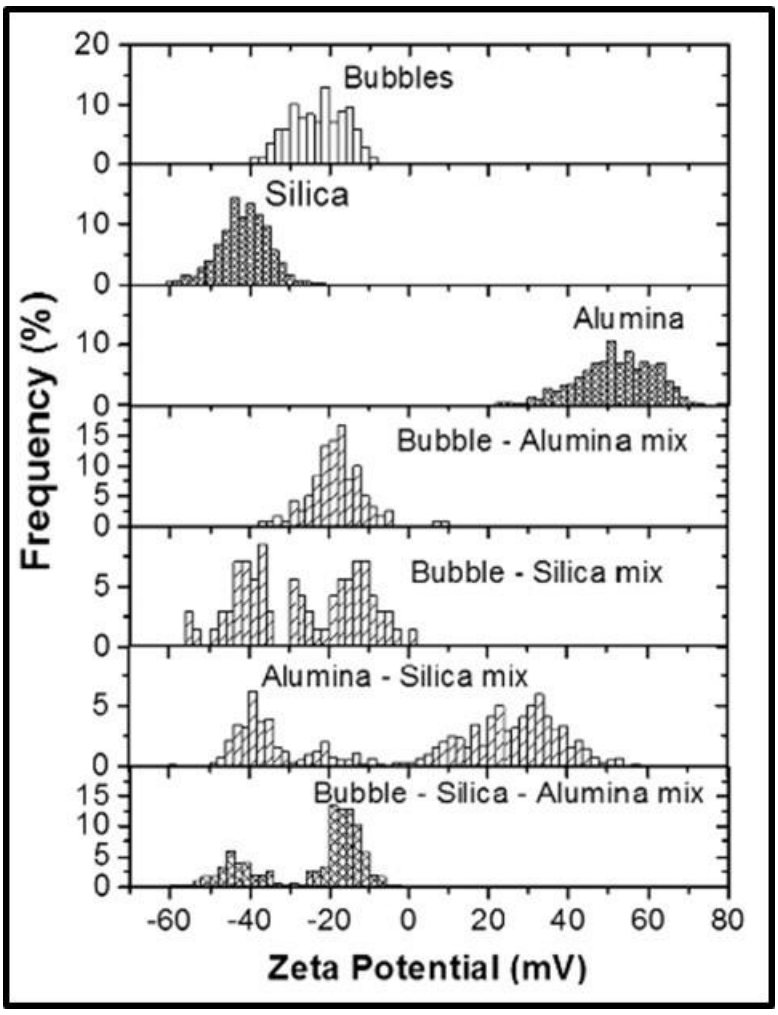

Figure 2-14. Shows the zeta potential distributions of micron size alumina, silica and nano size gas bubble for mono, binary and tertiary mixture. 1 nM of KCl was used as a background electrolyte with 0.1 mM of DF250 in all the suspensions. Figure is taken from ref. (1).

2.10.2 Rheology of Blended Suspensions

Wang and Guo studied the rheology of alumina and zirconia blended suspensions. The authors considered the influence of both volume and number fractions when modifying the yield stress and viscosity of the blended suspensions. Due to the differences in particle size and density, the volume and number fractions were different which led to differences in the behavior of the system. Fig. 2-15 shows how the yield stress of the suspension varied from an alumina suspension to a zirconia suspension. As the volume fraction of zirconia increased the yield stress of the suspension increased, with the increase in yield stress reflecting the increase in the solids volume fraction of zirconia. This gradual increase reflects that the two particle species are non-interacting and the yield stress is a function of the volume fraction of zirconia. On a number basis the number fraction of zirconia has to be significantly greater in order to induce a change in the suspension yield stress and this reflects the difference in the two particle sizes (63).

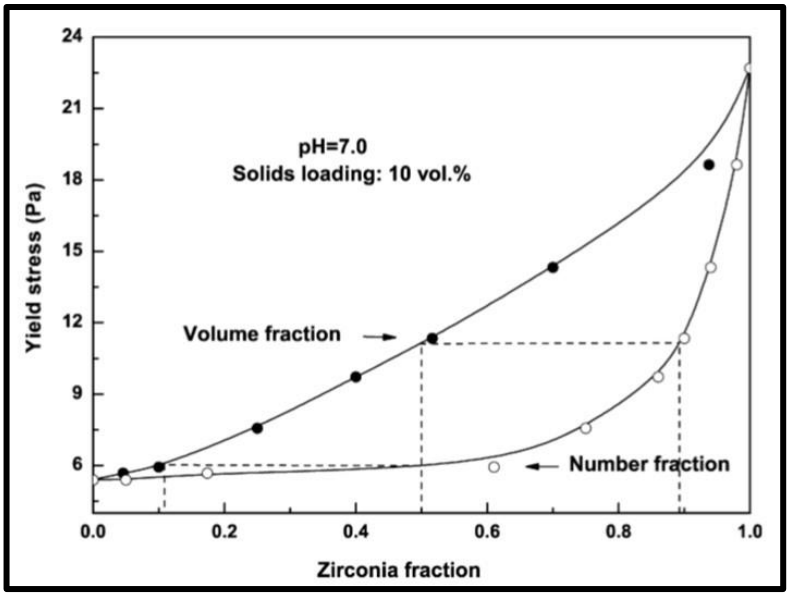

Figure 2-15. Shows the yield stress behavior of the binary (alumina/zirconia) suspensions as a function of zirconia fraction at pH 7.0, when using zirconia volume (closed circle) and number ratios (open circle). Figure is taken from ref. (63).

Greenwood et al. (64) studied the influence of blending two different particles on the relative viscosity of the blended suspension. The two particle species were small PMMA latex and large polystyrene latex. Fig. 2-16 shows the relative viscosity of the two individual particle species showing that the smaller PMMA latex exhibits a rapid increase in the suspension viscosity at a much lower volume fraction than the larger polystyrene latex, again representing the influence of the particle size on the suspension relative viscosity. When blending the two particle species at different volume fractions of the small PMMA latex particles, an interesting behavior was observed when at a low blend ratio, the relative viscosity of the suspension was below the relative viscosity of the large polystyrene latex particles only, indicating some influence of the smaller particles on the flowability of the larger particles. With

increasing concentration of the small PMMA latex particles the relative viscosity curve shifted towards the system of small PMMA latex particles only and showed an apparent thickening of the suspension relative to the pure large polystyrene latex suspension.

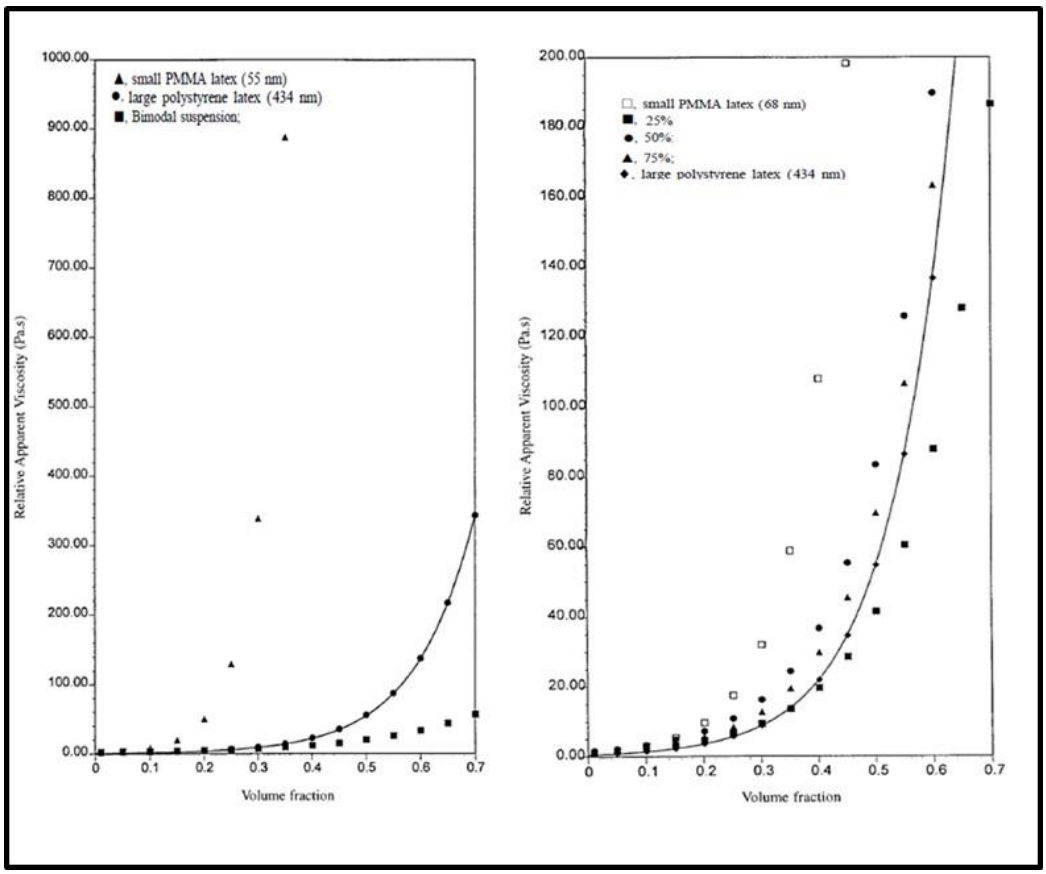

Figure 2-16. (Left) an illustration of the relative viscosity against volume fraction for a bimodal suspension, the chosen suspension in 25% small particles by volume at a diameter ratio of 7.83. (Right) effect of composition on the relative viscosity by varying small particle by volume for bimodal suspension at a diameter ratio of 6.37. Figure is taken from ref. (64).

2.11 Summary

While the concept of particle heteroaggregation has been extensively studied, much of the research to date has focused on very dilute and dilute suspensions, using heteroaggregation to modify the stability of the particle suspension. Few studies have considered the concept to modify the rheology of high solids content suspensions. The research discussed has provided insight on the critical blend ratio between the major and minor particle species to gradually change the behavior (stability or flow) of the particle suspension. It is evident a significant research gap exists whereby rheology modification of a high solids content particle suspension occurs by blending with another inorganic component that acts as a minor additive in the suspension. This contrasts the abundance of research in which organic modifiers such as polymers and surfactants have been used to modify the flow properties of concentrated particle suspensions.

References

1. Wu, C., Wang, L., Harbottle, D., Masliyah, J. and Xu, Z. Studying bubble-particle interactions by zeta potential distribution analysis. *Colloid Interface Sci* 2015.
2. Islam, A.M., Chowdhry, B.Z. and Snowden, M.J. Heteroaggregation in colloidal dispersions. *Advances in Colloid and Interface Science.* 1995, **62**(2–3), pp.109-136.
3. Overbeek, J.T.G. Recent developments in the understanding of colloid stability. *Journal of Colloid and Interface Science.* 1977, **58**(2), pp.408-422.
4. Wang, Q. A study on shear coagulation and heterocoagulation. *Journal of Colloid and Interface Science.* 1992, **150**(2), pp.418-427.
5. Chung, H. and Hogg, R. Stability criteria for fine-particle dispersions. *Colloids and surfaces.* 1985, **15**, pp.119-135.
6. Franks, G.V. *Collois and fine particles. Introduction to particle technology.* Second ed. UK: John Wiley & Sons, Ltd, 2008.
7. Perrin, J. *Atoms.* UK: Constable & Company, 1914.
8. Einstein, A. *Investigations on the Theory of the Brownian Movement.* Courier Corporation, 1956.
9. Einstein, A. *On the movement of small particles suspended in a stationary liquid demanded by the molecular-kinetic theory of heat* Annals of Physics. 1905, 17, pp.549-560.
10. Shaw, D.J. 8 - Colloid stability. In: Shaw, D.J. ed. *Introduction to Colloid and Surface Chemistry (Fourth Edition)*. Oxford: Butterworth-Heinemann, 1992, pp.210-243.
11. Shaw, D.J. 7 - Charged interfaces. In: Shaw, D.J. ed. *Introduction to Colloid and Surface Chemistry (Fourth Edition)*. Oxford: Butterworth-Heinemann, 1992, pp.174-209.
12. Hunter, R.J. *Foundations of colloid science.* Oxford university press, 2001.
13. Israelachvili, J.N. *Intermolecular and surface forces.* 3rd ed. Academic press, 2010.

14. Rhodes, M.J. *Introduction to particle technology.* John Wiley & Sons, 2008.
15. Helmholtz, H. Ueber einige Gesetze der Vertheilung elektrischer Ströme in körperlichen Leitern mit Anwendung auf die thierisch-elektrischen Versuche. 1853, **165**(6), pp.211-233.
16. Wang, H. and Pilon, L. Accurate simulations of electric double layer capacitance of ultramicroelectrodes. *The Journal of Physical Chemistry.* 2011, **115**(33), pp.16711-16719.
17. Ehrenstein, G.J.B.t.o.-l.B.S., Bethesda, Maryland. Available at: http:/www. biophysics. org/btol. Surface charge. 2001.
18. Butt, H.-J., Graf, K. and Kappl, M. *Physics and chemistry of interfaces.* John Wiley & Sons, 2013.
19. Grahame, D.C. The electrical double layer and the theory of electrocapillarity. *Chemical Reviews.* 1947, **41**(3), pp.441-501.
20. Singh, B.P., Menchavez, R., Takai, C., Fuji, M. and Takahashi, M. Stability of dispersions of colloidal alumina particles in aqueous suspensions. *Journal of Colloid and Interface Science.* 2005, **291**(1), pp.181-186.
21. Johnson, S.B., Franks, G.V., Scales, P.J., Boger, D.V. and Healy, T.W. Surface chemistry–rheology relationships in concentrated mineral suspensions. *International Journal of Mineral Processing.* 2000, **58**(1-4), pp.267-304.
22. Derjaguin, B. and Landau, L. The theory of stability of highly charged lyophobic sols and coalescence of highly charged particles in electrolyte solutions. *Acta Physicochim. URSS.* 1941, **14**, pp.633-652.
23. Verwey, E.J.W. Theory of the Stability of Lyophobic Colloids. *The Journal of Physical and Colloid Chemistry.* 1947, **51**(3), pp.631-636.
24. Li, D. *Electrokinetics in microfluidics.* Elsevier, 2004.
25. Butt, H.-J. and Kappl, M. *Surface and interfacial forces.* John Wiley & Sons, 2009.
26. Kitahara, A. Zeta potential in nonaqueous media and its effect on dispersion stability. *Progress in Organic Coatings.* 1973, **2**(2), pp.81-98.

27. Maroto, J. and De las Nieves, F. Optimization of the heterocoagulation process of polymer colloids with different particle size. *Colloids and Surfaces A: Physicochemical and Engineering Aspects.* 1995, **96**(1), pp.121-133.
28. Lopez-Lopez, J., Schmitt, A., Moncho-Jorda, A. and Hidalgo-Alvarez, R. Stability of binary colloids: kinetic and structural aspects of heteroaggregation processes. *Soft Matter.* 2006, **2**(12), pp.1025-1042.
29. Yates, P.D., Franks, G.V., Biggs, S. and Jameson, G.J. Heteroaggregation with nanoparticles: effect of particle size ratio on optimum particle dose. *Colloids and Surfaces A: Physicochemical and Engineering Aspects.* 2005, **255**(1), pp.85-90.
30. Hogg, R., Healy, T. and Fuerstenau, D. Mutual coagulation of colloidal dispersions. *Transactions of the Faraday Society.* 1966, **62**, pp.1638-1651.
31. Liddel, P.V. and Boger, D.V. Yield stress measurements with the vane. *Journal of Non-Newtonian Fluid Mechanics.* 1996, **63**(2), pp.235-261.
32. Dzuy, N.Q. and Boger, D.V. Yield Stress Measurement for Concentrated Suspensions. *Journal of Rheology.* 1983, **27**(4), pp.321-349.
33. Scales, P.J., Johnson, S.B., Healy, T.W. and Kapur, P.C. Shear yield stress of partially flocculated colloidal suspensions. *AIChE Journal.* 1998, **44**(3), pp.538-544.
34. Keentok, M. The measurement of the yield stress of liquids. *Rheologica acta.* 1982, **21**(3), pp.325-332.
35. McDowell, C. and Usher, F.L. Viscosity and rigidity in suspensions of fine particles. I–Aqueous suspensions. *Proceedings of the Royal Society of London. Series A, Containing Papers of a Mathematical Physical Character.* 1931, **131**(817), pp.409-427.
36. Goodeve, C.F. A general theory of thixotropy and viscosity. *Transactions of the Faraday Society.* 1939, **35**, pp.342-358.
37. Chow, M. and Zukoski, C. Nonequilibrium behavior of dense suspensions of uniform particles: Volume fraction and size

dependence of rheology and microstructure. *Journal of Rheology.* 1995, **39**(1), pp.33-59.

38. Dzuy, N.Q. and Boger, D. Direct yield stress measurement with the vane method. *Journal of Rheology.* 1985, **29**(3), pp.335-347.
39. Yoshimura, A.S., Prud'homme, R.K., Princen, H. and Kiss, A. A comparison of techniques for measuring yield stresses. *Journal of Rheology.* 1987, **31**(8), pp.699-710.
40. Keentok, M., Milthorpe, J. and O'donovan, E. On the shearing zone around rotating vanes in plastic liquids: theory and experiment. *Journal of Non-Newtonian Fluid Mechanics.* 1985, **17**(1), pp.23-35.
41. Yang, H.-G., Li, C.-Z., Gu, H.-C. and Fang, T.-N. Rheological behavior of titanium dioxide suspensions. *Journal of Colloid Interface Science.* 2001, **236**(1), pp.96-103.
42. Yang, H.-G., Li, C.-Z., Gu, H.-C., Fang, T.-N.J.J.o.c. and science, i. Rheological behavior of titanium dioxide suspensions. *Journal of Colloid Interface Science.* 2001, **236**(1), pp.96-103.
43. Mikulášek, P., Wakeman, R. and Marchant, J. The influence of pH and temperature on the rheology and stability of aqueous titanium dioxide dispersions. *Chemical Engineering Journal.* 1997, **67**(2), pp.97-102.
44. Leong, Y.K., Boger, D.V., Scales, P.J., Healy, T.W. and Buscall, R. Control of the rheology of concentrated aqueous colloidal systems by steric and hydrophobic forces. *Journal of the Chemical Society, Chemical Communications.* 1993, (7), pp.639-641.
45. Leong, Y.K. Rheological evidence of adsorbate-mediated short-range steric forces in concentrated dispersions. *Journal of the Chemical Society, Faraday Transactions.* 1993, **89**(14), pp.2473-2478.
46. Leong, Y.K. Interparticle forces arising from an adsorbed strong polyelectrolyte in colloidal dispersions: charged patch attraction. *Colloid and Polymer Science.* 1999, **277**(4), pp.299-305.
47. Johnson, S.B., Franks, G.V., Scales, P.J. and Healy, T.W. The binding of monovalent electrolyte ions on α-alumina. II. The shear yield stress of concentrated suspensions. *Langmuir.* 1999, **15**(8), pp.2844-2853.

48. Johnson, S.B., Scales, P.J. and Healy, T.W. The binding of monovalent electrolyte ions on α-alumina. I. Electroacoustic studies at high electrolyte concentrations. *Langmuir.* 1999, **15**(8), pp.2836-2843.
49. Franks, G.V., Zhou, Z., Duin, N.J. and Boger, D.V. Effect of interparticle forces on shear thickening of oxide suspensions. *Journal of Rheology.* 2000, **44**(4), pp.759-779.
50. Barten, D., Kleijn, J., Duval, J., Leeuwen, H.v., Lyklema, J. and Cohen Stuart, M. Double layer of a gold electrode probed by AFM force measurements. *Langmuir.* 2003, **19**(4), pp.1133-1139.
51. Kasuya, M., Sogawa, T., Masuda, T., Kamijo, T., Uosaki, K. and Kurihara, K. Anion adsorption on gold electrodes studied by electrochemical surface forces measurement. *The Journal of Physical Chemistry.* 2016, **120**(29), pp.15986-15992.
52. Kapur, P.C., Scales, P.J., Boger, D.V. and Healy, T.W. Yield stress of suspensions loaded with size distributed particles. *AIChE Journal.* 1997, **43**(5), pp.1171-1179.
53. Prestidge, C.A. Rheological investigations of galena particle interactions. *J Colloids Surfaces A: Physicochemical Engineering Aspects* 1997, **126**(2-3), pp.75-83.
54. Firth, B.A. Flow properties of coagulated colloidal suspensions: II. Experimental properties of the flow curve parameters. *Journal of Colloid and Interface Science* 1976, **57**(2), pp.257-265.
55. Hunter, R.J. The flow behavior of coagulated colloidal dispersions. *Advances in Colloid Interface Science.* 1982, **17**(1), pp.197-211.
56. Friend, J.P. and Hunter, R.J. Plastic flow behavior of coagulated suspensions treated as a repeptization phenomenon. *Journal of Colloid Interface Science* 1971, **37**(3), pp.548-556.
57. Avramidis, K.S. and Turian, R.M. Yield stress of laterite suspensions. *Journal of Colloid Interface Science* 1991, **143**(1), pp.54-68.
58. Phan-Thien, N. and Graham, A. A new constitutive model for fibre suspensions: flow past a sphere. *Rheologica acta.* 1991, **30**(1), pp.44-57.

59. Shijie, L. and Jacob, H.M. Rheology of Suspensions. In: *Suspensions: Fundamentals and Applications in the Petroleum Industry*. American Chemical Society, 1996, pp.107-176.
60. Jones, T. and Pilpel, N. Some physical properties of lactose and magnesia. *Journal of Pharmacy and Pharmacology.* 1965, **17**(7), pp.440-448.
61. Furusawa, K. and Anzai, C. Heterocoagulation behaviour of polymer latices with spherical silica. *Colloids and surfaces.* 1992, **63**(1), pp.103-111.
62. Fisher, M.L., Colic, M., Rao, M.P. and Lange, F.F. Effect of Silica Nanoparticle Size on the Stability of Alumina/Silica Suspensions. *Journal of the American Ceramic Society.* 2001, **84**(4), pp.713-718.
63. Wang, X. and Guo, L. Effect of ionic strength on rheological properties of binary Al2O3/ZrO2 suspensions. *Colloids and Surfaces A: Physicochemical and Engineering Aspects.* 2007, **297**(1–3), pp.7-13.
64. Greenwood, R., Luckham, P. and Gregory, T. The effect of diameter ratio and volume ratio on the viscosity of bimodal suspensions of polymer latices. *Journal of Colloid and Interface Science.* 1997, **191**(1), pp.11-21.

Chapter 3

Materials and Experimental Methods

3.1 Materials

3.1.1 Silica Surface Chemistry

The abundance of silica around us (i.e. soils and sands) has led to a vast amount of research been done on it. As a mineral oxide silica is an important commodity that is manufactured for industrial and domestic application. A silica molecule ($[SiO_4]^{-4}$) is a tetrahedral shape (see Fig. 3-1) consisting of an atom of silicon that is bonded to four atoms of oxygen. The molecules of silica when assembled together can form the following structures; crystalline, amorphous, soluble or chemically combined (1).

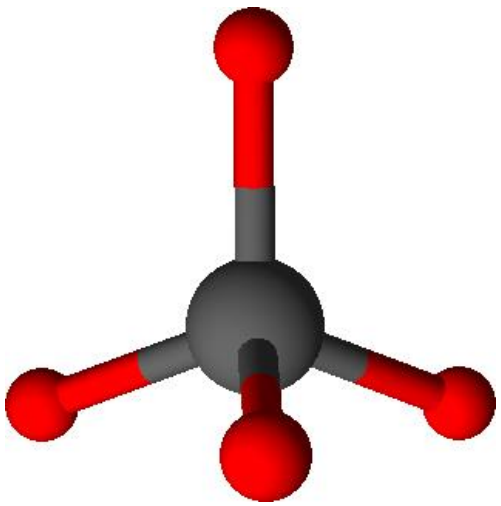

Figure 3-1. An illustration of the tetrahedral shape of a silica molecule ($[SiO_4]^{-4}$). Figure is drawn using ChemSkecth modelling software. One silica atom (grey) bonds with four neighbouring oxygen (red) atoms.

Furthermore, the behaviour of these silica structures as colloidal dispersions do not readily conform to the DLVO theory, unlike most other mineral oxides (2-4). For example, at the isoelectric point the expected stability of a mineral oxide weakens whereas silica exhibits a significantly stable colloidal dispersion (5). It is thought this anomalous stability behaviour of silica colloids in solution is due to surface chemical properties, which are controlled by the how the surface of the silica colloids was prepared as well as the nature of the solution.

With regards to the surface chemical properties of silica there are three main chemical groups and they are; siloxane groups (Si-O-Si), silanol groups (Si-OH), and silicic acid groups ($Si\text{-}O^-$) (see Fig. 3–2A-C). When in a solution the silanol groups (Si-OH) on the surface of a silica compound cause it to be hydrophilic when exposed. Contrastingly the siloxane groups (Si-O-Si) make the surface of silica to by hydrophobic. It is possible to change these surface properties by dehydroxylating a hydrophobic silica surface to make it hydrophilic and through rehydration the reverse is possible. These reversible changes that can be made to surface chemical properties of silica are ultimately governed by the silanol group density (silanol number). It has been found that for a complete hydrophilic surface of silica there is 4 – 8 OH groups per square nanometre (1, 6). The reason for the range is due to manufacturing processes and the surface area per colloid. During the manufacturing process the temperatures used in the heat treatment determine the hydrophilic/hydrophobic surface chemical properties of the silica colloids.

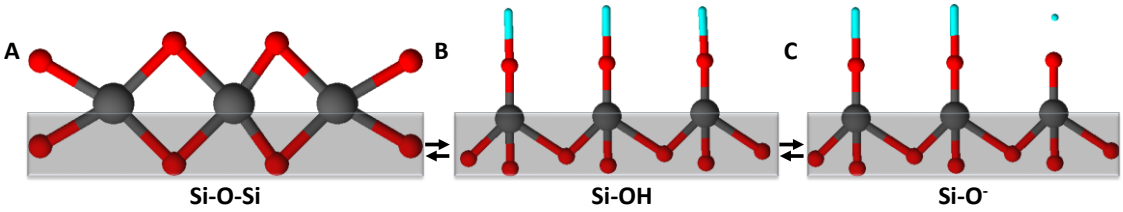

Figure 3-2. An illustration of the reversible nature of the three main chemical groups on the surface of silica. Siloxane groups (Si-O-Si), silanol groups (Si-OH), and silicic acid groups ($Si-O^-$) are shown as (A), (B) and (C), respectively. Figures are drawn using ChemSketch modelling software, where surface of silica, oxygen and hydrogen are shown with dark grey, red and cyan colour, respectively. whereas bulk silica is displayed as light grey.

3.1.2 Alumina Surface Chemistry

Corundium, which is also known as alpha alumina (α-Al_2O_3) is the most thermodynamically stable crystalline form of aluminium oxide (7). Depending on different heat process, there are many more metastable polymorphs of alumina which can be produced from aluminium salt or aluminium oxides such as γ-alumina, η-alumina, δ-alumina, β-alumina etc. and each metastable phase has different crystalline structure and physical properties, for example γ-Al_2O_3 has cubic structure and it is commonly used in advanced technical application. Different arrangement of oxygen ions in the crystal structure determine the metastable phase of alumina (8, 9). Powder X-ray diffractometry (XRD) and selected-area electron diffraction (SAD) are some of the few techniques, which commonly used to determine the metastable phase of alumina (9).

α-Al_2O_3 is the interest of this project, therefore its crystal structure and properties will be discussed only. In 1888, an Austrian chemist Carl Josef

Bayer, who developed and patented The Bayer process to produce α-Al_2O_3 from bauxite ore (7). In α-Al_2O_3, anions of oxygen has valence number -2, whereas cations of aluminium has valence of +3, which means oxygen ions are in access in the lattice, therefore oxygen ions form a top layer of hexagonal close-packed (HCP) structure and aluminium ions form octahedral layer beneath it in the lattice as shown in Fig. 3-3.

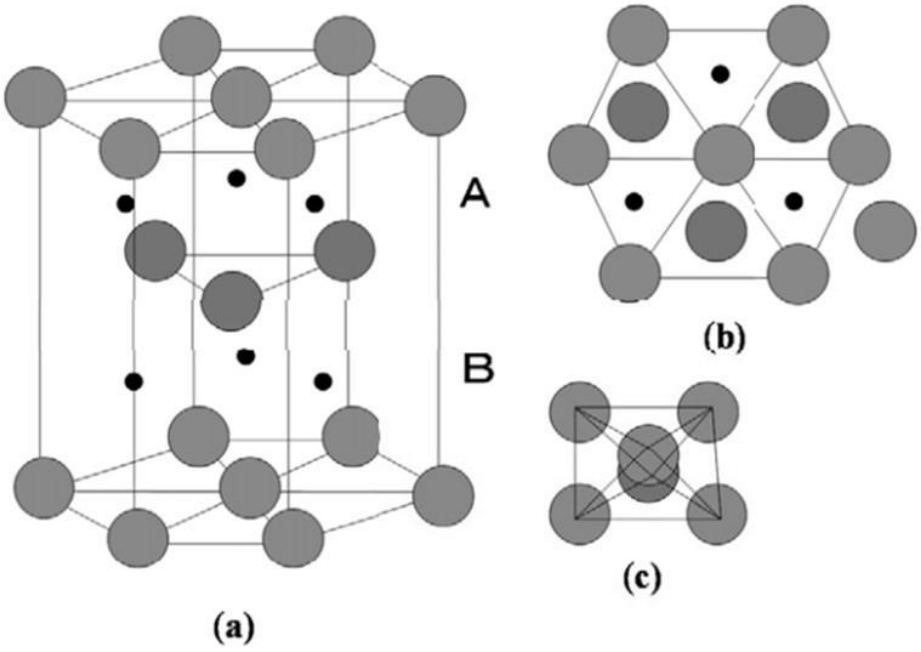

Figure 3-3. Schematic illustration of α-alumina as a balls and stick model, Al^{+3} ion and O^{-2} ion are displayed as black and grey balls. (a) Structure of α-Al_2O_3 also known as Corundum structure, (b) top view of the structure and (c) octahedral structure of alumina. Figure is taken from Shirai et al. (10).

Tsganenko (10) developed a model, which shows three types of OH groups can attach to the nearest neighbouring transition aluminium cations (Al^+) (see Fig. 3-4). Having a high boiling point, α-Al_2O_3 can be used in many application it can be used as fillers, glass, catalyst, gas purification and paint etc. (11).

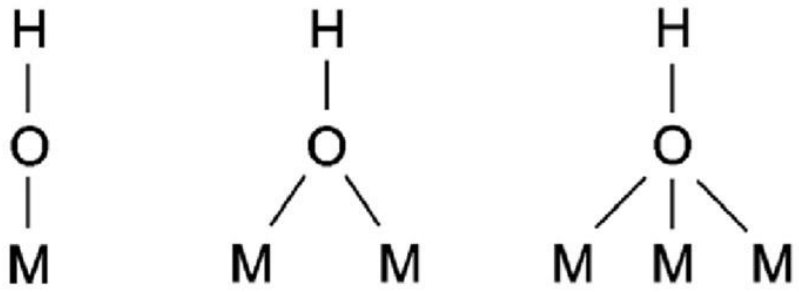

Figure 3-4. Transition alumina can be hosted to three different hydroxyl groups. Figure is redrawn from Shirai et al. (10).

3.2 Methods

3.2.1 Zeta Potential Measurements

The magnitude of electrostatic repulsion or attraction between the particles is measured as Zeta potential which is helpful in ascertaining the stability of the colloidal suspensions (12). In a stationary solution, it is described by the potential at the surface of a moving charged particle. The continuous phase can be distinguished from the stationary layer of the fluid attached to colloid using the surface potential which is influenced by the surrounding environment. The EDL region possesses greater ionic charge as compared to the bulk. Increase in concentration of the anions occurs since an adjacent layer of counter anions is provided by the EDL. Overall surface potential of the particle is therefore reduced. Zeta potential of the charged particle is illustrated in Fig. 3-5.

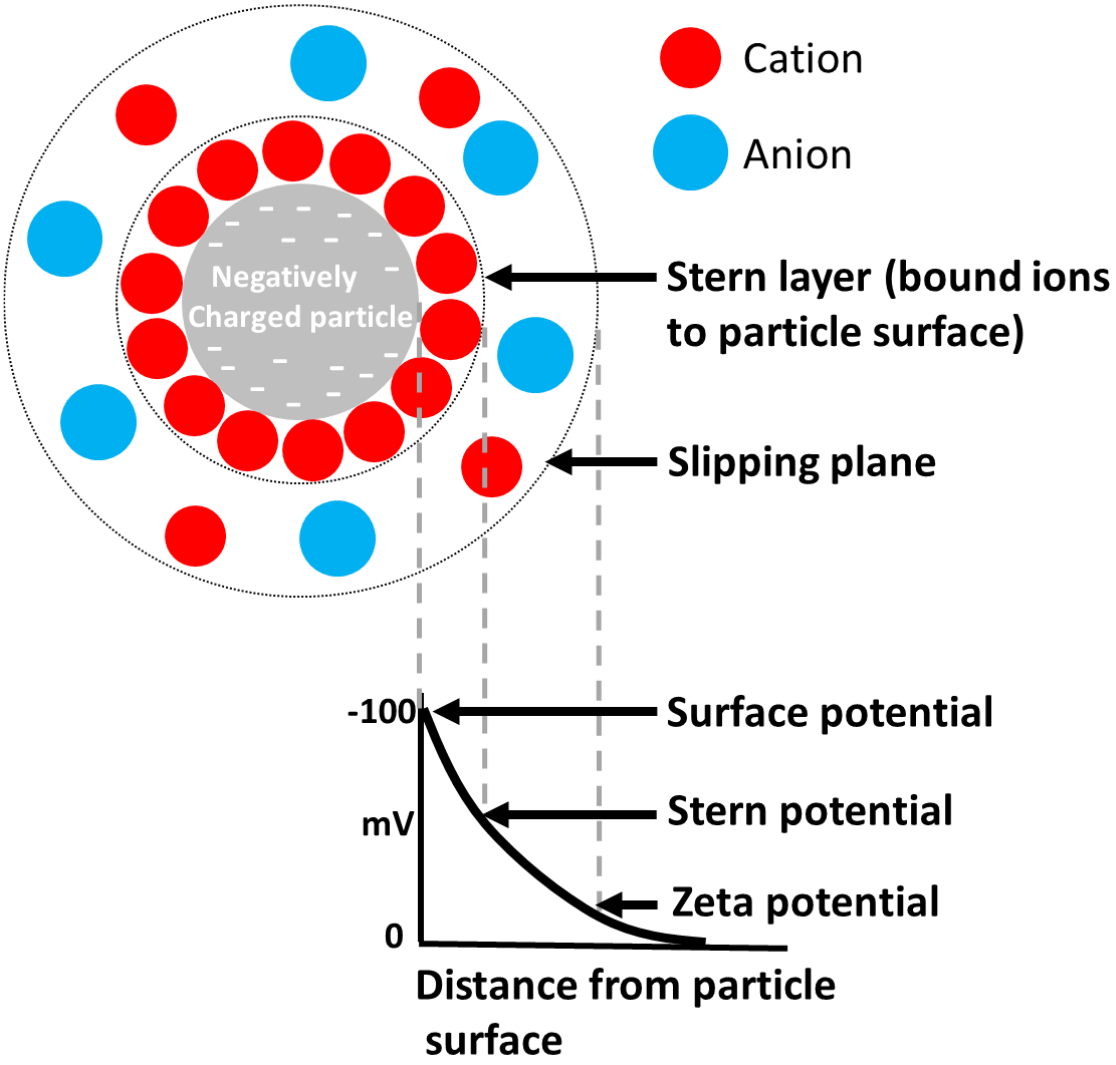

Figure 3-5. A schematic displays the zeta potential according to DLVO theory. Figure redrawn from ref. (13).

The stability of dispersion is greatly augmented by these fundamental parameters. The Zetasizer Nano uses electrophoretic light scattering to measure the zeta potential and the electrophoretic mobility (Malvern, 2004). The solution comprising dispersed particles is applied with an electric field. Migration of the charged particles towards the opposite charged electrode is described by the process of electrophoresis. These moving particles face resistance due to viscous forces of the medium. The particles move at a

constant velocity when equilibrium is maintained between the electric and viscous forces in the medium. This movement of particles is termed as electrophoretic mobility. The velocity of particles in such state is influenced by various factors such as:

- Strength of the applied force
- Zeta potential of the particle
- Viscosity of the medium
- Dielectric constant of the medium

The zeta potential of a particle can be obtained by directly measuring the electrophoretic mobility (U_E) and using the Henry equation as expressed in Eq. 3.1 below:

$$\boldsymbol{U_E = \frac{2\varepsilon\zeta f(Ka)}{3\mu}} \qquad \textbf{Eq. 3.1}$$

where; ε is the dielectric constant, ζ is the zeta potential, $f(\kappa a)$ is the Henry's function and μ is the viscosity of the medium. Henry's constant can take a value of either 1.5 or 1.0. For aqueous solutions of moderate electrolyte concentrations the Smoluchowski approximation is used, where *f(Ka*) is set to 1.5. For non-polar solvents the Huckel approximation is used, where $f(\kappa a)$ is set to 1.0.

3.2.2 Sample Preparation for Zeta Potential Measurements

Alumina and silica were used throughout the study as primary and secondary particles, respectively. The particle information provided by the manufacturer is shown in Table 3-1.

Table 3-1. Illustrates the manufacturer quoted size of all the particles and their relative information.

Particle	d_{50} (µm)	Shape	Density (g/cm^3)	Supplier	Refractive index	Adsorption
Alumina (alpha)	0.52	Irregu-lar	3.88	AL-160SG-4, Showa Denko, Japan	1.766	0.001
Silica	0.1	Spher e	1.88	SIOP010-01, AngstromSph -ere, Fiber Optic Center, USA	1.544	0.001

Sodium chloride (NaCl) of average molecular weight 58.44g/mol was obtained from Fisher Scientific (product number: 10616082; Lot: 1721643). Hydrochloric acid (HCl) of average molecular weight 36.46 g/mol and weight concentration 37% wt/wt (product number: 10499360; Lot: 1563302) was obtained from Fisher Scientific. Sodium hydroxide (NaOH) solution of average molecular weight 40 g/mol and concentration of 50% wt/wt (product number: 415413) was obtained from Sigma-Aldrich. All the material were used to make stock solutions as received.

A zetasizer nano system (NS) is used to measure particles sizes and zeta potential of mono systems. Prior to the experiment all glassware was washed with 1 wt% Decon 90 solution and rinsed with Milli-Q water thoroughly to prevent contamination, then all glassware were placed in the oven for 5 minutes to dry.

Mostly 0.1 wt% (otherwise stated) concentration of the particles was used with 10^{-3} M (otherwise stated) background electrolyte of NaCl. Diluted HCl and NaOH were used for titration process.

Initially, 2 x 40 mL glass vials were used to measure the zeta potential of alumina or silica. Each vial was used separately for varying low and high pH. 0.1 wt% particular powered was weighted in each vial, then 30 mL of 10^{-3} M, NaCl was added. Ultra-sonication was allowed for 5 minutes to each vial to ensure the particles are dispersed fully, then magnetic stirrer was added, and vials were left on the stirrer for overnight to reach charge equilibrium. Zeta potential was measured using the Malvern Zetasizer Nano. A Mettler Toledo pH meter (MP225, UK) was used varying pH 2, 4, 6, 8 and 10. Prior to the measurements, it was made sure that there is no air bubble trapped in the capillary cell and electrodes of the capillary cell were dried. Again, 5 experimental runs were conducted for each type of powder and mean value was taken. All the data was analysed using Origin lab pro (version 9.0).

3.3 Dynamic Light Scattering

When a light source, such as a laser, illuminates a small particle, the light will be scattered in all directions by the surface of the particle. So when the incident light is scattered by thousands of particles in a solution the pattern seen on a screen that is close enough to the particles is speckled (as shown in Fig. 3-6 a). The speckles pattern consists of areas of bright light (i.e. where light waves reaching the screen interfere constructively with one) and dark areas (i.e. where the light waves reaching the screen interfere destructively with one) (14).

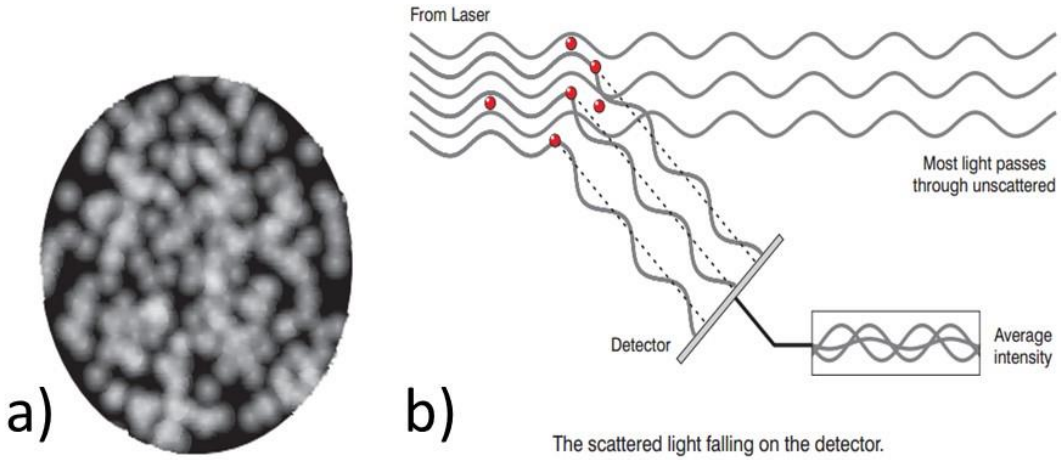

Figure 3-6. A is the speckled pattern is shown in (a), whereas (b) shows how dynamic laser scattering (DLS) theory works. In order to construct a speckled, light waves that have been scattered by particles in the solution and are been detected by the detector; two of the three wave would interfere constructively and one of them would interfere destructively with the other two. Images are taken from ref. (14).

The particles in solution or slurry are not stationary when there is some thermal energy in the medium. The thermal energy causes the particles to

move through solution and this is known as Brownian motion. The resulting constant motion of the particle at any time causes the scattering pattern of light from the particle to be changing (15). The size of the particle is related to the rate of fluctuating intensity from the scattered light. The DLS working principle is based upon the knowledge that the small particles move faster, in other word small particles diffuse in the solution quicker than the large particles. Stokes and Einstein derived a fundamental equation to represent this relationship as (14):

$$\boldsymbol{D_H = \frac{kT}{3\pi\eta D}} \qquad \textbf{Eq. 3.2}$$

where the hydrodynamic diameter of the particle is given by D_H, the Boltzmann constant is represented by k, the absolute temperature is represented by T, the viscosity is given by η and D is the translation diffusion coefficient.

There are a few factors that affect the diffusion speed on a particle and these are; (i) electrolyte(ionic) concentration, (ii) temperature, (iii) surface structure, (iv) non-spherical particle shapes (14). There have been number of different theories proposed for light scattering such as the Rayleigh scattering theory and the Mie theory. Mia theory is a complex theory derived by Gustav Mie in 1908 from the Maxwell's equation to obtain the incident, scattered and internal fields (16). To implement this theory, one should have the knowledge of optical properties like the refractive index and the imaginary component of both the fluid and the dispersant. Rayleigh scattering theory is also a complex theory,

which is named after British scientist Lord Rayleigh, who was the first person to described this theory in 19th century (17). According to this theory, charge particle becomes polarized when light struck on the surface of the particle, thus particle moves with the same frequency and particle becomes radiating dipole and its radiation can be seen as scattered light.(17). The Rayleigh scattering-probability is described as:

$$p \backsim \frac{1}{\lambda^4} \qquad \textbf{Eq. 3.3}$$

where p and λ are the scattering probability and the wavelength of radiation, respectively.

To describe the non-spherical particles, comparison of such particles should be drawn to an imaginary spherical particle. In such cases, a single unique number should be defined to describe the size of non-spherical particle. The methods of such comparisons include:

- Equivalent surface area: A theoretical sphere having the same surface area as that of the actual non-spherical particle is assumed.
- Equivalent length: A theoretical sphere having the same diameter as the maximum or minimum length of the actual particle is assumed.

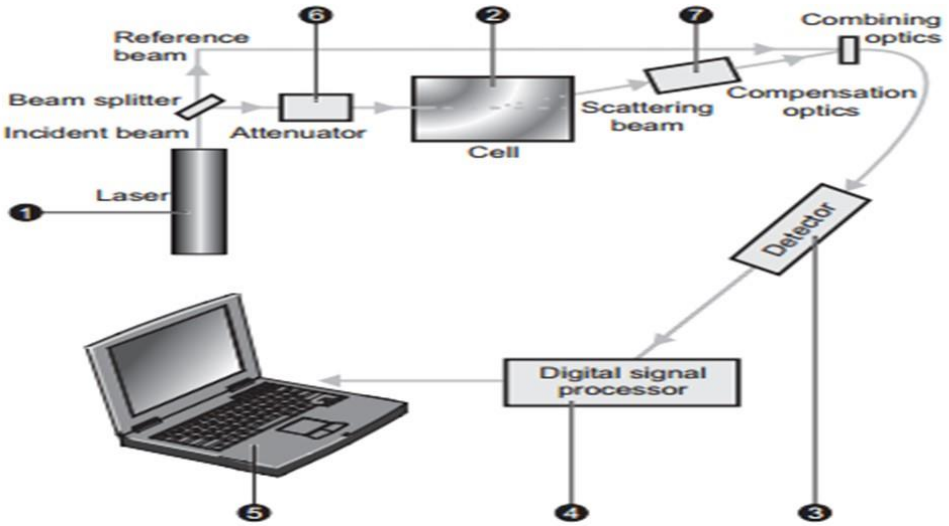

Figure 3-7. Illustrates the key components of dynamic laser scattering (DLS) set-up. Image is taken from ref. (14).

A zetasizer nano system (NS) is used to measure particles sizes in this research project, therefore it is important to describe its key components. There are six main components in the zetasizer measurement system as illustrated in Fig. 3-7. The measurement system begins with the laser at point 1. The laser light is the source used to illuminate the particles within the sample under test. Before the light reaches the sample it is split in two to provide an incident and a reference beam. The incident beam is directed towards the sample cell and such that it passes through the sample centre (as shown at point 2). The light scattered by the sample at an angle of 13° is detected at point 3 on Fig. 3-7. For the detector to function successfully the intensity of the scatter light it detects needs to be within a specific frequency range. To aid with the scattered light intensity range an attenuator (given at point 6) is used to adjust the right prior to it reaching the sample cell (14).

The working principle of electrophoresis is used to cause fluctuations in the scattered light intensity to give more information on the particles in the suspension. The electrophoresis phenomenon is when an electric field is applied to a colloidal sample causing the suspended particles to begin to move. The frequency of the fluctuations in the scattered light intensity are proportional to the speed of the moving particles. The digital processor at point 4 collects this information and then passes it on to the computer (at point 5). For specific case of the Zetasizer Nano the computer software it uses presents the measurements data as a frequency spectrum from which the zeta potential can be calculated after calculating the electrophoretic mobility. And lastly, at point 7 of Fig. 3-7 is the compensation optics unit which corrects for any differences in the cell wall thickness and dispersant refraction in order to maintain optimum alignment (14).

3.3.1 Particle Size Distribution

Initially, a 40 mL glass vial was used. 1 wt% (10^4 ppm) i.e. silica or alumina powder was weighted, then 30 mL of 10^{-3} M NaCl was added in the vial. Ultra sonication was allowed for 5 minutes, followed by tip sonication for 3 minutes to ensure that the particles are dispersed completely, then magnetic stirrer and left the vial on the stirrer plate. PH of the sample was adjusted to 10 using a Mettler Toledo pH meter (MP225, UK) as particles should be highly charged and well away from isoelectric point (IEP) at this environment, which keep dispersed particles in the solution. Prior to the measurements using zetasizer for sizing, it was made sure that there is no air bubbles trapped in the 12 mm square polystyrene cuvettes. 5 experimental runs were conducted for each

type of powder and mean value was taken. All the data was analysed using Origin lab pro (version 9.0).

3.4 Rheometer

A rheometer is an important instrumental device, which is mostly used to measure the deformation and the rheological flow properties of the material, when material undergoes applied forces. It is also very useful for handling complex fluids, whose flow or viscoelastic behaviour cannot be studied by a single parameter. Therefore rheometer is more preferable to use by most researchers than viscometer (18).

Therefore, it is necessary to describe how rheometer works. Primarily rheometer measures or applies three fundamental parameters, which are torque, angular displacement and angular velocity. All rheological parameters such as shear stress, shear rate, shear strain, viscosity and complex modulus can be calculated using those three parameters (19). For example:

$$\boldsymbol{Shear\ stress, \sigma\ (Pa) = M\ .\ K_{\sigma}} \qquad \textbf{Eq. 3.4}$$

where torque is represented by M (Nm). K_{σ} is a stress constant and it is a geometry dependant:

$$\boldsymbol{Shear\ strain\ , \gamma = \ K_{\gamma}\ .\ \theta} \qquad \textbf{Eq. 3.5}$$

where θ is angular motor deflection in radians and K_γ is a strain constant, which is also geometry dependant:

$$\boldsymbol{Shear\ rate, \gamma\ (s^{-1}) = K_\gamma . \Omega} \qquad \textbf{Eq. 3.6}$$

where Ω (rad s-1) is angular velocity and K_γ is strain constant, which is geometry dependant. From above all three equations, it is noticed selecting a right geometry for a particular material or suspension is very important.

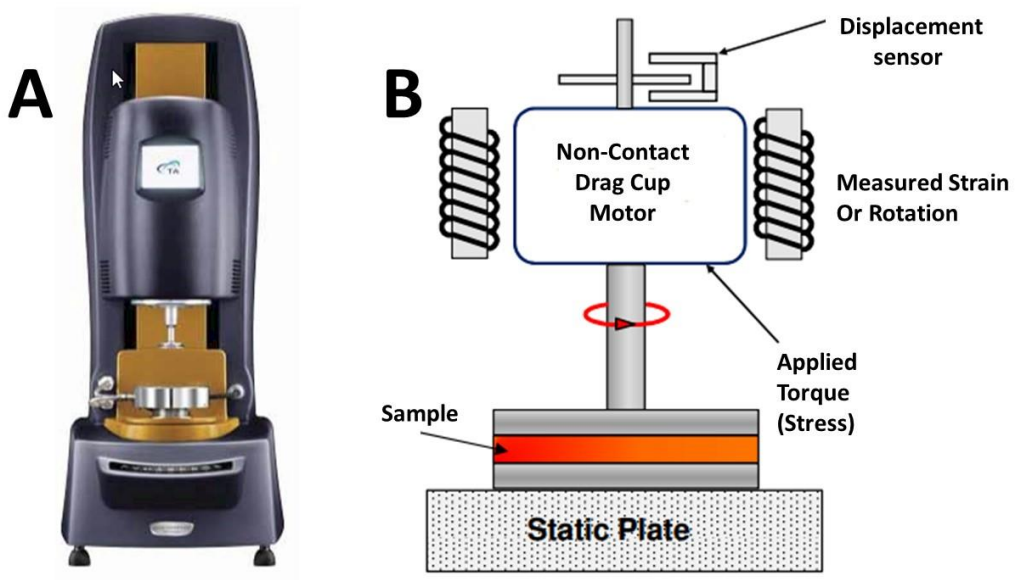

Figure 3-8. (A) A stress-controlled TA Discovery HR-2 rheometer (B) Schematic illustration of key components of a stress-controlled rheometer. Rheometer measures strain or rotation when torque is applied to the sample. Figures are adapted from Ewoldt (19).

A stress-controlled TA Discovery HR-2 rheometer (see Fig. 3-8) was used in this project. Vane (diameter 15mm, length 38 mm) was applied for solid-like suspensions. Loading gap and operating gap were allowed as 90000 µm and

8800 µm, respectively. Whereas bob (diameter 28.02 mm, length 41.94 mm) geometry was applied with Peltier concentric cylinder (30.4 mm) for liquid-like suspensions as shown in Fig. 3-9. Loading gap of 90000 µm was allowed. A Solvent Trap was used to offer a vapour barrier to seal the samples. All rheological tests were conducted at 25°C.

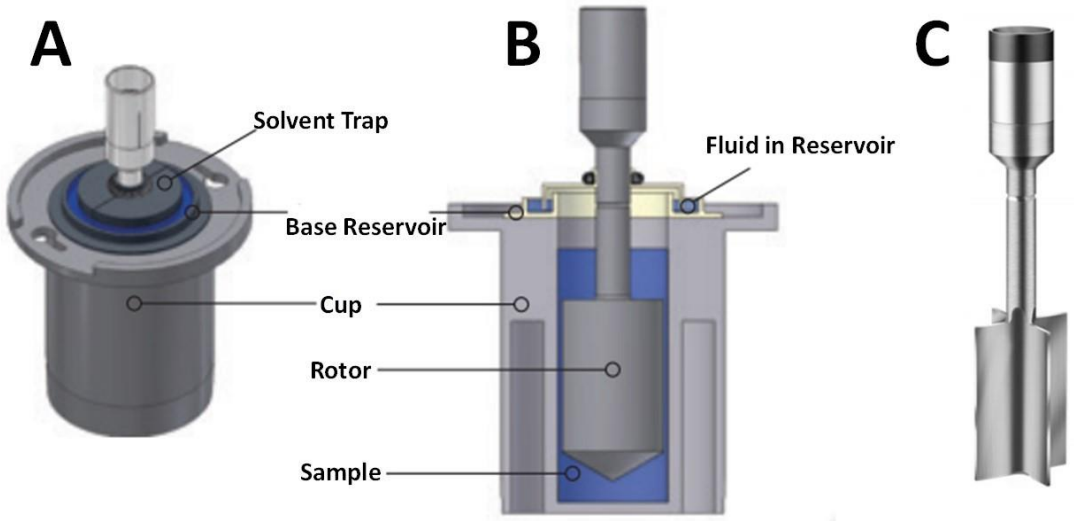

Figure 3-9. Rheometer geometries, (A) a schematic illustration of cup and bob with a Solvent Trap, (B) a schematic diagram of cross section of bob (Din rotor)(C) Vane. Figures are adapted from TA Instruments (20).

3.5 Suspension viscoelasticity

To determine the rheological properties i.e. Viscosity and viscoelasticity in fluids, solids or semi solids, rheometer is the device which has conventionally been employed (21-23). This work involved drawing comparisons between the rheological properties of concentrated particulate solutions using different experimental frequency amplitude sweep and shear strains amplitude sweep experiments. It was revealed that the G' (viscoelastic storage modulus) and

G” (the loss modulus) of soft materials can change over broad experimental frequency ranges (24). This indicates the fact that while drawing such comparisons, it is of significant importance to ascertain the frequency dependent behaviour of concentrated suspensions. The viscoelastic behaviour of concentrated suspensions can be directly measured by using the devices which have integral software for this purpose e.g. Discovery HR-2 rheometer (TA Instruments, UK). The region of linear viscoelasticity range (LVR) needs to be identified prior to taking frequency sweep measurements for a particular sample (21). To do that, the viscoelastic properties of the sample are measured by undertaking an amplitude sweep which involves varying strain i.e. amplitude of oscillation as indicated in Fig. 3-10. The set up for this test is shown in Fig. 3-9, which indicates that a 4-bladed vane having length of 42 mm and diameter of 28 mm is gently inserted into the suspension after placing the sample in a cup of 30.4mm diameter. It was ensured that a van was fixed at a constant height of 9.6 mm above the bottom of the cup. To guard against the phenomenon of thixotropy i.e. any history effects on the specimen, a pre-shear was applied to the suspension which helped to re-form the experimental conditions for the intended test. Selecting a reasonably low frequency, the amplitude test was then performed on the specimen which yielded a response identical to the one shown in Fig. 3-10.

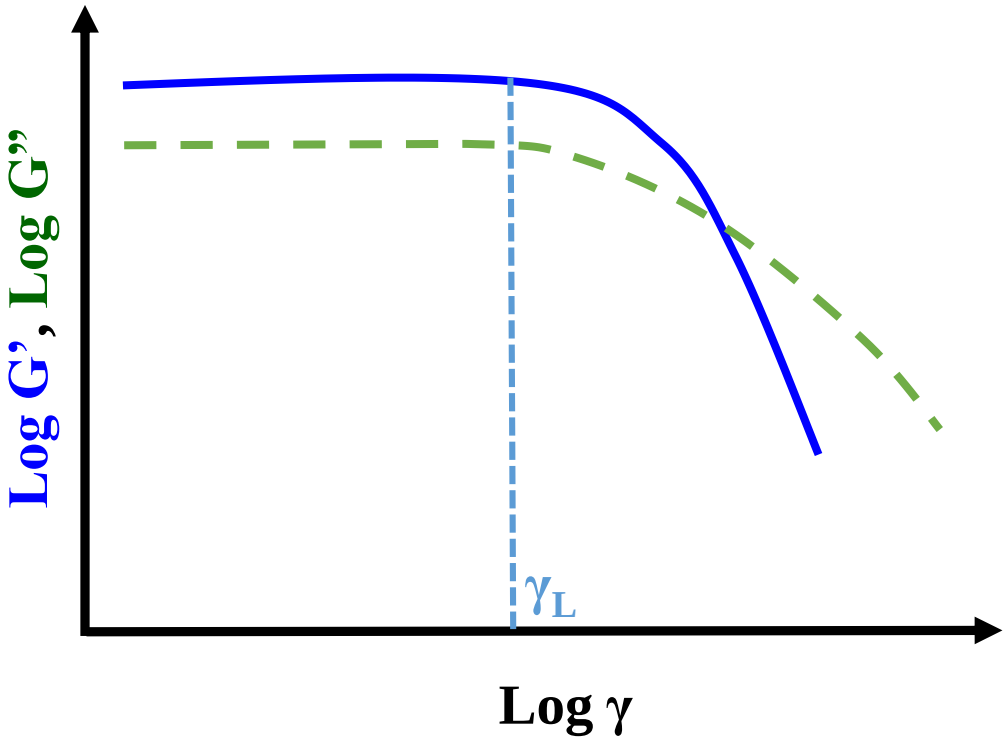

Figure 3-10. Illustrates a typical measurement from oscillation shear strain sweep with a constant angular frequency of a concentrated suspension. Stored modulus (G') and loss modulus (G") are shown as a function of shear strain. Rheometer measures expected response from the material with changing oscillation shear strain. Linear viscoelastic region (LVR) can be observed, when shear strain value is lower than linear viscoelasticity (γ_L). In LVR, Sample behaves solid-like material and G' is independent of oscillation shear strain and shows linear response. Figure is redrawn from Ferry (25).

The equilibrium is generally maintained resulting in insignificant stretching or bond breaking of the particle-particle links, once the test is performed while remaining within the LVR of the suspension (25, 26). The material's behaviour in such test can be described to be a single function of time since the kinematic i.e. magnitudes of stress and strain are seen to vary linearly (26).

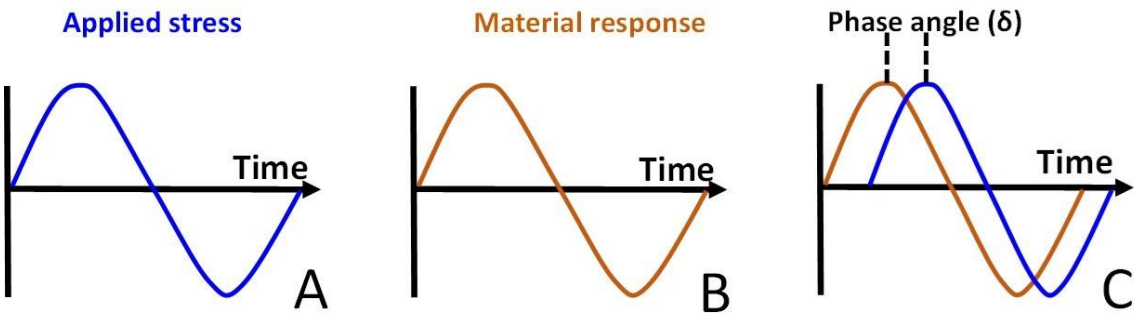

Figure 3-11. In Oscillation rheology, viscoelastic properties are measured by rheometer, when stress (A) is applied to the material and material shows response (B) accordingly. Phase angle (δ) can be calculated, which is the difference between applied stress curve and material response curve. Figure is redrawn from Ferry (25).

Figure 3-11A indicates the application of stress in the form of a sinusoidal or oscillatory deformation. The material response obtained as a result of such oscillatory application of stress is shown in Fig. 3-11B (25). Variation between the material response and the applied stress in the form of deformation is measured in terms of a phase angle (δ) as indicated in Fig. 3-11C.

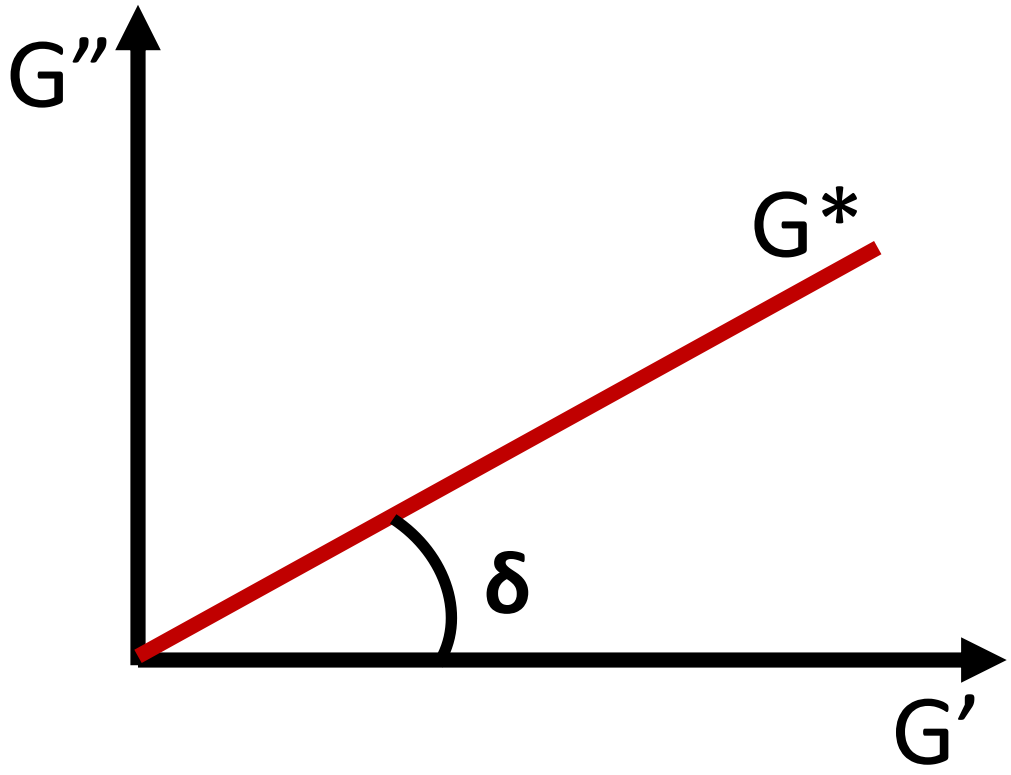

Figure 3-12. Illustrates a vector diagram of the complex modulus G*, where its real part corresponds to the elastic modulus G' and its imaginary part corresponds to the viscous modulus G". Therefore, viscoelastic properties can be calculated mathematically using phase angle (δ) value. Figure is redrawn from Ferry (25).

A vector diagram as shown in Fig. 3-12 can then be used to manifest the G’ and G” (viscoelastic properties) of the material. In this representation, the complex shear (G*) modulus is taken as equivalent to the stress strain ratio i.e. $G*=\tau/\gamma$.

It is also possible to represent δ in the form of tan (δ) and here δ = 0° indicates a fully elastic medium whereas, δ = 90° indicates a fully viscous medium (25). The tan (δ) can be termed as a damping or loss factor here. Having obtained

the viscoelastic properties at variable strains, a frequency sweep can then be undertaken. The frequency of the oscillating stress curve (as given in Fig. 3-11A) is varied (generally within the range of 0.1-100 rad/s) while keeping the strain on the sample constant having a value within the LVR of suspension. For every selected frequency point, the corresponding G' and G" values are measured as indicated in Fig. 3-13 (25).

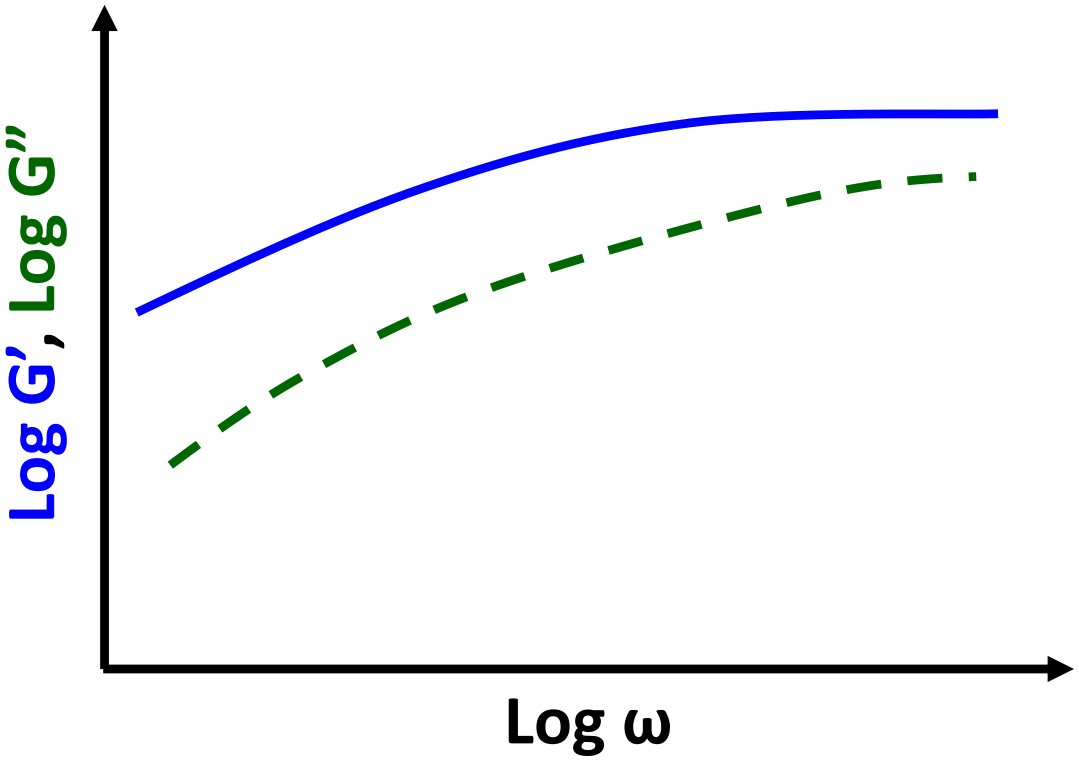

Figure 3-13. Illustrates a typical measurement from frequency amplitude sweep with a constant shear strain. G' and G" are shown as a function of angular frequency. Frequency dependant response from the material is observed. Figure is redrawn from Rudraraju and Wyandt (21).

In order to draw comparisons between mono and binary concentrated suspensions, the viscoelastic behaviour of the suspensions at varying shear strains and frequencies is therefore obtained.

3.6 Scanning Electron Microscopy

In this technique, high energy electron beam is fired on to the sample using a scanning electron microscope model FE-SEM SU8230 (Hitachi, UK). Electrons are bombarded on to the sample which cause emission of secondary electrons and X-rays (27). Schematic illustration of the key components of the SEM technique is provided in Fig. 3-14 which depicts the electron beam generation, electron beam manipulation and the beam-sample interaction. The primary electron beam is generated by the electron beam gun located at the top of microscope. Characteristics like size, shape and position of the electron beam are controlled through electron beam manipulation. Beam-sample interaction implies the contact of electron beam with the sample resulting in release of various types of signals. Main components of the electron gun includes a filament, grid gap which controls the flow of electrons, and a positively charged anode to attract and accelerate electrons down the microscope. The microscope coil houses the electromagnetic lenses and coils.

The electron beam tries to diverge as it passes through the column but the electromagnetic lens converges it and is thus directed onto the sample. Electric and magnetic fields influence the moving electrons. The converging lenses are controlled by the magnetic fields which are generated by passing

an electric current through the copper wire (hence calling them electromagnetic lenses), whereas the electron gun itself is controlled by the electrostatic fields. Once a primary electron enters the sample, the signal detection is indicated. The electrons, upon interaction with sample, form a new trajectory and this phenomenon is termed as scattering. These electrons can then be detected as secondary or backscattered. When a new electron is emitted from an atomic orbital, the secondary electrons are detected and resultantly the energy from the electron emitted by the focus beam is lost to the atom from which electron is ejected and this phenomenon is termed as inelastic scattering. Whereas when an electron coming from the electron gun rebounds, the backscattering of electron is said to occur and it is a form of elastic scattering. A plot of secondary electron is viewed at a typical SEM image where the detected intensity is plotted against the detector position. The image thus generated depends primarily on the surface of the particles.

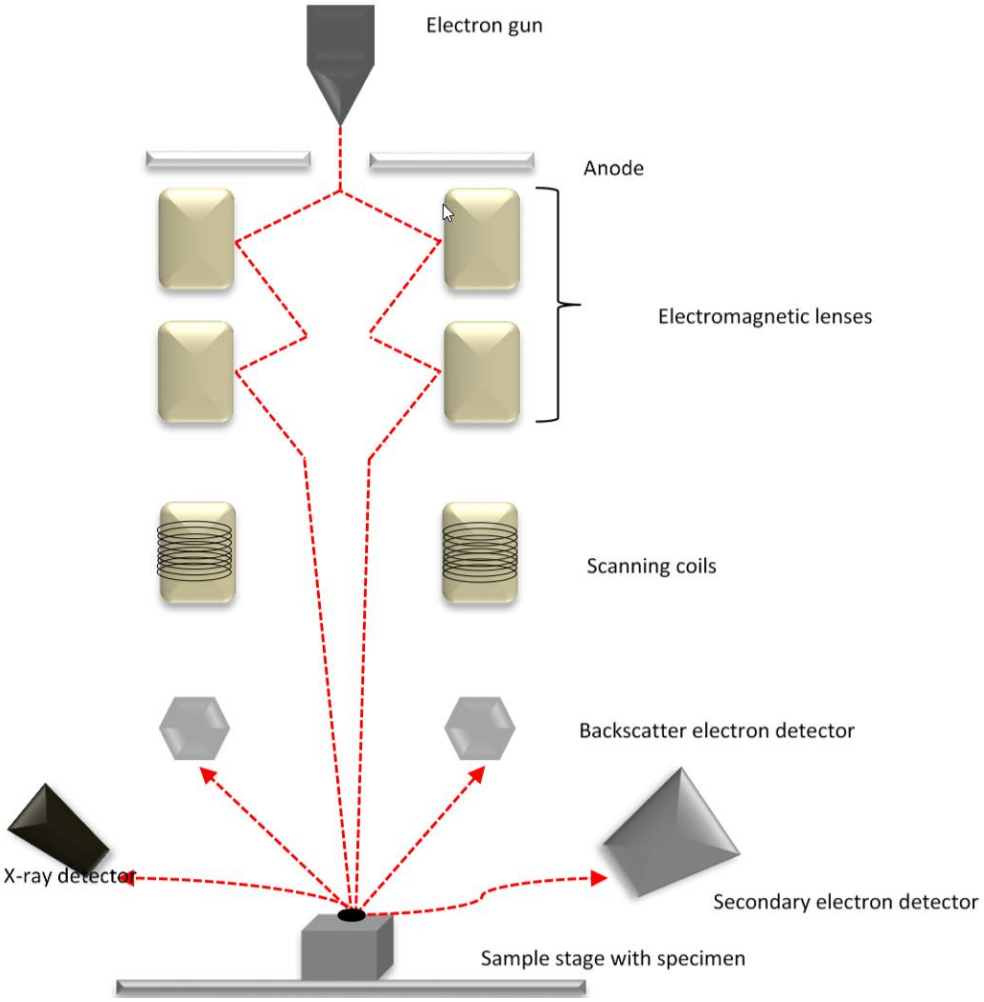

Figure 3-14. A schematic demonstrates the key mechanisms of SEM. The electron beam is displayed by a red dotted line. Once the electron beams hit the sample, then scattered beams are detected by various detectors. Figure is taken from ref. (28).

3.6.1 Energy Dispersive X-ray Analyser (EDX)

Radiations in the form of x-rays are released once the ejection of electrons from specific orbits of an atom in the sample takes place (29). The x-rays thus generated can provide elemental information. The detection unit for the x-rays is also contained in the SEM. The mechanism of x-rays generation is depicted in Fig. 3-15. As described in the phenomenon of generation of secondary electrons, the emission of x-rays takes place when the high energy electron

beam is focused on to the sample. The atom within the sample, while at rest, contains ground state electron which exists in the discrete energy orbital bound to the nucleus. This electron is excited due to the electron beam and is ejected from the discrete orbital thus becoming secondary electrons and an electron hole gets created. The electron released in this manner from the atom gets replaced by another electron from higher energy orbital. Due to the difference between the energy levels of higher and lower energy orbital, the x-rays are formed. It becomes difficult to classify the x-rays as being emitted from the originating element because they will not have sufficient energy when the number of hits increases. In such conditions these are known as background x-rays. The EDX measures the number and energy level of x-rays emitted from the sample.

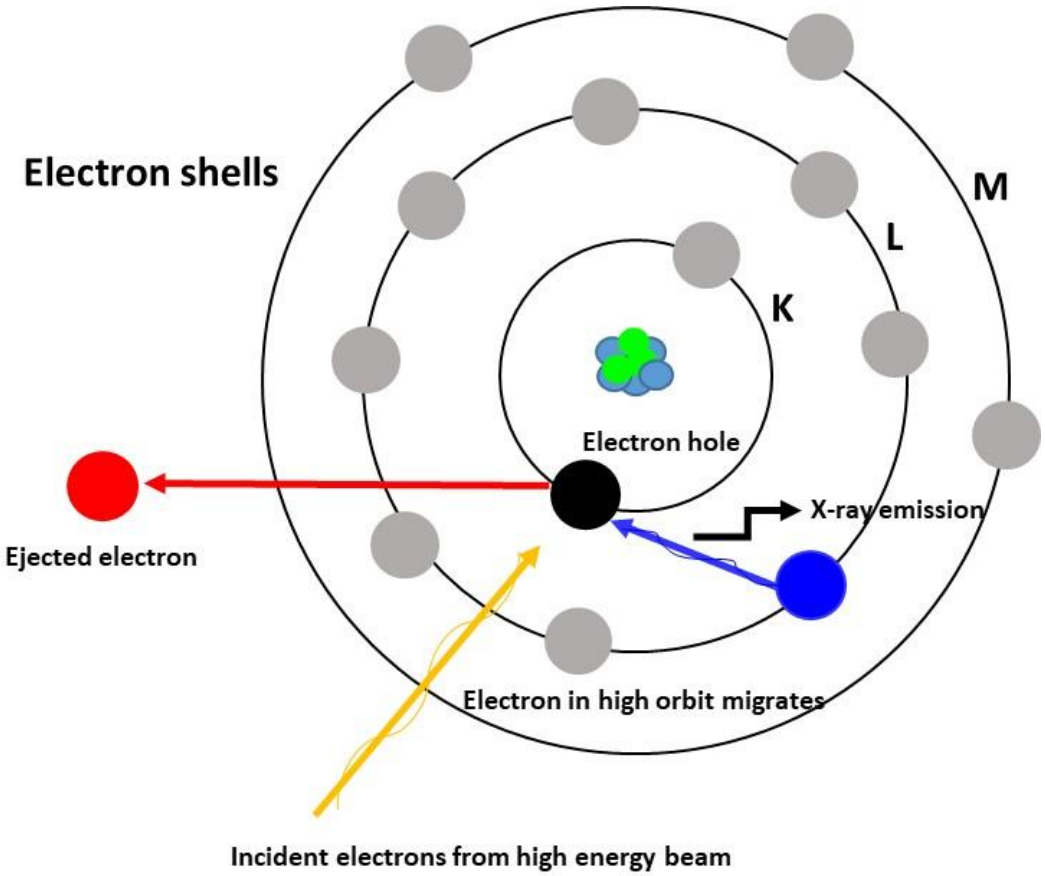

Figure 3-15. A schematic shows the atomic structure with electron shells of an atom. When high energy electrons beam ejected the electron and another electron replaced from high orbit, x-rays can be formed in this process, which holds the information of the element. Therefore this technique (EDX) is widely used in SEMs.

3.7 Cryo-SEM

A sample of binary suspension of alumina (33 vol%) and silica (2 vol%) was prepared at pH 9 using standard protocol for oscillation rheology (see Chapter 4). Cryo-SEM (from Quorum Technologies, UK) was used (see Fig. 3-16a) to study the particle-particle interaction between same charged particles as alumina and silica particles have negative surface charge at pH 9. Two rivets (328116510), were used and approximately 0.5 mL of the sample pipetted on

to the each rivet which were connected (see Fig. 3-16b) with a specimen shuttle (20530). Then specimen shuttle was connected with the Cryo transfer device (see Fig. 3-16c) and samples (included shuttle) were transferred into slushed nitrogen (PP3010, Prepdek™). Vacuum was created by pump which was attached with Prepdek™ and then just before N_2 turned solid again, the samples were placed into vacuum pot. Sublimation process was applied to samples for 2 minutes to remove the subliming ice from the surface of the samples (T = -90 °C). Once ice is removed, temperature was reduced to -140 °C. after that a coating of iridium was applied for 45 s At 10 mA. Then the Cryo transferred device was used to transfer the samples to a Quilo cryo preparation chamber (see Fig. 3-16d), where it was ensured that samples are frost free. This process takes time between 5-10 minutes. Cryo preparation chamber is also installed with twin fracturing tools manipulators (see Fig. 3-16e), which were used to form a cracked onto the surface of the samples. Then samples were transferred into SEM (Hitachi, UK) for further observations.

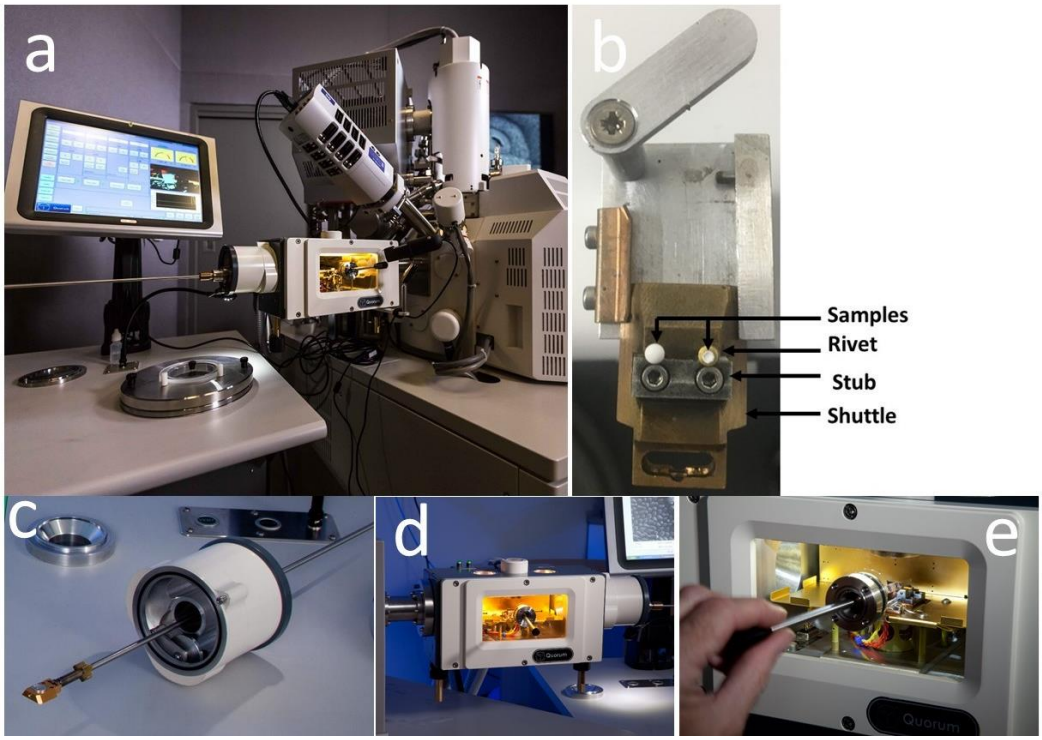

Figure 3-16. Digital images of (a) Cryo-SEM system (b) samples were pipetted on the rivets, which was attached with a shuttle (c) The cryo transfer device with shuttle and rivets (d) a cryo preparation chamber (Quilo) and (e) Twin fracturing tools manipulators.

3.8 Centrifuge

Primarily, a centrifugation process is commonly used to separate mixtures using the principles of sedimentation. A gravitational force (g-force) is applied to the samples and therefore, due to difference in density gradient between medium and particles, heavy particles form a sediment bed at the bottom of a centrifuge tube and light particles or liquid stay above, which is called supernatant (see Fig. 3-17c) and can be pipetted out. The rate of sedimentation can be calculated by Stoke's law (30, 31) as:

$$\boldsymbol{v = \frac{d^2(\rho_p - \rho_L)\ g}{18\eta}}$$ **Eq. 3.7**

where v is rate of sedimentation or velocity, d is a diameter of the sphere particle, ρ_p is a particle density, ρ_L is a medium density, g is a gravitational force and η is a viscosity of medium.

It can be seen from the equation 3.7 that the rate of sedimentation can be influenced by particle size, particle density and viscosity of the medium. it should be noted that Stoke's law applies on spherical particles (32).

RCF is reliant on the rotational speed (rpm) of the rotor (mechanical motor) in minute. RCF can be calculated as:

$$\boldsymbol{RCF = 11.18\ (r)\ (\frac{rpm}{1000})^2}$$ **Eq. 3.8**

where r is the rotational radius in centimetre (cm) and rpm is revolutions per minute (32).

Centrifuge device, Heraeus™ Megafuge™ 16 R (75004270) from Thermo Fisher Scientific, UK (see Fig. 3-17a) was used to study consolidation of binary suspensions (see Chapter 5). This device (see Fig. 3-17a) has a maximum speed of 13000 rpm and a maximum Relative Centrifuge Force (RCF) is 15777. Minimum and maximum rotor radius is 25 mm and 98 mm (see Fig. 3-17b), respectively.

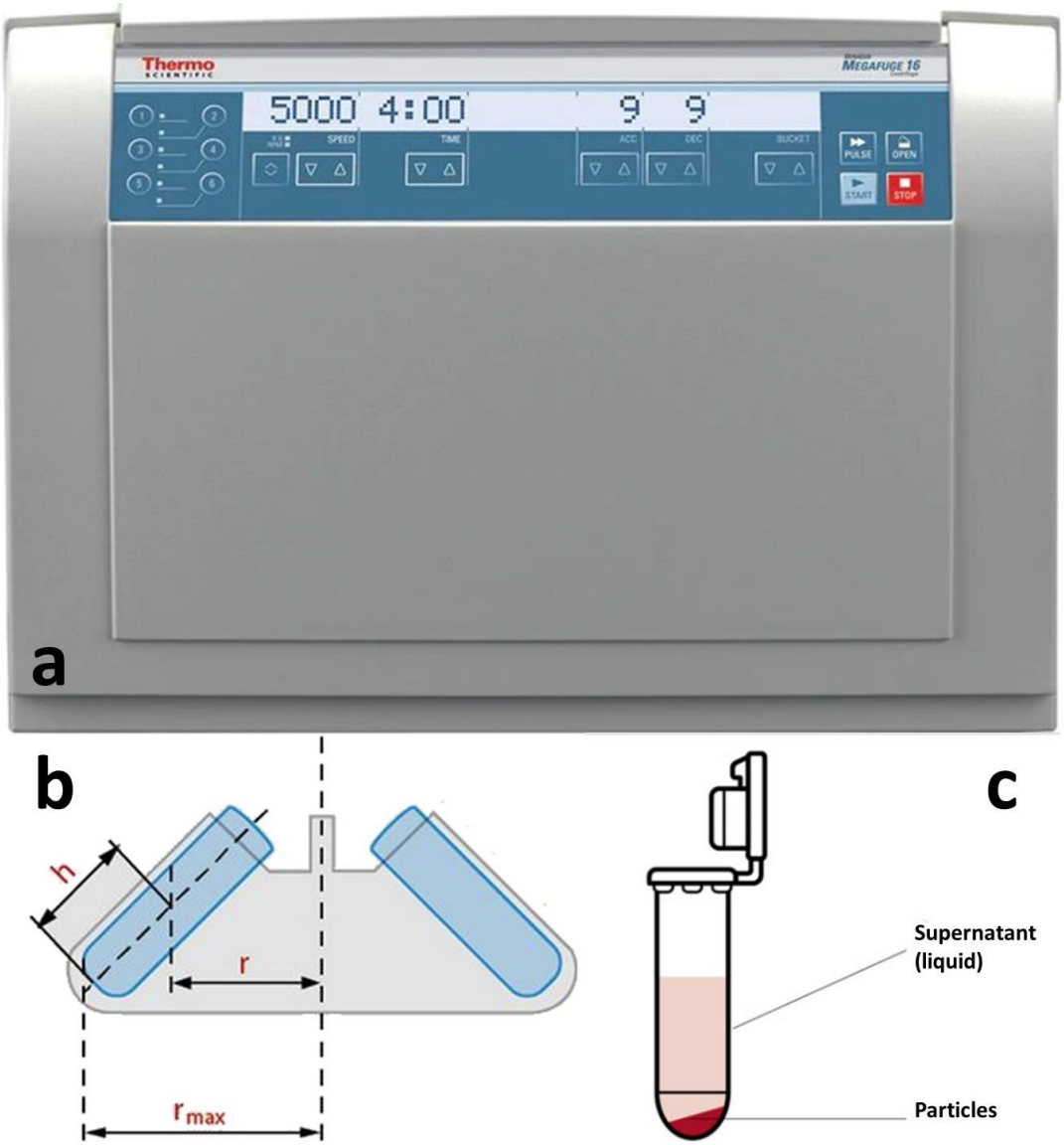

Figure 3-17. Photo of (a) Heraeus™ Megafuge™ 16 R Centrifuge device from Thermo Fisher Scientific, UK, (b) a schematic diagram of rotor with centrifuge tubes, (c) schematic illustration of centrifuge tube, where heavy particles are shown at the bottom and supernatant are shown at the top of the centrifuge tube. Figures are taken from Frei (32).

References

1. Bergna, H.E. Colloid chemistry of silica: An overview. In: ACS Publications, 1994.
2. Derjaguin, B. and Landau, L. The theory of stability of highly charged lyophobic sols and coalescence of highly charged particles in electrolyte solutions. *Acta Physicochim. URSS.* 1941, **14**, pp.633-652.
3. Verwey, E. Theory of the stability of lyophobic colloids. *The Journal of Physical Chemistry.* 1947, **51**(3), pp.631-636.
4. Verwey, E.J.W., Overbeek, J.T.G. and Van Nes, K. *Theory of the stability of lyophobic colloids: the interaction of sol particles having an electric double layer.* Elsevier Publishing Company, 1948.
5. Healy, T.W. Stability of aqueous silica sols: Fundamentals and Applications. *Surfactant science series.* 2006, **131**, pp.247-252.
6. Chuiko, A., Lobanov, V. and Grebenyuk, A. Structure of disperse silica surface and electrostatic aspects of adsorption. *Surfactant science series.* 2006, **131**, pp.331-360.
7. Hind, A.R., Bhargava, S.K. and Grocott, S.C. The surface chemistry of Bayer process solids: a review. *Colloids and Surfaces A: Physicochemical and Engineering Aspects.* 1999, **146**(1), pp.359-374.
8. Tsyganenko, A.A. and Mardilovich, P.P. Structure of alumina surfaces. *Journal of the Chemical Society, Faraday Transactions.* 1996, **92**(23), pp.4843-4852.
9. Levin, I. and Brandon, D. Metastable alumina polymorphs: crystal structures and transition sequences. *Journal of the American Ceramic Society.* 1998, **81**(8), pp.1995-2012.
10. Shirai, T., Watanabe, H., Fuji, M. and Takahashi, M. Structural properties and surface characteristics on aluminum oxide powders. 2010, pp.23-31.
11. Tougerti, A., Methivier, C., Cristol, S., Tielens, F., Che, M. and Carrier, X. Structure of clean and hydrated α-Al 2 O 3 (11 [combining macron] 02) surfaces: implication on surface charge. *Physical Chemistry Chemical Physics.* 2011, **13**(14), pp.6531-6543.
12. Hamley, I.W. *Introduction to soft matter.* Wiley, 2000.

13. Malvern. *Zetasizer Nano Z* [Online]. 2015. [Accessed 18.04.2015]. Available from: http://www.malvern.com/en/products/product-range/zetasizer-range/zetasizer-nano-range/zetasizer-nano-z/default.aspx?gclid=CJS6nYqa-MQCFYzMtAodjUAAKw
14. Malvern. *Zetasizer nano User Manual.* 11 ed. Worcestershire: Malvern Instruments Ltd, 2013.
15. Shaw, D.J. 1 - The colloidal state. In: Shaw, D.J. ed. *Introduction to Colloid and Surface Chemistry (Fourth Edition)*. Oxford: Butterworth-Heinemann, 1992, pp.1-20.
16. Mie, G. Contributions to the optics of cloudy media, particularly of colloidal metal solutions. *Ann Phys.* 1908, **330**, pp.377-445.
17. Blackledge, J.M. Chapter 6 - Scattering Theory. In: Blackledge, J.M. ed. *Digital Image Processing*. Woodhead Publishing, 2005, pp.160-197.
18. Wang, Q., Shi, A. and Shah, F. 18 - Rheology instruments for food quality evaluation. In: Zhong, J. and Wang, X. eds. *Evaluation Technologies for Food Quality*. Woodhead Publishing, 2019, pp.465-490.
19. Ewoldt, R.H. *Rheology, Theory and Applications.* [Online]. 2019. [Accessed 15th May 2020]. Available from: https://www.tainstruments.com/wp-content/uploads/Boston-Rheology-Training-2019.pdf
20. Instruments, T. *Discovery Hybrid Rheometers Temperature Systems And Accessories* [Exhibition catalogue]. TA Instruments, 2019.
21. Rudraraju, V.S. and Wyandt, C.M. Rheology of microcrystalline cellulose and sodiumcarboxymethyl cellulose hydrogels using a controlled stress rheometer: part II. *International journal of pharmaceutics.* 2005, **292**(1-2), pp.63-73.
22. Fisher, D.T., Clayton, S.A., Boger, D.V. and Scales, P.J. The bucket rheometer for shear stress-shear rate measurement of industrial suspensions. *Journal of Rheology.* 2007, **51**(5), pp.821-831.
23. Fischer, P. and Windhab, E.J. Rheology of food materials. *Current Opinion in Colloid Interface Science.* 2011, **16**(1), pp.36-40.

24. Pakula, T., Geyler, S., Edling, T. and Boese, D. Relaxation and viscoelastic properties of complex polymer systems. *Rheologica acta.* 1996, **35**(6), pp.631-644.
25. Ferry, J.D. *Viscoelastic properties of polymers.* John Wiley & Sons, 1980.
26. Pryamitsyn, V. and Ganesan, V. Origins of Linear Viscoelastic Behavior of Polymer− Nanoparticle Composites. *Macromolecules.* 2006, **39**(2), pp.844-856.
27. Dunlap, M. and Adaskaveg, J. *Introduction to the scanning electron microscope.* UC Davis: Facility for Advance Instrumentation. UC Davis, 1997.
28. Paul, N. *Characterisation of highly active nuclear waste simulants*. thesis, University of Leeds, 2014.
29. YURUGI, T., ITO, S., NUMATA, Y. and SYKES, K.J.H.E.t.f. *SEM/EDX-Integrated Analysis System SEMEDX Series.* 2001.
30. Stokes, J.R. and Telford, J.H. Measuring the yield behaviour of structured fluids. *Journal of Non-Newtonian Fluid Mechanics.* 2004, **124**(1), pp.137-146.
31. Robinson, C.D. Some factors influencing sedimentation. *industrial & Engineering Chemistry.* 1926, **18**(8), pp.869-871.
32. Frei, M. *Centrifugation Basics,* [Exhibition catalogue]. SIGMA-AlDRICH, 2019.

Chapter 4

Method Development

4.1 Synopsis

This chapter provides a comprehensive discussion assessing different methods to measure the yield stress of high solid content suspensions. Several challenges associated with repeatability and accurate measurements of yield stress are highlighted considering the different methods to measure yield stress as well as different rheometer geometries. The chapter focuses on single component (alumina), highly concentrated colloidal suspensions, and concludes with the recommendation on the method that was used throughout the research to study the blended colloidal systems.

4.2 Literature Review

Concentrated suspensions are widely found in many industrial processes, and their behavior is often dominated by their flow properties, or rheology. A large number of consumer products, especially food and personal care products depend on structured fluids (multiphase systems) (1, 2). The mixing, casting and forming, of these fluids requires basic knowledge of their rheological behaviour, *i.e*. fluid viscosity as a function of shear stress, which is highly dependent on the solids concentration and particle size (3).

Complex fluids or highly structured fluids often exhibit a yield stress and do not flow unless a certain force (stress) is exceeded, with yielding leading to deformation and breakdown of the microstructure (1, 2, 4). For example, squeezing toothpaste from a tube is demonstration of a yield stress.

The idea of yield stress is highly debated and by far the most controversial subject for more than 3 decades in the rheological literature. In 1985, Barnes and Walters started this debate with their paper " The yield stress myth?" (5) and tried to explain that if accurate measurements and precise experimental protocol was followed then there would be no yield stress (5, 6). Many researchers have taken up this challenge to validate the yield stress of various systems using different measurements techniques (1, 6-9). Barnes published a follow-on paper "The yield stress—a review or 'παντα ρει'—everything flows?" in 1999 (10), where he reviewed many authors work and quoted their thoughts about the yield stress whether they are agreed or disagreed with the existence of yield stress. The common understanding of yield stress is a

minimum stress required to initiate flow. Below the yield stress a material can behave elastically, (with yielding promoting flow, and rheology is described by its viscous properties (1, 2, 10).

A first rheological model to account for yield stress was introduced by Eugene Cook Bingham in his book named Fluidity and Plasticity in 1922, although Bingham published his model equation in 1916 (11), which is as follows

$$\boldsymbol{\sigma = \sigma_y + \eta\dot{\gamma}} \qquad \textbf{Eq. 4.1}$$

where σ is the shear stress, σ_y the yield stress, η the viscosity and $\dot{\gamma}$ the shear rate. Bingham's law describes the elastic and viscous behaviour of yield stress fluids when applying stress.

In 1927, Professor Thomas Parnell from University of Queensland, Brisbane, conducted an experiment to measure the viscosity of a high yield stress material. He poured a sample of warm pitch into a glass funnel, which was attached to a sealed stem. 3 years were allowed for the pitch to obtain an equilibrium state. The bottom of the stem was cut in 1930 to allow the pitch to flow. 9 drops of the pitch were formed since then and the 10th drop is supposed to be due in 2020. The viscosity of the pitch is calculated and found to be about 20 billion times greater than viscosity of water. This experiment proves that flow can be achieved if enough time is given to any system. This is the longest experiment in history and is called a "Pitch drop experiment", which is illustrated in Fig. 4-1 (12).

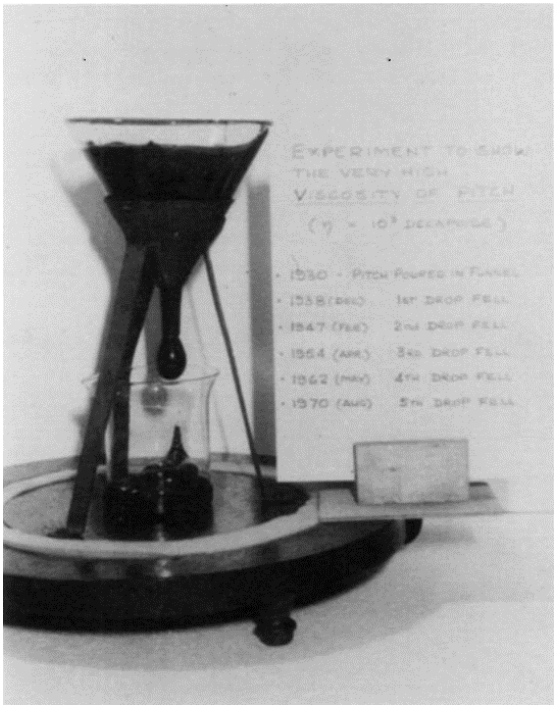

Figure 4-1. Apparatus of the pitch drop experiment with the recorded dates of first 5 drops (image taken from ref. (12)).

Measuring the yield stress of concentrated suspensions is extremely difficult. According to a classic definition, yield stress is the critical stress at which the fluid starts to move. In other words the fluid viscosity is infinitely large (2, 10, 13-15). Since this cannot be measured, it is generally accepted that the yield stress is the highest stress at which no flow is observed during the experimental time. Hence, the measured yield stress may change because it depends on the experimental protocol (2).

James et al. studied the yield stress of illitic (clay) suspensions using two different devices, the pulse shearometer and the constant stress rheometer using a vane and bob geometry. The authors showed that a yield stress

variation of more than 1 order of magnitude can result just by using different measurement techniques (16).

Mujumdar et al. (17) developed a model to describe the flow behaviour of yield stress fluids. Instead of using one yield stress value, two yield stress values describing the static and dynamic yield stress were used to describe the elastic and viscous responses. This work certainly contradicted the classical definition of yield stress (17). Despite the difficulties to accurately measure yield stress fluids, it is a commonly reported property that is used by engineers in design calculations. While values can vary, trends are consistent, independent of the measurement technique.

Figure 4-2(a) shows the increase in shear stress as a function of time for varying constant shear rates. The yield stress point can be described in three different regions, which are the linear elastic region, the maximum shear stress region and plateau region. All these regions satisfy the classic definition of yield stress. Figure 4-2(b) shows the time evolution fluid shear stress at different constant shear rates measured on two instruments, as rotational rheometer and a strain-controlled Haake viscometer. Again the lack of consistency underlines the challenge in making accurate yield stress measurements. Many experiments insufficiently define experimental

conditions when making yield stress measurements and fail to explain how the structured fluid flows under those conditions (2, 10, 13-15, 18).

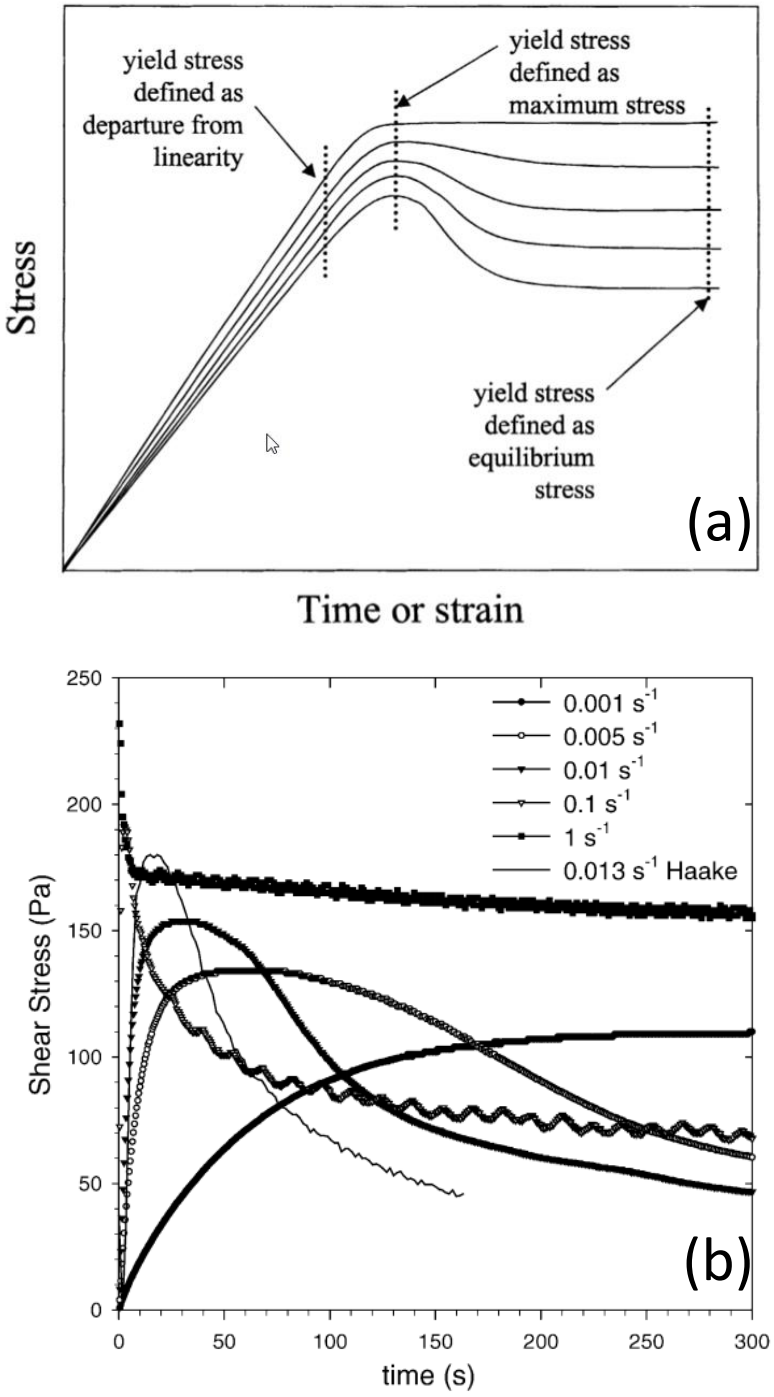

Figure 4-2. (a) Schematic showing the different definition of yield stress at different shear rates (image taken from ref. (18)). (b) Data showing the time evolution of stress at different shear rates measured using different instruments (image taken from ref. (1)).

One of the challenges in making reliable yield stress measurements is understanding the shear history of the sample. Since yield stress signifies the breaking of a structure, if a structure has been broken and then allowed to rest, the sample may exhibit some recovery, as described by a thixotropic fluid. If the start condition is not equivalent then it is hard to ensure the measured yield stress will be consistent (3, 19, 20).

A number of methods and techniques have been developed to determine yield stress. A review of those common approaches is described below.

4.2.1 Stress Ramp

A stress ramp is the most common and simplest method to measure yield stress. A stress controlled rheometer is required to perform this test. A linear shear stress ramp is applied and the fluid viscosity measured. The shear viscosity as a function of time or stress shows a maximum in fluid viscosity. The stress at which the viscosity is a maximum is taken to be the yield stress. Prior to the viscosity maximum in the low shear stress region, the material behaves solid-like and experiences elastic deformation. Elastic deformation of the microstructure eventually leads to plastic deformation and the material starts to flow (3, 4, 10, 19). A schematic of this test protocol is shown in Fig. 4-3(a) for yield stress and no yield stress fluids (4). Derakhshandeh et al. (21) measured the yield stress of 1 wt% bleached softwood kraft pulp suspension (SBK) using a linear stress ramp at 23°C, see Fig. 4-3(b). In order to obtain reproducibility, all measurements were conducted a minimum of 5 times.

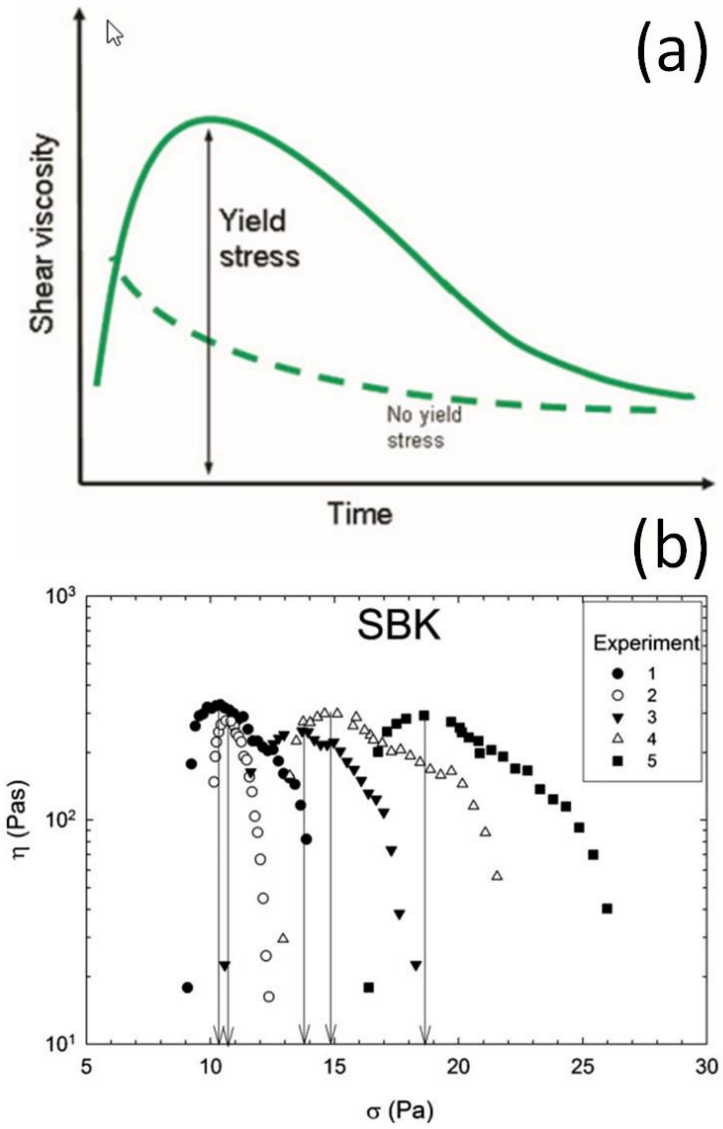

Figure 4-3. (a) Schematic of a yield stress and no yield stress materials undergoing a linear stress ramp. A peak viscosity is characteristic of a yield stress material (image taken from ref. (4)). (b) Multiple yield stress measurements of 1 wt% SBK suspension at 23°C using a linear stress ramp (image taken from ref. (21)).

4.2.2 Stress Growth

Using a stress control rheometer or viscometer to shear a fluid at a constant shear rate (constant increasingly strain), the shear stress is measured as a function of time, see Fig. 4-4. Three different regions are observed including i) linear region, ii) nonlinear region and iii) stress decline region. Once shear is initiated, the solid-like structure undergoes gradual deformation/compression, as shown by the linear increase in stress, where the particle network is able to retain the increasing stress. Eventually the stress can no longer be retained in the particle network and the system begins to flow, signified by point (A) which is often taken to be the fluid yield stress (3, 10, 18, 19, 22). However some researchers (13, 23) have suggested that the yield stress is at point (B), where the stress profile begins to deviate from non-linearity, and is the incipient point of yielding. Another cause of error when conducting rotational measurements is the potential for wall slip, where the sample first yields at the geometry wall prior to yielding itself. To overcome this issue it is advisable to used roughened geometries, or change the gap size (8, 21, 24, 25).

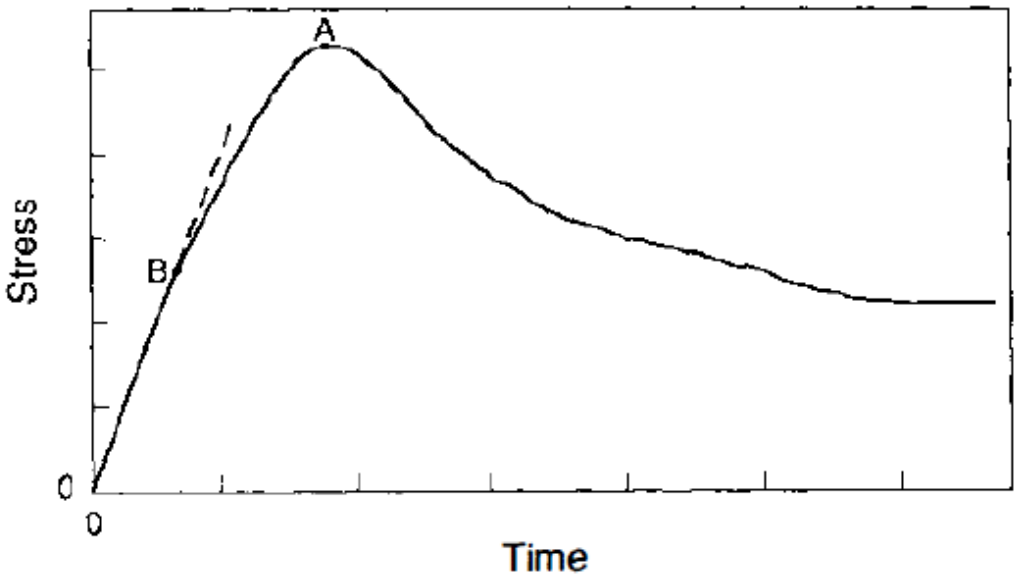

Figure 4-4. Schematic of a stress growth experiment showing the stress response with overshoot (image taken from ref. (13)).

James et al. (25) used a bob geometry to measure the yield stress of a 2.5 vol% illite suspension using the stress growth method in controlled strain. A constant shear rate of 6.63×10^{-3} s^{-1} was applied for 50 s and the stress response was measured as shown in Fig. 4-5. Between points A and B the stress increased linearly with time, which describes the intrinsic mechanical response of the particle network below the yield point. Here the particle network is slightly stretched and corresponds to the elastic deformation of the suspension. At Point C, the maximum stress is measured and corresponds to the yield stress of the suspension. Here the network is broken as the particle-particle contacts are disrupted and the material starts to flow. This is seen as a reduction in the stress to a new steady state which depends on the applied share rate.

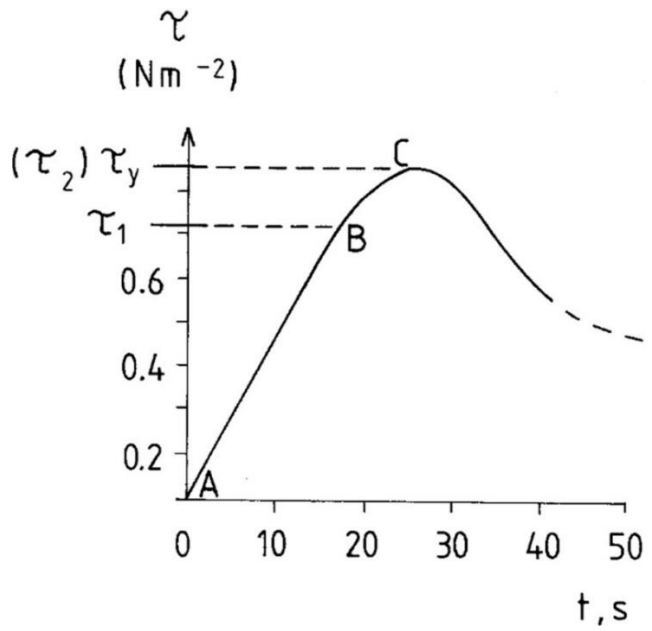

Figure 4-5. Experimental data of 2.5 vol% illite suspension was conducted using stress growth method at constant shear rate of 6.6 × 10^{-3} s^{-1} (image is taken from ref. (25)).

4.2.3 Creep and Creep Recovery

Creep is a more accurate method to measure yield stress of complex fluids. A constant stress is applied in a series of incremental stresses and the strain (creep) of the material measured as a function of time, see Fig. 4-6(a) (26). When the strain increases linearly with time the material is said to have yielded (Fig. 4-6(b)) (26).

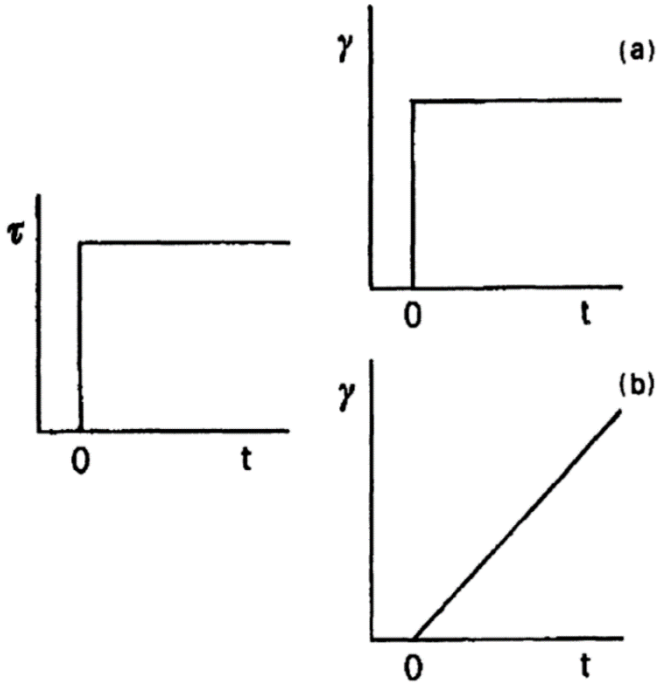

Figure 4-6. For a step-change in stress a material behaves elastically (a) or as a viscous fluid (b) (image taken from ref. (26)).

Since the applied stress governs the strain, the relationship between stress and strain is described by the creep compliance (J):

$$J(t) = \frac{\gamma(t)}{\sigma} \qquad \textbf{Eq. 4-1}$$

where J is the compliance, γ the strain (deformation) and σ the shear stress. The creep compliance (J) vs. time can be compared for different applied stress. If the applied stress is below the yield stress, then creep compliance curve should collapse on each other (Fig. 4-7(a)) because strain should be independent of the applied stress and constant within the viscoelastic region, therefore material is said to be elastic solid. If the applied stress is higher than

the yield stress the creep compliance would increase linearly (Fig. 4-7(b)) and the material behaves as a viscous fluid (10, 13, 26, 27).

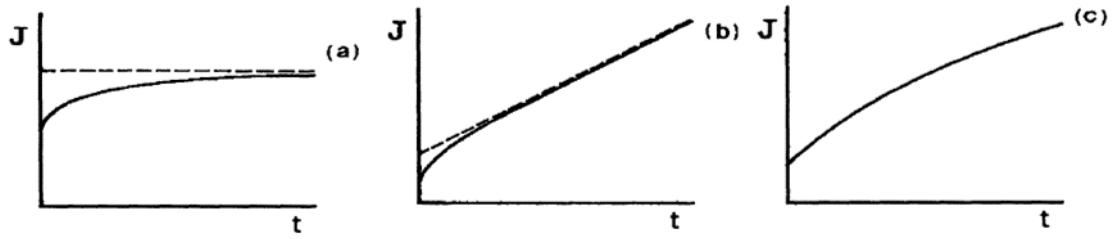

Figure 4-7. Creep compliance for (a) an elastic solid, (b) a viscous fluid and (c) a characteristic viscoelastic fluid (image is taken from ref. (26)).

Creep recovery is another method to determine yield stress and viscoelastic properties of complex fluids. A constant stress is applied to a material for a period of time before the stress is rapidly removed and the material left undisturbed for a fixed time (usually applied stress time = undisturbed time). The resultant strain (deformation) is measured under applied stress and after stress removal (Fig. 4-8(a)). The process is repeated several times with the constant applied stress being slightly increased at each step to study the elastic and viscous responses of the material. If the material strain (deformation) is fully recovered ($\gamma = 0$), then the material is said to be elastic (Fig. 4-8(b)). If the strain value is constant (permanent plastic) then the material is said to be viscous (Fig. 4-7(c)). If the material exhibits partial recovery it is described as a viscoelastic solid. If there is almost no decrease in strain, the material is said to be a viscoelastic fluid (Fig. 4- 8(e)) (16, 28, 29).

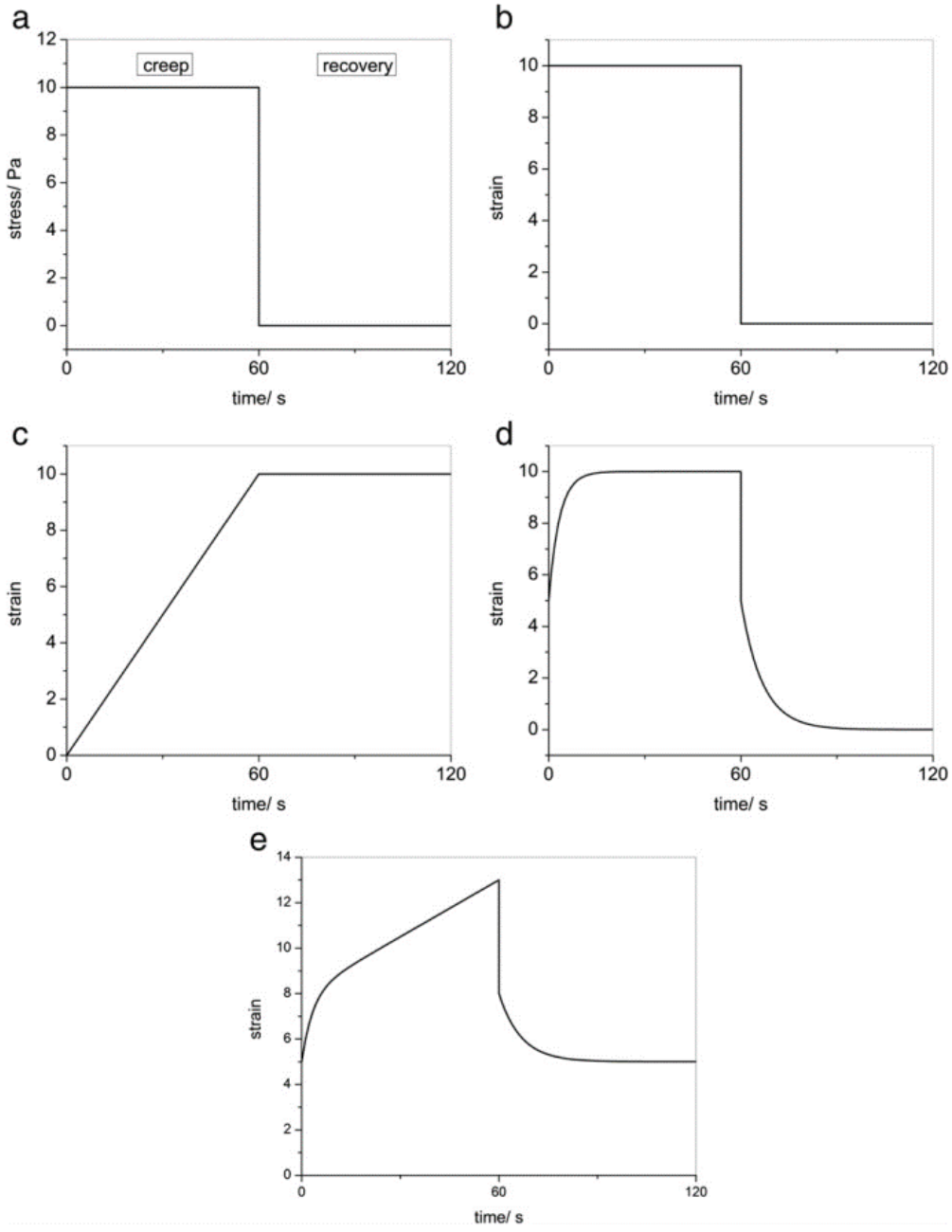

Figure 4-8. (a) Stress decrease for creep recovery assessment. Characteristic behavior of (b) an elastic solid, (c) a viscous liquid, (d) a viscoelastic solid, (e) a viscoelastic liquid (image taken from ref. (28)).

In creep recovery, applied stress is described by the creep compliance (J). James et al. (28) measured the yield stress of 2.5 vol% and 5 vol% illite suspensions using the creep recovery method. Figure 4-9 shows the viscosity

and yield stress to be lower for 2.5 vol% solids compared to 5 vol% solids. Figure 4-9(a) shows both suspensions exhibit elastic behaviour at low constant stress, as shown by an independence in the creep compliance with stress. When the constant stress is increased beyond the yield stress the creep compliance increases, and the yield stress is taken to be the stress at which the creep compliance significantly deviates from the constant compliance behavior. Deviation in the creep compliance corresponds with a sharp decrease in the fluid viscosity, as shown by orders of magnitude decrease in suspension viscosity. There is only one drawback of the creep and creep recovery methods which relates to the lengthy experimental time associated with the measurement itself, and identifying the stress region of interest. The long experimental time may cause issues of sample drying, and therefore the user must be aware that the sample is not changing during the experiment (13, 16).

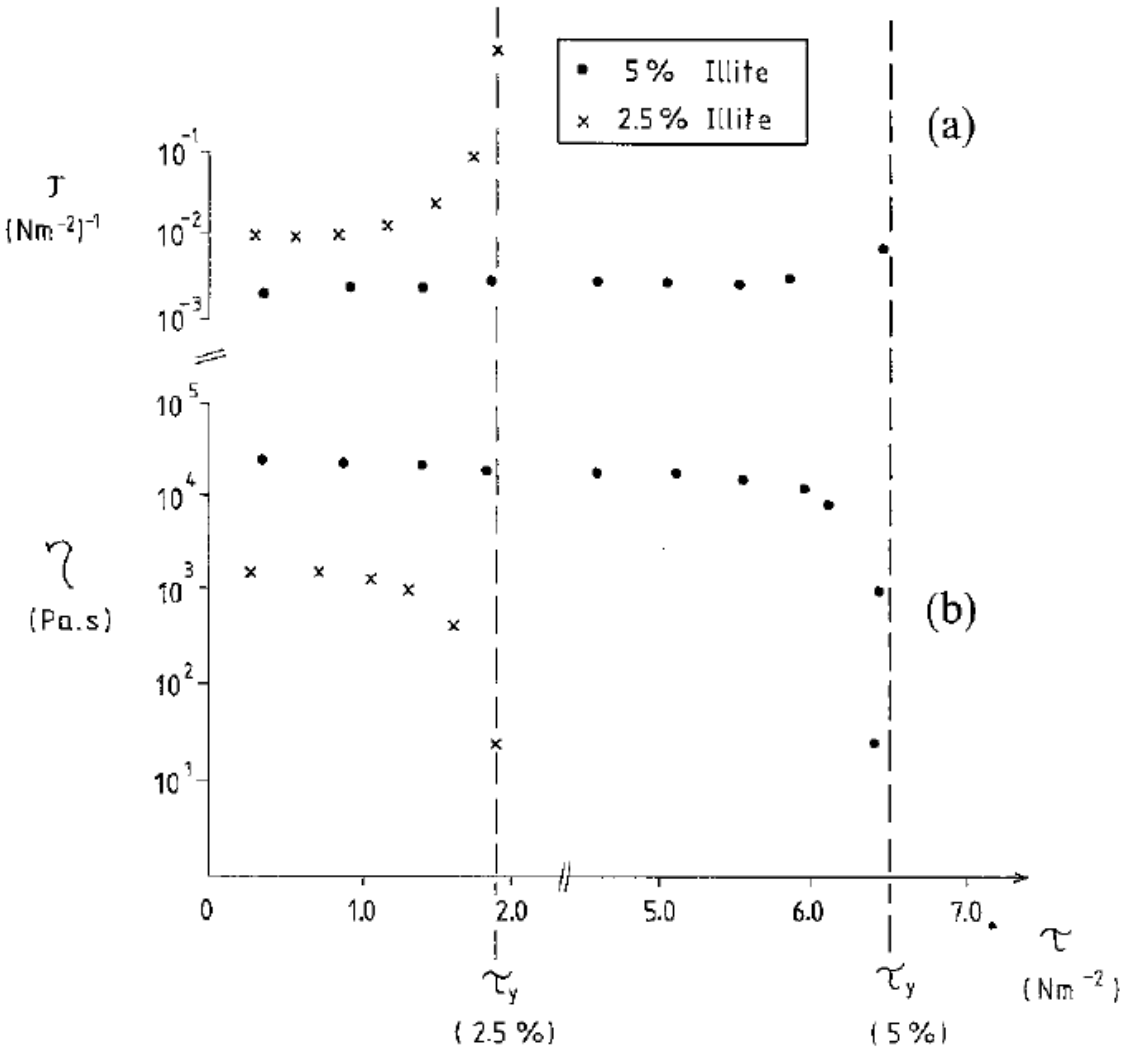

Figure 4-9. Experimental data of creep compliance (J) and viscosity (η) as a function of applied stress (σ) for a 2.5 and 5 vol% illite (clay) suspension (image taken from ref. (16)).

4.2.4 Oscillation Amplitude Sweep

Oscillation amplitude sweep is another method to measure yield stress, and shows good data reproducibility (30). This method includes increasing the oscillatory strain or stress at a constant frequency and measuring the storage modulus (G'). Figure 1-10(a) shows a schematic of typical oscillatory behavior of a complex fluid. The elastic (G') and viscous (G") moduli as a function of

the oscillation strain (ε) shows three regions. At low strain, region (I), G' > G the material is considered solid-like. The independence with strain confirms that the material is in the linear viscoelastic region (LVR). Region (II) occurs at intermediate strain and both G' and G" begin to fluctuate. A crossover with G' = G" occurs and signifies structural yielding. The increase in G" reflects the internal re-ordering of the structure prior to yielding, and is common with the build-up of stress in a constant shear rate test. At a high strain, region (III) G" > G' and the material is now considered liquid-like. Determination of yield stress is again assessed differently. Some researchers identify the first decrease in elastic modulus (G') as a yield stress value (dotted line at the edge of LVR in Fig. 4-10(a)), as this identifies the condition of non-linearity (4, 8, 13), while others (30, 31) consider the crossover point of G' and G" as a yield stress point (region (II) in Fig. 4-10(a)). For example, Shih et al. used Rheometrics Fluids Spectrometer (RFS-8400) with parallel plates to measure the elastic and viscous moduli of a 4.5 vol% alumina (spherical) suspension (Dispal) at pH 3.5 as a function of strain amplitude, and the authors determined the yield stress by the crossover point as shown in Fig. 4-10(b) (31).

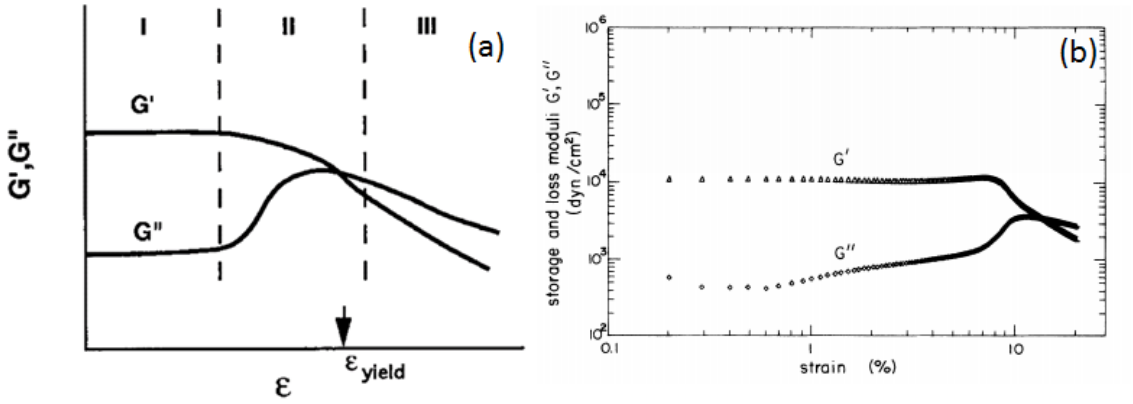

Figure 4-10. (a) Schematic showing an oscillation amplitude sweep. Elastic modulus (G') and viscous modulus (G") are shown as a function of the strain (ε). Region (I) is the linear viscoelastic region (LVR), where elastic modulus is greater than viscous modulus (G' > G"). Region (II) is the solid-liquid transition region, where G' decreases abruptly and G" goes through a maximum. Region (III) is the liquid region, where the viscous modulus is greater than the elastic modulus (G" > G') (Figure is taken from ref. (30)). (b) G' and G" viscoelasticity of a 4.5 vol% Dispal boehmite alumina gel as a function of strain amplitude at constant frequency of 1.0 rad s^{-1}. 0.244 M KCl electrolyte was used (image taken from ref. (31)).

More recently researchers developed an alternative method to determine the yield stress using oscillatory amplitude sweep. The maximum (peak) in the elastic stress is considered to be a yield stress point on an elastic stress-strain curve, as structure deformation occurs beyond that point and elastic stress decreases (32, 33). Elastic stress is defined as

$$\boldsymbol{Elastic\ stress = G'\gamma} \qquad \textbf{Eq. 4-2}$$

where G' is the storage modulus and γ the strain.

Walls et al. (33) measured the yield stress of 0.051 vol% of hydrophobic fumed silica (Aerosil R805) suspension conducting oscillatory stress amplitude using a Rheometrics Dynamic Stress Rheometer (DSR II). G' and G" values are shown in Fig. 4-11(a) as a function of increasing stress amplitude. At low shear stress, G' is approximately constant in the LVR with the corresponding elastic stress increasing with strain. As G' decreases and goes through the crossover point, the elastic stress plateaus begins to decrease Fig. 4-11(b). The maximum in elastic stress corresponds to the yield stress.

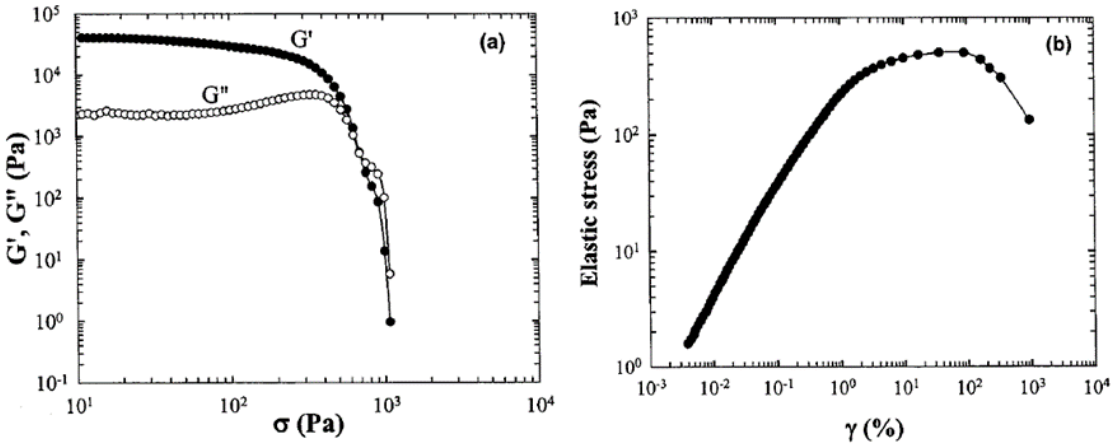

Figure 4-11. (a) Viscoelasticity of hydrophobic fumed silica (12 nm) suspension containing 1.07 M lithuum bis(trifluoromethanesulfonyl)imide (LiTFSI) in Poly (ethylene glycol) dimethyl ether (PEGdm 250). Classical yielding is shown by the decrease in G' and the crossover of G' and G". (b) Elastic stress $(G'\gamma)$ as a function of strain (γ), where the yield stress is taken as the maximum value of elastic stress (image taken from ref. (33)).

4.2.5 Tangent Analysis Method

Tangent analysis is another method of interpreting data to determine the yield stress. This method is suitable for steady state (Figs. 4-12(a) and (b)) and oscillatory amplitude tests (Fig. 4-12(c)). In oscillatory amplitude tests, a tangent is drawn to the G' plateau of the linear viscoelastic region (LVR) and the initial slope in G', with the intersect of both tangent lines considered to be the yield stress (3, 4, 8, 13, 19, 34). Using the tangent method, a logarithmic scale should be used to provide clear fits of the tangents.

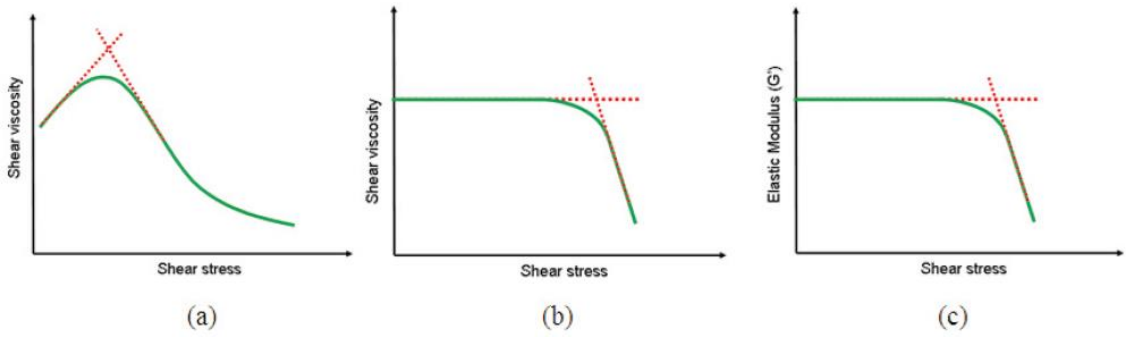

Figure 4-12. Tangent analysis method to determine the yield stress of materials by rotational (a and b) and oscillatory (c) measurements (image taken from ref. (4)).

Yanez et al. (34) used the oscillatory strain amplitude method to determine the yield stress of 20 vol% alumina suspension at pH 4. Figure 4-13 shows the G' and G" response as a function of strain. Using the tangent method, with a line fitted to the LVR (line d) and the flow region (line e), point (J), identifies the intersect of the two lines which is called the yield strain. The yield stress is the determined by: (34)

$$\sigma_y = \gamma_y G' \qquad \text{Eq. 4-3}$$

where σ_y is the yield stress, G' the elastic modulus and γ_y the yield strain.

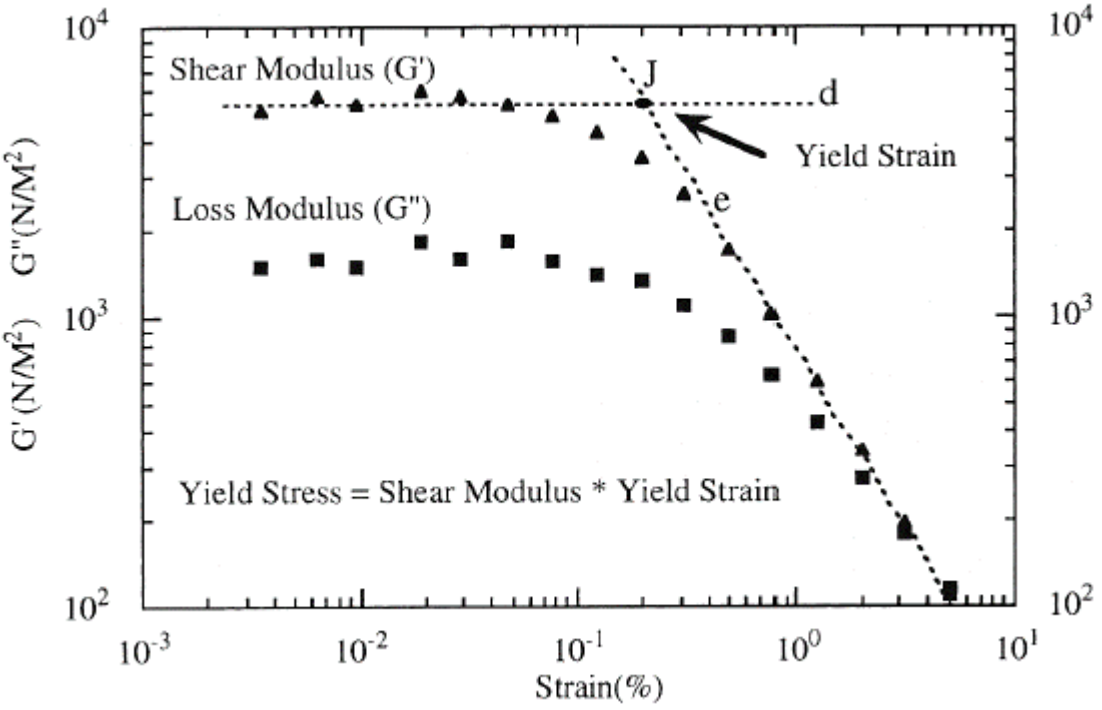

Figure 4-13. Viscoelastic behavior of 20 vol% alumina in 2.5 M NH_4Cl at pH 4. Tangent analysis method was used to determine the yield stress as the intercept of the two tangent lines (image taken from ref. (34)).

4.3 Materials and Methods

4.3.1 Materials

Alumina powder (Al_2O_3) (product number: AL-160SG-3) with average particle size of 0.52 µm was obtained from Showa Denko, Japan . Angstromsphere silica (SiO_2) powder of average size 0.1 µm was obtained from Fibre Optic Centre. Scanning electron microscope (SEM) images confirmed the alumina particles to be irregularly shaped (plate-like) and the silica particles to be spherical. Ultrapure Milli-Q water (Merck Millipore, USA) with a conductivity of 0.055 µS cm^{-1} and resistivity of 18.2 MΩ cm at 25°C was used throughout the study. Sodium chloride (NaCl) and hydrochloric acid (HCl) (37% wt/wt) were obtained from Fisher Scientific. Sodium hydroxide (NaOH) (50% wt/wt) was obtained from Sigma-Aldrich. All chemicals were used without further purification.

To prepare all suspensions, a 4 blade impeller (d = 30mm) with overhead stirrer (Cole-Parmer) was used. With samples prepared, samples were sealed in plastic containers and placed on a tube roller for sample aging. Further details on sample preparation and measurement are provided in Section 4.3.2.

4.3.2 Experimental Methods

4.3.2.1 Experimental Protocol: Stress Ramp

This section describes the experimental method to prepare high concentrated alumina suspensions (35 vol%) at pH 8. 1 mM NaCl solution was prepared as a background electrolyte and used for all samples. Firstly (day 0, t = 0 h), 89 g of alumina (0.52 µm) was added slowly to 39 mL of 1 mM NaCl solution under gentle stirring at 500 rpm. With all the alumina added, the pH of the suspension was checked (in general, pH of alumina suspension is around 8.5) and adjusted to the desired pH using 5 M HCl to avoid any dilution effects. One drop of 5 M HCl was added to the suspension and then manually mixed by hand for 3 min. The pH adjustment protocol was optimized and found to shift the suspension pH to pH 8. The prepared samples were then left on the roller overnight to ensure homogeneous ionic concentration had been attained. It is worth noting that the suspension conditions were mostly determined from preliminary laboratory work. Since the overall objective of the study was to modify the yield stress of high solids content suspensions, the initial condition was set so that the suspension yield stress was approximately 100 Pa at the different pH conditions to be tested. The solids concentration of 35 vol% was found to meet this criterion, and when the solids concentration was increased to 40 vol%, the torsional limit of the rheometer was approached thus limiting the reliability of the measured data. Two pH conditions were considered at pH 8 and pH 9 to vary the strength of the colloidal interaction between the major and minor component particle species. Further details regarding this are provided in Chapter 5.

Day 1, t = 24 h, the pH of the suspension was rechecked and readjusted by adding one drop of 5 M HCl if required, and mixed manually for 3 min. With the alumina suspensions prepared to pH 8, 40 mL of sample was gently transferred to the concentric cylinder geometry of the rheometer (DHR-2, TA Instruments), and the stress ramp run following the protocol, which is described in Section 4.3.2.4. Calibration of the rheometer is described in Section 4.3.2.3.

The experimental protocol to prepare the Al_2O_3 suspensions is shown in Fig. 4-14 for the stress controlled measurements. While not discussed in the current chapter, the sample preparation protocol over 2 days became the standard when testing both single and dual component suspensions. As discussed in Chapter 5, Section 5.3.3, the blending time to strongly modify the suspension rheology was found to be 2 days. The mechanism for the flow modification is discussed in Chapter 5 and describes the improved distribution (dispersion) of the minor component throughout the high solid content alumina suspension. For comparison, the blending protocol over 2 days was used for all samples.

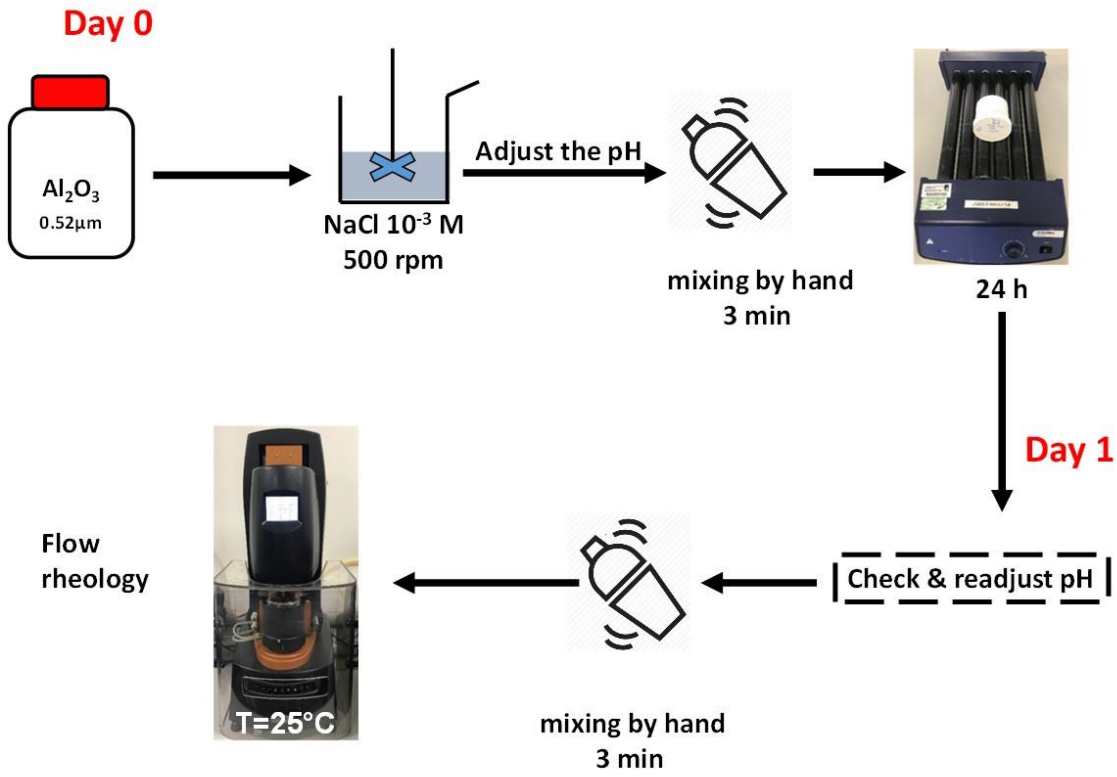

Figure 4-14. Experimental protocol used to prepare mono-system (alumina only) and binary system (alumina and silica) suspensions for stress-controlled rheology measurements.

4.3.2.2 Experimental Protocol: Oscillatory Rheology

This section describes the experimental method for the oscillatory measurement of Al_2O_3 suspensions. The sample preparation protocol for Day 0 and Day 1 was followed as described in Section 4.3.2.1. However, rather than applying manual mixing, a 4 blade overhead stirrer was used to improve the blending process. The blending time was 5 min at 1500 rpm. For samples studied on Day 2 the blending time was 3 min at 1500 rpm. The alumina suspension was transferred to the concentric cylinder using spatula then the concentric cylinder was placed on the vortex (from SciQuip) for 1 min at maximum vibration speed (2500 rpm) to ensure that no air bubble was left in

the system, otherwise it could be challenging to produce good rheology data. Finally, the concentric cylinder attached to rheometer. The experimental protocol to prepare the Al_2O_3 suspensions is shown in Fig. 4-15 for oscillatory rheology measurements.

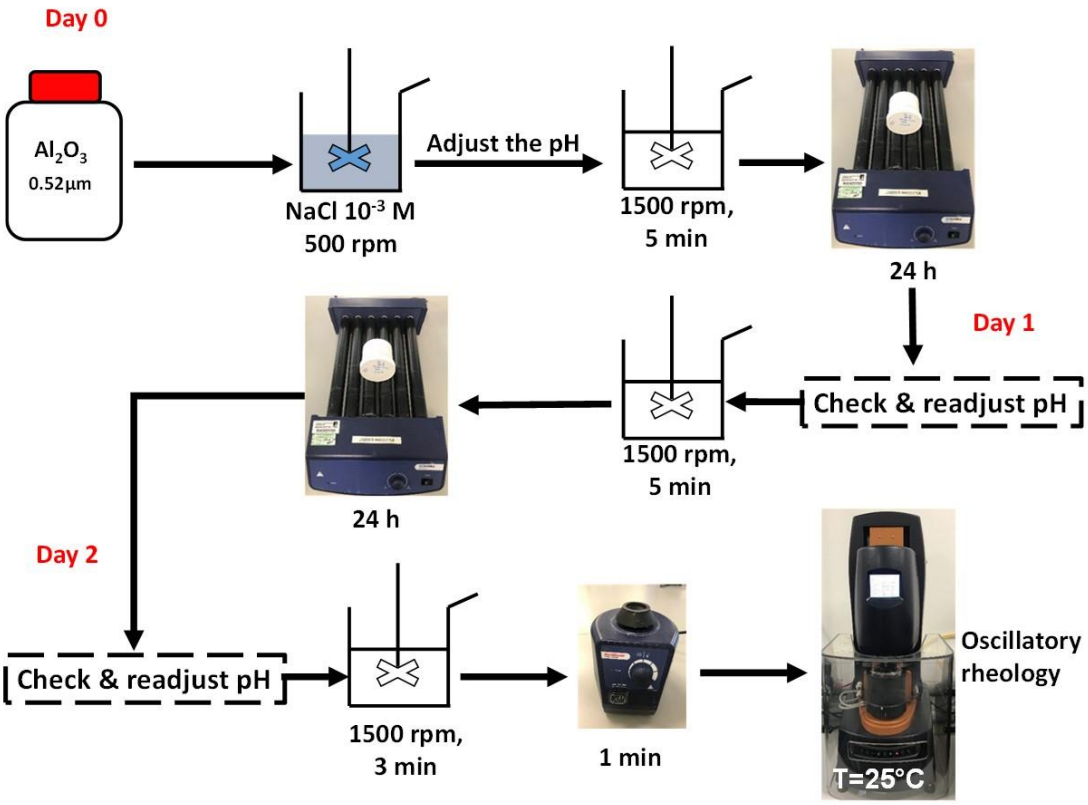

Figure 4-15. Experimental protocol used to prepare mono-system (alumina only) and binary system (alumina and silica) suspensions for oscillatory rheology measurements.

4.3.2.3 Rheometer Set-up and Calibration Protocol

The rheometer was set up and calibrated following the standard method in the rheometer manual. Firstly, the instrument inertia was calibrated in the absence of a rheometer geometry and the instrument inertia was found to be 21.4548 µN m s^{-2}, with the acceptable range between 21 and 22 µN m s^{-2}. It was then

important to calibrate the geometry used for each experiment, either bob or vane geometry. With the geometry attached, the geometry inertia was calibrated with values of 1.59 µN m s^{-2} for the vane and 12.82 µN m s^{-2} for the bob. It also important that the geometry was mapped in the relevant mode of operation either rotational mode or oscillation mode. When mapping the mode of operation, the bearing mode was set to precision level and the number of iterations for the calibration was 5. With the instrument calibrated and mapped, the geometry was then calibrated with the measurement cylinder by zeroing the gap. With the gap zeroed, the geometry could then be precisely positioned at the gap setting of the different geometries, which were 4 mm for the vane and 5.62 mm for the bob geometry. To minimize any solvent loss during the measurement all measurements were conducted with the solvent trap positioned on top of the measurement cylinder.

4.3.2.4 Rheometer Protocol: Stress Controlled Measurement

Figure 4-16 shows the basis for a stress-controlled rheology measurement. For a stress ramp, the user inputs the stress range, the rheometer executes this stress range and programs the shear rates based upon either linear or logarithmic ramping and the shear rate is measured.

Figure 4-16. Steps for a stress-controlled measurement when conducting a continuous stress ramp.

All rheology measurements were conducted at T = 25°C using a Discovery HR-2 rheometer (TA Instruments) equipped with vane (diameter = 28 mm, length = 42 mm) and cup (diameter = 42 mm) geometry.

Initially, a 35 vol% alumina suspension was prepared at pH 9 following the experimental protocol described in Section 4.3.2.1. With the sample transferred to the rheometer cup, the vane was immersed into the suspension to a gap height of 8800 µm. In order to minimise drying of the suspension, a solvent trap with wet tissue attached inside the solvent trap was placed on the measurement cup.

Figure 4-17 shows the experimental protocol for conducting a stress ramp test. Four steps from (a) to (d) were run as follows: step (a), the suspension was pre-sheared at 500 s^{-1} for 1 min to ensure any sample history effects were removed (35); step (b), the sample was allowed to rest (0 s^{-1}) for 3 min to reach a consistent structure prior to measurement (14, 36); step (c), a stress ramp between 0.01 and 1000 Pa was applied over 5 min, collecting 2000 data points with a linear increase in stress; step (d), a stress ramp between 1000 and 0.01 Pa was applied over 5 min, collecting 2000 data points with a linear decrease in stress. Ascending and descending stress ramps are shown by the closed and open blue symbols in Fig. 4-17. Each test was repeated in triplicate to ensure any influence of batch variability was seen.

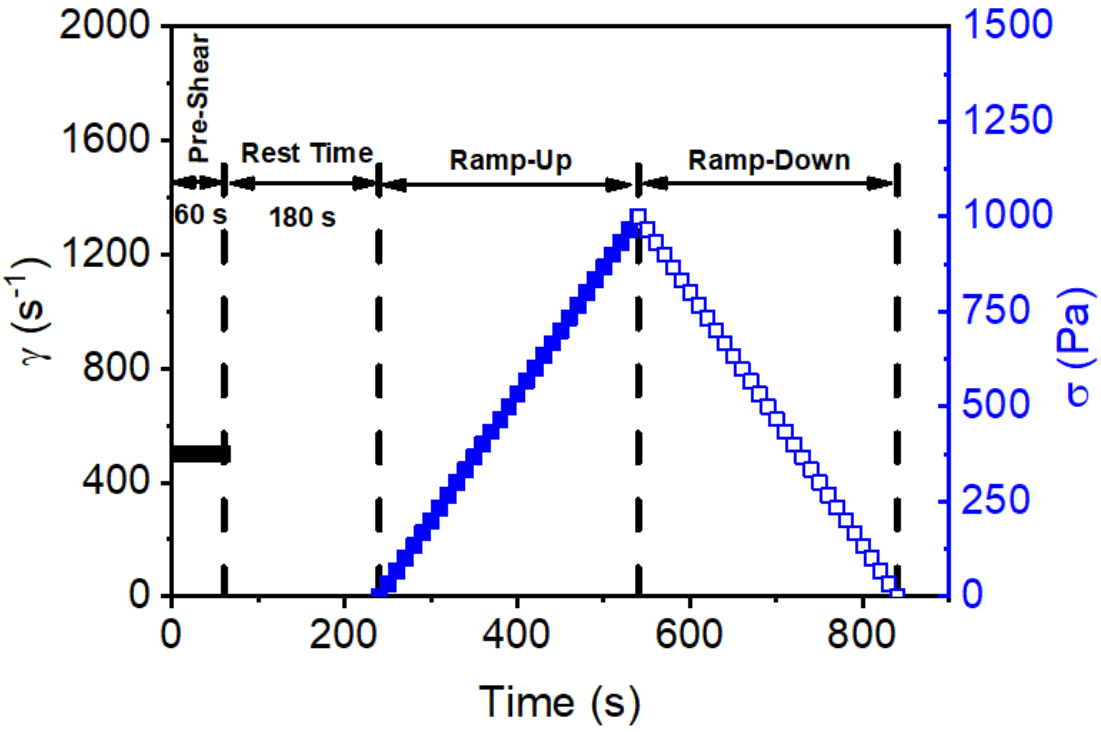

Figure 4-17. Procedure for conducting a stress-controlled measurement. Sample: 35 vol% of alumina slurry at pH 9. (a) pre-shear 500 s^{-1} for 60 s, (b) rest time was applied for 180 s, (c) closed symbols represent the ascending stress ramp, (d) open symbols represent the descending stress ramp.

4.4 Results and Discussion

4.4.1 Stress Ramp: Batch to Batch Variability

Three separate alumina suspensions of 35 vol% were prepared at pH 9 to assess batch to batch variability. The shear stress profiles as a function of shear rate are shown in Fig. 4-18(A) and the corresponding linear transient stress ramp up and down is shown in Fig. 4-18(B).

Even though samples were prepared following the same protocol, and the samples tested using the same experimental protocol, the three stress profiles do not exactly overlay one another. Interestingly, two samples (identified by the black and blue symbols) showed some degree of hysteresis between the shear rate ramp up and down. This behavior is usually described as thixotropy (37-43), with samples showing time-dependent shear thinning behavior. Hysteresis in high solids content suspensions is typical because the time to rebuild the structure is often longer than the structural breakdown under applied shear. Qualitatively the degree of thixotropy, as determined by the hysteresis loop area, usually increases with gel strength (44). Even though all samples exhibit a significant yield stress of a few hundred Pa, those small differences in yield stress values, as seen by the incipient point for non-linear stress build up, is not reflected in the degree of thixotropy. Since the rate of shear rate ramp up and down is constant for all three experiments, the loss of thixotropy (red symbols) cannot be attributed to an imposed rate effect.

An attempt was made to fit Herschel-Bulkley and Bingham models to the experimental data, but the rapid jump in shear rate (inset Fig. 4-18(A)) after

yielding prohibited good fits. More reliable fits could be made by fitting the models to the shear rate ramp down data, but still a jump in shear rate close to the yield stress can lead to significant variability in the determined yield stress, when selecting those data points to fit. Taking the point at which the shear rate jumps from very small values, the yield stress on the up and down cycle is shown by the yellow and green symbols in the inset Fig. 4-18 (A). Taking this approach, the yield stress values of the 3 suspensions (using shear rate up data) were 525 Pa (sample 1), 480 Pa (sample 2) and 445 Pa (sample 3). For the shear rate down data the yield stress values were 380 Pa (sample 1), 265 Pa (sample 2) and 310 Pa (sample 3). The significant difference between yield stress values when ramping up and down is expected when samples exhibit thixotropy and the steady-state condition has not been recovered. As a result of these differences between yield stress values, the shear rate ramp measurement is sensitive to the ramp rate both upwards and downwards, and can introduce variability that reduces the reliability of the method. This observation is widely reported and is consistent with thixotropic effects that are observed in suspensions in the crystalline-liquid coexistence phase (2, 19, 38, 45, 46). The significant differences between yield stress values of each sample proved that such a method could not be reliably used to measure high yield stress values.

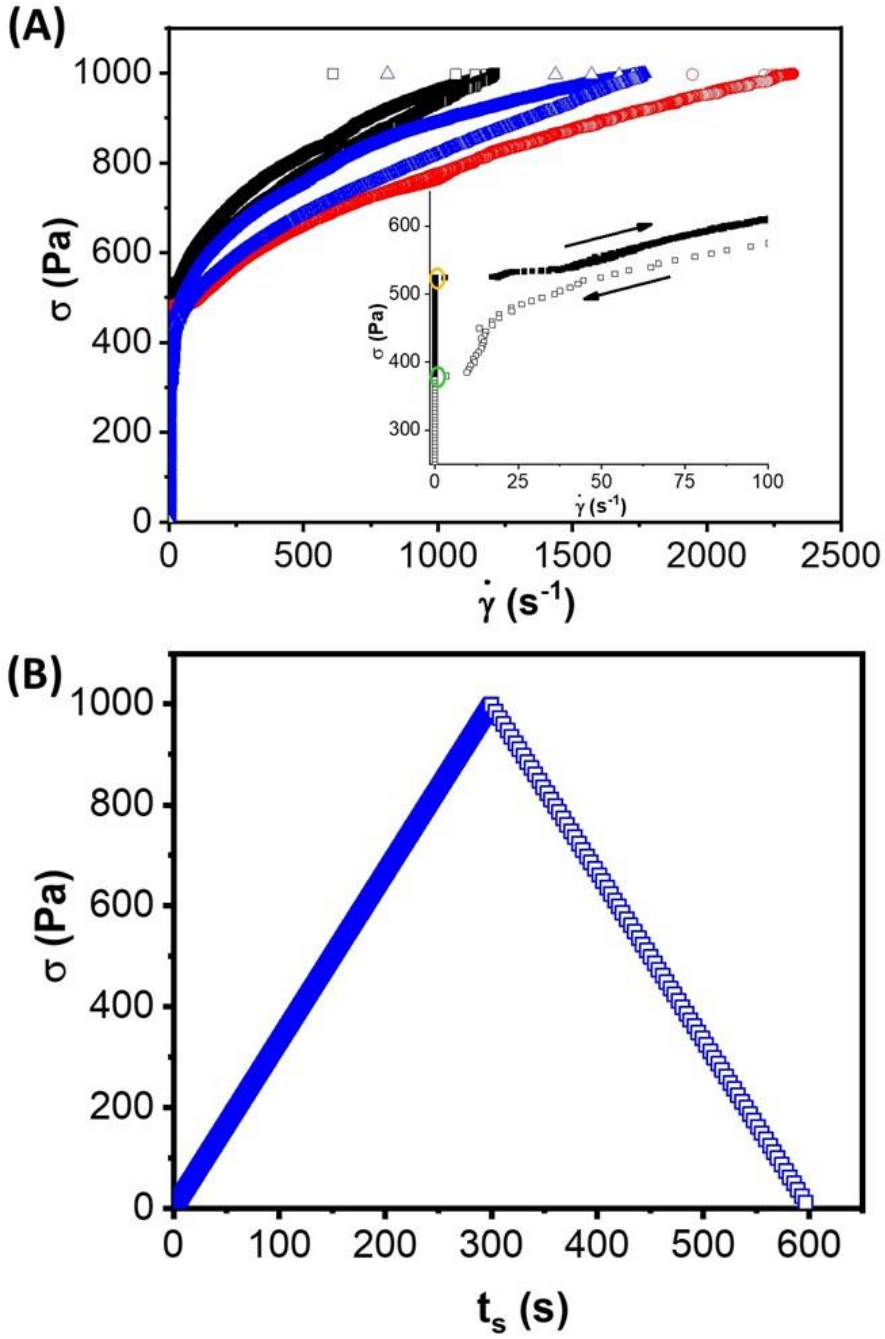

Figure 4-18. Stress ramp up (full symbols) and down (empty symbols) for 35 vol% alumina suspension at pH 9. (a) Three samples are compared (black, red and blue symbols). All suspensions were prepared as small batches (batch to batch variability system). Inset highlights the suspension rheology at shear rate less than 100 s^{-1}. The yield stress values for ascending and descending stress ramps are shown by the yellow and green symbols, respectively. (b) A linear transient stress ramp up (blue full symbols) and ramp down (blue empty symbols).

4.4.2 Stress Ramp: In-batch Variability (single large batch)

4.4.2.1 Alumina Slurry Preparation

To ensure the previous data was not influenced by the sample preparation method, a 200 mL batch (larger batch) of alumina suspension was prepared at pH 9. Initially, 130 mL of 1 mM NaCl was poured into a 1 L glass beaker using a 10 mL Eppendorf pipette. 271.6 g of alumina powder was then added slowly to the NaCl solution using a stainless steel spatula, with the suspension gently stirred using an overhead stirrer (Cole-Parmer) at 500 rpm. Any adjustments in pH were made using 5 M NaOH to avoid any dilution effects. The suspension was stirred for a further 10 min at 1500 rpm to ensure the alumina powder was fully blended.

The alumina suspension was divided into 3 equal smaller batches and left overnight gently rolling (Scilogex) to ensure the suspension reached had reached an ionic equilibrium between the solids and solvent. After 24 h the pH of each alumina suspension was re-checked and re-adjusted to pH 9 using one drop of 5 M NaOH if needed. The suspensions were manually mixed for 5 min. Each alumina suspension (sample volume = 40 mL) was transferred to the concentric cylinder of the rheometer using a spatula. The vane geometry was lowered into the sample to a gap setting of 4000 µm (the operating gap for the vane geometry), and the standard experimental protocol run.

4.4.2.2 In Sample Assessment

All rheology experiments were conducted at T = 25°C. The shear stress profiles as a function of shear rate for the three samples prepared from the same larger batch are shown in Fig. 4-19. Briefly, the experimental protocol involved a constant pre-shear at 500 s^{-1} for 5 min, followed by 3 min rest at 0 s^{-1}, then the shear stress was linearly increased between 0.01 to 1000 Pa over 5 min, and then linearly decreased from 1000 to 0.01 Pa over the same time interval.

Figure 4-19(A) shows a similar behavior to that shown in Fig. 4-18(A). For all samples, some degree of hysteresis is shown, but again the data is not consistent. For example, considering sample 1 (black symbols), the stress profile on the shear rate ramp up is greater than the stress profile on the shear rate ramp down. While for samples 2 and 3 (red and blue symbols), the opposite behavior is observed, and a higher stress is measured on the shear rate ramp down. A higher stress on the ramp down would indicate some structure building during the shear rate ramp up, which is commonly described as a rheopectic fluid. The anti-thixotropic behaviour has previously been reported for alumina particles with the effect attributed to the formation of agglomerates and the possible onset of gelling which is more apparent at higher solids concentrations (47, 48).

Taking the approach that the yield stress is the stress value when the shear rate significantly deviates from small shear rate values, the yield stress of the three samples during shear rate ramp up was 860 Pa (sample 1), 865 Pa

(sample 2), and 738 Pa (sample), while for the shear rate ramp down the values were 478 Pa (sample 1), 488 Pa (sample 2) and 422 Pa (sample 3). Again for the supposed same sample, prepared by the same protocol, the measured yield stress can vary by 15% which is far too large when looking for smaller changes in yield stress, see Chapter 2.

Figure 4-19 (B) shows the shear stress as a function of time (t_s) while a constant shear rate of 500 s^{-1} is applied (representing the pre-shear protocol). The black, red and blue symbols correspond to those in Fig. 4-19(A), and were conducted before any shear rate ramp experiments were performed. The green symbol represents a subsequent measurement following a pre-shear and stress ramp protocol in Fig. 4-19(A). The data corresponds with the blue symbols. Three things to note: i) a shear rate of 500 s^{-1} is sufficiently high that the shear stress generated exceeds the yield stress, hence the suspension will undergo structure breakdown and remove any history effects; ii) for the sample identified by the black symbols, a slight time dependence is observed and confirms a thixotropic behavior; and iii) the difference between the blue and green symbols is marginal suggesting there is a negligible effect of sample drying during the experimental protocol. If the sample had shown effects of drying, it would be expected that the green data set is above the blue data set, due to a higher solids concentration.

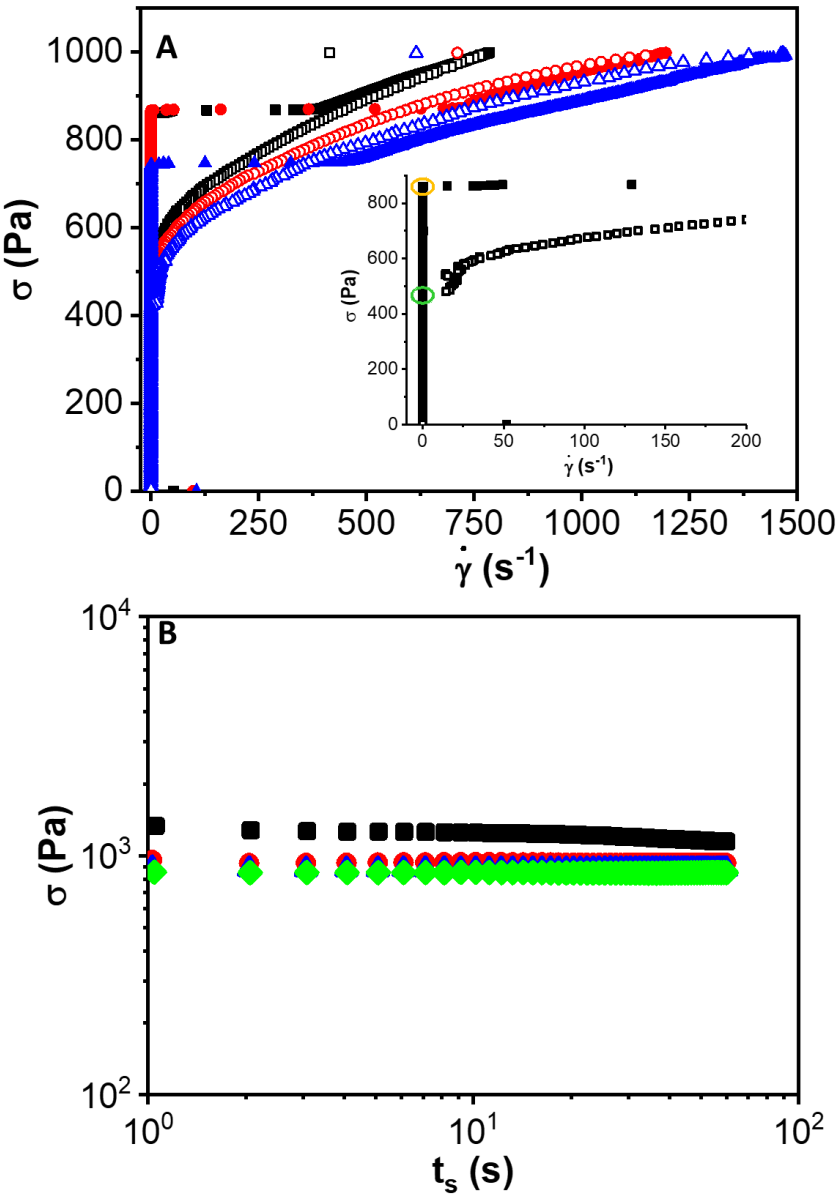

Figure 4-19. Three alumina suspensions (black, red and blue symbols) prepared by the in-batch-variability system (single large batch). All samples were 35 vol% alumina in 1 mM NaCl at pH 9. Closed symbols represent the shear stress ramp up and open symbols represent the shear stress ramp down. Inset highlights the suspension rheology at shear rate less than 100 s^{-1}. The yield stress values for ascending and descending stress ramps are shown by the yellow and green symbols, respectively. (B) Shear stress as a function of a step time at constant shear, 500 s^{-1} (pre-shear protocol). Green symbols represent stress profile following the shear stress ramp down of sample 3 (blue symbols).

4.4.2.3 Consecutive Repeats

To assess any sample aging effects, three consecutive tests were performed on two alumina suspensions prepared to 35 vol% at pH 9. Figure 4-20 shows sample A (Figure A) and sample B (Figure B). Black, red and blue symbols represent the three consecutive shear rate ramp cycles. Closed symbols represent and increase and open symbols a decrease in shear rate. While behavior is very consistent with what has previously been described, it is important to note how the yield stress randomly changes from run to run for both samples. For sample A the yield stress increases with the number of cycles, but for sample B it increases and then decreases slightly. This again highlights the limitation of using such an approach to collect reliable yield stress data.

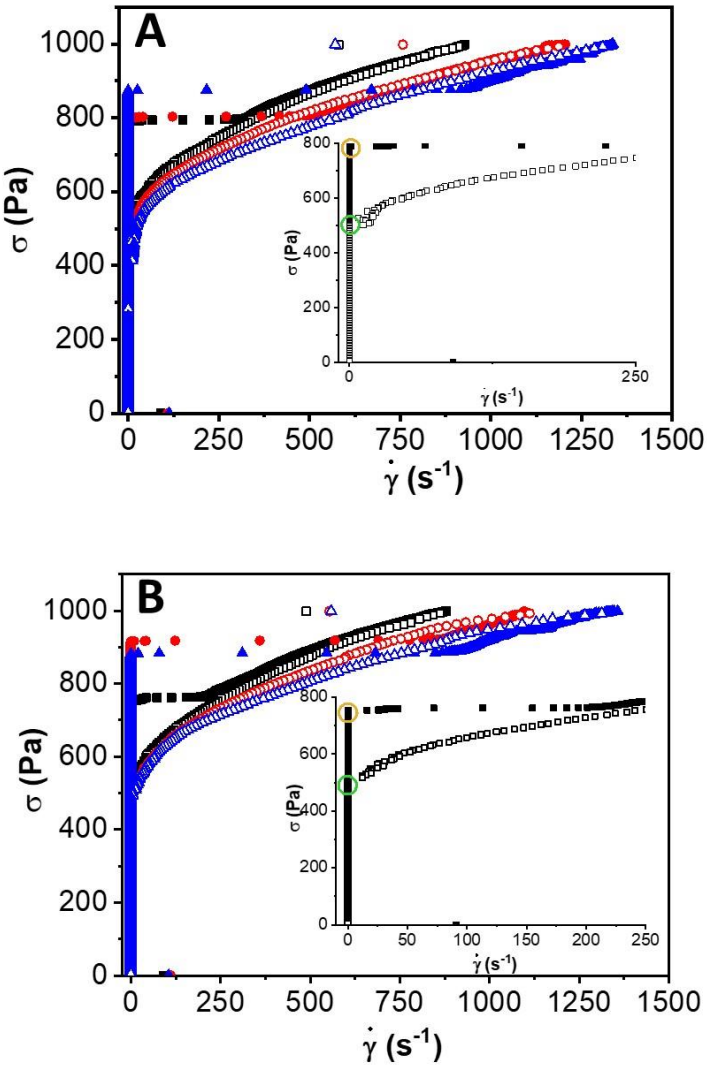

Figure 4-20. Consecutive cycling of a 35 vol% alumina suspension in 1 mM NaCl and pH 9. First, second and third cycles are represented by black, red and blue symbols. Closed symbols are shear stress ramp up and open symbols are shear stress ramp down. (A) is sample 1 and (B) is sample 2. Both samples prepared by the in-batch variability (single large batch) method. Inset highlights the suspension rheology at shear rate less than 100 s^{-1}. The yield stress values for ascending and descending stress ramps are shown by the yellow and green symbols, respectively.

Figure 4-21 shows the suspension shear stress at a constant shear rate of 500 s^{-1}. Figures A and B correspond to samples A and B, and the black, red and blue symbols correspond to the pre-shear protocols for the three consecutive tests shown in Fig. 4-20. The green symbols represents a final pre-shear test following the 3rd shear rate ramp test (blue symbols). Again, nothing unexpected was found and proves that the pre-shear protocol exceeds the yield stress of the sample. However, even with history removed it was difficult to achieve repeatable data using this method.

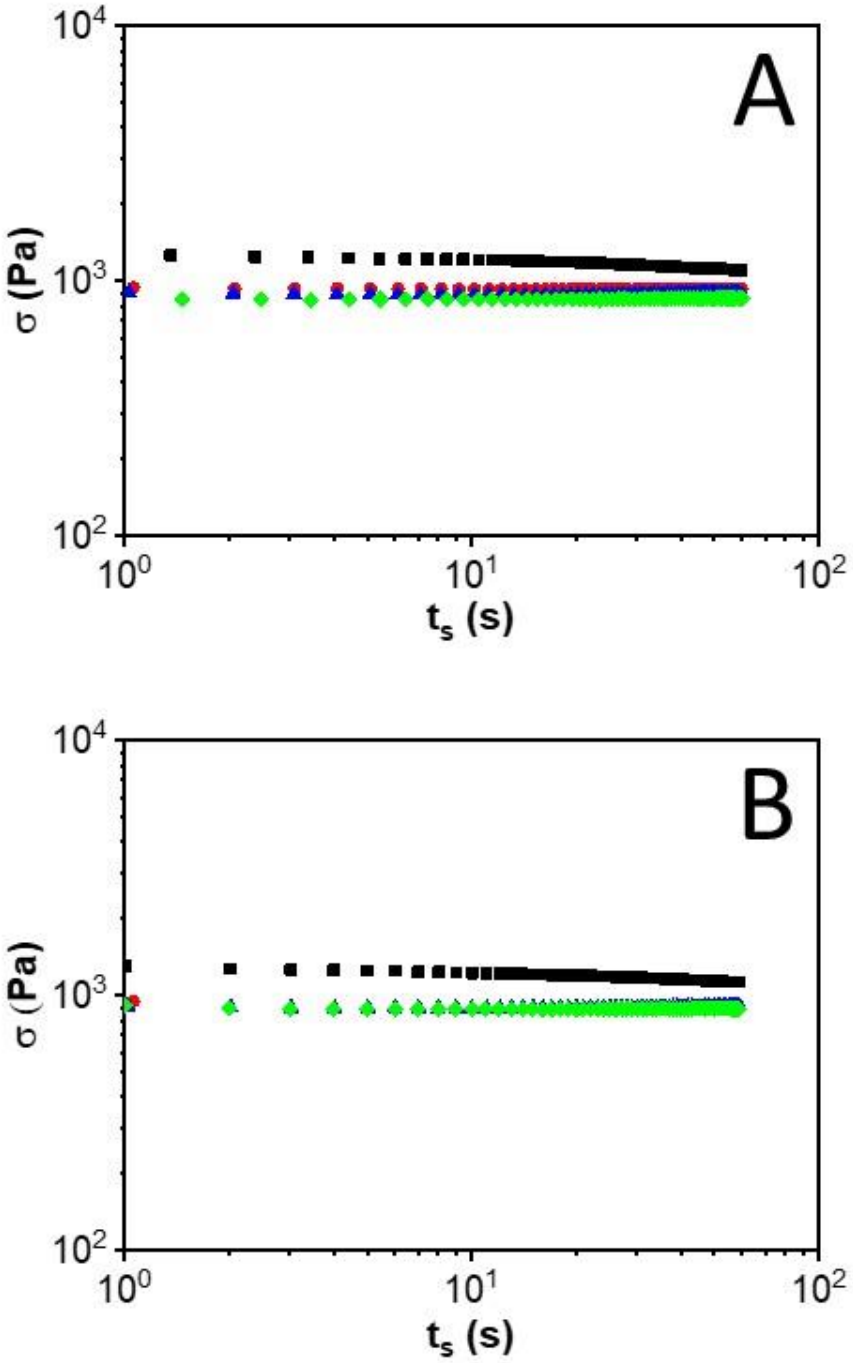

Figure 4-21. Shear stress as a function of a step time at constant shear, 500 s^{-1} (pre-shear protocol). (A) is sample 1 and (B) is sample 2. Both samples prepared by the in-batch variability (single large batch) method. Data corresponds to that shown in Fig. 1-19. Green symbols represent stress profile following the shear rate ramp down of sample 3 (blue symbols).

4.4.3 Blending Time Effect

To ensure some of the differences were not a result of poor blending of alumina powder in the NaCl solution, two 35 vol% alumina suspensions prepared as separate small batches at pH 9 in 1 mM NaCl were mixed using an overhead stirrer for 10 min and 30 min. Following mixing the samples were left on the rollers overnight. Figure 4-22 shows the shear rate ramp data for sample 1 (black symbols) mixed for 10 min, and sample 2 (green symbols) mixed for 30 min. It was found that the yield stress decreased with increased mixing time, 740 Pa for 10 min mixing, and 620 Pa for 30 min mixing. The difference is ~16% and again falls within the measurement error previously reported. As such, it cannot be confidently stated that blending has a marked effect on preparing a more homogenous sample.

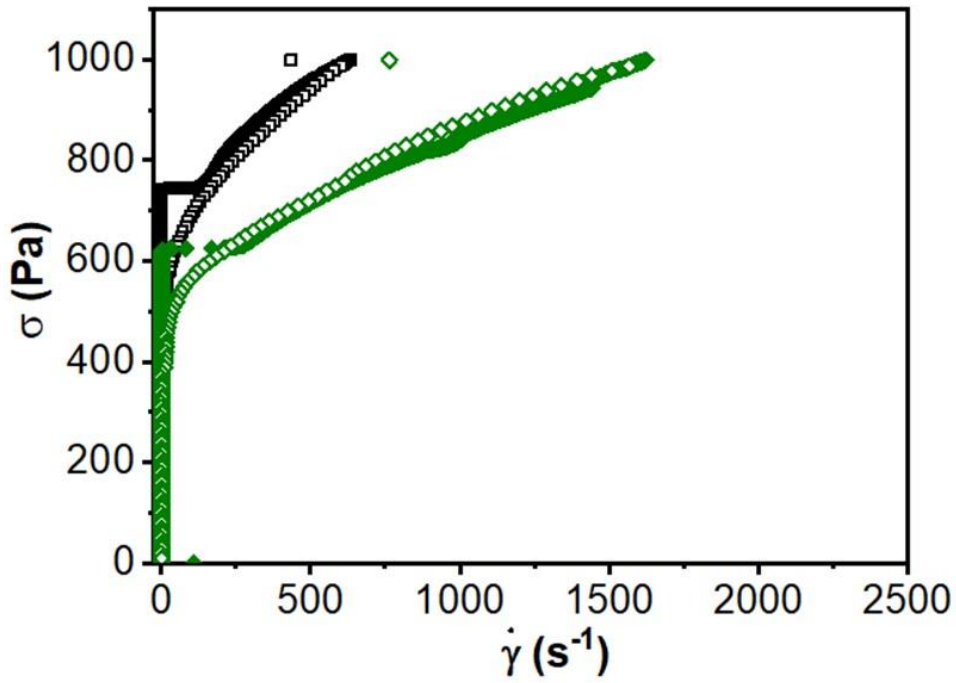

Figure 4-22. 35 vol% alumina suspensions prepared (as small batches) in 1 mM NaCl and pH 9. Closed symbols are shear stress ramp up and open symbols are shear stress ramp down. Black symbols represent 10 min mixing time and green symbols represent 30 min mixing time (when t = 0).

Using the stress ramp protocol both batch to batch (small repeated batches) and in-batch (single large batch) variability was considered. While the concentrated alumina suspensions exhibited high yield stress values, and generally showed some degree of thixotropy, the data collected demonstrated that the common stress ramp for measuring the yield stress of concentrated alumina suspensions was not appropriate, due to a lack of reproducibility and variation up to 16%. As such, an alternative method was considered wherein the rheological properties prior to yielding are well characterized along with the incipient point of yielding.

4.4.4 Oscillatory Rheology

This section discusses two different methods of oscillation measurement (1) strain-controlled and (2) torque-controlled.

4.4.4.1 Strain Control – Preliminary Testing

Figure 4-23 describes the steps of operating a stress-controlled rheometer in continuous strain. For strain controlled, an strain level is inputted, however, because the rheometer is stress-controlled, a torque to deliver the desired stain is estimated. The torque is then optimized until the desired strain is attained. With the correct strain achieved the measurement is then made.

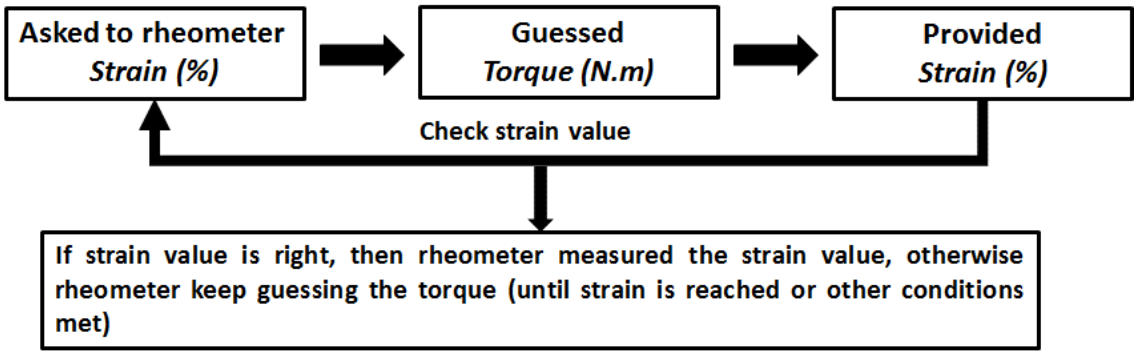

Figure 4-23. Steps for a strain-controlled measurement using a stress-controlled rheometer.

The DHR-2 rheometer (TA Instruments) was used with a vane (diameter = 15 mm, length = 38 mm) and cup (diameter = 42 mm) geometry. An alumina suspension of 35 vol% and prepared to pH 8 was tested following the experimental protocol for oscillatory rheology described in Section 4.3.2.2. All tests were performed at 25°C. With the suspension placed in the rheometer,

the vane geometry was lowered into the sample to a gap setting of 8800 µm and the solvent trap fitted, the suspension underwent a pre-shear of 800 s^{-1} for 5 min followed by 3 min rest to remove any sample history.

To conduct the oscillatory strain measurement, the strain amplitude was increased logarithmically from 0.0004 – 100%, at a fixed frequency of 10 rad/s and 5 points per decade. Continuous oscillation (direct strain) and soft motor mode were selected for the measurement to provide the highest measurement sensitivity. Correlation mode was selected for data acquisition, where the software assesses the torque and displacement data in real time and provides data that is only frequency dependant (36). A conditioning time of 30 s was chosen which reflects the time over which the oscillation torque is applied to the sample before measuring the sample. The number of oscillation cycles was set to 5, with the oscillation torque applied to the sample and data acquired (36). Number of points in a waveform was 1024, which is maximum number of data points that could be collected.

Figure 4-24 compares the storage (G') and loss (G") moduli as a function of strain (%) for the 35 vol% alumina suspension at pH 8. The storage (G') and loss (G") moduli are shown by blue and green symbols, respectively. It is generally seen that at low strain (%) G' is greater than G", and reflects a solid-like behavior, and at high strain (%) G" is greater than G', and reflects a liquid-liquid behavior. Prior to yielding, G' is independent of the oscillation strain between 10^{-4}-10^{-2} %, and is in the Linear Viscoelastic Region (LVR). After yielding the data becomes very noisy and the viscoelastic moduli are seen to

be very sporadic. This behavior is due to the stress-controlled operation of the rheometer, and the variability results from the need to optimize torque to achieve the next target strain value. Since the suspension exhibits high elasticity, a high torque value is required to initiate flow, thus when the suspension yields, optimization of strain from torque adjustments is difficult to achieve. For example, when the suspension suddenly flows at high strain values, the rheometer records a low G' and to compensate the rheometer then applies a low strain value which results in high values of G'.

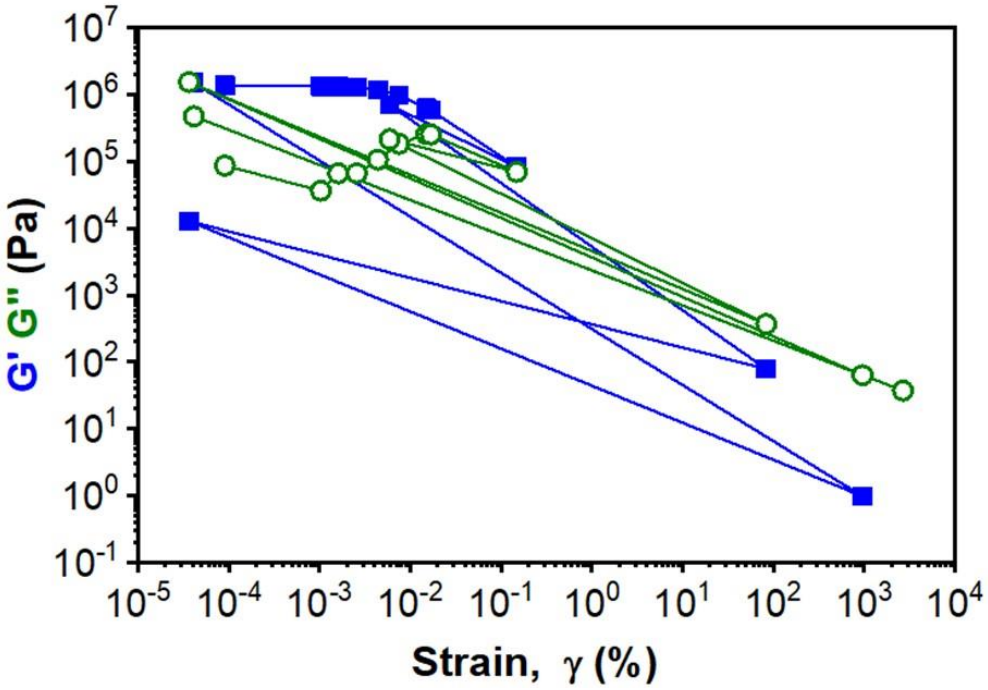

Figure 4-24. 35 vol% alumina suspension in 1 mM NaCl and pH 8. Strain-controlled measurement. G' and G" represented by blue and green symbols, respectively. Strain is increased logarithmically from 0.0004 to 100 % strain at a constant angular frequency of 10 rad/s.

Table 4-1 shows the difference between the calculated (expected) strain and the strain values applied by the rheometer, with a large difference seen between both values. Two types of errors are illustrated in Table 1-1. An orange flag (cross) error indicates the applied strain is very low and is close to the machine limit, while the red flag error indicates that the target value was not achieved This red error (cross) means the rheometer struggles to apply the true strain value to the sample because (a) the rheometer is not strain-controlled, and (b) the suspension is very stiff, therefore the instrument cannot accurately control torque adjustment to obtain target strains.

Table 4-1. Comparison of expected strain and applied strain values using a stress-controlled rheometer. Sample: 35 vol% alumina suspension in 1 mM NaCl at pH 8. Strain-controlled method.

Expected strain	Applied strain by rheometer	Error	Flags comments
%	%		
4.00×10^{-4}	9.15×10^{-6}	X	close to machine limits
6.34×10^{-4}	1.51×10^{-4}	X	close to machine limits
1.00×10^{-3}	1.02×10^{-3}	X	close to machine limits
1.59×10^{-3}	1.65×10^{-3}		
2.52×10^{-3}	2.61×10^{-3}		
4.00×10^{-3}	4.28×10^{-3}	X	requested value not attained
6.34×10^{-3}	6.64×10^{-3}		
1.00×10^{-2}	1.18×10^{-1}	X	requested value not attained
1.59×10^{-2}	1.25×10^{-3}	X	requested value not attained
2.52×10^{-2}	4.79×10	X	requested value not attained
4.00×10^{-2}	4.11×10^{-4}	X	requested value not attained

4.4.4.2 Torque Control – Preliminary Testing

This section describes how the stress-controlled rheometer operates in continuous torque mode (Fig. 4-25). For the torque controlled method, a torque value is set and the rheometer applies the torque to the sample and the resultant strain is provided. In this way there is no feedback or optimization to reach a desired strain value.

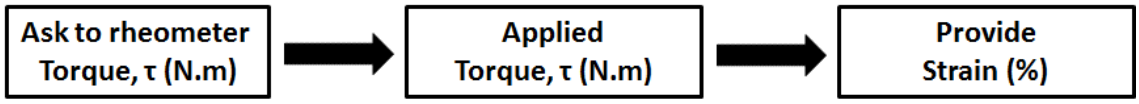

Figure 4-25. Steps for a torque-controlled measurement using a stress-controlled rheometer.

A 35 vol% alumina suspension at pH 8 was prepared and loaded into the rheometer as previously described, using the vane and cylinder geometry, and applying the same pre-shear protocol. In the torque controlled method, a continuous torque is ramped up from 20 to 40000 µNm, using a logarithmic step increase. Continuous oscillation was used and 10 data points per decade were collected. A sample conditioning time of 30 s was chosen and 5 cycles were averaged to provide the viscoelastic moduli at a particular stain (%). The angular frequency was set to 10 rad/s. Figure 4-26 shows typical viscoelastic data for a 35 vol% alumina suspension undergoing yielding with increasing strain. The elastic (G') and viscous (G") moduli are shown by the blue and green symbols, respectively.

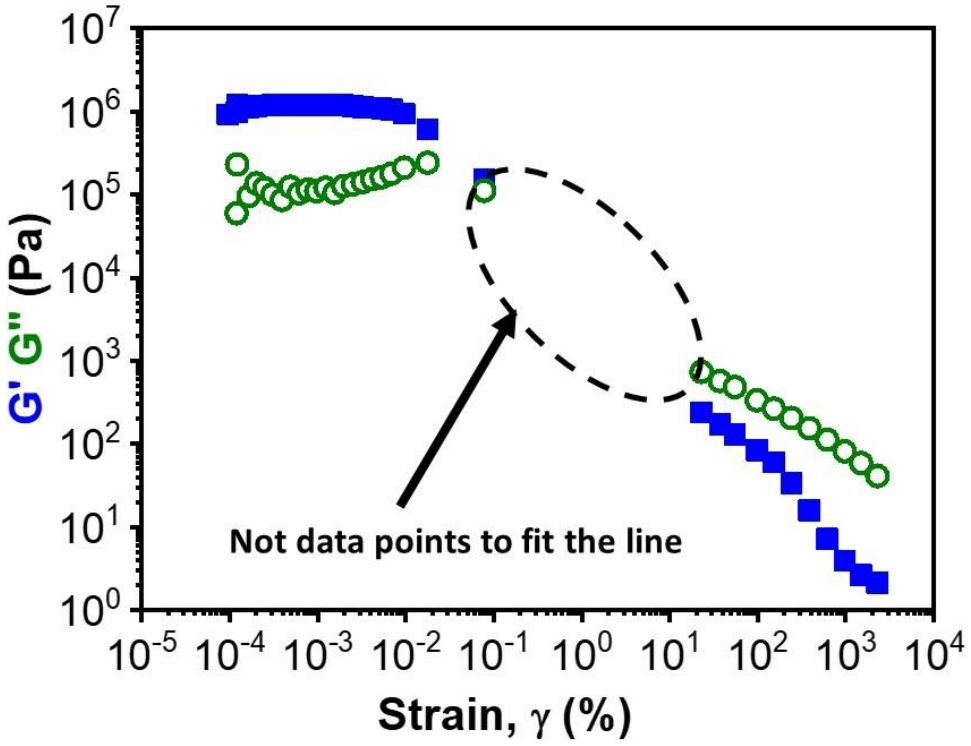

Figure 4-26. 35 vol% alumina suspension in 1 mM NaCl and pH 8. Torque-controlled measurement. G' and G" represented by blue and green symbols, respectively. Torque is increased logarithmically from 20 to 40000 μNm at a constant angular frequency of 10 rad/s.

When using the torque controlled method the data is less noisy and a clear yielding point is observed. Similar to the strain-controlled data, G' is independent of strain (%) in the LVR and then decreases beyond the yield point. Also, the transition from solid-like to liquid-like behavior is seen and the crossover point can be estimated from simple fits of the viscoelastic moduli in the decay zone. Unfortunately, for the torque controlled method, following initial yielding, there are no data points collected between strain values of 10^{-1} and 10^{1} % (as circled in Fig. 4-26). The missed data results from the inputted torque range for the measurement. However, the missing data can be

minimized by sub-dividing the torque range into two measurements. Figures 4-27(a) and (b) show how sub-dividing the torque range can result in higher quality data. The sample was 35 vol% alumina suspension at pH 8 and the torque range was divided into i) 250 – 700 µNm collecting 10 points per decade, and ii) 700 – 20000 µNm collecting 40 points per decade. There was no time delay from transitioning from the first to the second torque range. This approach of sub-dividing the torque range allowed for sufficient data to be collected within a reasonable time frame. Plotting the two data sets together, Figure 4-27(c) shows a complete viscoelastic moduli response of the concentrated alumina suspension, and allows for accurate determination of the crossover point.

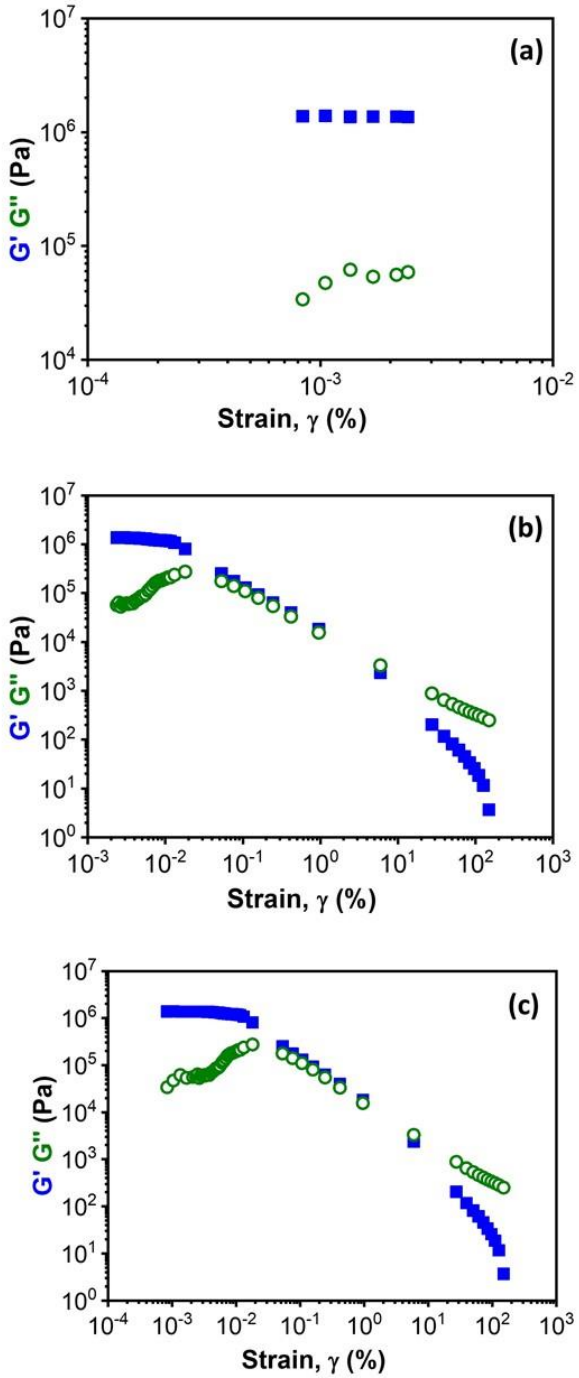

Figure 4-27. 35 vol% alumina suspension in 1 mM NaCl and pH 8. Torque-controlled measurement. G' and G" represented by blue and green symbols, respectively. Torque is increased logarithmically from 250 to 20000 μNm at a constant angular frequency of 10 rad/s. Figure (a) shows the first torque-step between 250 and 700 μNm with 10 data points per decade collected. Figure (b) shows the second torque-step between 700 and 20000 μNm with 40 data points per decade collected. Figure (c) is the combined data sets.

Table 4-2 compares the expected torque and the applied torque values when completing the two torque ramps shown in Fig. 4-27. Measurement errors are shown by the orange flags (crosses). Unlike the strain-controlled method which showed multiple errors and instrument sensitivity limits, the torque-controlled method provides a much higher quality and reliable measurement with few errors reported, and only reported in the strongly-elastic region where the torque limits of the motor are reached.

Table 4-2. Comparison of expected torque and applied torque values using a stress-controlled rheometer. Sample: 35 vol% alumina suspension in 1 mM NaCl at pH 8. Torque-controlled method. Torque-controlled method. Step (a) and (b) reflect the two-step torque measurement.

Step	Expected Torque	Applied torque by rheometer	Error	Flags comments
	µN.m	µN.m		
a	2.50×10^2	2.50×10^2	x	close to machine limits
	3.15×10^2	3.15×10^2	x	close to machine limits
	3.96×10^2	3.96×10^2	x	close to machine limits
	4.99×10^2	4.99×10^2		
	6.28×10^2	6.28×10^2		
	7.00×10^2	7.00×10^2		
b	7.41×10^2	7.41×10^2		
	7.85×10^2	7.85×10^2		
	8.32×10^2	8.32×10^2		
	8.81×10^2	8.81×10^2		
	9.33×10^2	9.33×10^2		
	9.89×10^2	9.89×10^2		
	1.05×10^3	1.05×10^3		
	1.11×10^3	1.11×10^3		

To verify that the oscillatory mode, torque-controlled method could provide repeatable and reliable yield stress data, 3 samples of 35 vol% alumina

suspensions were prepared at pH 8 following the protocol previously described. Figure 4-28 shows the viscoelastic moduli for the 3 suspensions, with the elastic and viscous moduli shown by blue and green symbols respectively. As shown, the 3 data sets show consistent behavior and appear to overlay. Using the tangent analysis method, the yield stress of the three samples was 128.51 Pa, 122.99 Pa and 124.73 Pa. The crossover modulus point (G' = G") was 9521.47 Pa, 9860.39 Pa and 9391.70 Pa, with the crossover occurring at strain values of 1.53 %, 1.70 % and 1.73 %. The quantitative assessment of the data in Figure 4-28 confirms that the oscillatory method is superior in measuring the yield stress of concentrated alumina suspensions and can provide very good batch-to-batch reproducibility. Therefore, this method was used for all yield stress measurements of binary suspensions.

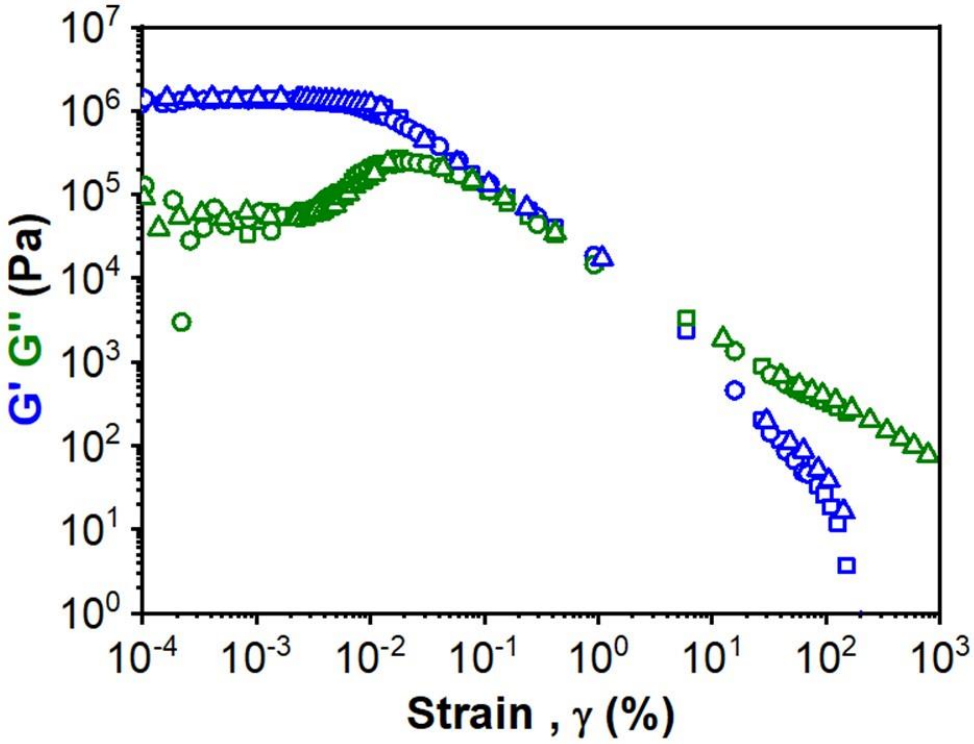

Figure 4-28. 35 vol% alumina suspension in 1 mM NaCl and pH 8. Torque-controlled measurement. G' and G" represented by blue and green symbols, respectively. Torque is increased logarithmically from 250 to 20000 μNm at a constant angular frequency of 10 rad/s. A two-step torque measurement was applied with the first-step adjusting torque between 250 and 700 μNm, and the second-step adjusting torque between 700 and 20000 μNm. The number of data points per decade was 10 and 40 in the first and second-steps, respectively. Three samples are compared and shown by the different shaped symbols.

4.5 Conclusions

The study considered different methods to accurately measure the shear yield stress of high solids content suspensions. There were many challenges in sample preparation and measurement, and through iteration of the method, an approach was successfully demonstrated to accurately and reproducibly measure the high yield stress values of high solids content alumina suspensions. In rotational mode, the stress ramp proved difficult to generate repeatable data, with consecutive cycles in the stress producing little consistency. In addition, the fitting of a flow curve to a standard yield stress model (for example the Herschel-Bulkley model) proved very challenging with small sensitivities in the fitting parameters strongly influencing the shear yield stress. While not extensively considered in the current chapter, creep rheology is another alternative rotational technique that can be used to measure the suspension yield stress. Through preliminary testing (data not shown), there was concern that the duration of the measurement was too long and potentially led to slight sample drying which would modify the suspension rheology. Hence, a more direct and faster method to measure the suspension yield stress was preferred.

Operating the rheometer in oscillation mode proved to be more successful and the yield stress was first examined using strain control method. However, because the rheometer is stress controlled, the strain-stress feedback loop created several difficulties in smoothly executing the strain ramp, with the rheometer strain often overshooting the desired strain due to difficulties in ramping up the rheometer stress. To overcome this issue the method was

adapted to follow a torque ramp, thus eliminating the need for a feedback, with the torque being directly applied to the sample and the strain determined from the torque applied. This method is used throughout the study as described in the following Chapters.

References

1. Stokes, J.R. and Telford, J.H. Measuring the yield behaviour of structured fluids. *Journal of Non-Newtonian Fluid Mechanics.* 2004, **124**(1), pp.137-146.
2. Møller, P.C.F., Mewis, J. and Bonn, D. Yield stress and thixotropy: on the difficulty of measuring yield stresses in practice. *Soft Matter.* 2006, **2**(4), pp.274-283.
3. Chong, J., Christiansen, E. and Baer, A. Rheology of concentrated suspensions. *Journal of applied polymer science.* 1971, **15**(8), pp.2007-2021.
4. Instrument, M. *INFORM WHITE PAPER: UNDERSTANDING YIELD STRESS MEASUREMENTS.* [Online]. 2012. [Accessed]. Available from: https://www.atascientific.com.au/wp-content/uploads/2017/02/MRK1782-01.pdf
5. Barnes, H.A. and Walters, K. The yield stress myth? *Rheologica acta.* 1985, **24**(4), pp.323-326.
6. Evans, I.D. Letter to the editor: On the nature of the yield stress. *Journal of Rheology.* 1992, **36**(7), pp.1313-1318.
7. Hartnett, J.P. and Hu, R.Y.Z. Technical note: The yield stress—An engineering reality. *Journal of Rheology.* 1989, **33**(4), pp.671-679.
8. Dzuy, N.Q. and Boger, D.V. Yield Stress Measurement for Concentrated Suspensions. *Journal of Rheology.* 1983, **27**(4), pp.321-349.
9. Papanastasiou, T.C. Flows of Materials with Yield. *Journal of Rheology.* 1987, **31**(5), pp.385-404.
10. Barnes, H.A. The yield stress—a review or 'panta roi'—everything flows? *Journal of Non-Newtonian Fluid Mechanics.* 1999, **81**(1999), pp.133-178.
11. Bingham, E.C. *Fluidity and plasticity: by Eugene C. Bingham.* New York: McGraw-Hill Book Company, Inc, 1922.
12. Edgeworth, R., Dalton, B.J. and Parnell, T. The pitch drop experiment. *European Journal of Physics.* 1984, **5**(4), p.198.

13. Q D Nguyen, a. and Boger, D.V. Measuring the Flow Properties of Yield Stress Fluids. *Annual Review of Fluid Mechanics.* 1992, **24**(1), pp.47-88.
14. Barnes, H.A. Thixotropy—a review. *Journal of Non-Newtonian Fluid Mechanics.* 1997, **70**(1), pp.1-33.
15. Mewis, J. Thixotropy - a general review. *Journal of Non-Newtonian Fluid Mechanics.* 1979, **6**(1), pp.1-20.
16. James, A.E., Williams, D.J.A. and Williams, P.R. Direct measurement of static yield properties of cohesive suspensions. *Rheologica acta.* 1987, **26**(5), pp.437-446.
17. Mujumdar, A., Beris, A.N. and Metzner, A.B. Transient phenomena in thixotropic systems. *Journal of Non-Newtonian Fluid Mechanics.* 2002, **102**(2), pp.157-178.
18. Barnes, H.A. and Nguyen, Q.D. Rotating vane rheometry — a review. *Journal of Non-Newtonian Fluid Mechanics.* 2001, **98**(1), pp.1-14.
19. Cheng, D.C.H. Yield stress: A time-dependent property and how to measure it. *Rheologica acta.* 1986, **25**(5), pp.542-554.
20. Rohn, C. Ten Rotational Rheometry questions you may have but did not know who to ask ? 2015.
21. Derakhshandeh, B., Hatzikiriakos, S.G. and Bennington, C.P.J. The apparent yield stress of pulp fiber suspensions. *Journal of Rheology.* 2010, **54**(5), pp.1137-1154.
22. Barnes, H.A. A review of the slip (wall depletion) of polymer solutions, emulsions and particle suspensions in viscometers: its cause, character, and cure. *Journal of Non-Newtonian Fluid Mechanics.* 1995, **56**(3), pp.221-251.
23. Lin, S.F. and Brodkey, R.S. Rheological Properties of Slurry Fuels. *Journal of Rheology.* 1985, **29**(2), pp.147-175.
24. Dzuy, N.Q. and Boger, D. Direct yield stress measurement with the vane method. *Journal of Rheology.* 1985, **29**(3), pp.335-347.
25. James, A., Williams, D. and Williams, P. Direct measurement of static yield properties of cohesive suspensions. *Rheologica acta.* 1987, **26**(5), pp.437-446.

26. R Lapasin and Pricl, S. *Rheology of Industrial Polysaccharides: Theory and Applications.* 1 ed. Springer US, 1995.
27. Mitchell, J.R. The Rheology of Gels. *Journal of Texture Studies.* 1980, **11**(4), pp.315-337.
28. Qian, Y. and Kawashima, S. Use of creep recovery protocol to measure static yield stress and structural rebuilding of fresh cement pastes. *Cement and concrete research.* 2016, **90**, pp.73-79.
29. Zosel, A. Rheological properties of disperse systems at low shear stresses. *Rheologica acta.* 1982, **21**(1), pp.72-80.
30. Shih, W.Y., Shih, W.-H. and Aksay, I.A. Elastic and Yield Behavior of Strongly Flocculated Colloids. *Journal of the American Ceramic Society.* 1999, **82**(3), pp.616-624.
31. Shih, W.-H., Shih, W.Y., Kim, S.-I., Liu, J. and Aksay, I.A. Scaling behavior of the elastic properties of colloidal gels. *Physical Review A.* 1990, **42**(8), pp.4772-4779.
32. Yang, M.C., Scriven, L.E. and Macosko, C.W. Some Rheological Measurements on Magnetic Iron Oxide Suspensions in Silicone Oil. *Journal of Rheology.* 1986, **30**(5), pp.1015-1029.
33. Walls, H.J., Caines, S.B., Sanchez, A.M. and Khan, S.A. Yield stress and wall slip phenomena in colloidal silica gels. *Journal of Rheology.* 2003, **47**(4), pp.847-868.
34. Yanez, J.A., Shikata, T., Lange, F.F. and Pearson, D.S. Shear Modulus and Yield Stress Measurements of Attractive Alumina Particle Networks in Aqueous Slurries. *Journal of the American Ceramic Society.* 1996, **79**(11), pp.2917-2917.
35. Mahaut, F., Mokéddem, S., Chateau, X., Roussel, N. and Ovarlez, G. Effect of coarse particle volume fraction on the yield stress and thixotropy of cementitious materials. *Cement and concrete research.* 2008, **38**(11), pp.1276-1285.
36. *T A Instruments.* [G'- G" Crossoevr]. New Castle USE: T A Instruments, 2018.
37. Choi, H.J., Kim, S.G., Hyun, Y.H. and Jhon, M.S. Preparation and Rheological Characteristics of Solvent-Cast Poly(ethylene

oxide)/Montmorillonite Nanocomposites. *Macromolecular Rapid Communications.* 2001, **22**(5), pp.320-325.

38. Green, H. and Weltmann, R. Analysis of Thixotropy of Pigment-Vehicle Suspensions - Basic Principles of the Hysteresis Loop. *Industrial & Engineering Chemistry Analytical Edition.* 1943, **15**(3), pp.201-206.
39. Green, H. High-Speed Rotational Viscometer of Wide Range. Confirmation of the Reiner Equation of Flow. *Industrial & Engineering Chemistry Analytical Edition.* 1942, **14**(7), pp.576-585.
40. Joly, P.A. and Mehrabian, R. The rheology of a partially solid alloy. *Journal of materials science.* 1976, **11**(8), pp.1393-1418.
41. Williams, D.A., Saak, A.W. and Jennings, H.M. The influence of mixing on the rheology of fresh cement paste. *Cement and concrete research.* 1999, **29**(9), pp.1491-1496.
42. Krieger, I.M. Rheology of monodisperse latices. *Advances in Colloid and Interface Science.* 1972, **3**(2), pp.111-136.
43. Mewis, J. and Wagner, N.J. *Colloidal Suspension Rheology.* Cambridge: Cambridge University Press, 2011.
44. Zhu, C. and Smay, J.E. Thixotropic rheology of concentrated alumina colloidal gels for solid freeform fabrication. *Journal of Rheology.* 2011, **55**(3), pp.655-672.
45. Jamali, S., Armstrong, R.C. and McKinley, G.H. Multiscale nature of thixotropy and rheological hysteresis in attractive colloidal suspensions under shear. *Physical review letters.* 2019, **123**(24), p.248003.
46. Dinkgreve, M., Paredes, J., Denn, M.M. and Bonn, D. On different ways of measuring “the” yield stress. *Journal of non-Newtonian fluid mechanics.* 2016, **238**, pp.233-241.
47. Song, K.C. and Chung, I.J. Rheological properties of aluminum hydroxide sols during sol-gel transition. *Journal of non-crystalline solids.* 1989, **107**(2-3), pp.193-198.
48. Çetinel, A.F. and Simon, R.A. Nanoparticle assisted coagulation of aqueous alumina suspensions. *Materials Research.* 2012, **15**(1), pp.81-89.

Chapter 5

Flow Modification of Concentrated Particle Suspensions

Hypothesis: The flow of highly concentrated particle suspensions with particles that are colloidal in nature and irregular-shaped is very difficult. It is hypothesized that the yield stress and suspension viscosity can be dramatically reduced through the addition of small spherical particles, i.e. improved flow through a possible lubrication effect.

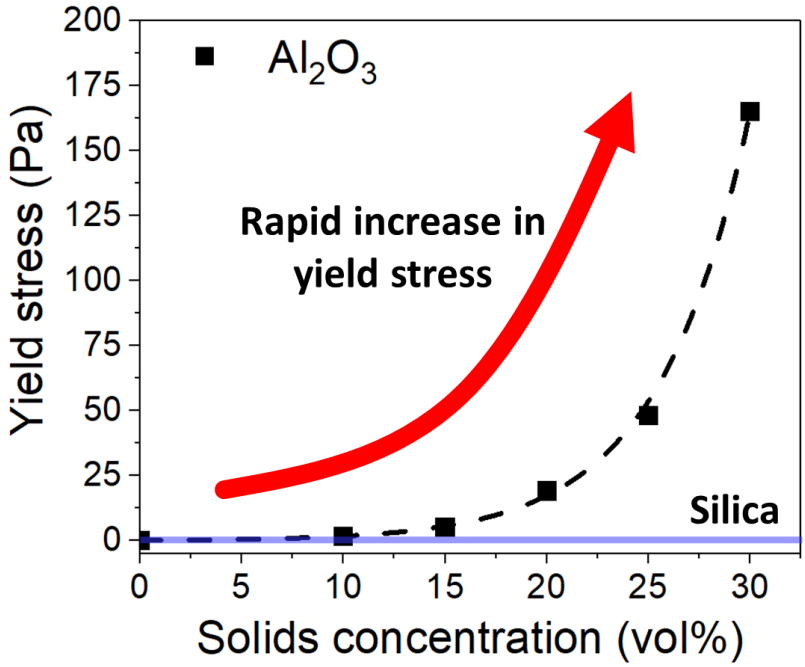

Figure 5-1. Baseline experimental data used to underpin the research hypothesis. The yield stress of alumina increases rapidly as a function of the solids concentration, while the yield stress of silica remains low until very high solids concentrations close to the maximum packing fraction.

Results: Two particle systems were considered, the first being alumina which is the main component of the suspension and the second component being colloidal silica which is a minor component of the suspension. Two pH conditions were considered that were approximately one pH unit either side of the isoelectric point. This allowed for suspensions to be studied where the alumina and silica were colloidally attractive and repulsive. In the absence of colloidal silica, the alumina suspensions exhibited high yield stresses characteristic of high particle concentration suspensions. These yield stresses could be reduced through adding small quantities of colloidal silica. For the best case, the yield stress of the alumina suspension at pH 9 could be reduced from over 100 Pa to 0 Pa by adding 1 vol% colloidal silica. All suspensions were kept at 35 vol%, thus showing a dramatic reduction in the suspension yield stress through the addition of colloidal silica.

Conclusions and Future Perspective: The contribution of colloidal silica to modify the rheology and eliminate yield stress in concentrated particle suspensions has been highlighted. It is hypothesized that the role of the colloidal silica is to act as a “ball bearing” and lubricate the contacts between the irregular shaped particles. Through greater dispersion of the colloidal silica throughout the alumina network, it may be possible to further reduce the concentration of the minor additive such that the levels of dosing are a fraction of a percent. The current study highlighted the presence of colloidal silica “islands” and it is thought that the effectiveness

of these islands to modify the flow rheology is negligible. Better dispersion should lead to better performance.

5.1 Introduction

Colloidal particles are encountered in a wide range of industrial environments from pharmaceuticals through to mining, with their presence often leading to challenges in handling if their properties are not controlled. In the nuclear industry, colloidal particles are often encountered in legacy wastes which have resulted from the corrosion of fuel and fuel cladding. In the UK (1-4), legacy waste is mostly a magnesium hydroxide-based material resulting from the corrosion of Magnox fuels, while in the US the legacy waste is mostly alumina-based material resulting from the corrosion of the aluminum clad fuels (5-9). The corrosion and subsequent formation of colloidal particles which have settled over many years to form a sludge layer in tanks and silos is now creating challenges in the decommissioning of legacy facilities. Remobilization of the material is difficult and its subsequent preparation for interim storage is challenging because it is envisaged that the material will be required to readily flow many years from now when it is transferred to an ultimate storage facility for very long-term disposal.

The viscosity of a suspension correlates to the ease of flow, with high viscosity suspensions exhibiting increased resistance to flow. The contribution of solids to modify the relative viscosity of a suspension was first considered by Einstein (10) who wrote a general equation for the changing relative viscosity dependent on the solid volume fraction. The relationship is valid for low solids

concentrations typically less than one volume percent. This general relationship was expanded by Batchelor (11, 12) to increase the validity of the model up to approximately 10 vol%. These two theoretical correlations account for very dilute and dilute particle suspensions in which hydrodynamic interactions are weakly considered. However, beyond this concentration range, particle-particle interactions become important wherein confinement by neighboring particles severely inhibits flow, hence leading to a rapid rise in the relative viscosity of a suspension as the jamming point or the maximum packing fraction of the suspension is approached. Such characteristic behavior is described by the semi-empirical equation of Krieger and Dougherty (13). As show in Eq. 7.1, the relative viscosity is dependent on the solids volume fraction (Φ), the maximum packing volume fraction (Φ_m) of the particle suspension and the intrinsic viscosity (B) which for hard spheres is taken to be 2.5.

$$\eta_r = \left(1 - \frac{\Phi}{\Phi_m}\right)^{-B\Phi_m} \qquad \textbf{Eq. 5-1}$$

The importance of particle shape on the suspension viscosity has been highlighted by several researchers (14-17). Particles that exhibit an increasing aspect ratio are more problematic to flow because their rotational space in flow is much greater than a sphere of an equivalent volume. As such, the occupied volume per particle is greater and thus the apparent particle volume fraction is higher. This simple explanation partly justifies why the flow of

colloidal particles, which are irregularly shaped, is more challenging than colloidal spheres, with the increase in relative viscosity observed at much lower particle concentrations than those of spheres.

Flow modification of concentrated particle suspensions has been considered by numerous researches (18-21), particularly focusing on preventing the rapid onset of shear thickening which occurs at a critical shear rate and is dependent on the solid volume fraction. The chemical additives which are used to modify the flow are mostly organic species such as surfactants and polymers.

The addition of inorganic species to modify the flow of concentrated particle suspensions has received less attention, with more interest in controlling the stability of a colloidal suspension. For example, the use of heteroaggregation to modify the stability of dilute particle suspensions is widely reported (22-24). Mixing particles of opposite charge promotes particle-particle interaction with the smaller additive particle often surrounding the larger particle, lowering the apparent particle zeta potential and driving aggregation of the larger particles. Researchers have considered several properties including particle size and particle zeta potential to promote a change in the stability of the dilute suspension.

5.2 Materials and Methods

Two particles were used throughout this study. Colloidal alumina was purchased from Showa Denko, Japan (AL160SG-3), with a density of 3.9 g/cm^3. Colloidal silica was purchased from Angstromsphere, USA, with a density of 1.9 g/cm^3. All particles were used without further purification. All particle suspensions were prepared in 10^{-3} M NaCl. The electrolyte concentration was chosen to allow pH adjustments without influencing the ionic concentration of the suspension. A stock solution of 10^{-3} M NaCl was prepared and used within one month.

5.2.1 Particle Sizing

Suspensions of 10000 ppm were prepared at pH 10 and tip sonicated for 3 min prior to measurement. The particle size distribution was measured 10 times and averaged. The d_{50} measured particle sizes were in good agreement with those reported by the manufacturer. The alumina particles had a d_{50} of 500 nm, and a d_{10} and d_{90} of 380 nm and 520 nm, see Fig. 5-2. The silica particles had a d_{50} of 100 nm, and a d_{10} and d_{90} of 90 nm and 100 nm, see Fig. 5-2. The two particle sizes are clearly distinct for the two particle types, with the alumina particles, which are the main component of the particle suspension, being larger than the minor component of silica.

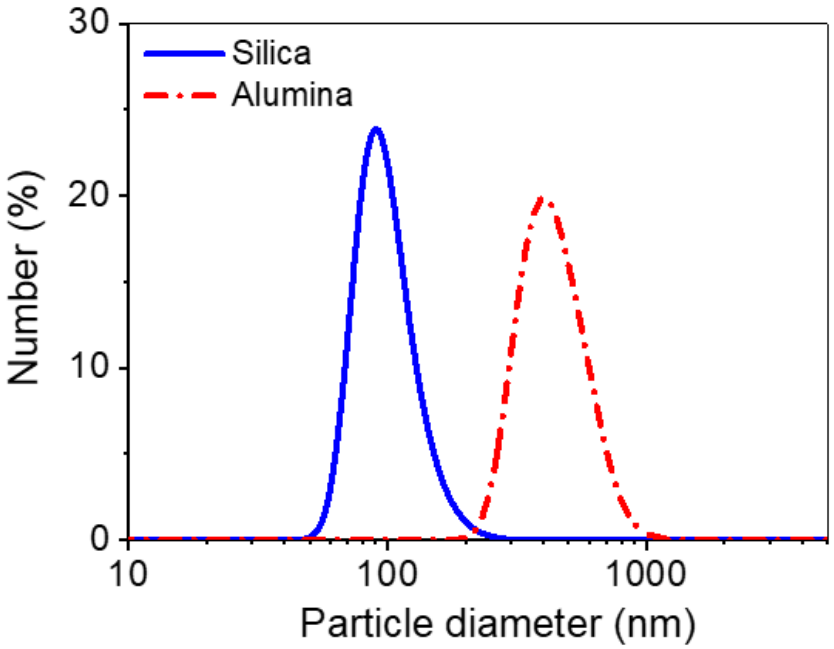

Figure 5-2. Particle size distributions for the two particle species used throughout study. The alumina particle is the main component in the suspension and the silica particle is the additive to modify the rheology.

5.2.2 Particle Shape

The silica and alumina particles were imaged under SEM SU8230 (Hitachi, UK). Samples were prepared to 10000 ppm in Milli-Q water and one drop of the suspension was deposited onto a SEM stub and allowed to dry. Samples were imaged at several magnifications, with the images collected at 50000 magnification shown in Fig. 5-3. The scale bar for each image is 2 µm. The spherical nature of the silica particles is clearly observed with very few fragments, very few fused particles and a very narrow particle size distribution. For the alumina particles, the particles appear to be agglomerated with the true particle size measured by the Malvern ZetaSizer Nano. Compared with silica, clearly there is a greater distribution in particle size and the particle shape is irregular and of higher aspect ratio.

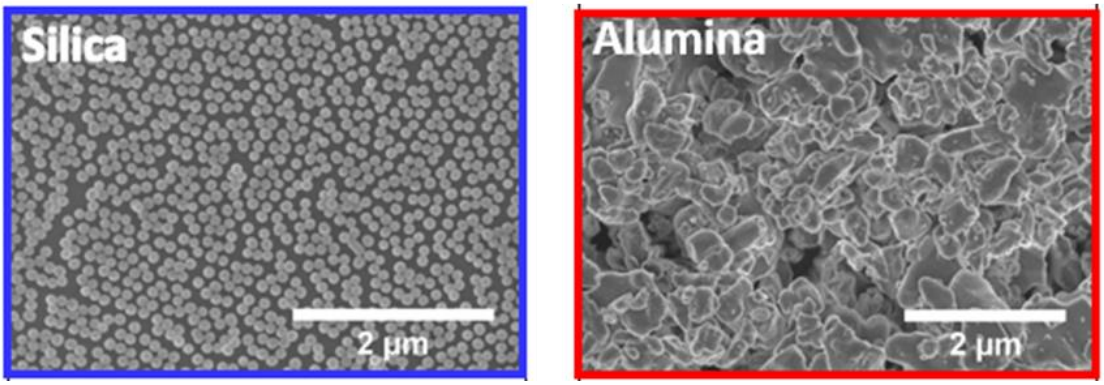

Figure 5-3. SEM images of the colloidal silica and alumina. The silica particles are spherical with a low polydispersity. The alumina particles appear aggregated due to drying of the particles on the SEM stub.

5.2.3 Particle Zeta Potential

The particles zeta potential as a function of pH was measured using a Malvern ZetaSizer Nano. The zeta potential was measured in 10^{-3} M NaCl and the pH adjusted from pH 6.5 to either acidic or basic pH values. This practice was adopted to ensure the background electrolyte concentration did not change significantly during the measurement. To adjust the pH slightly, either 10^{-3} HCl or 10^{-3} NaOH was used. At each pH, the suspensions were measured 10 times for 10 measurements and then averaged. In addition, two further repeats on freshly prepared samples were made and the data in Fig. 5-6 shows the average and error bars which represent the variation of the three measurements.

5.2.4 Rheology

All suspensions were measured using a DHR-2 rheometer (TA Instruments). The yield stress of each suspension was measured in oscillatory mode. The rheometer was calibrated using the standard procedure of first calibrating the inertia of the spindle, then calibrating the spindle in the presence of the geometry, and all measurements were conducted in precision mode and soft bearing mode for maximum measurement sensitivity. The geometry used was a vane of dimensions, d = 15 mm and l = 38 mm, with the vane inserted into a 50 mL cup. Before each measurement the gap spacing was calibrated at 8800 µm. The prepared sample was loaded into the cup using a spatula and to ensure the vane was fully submerged in the sample, 35 mL of sample was loaded into the cup. The vane was then gently rotated at 100 s^{-1} to ensure the sample is uniformly distributed in the cup and any trapped air is removed from the sample. Prior to measurement, all samples went through a pre-shear protocol of 400 s^{-1} for 5 min. This pre-shear protocol ensured that any history effects in the sample were removed, as well as any possible trapped air. The pre-shear protocol was optimized to ensure that the yield stress of the prepared suspension was greatly exceeded. Following pre-shear, the sample was allowed to rest at 0 s^{-1} for 180 s so that the structure could rebuild prior to measurement. At a fixed frequency of 50 rad s^{-1} the oscillation strain was increased from 0.0001 % to 100 %, with the strain step increasing 40 points per decade.

A typical oscillation strain measurement is shown in Fig. 5-4. The strain is varied sinusoidally and the resultant stress measured. The relationship

between the strain, stress and phase angle are then used to determine the viscous (G") and elastic (G') contributions of the suspension as a function of increasing strain. The yield stress was then determined from the G' plateau multiplied by the yield strain, which is taken to be the intercept between the plateau of log G' and the slope of log G', see Fig. 5-5 (25).

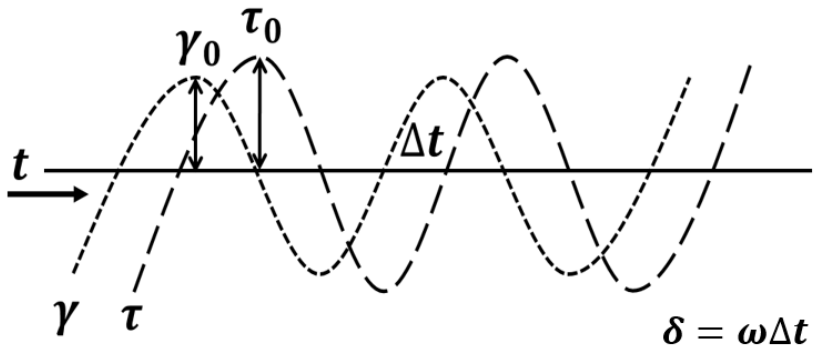

$$|G_s^*| = \frac{\tau_0}{\gamma_0} \qquad G_s' = |G_s^*| cos\delta \qquad G_s'' = |G_s^*| sin\delta$$

Figure 5-4. Schematic of the sinusoidal wave profiles of the applied strain and measured stress. From the wave form the complex modulus is determined and using the phase angle the viscous (G') and elastic (G") moduli are calculated.

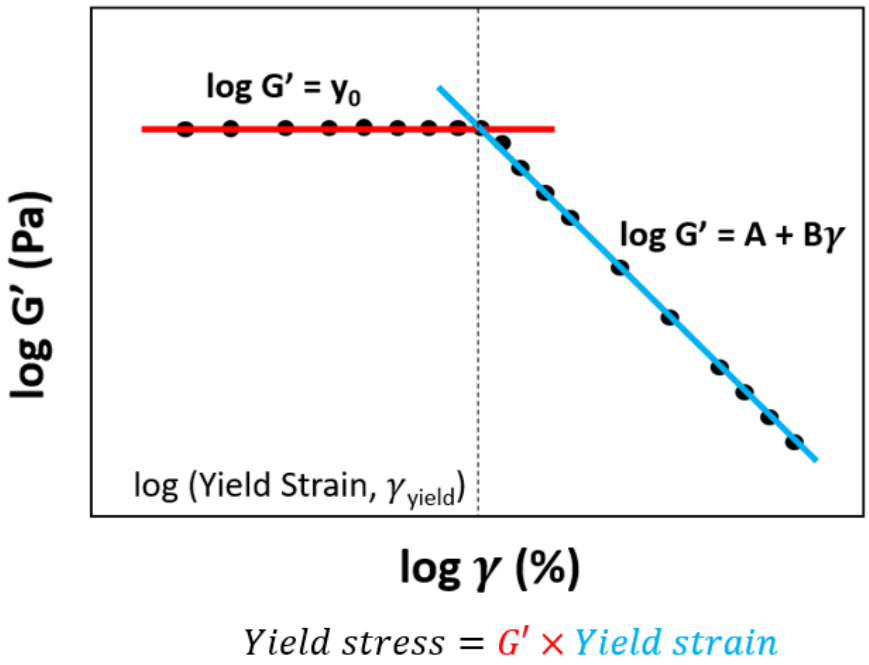

Figure 5-5. Typical viscoelastic data used to determine the yield stress of the concentrated particle suspensions. The yield stress is the product of the G' plateau and yield strain.

5.2.5 Sample Preparation Method

All samples were prepared following the same protocol. Separate batches of silica and alumina were initially prepared to the desired solids concentration in 10^{-3} M NaCl and then pH adjusted to the specified value. The prepared suspensions were gently agitated overnight on a tube roller to ensure the solution and the particle surface had reached ionic equilibrium. The silica suspension was then added gradually to the alumina suspension and the combined suspension was continually mixed using an overhead stirrer at 1500 rpm for 5 min. With the two suspensions combined, the suspension was continually agitated for a further 30 min and then sealed in a plastic container and left on the vibrating table for 24 hr. The blended suspension was pH checked and adjusted accordingly if needed. The suspension was then

resealed, left to agitate for a further 24 hr and finally pH checked and adjusted if needed prior to measurement.

5.2.6 SEM Methods

Two methods of sample preparation for SEM were used in the study, with the methods dependent on the suspension concentration. For dilute suspensions of approximately 10,000 ppm, it is possible visualize the likely interactions between the major and minor particles by isolating just a few particles. The method for dilute suspensions is called plunge freezing (26) and follows a protocol to minimize the effect of sample drying on the observed particle interaction. A 3.5 µL droplet of dispersion was placed on a glow discharge treated carbon support film, blotted, and plunge frozen in liquid ethane. The method is designed to ensure that the formed ice layer is as thin as possible without distorting the specimen, whilst fully embedding the particles to maximize sample contrast. The as prepared samples were then transferred cold to the cryo-holder for imaging.

The second method (27) of SEM allows for the visualization of the two particle types in the concentrated suspension, i.e., no dilution of the sample is needed. Cryo-SEM (Quorum Technologies, UK) requires approximately 0.5 mL of the suspension and this was extracted from the sample vial using a small spatula and placed onto a universal specimen shuttle. The sample was then plunged into liquid nitrogen at –90 ^{o}C for 2 min. The frozen sample was then transferred to a Quilo cryo preparation chamber (T = –140 ^{o}C) under high vacuum (1 ×

10^{-7} mbar) using the system cryo transfer device. The preparation chamber with viewing window was used to remove ice by the twin fracturing manipulators. The prepared sample was then transferred onto the SEM cold stage for imaging at –140 ^{o}C. Several samples and several magnifications were collected to determine the typical nature of the prepared blended suspensions.

5.3 Results and Discussion

The zeta potentials of the colloidal silica and colloidal alumina were measured in 10^{-3} M NaCl as a function of pH, see Fig. 5-6. The zeta potential of the colloidal silica was found to be negative across the pH range, with the particle isoelectric point being measured at pH 2. In basic conditions, the zeta potential of the silica was approximately – 40 mV and independent of any pH change. For the alumina particles, the zeta potential shows a particle isoelectric point at pH 8.5. Below this critical pH the particle zeta potential increased to 42 mV at pH 4. Above this critical pH the particle zeta potential decreased, with the zeta potential approaching that of silica in very high pH environment. The data in Fig. 5-6 shows that the two particles will be colloidally repulsive when the pH is pH 9 or greater and colloidally attractive when the pH is pH 8 or lower. Additional zeta potential data is shown in Appendix A4 for the blended system of alumina and silica particles. With increasing number ratio of silica-to-alumina, the zeta potential curve shifts to the left, with the condition of 1:100 (alumina:silica) producing a zeta potential curve which resembles that of silica only. Caution should be given to this data as the shift in i.e.p. may not relate

to coating of the alumina particles by silica particles, but may result from the greater abundance of silica particles.

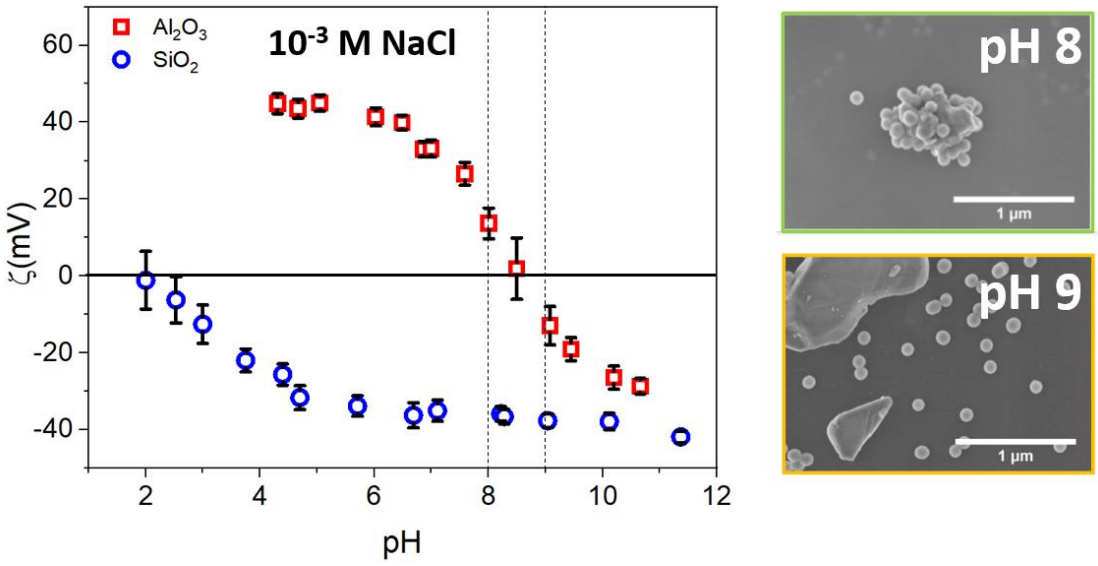

Figure 5-6. Zeta potential curves for the colloidal silica and alumina particles. The isoelectric point of silica is pH 2, while for alumina the isoelectric point is pH 8.5. The dashed lines represent the two pH conditions considered in the current study. The SEM images show the nature of interaction between the colloidal silica and alumina particles at the two pH conditions. Additional SEM images at different magnifications are shown in Appendix A3.

In an attempt to visualize the type of interaction between the alumina and silica particles, a very dilute suspension was prepared at a number ratio of 1:1000 for alumina and silica, respectively. The suspensions were prepared in 10^{-3} M NaCl and the pH adjusted to pH 8 and pH 9. The samples were left to gently rotate for 24 hr prior to measurement. One drop of each suspension was pipetted onto an SEM stub which was then plunge freezed following the method previously described (26). The plunge freeze method was used to avoid any potential drying effects. The images in Fig. 5-6 are typical of the particles in the pH 8 and pH 9 environments. In pH 8, colloidal silica which is

significantly smaller than the alumina particles stick to the surface of the alumina particle, while for pH 9 both particles exhibit negative zeta potentials and thus the interaction is repulsive, and colloidal silica does not coat the larger alumina particles.

The strength of the interaction potential can be calculated using the Hogg, Healy and Fuersenau (HHF) equation (28). This equation describes the electrical double layer forces acting between two particles of different zeta potentials. The interaction only considers the electrostatic repulsive force and the van der Waals attractive forces, with the total interaction being the summation of the two forces. Eq. 5.3 describes the van der Waals attractive forces, and Eq. 5.2 describes the electrostatic repulsive force.

$$V_R = -\frac{\pi\varepsilon_0\varepsilon_r a_1 a_2}{(a_1+a_2)}\left(2\psi_1\psi_2 \ln\left[\frac{1+e^{-\varkappa H}}{1-e^{-\varkappa H}}\right] + (\psi_1^2+\psi_2^2)\ln[1-e^{-2\varkappa H}]\right) \quad \textbf{Eq. 5-2}$$

where a is the particle radius, ε_0 is the permittivity of a vacuum, ε is the relative dieletric constant, Ψ is the zeta potential, κ is the inverse of the Debye length and H is the separation distance.

$$V_A = -\frac{A_{132}}{6H}\frac{a_1 a_2}{a_1+a_2} \quad \textbf{Eq. 5-3}$$

where the Hamaker constant is given by A. The subscripts 1 and 2 represent the two different particle types. The total interaction potential (V_T) is the summation of V_A and V_R.

$$V_T = V_R + V_A \qquad \textbf{Eq. 5-4}$$

Table 5-1. Fitting parameters used to calculate V_T as a function of the particle-particle separation distance.

	Radius (m)	Zeta potential (V), at pH 8	Zeta potential (V), at pH 9
Alumina (a_1)	2.6×10^{-7}	1.37×10^{-2}	-1.29×10^{-2}
Silica (a_2)	5.0×10^{-8}	-3.50×10^{-2}	-3.76×10^{-2}
Permittivity of water, ε_r	80.3		
Permittivity of vacuum, ε_r	8.85×10^{-12}		
Debye length (m^{-1}), κ	8.85×10^{-8}		
Hamaker constant (J), A_{123}	1.14×10^{-20}		

Fig. 5-7 shows the total interaction potential between silica and alumina surfaces at pH 8 and pH 9. The values used for each parameter are provided in Table 5-1. The zeta potential values are taken from the respective pH values in Fig. 5-6. When the aqueous phase is adjusted to pH 8, the interaction potential is purely attractive, a result of the opposite zeta potential values of the two surfaces. At pH 9, a weak repulsive energy barrier is observed at

short separation distances. It should be noted that strong colloidal stability is often described when the total interaction potential is greater > 25 kT, hence even for the case of pH 9, some interaction and weak aggregation of the two particle species is anticipated.

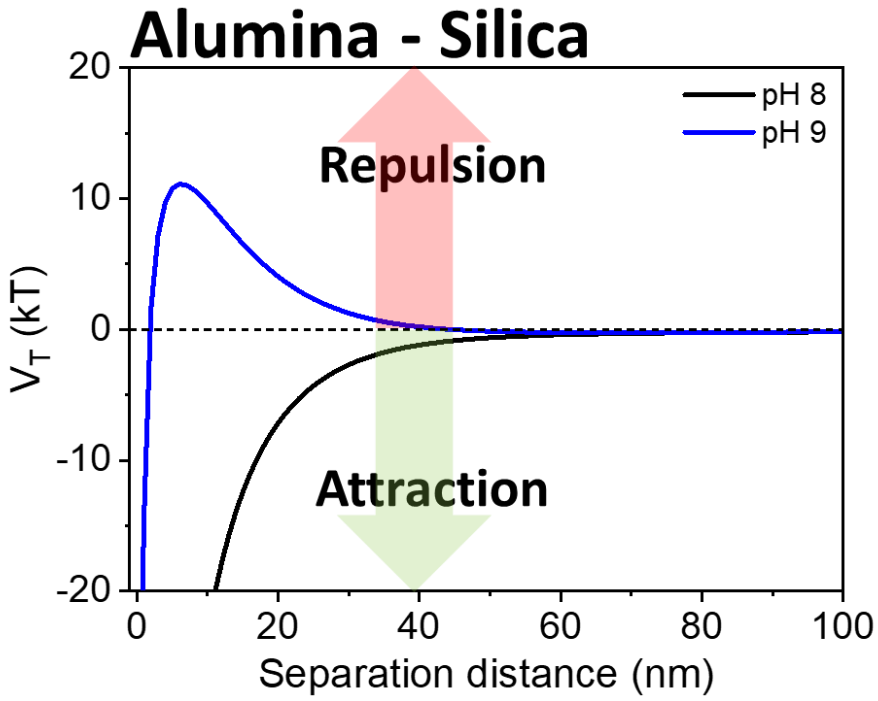

Figure 5-7. The theoretical total interaction potential between alumina and silica surfaces at the two pH conditions of interest. At pH 9 the total interaction potential shows a weak repulsive barrier, while at pH 8 the interaction is purely attractive.

5.3.1 Rheology Modification of Concentrated Particle Suspensions

The viscoelasticity of suspensions prepared to a constant concentration of 35 vol% with varying amounts of alumina and silica are shown in Fig. 5-8. All suspensions were measured at a constant frequency (50 rad s^{-1}) and

increasing strain (%) from 0.0001% to 100%, with a linear strain increment and 40 points per decade. For the data shown in Fig. 5-8, the open symbols represent the viscous component (G") and the closed symbols represent the elastic component (G'). At very low strain, most suspensions exhibit a solid-like behavior where the elastic component exceeds the viscous component. Above a critical strain the suspensions start to flow and this is shown by a decrease in the elastic component where eventually the viscous component exceeds the elastic component and the suspensions can be described as liquid-like. As the suspension approaches the yielding condition, the viscous component is seen to increase before gradually decreasing beyond the yield point. This increase has been discussed in the literature and can be attributed to a reordering and densification of the particle network prior to yielding. (29, 30) Such behavior is common for strongly yielding materials. Only for the sample 32:3 (32 vol% alumina + 3 vol% silica) is the characteristic shape (referring to the G' plateau at low strain values followed by a linear decay beyond the yield point) of the viscoelastic behavior no longer observed. No viscoelastic properties could be measured at low strain and the values reported above 10% strain are associated to instrument inertia, since the reported G' values at high strain result from an apparent phase angle induced by the inertia of the oscillating vane geometry. Since the vane geometry has a large contact area, the instrument inertia is increased. Further validation of instrument inertia is observed when reviewing the raw phase angle data, which showed the raw phase to be greater than 179^{o}, confirming the strong contribution of instrument inertia.

.

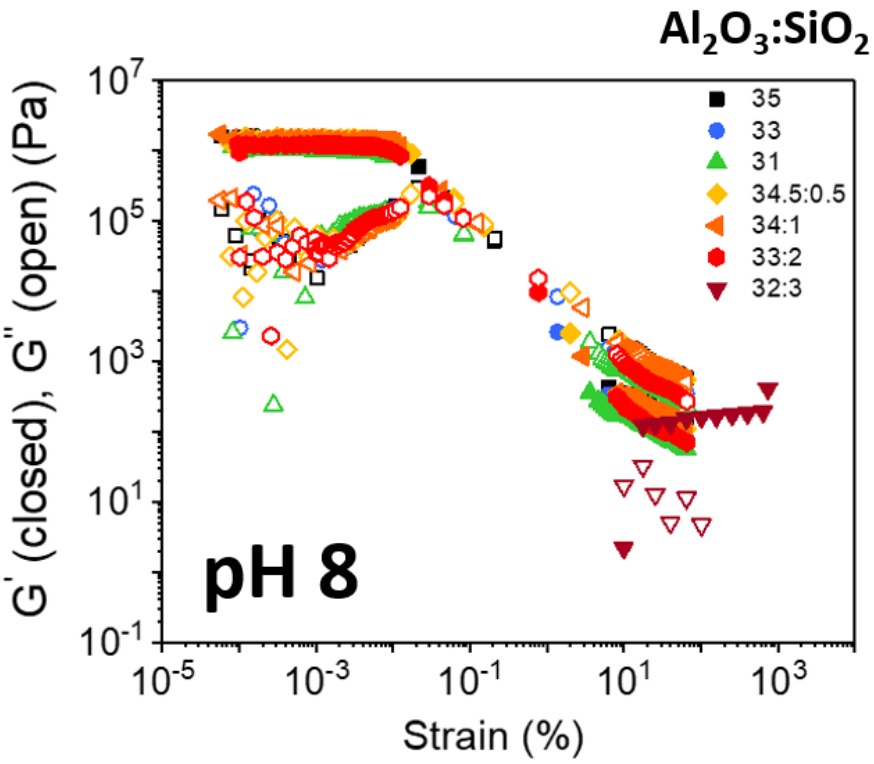

Figure 5-8. The viscoelastic data for pure alumina (35, 33, 31 vol%) and blended alumina:silica (34.5:0.5, 34:1, 33:2, 32:3) suspensions of a total solids content of 35 vol%. All suspensions were prepared in 10^{-3} M NaCl at pH 8.

The equivalent data for the alumina and silica suspensions at 35 vol% and pH 9 are shown in Fig. 5-9. Similar to the data at pH 8, most samples exhibit a solid-to-liquid transition, with the sample at 33:2 showing a liquid-like behavior and the viscoelastic response dominated by the instrument inertia. The frequency-dependent data for all suspensions at pH 8 and pH 9 are provided in Appendix A5 for reference. The data confirms that all yield stress suspensions form a strong gel-network.

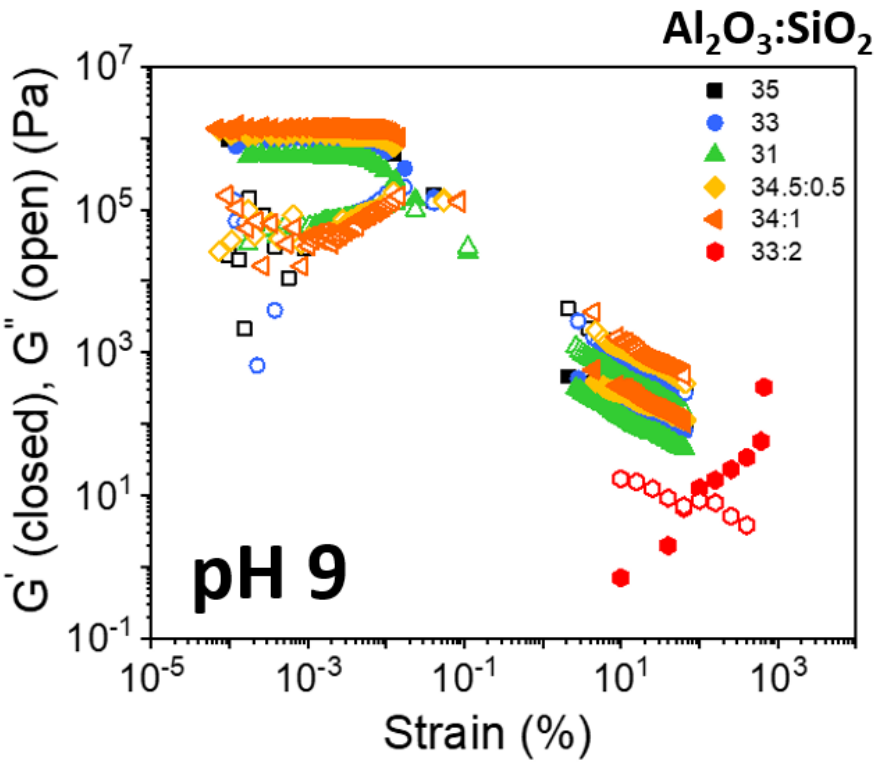

Figure 5-9. The viscoelastic data for pure alumina (35, 33, 31 vol%) and blended alumina:silica (34.5:0.5, 34:1, 33:2) suspensions of a total solids content of 35 vol%. All suspensions were prepared in 10^{-3} M NaCl at pH 9.

Figure 5-10 compares all the yield stress values from the data shown in Figs. 5-8 and 5-9. Yield stress values were determined from the yield strain as previously described (25). The open symbols in Fig. 5-10 represent a single component system of alumina. For pH 9, the yield stress of 35 vol% alumina is approximately 75 – 80 Pa. When the solids concentration of the alumina suspension is decreased, the suspension yield stress gradually decreased to < 50 Pa. For pH 8, the yield stress of a 35 vol% alumina suspension is approximately 135 – 140 Pa, almost double that of the pH 8 alumina suspension at the same solids concentration. At all other solids

concentrations, the suspensions prepared at pH 8 exhibit higher yield stress values. While it is not immediately apparent why the yield stress values at pH 8 and pH 9 differ, it may relate to an asymmetry around the particle isoelectric point, although such asymmetry is not easily distinguishable from the zeta potential curve shown in Fig. 5-6. This is not to say there is no asymmetry in the particle zeta potential around the isoelectric point, because a measurement of zeta potential by electrophoretic mobility becomes more challenging as the isoelectric point is approached, and rheological measurements at high solids concentrations a more sensitive to these small differences near the particle isoelectric point (31, 32).

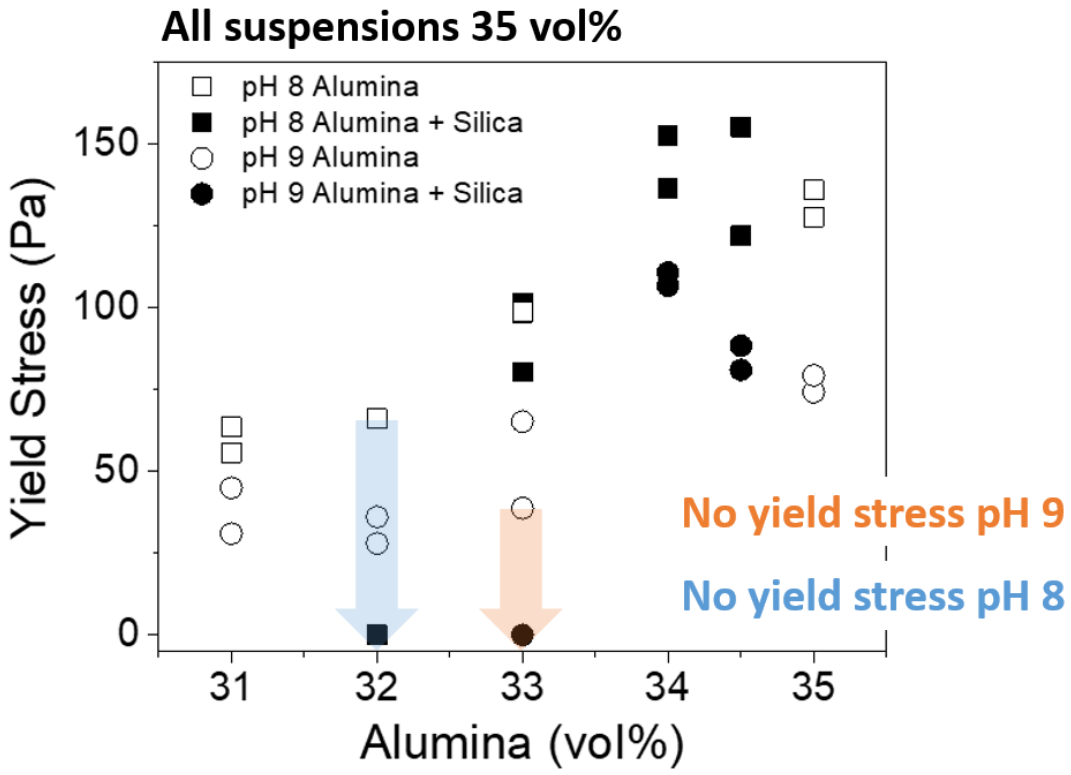

Figure 5-10. A comparison of all the yield stress data for alumina only (open symbols) and alumina:silica blended (closed symbols) suspensions at pH 8 (square symbols) and pH 9 (circle symbols). The arrows indicate the critical blend ratio when the yield stress of the suspension is eliminated.

The closed symbols in Fig. 5-10 represent the blended suspensions of alumina and silica. All suspensions were prepared to a total concentration of 35 vol%. For the case of pH 8, increasing the silica concentration by reducing the alumina concentration led to almost no significant change in the suspension yield stress when the blend ratio was changed to 34.5:0.5 and 34:1 (alumina:silica, vol:vol). However, there was some variation in the measured yield stress (at the same solids concentration) and this can likely be attributed to difficulties in preparing high solids content suspensions containing two components, i.e. ensuring a uniform distribution of the minor

component throughout the suspension. Further increasing the silica concentration to an equivalence of 2 vol% (i.e. 33 vol% alumina + 2 vol% silica), led to a reduction in the suspension yield stress relative to the single component (alumina) at 35 vol%. This yield stress was measured to be in the region of 100 Pa. Further increasing the silica concentration resulted in a dramatic change in the rheology of the concentrated particle suspension. A suspension with no yield stress was observed, and thus a critical blend ratio was achieved where the yield stress was eliminated. When compared to the single component (alumina) at a solids concentration of 32 vol%, the yield stress was approximately 70 Pa. Therefore, even though the alumina solids concentration is the same, addition of the colloidal silica resulted in eliminating the suspension yield stress.

A similar behavior with the changing blend ratio was observed at pH 9. Initially increasing the silica concentration led to a slight increase in the suspension yield stress, increasing from 75 Pa (35 vol% alumina) to 110 Pa (34 vol% alumina + 1 vol% silica). In this suspension, the particles are only weakly attractive at short range distances so it is not fully understood why the suspension at pH 9 shows an increase in yield stress with increasing silica concentration. Such behavior may be more characteristic of the pH 8 suspension, where the silica and alumina particles are attractive, and addition of silica promotes aggregation of the abundant alumina particles, thus increasing the strength of the particle network. One further increase in the silica concentration (33 vol% alumina + 2 vol% silica) led to the yield stress of the concentrated particle suspension disappearing. This condition is achieved

at a lower silica concentration than at pH 8. Taking an equivalent alumina concentration of 33 vol%, addition of the colloidal silica can lower the suspension yield stress from approximately 50 Pa to 0 Pa.

At the critical condition when the yield stress is eliminated, the particle number ratio is found to be 1:15 and 1:10 Al_2O_3 and SiO_2, as shown in Table 5-2. Due to the difference in particle size and density, at the critical concentration, there is an abundance of silica particles relative to alumina particles. This may suggest a requirement of the silica particles to coat the larger alumina particles thus inhibiting the interaction between alumina particles providing a mechanism for the particles to flow past one another with little resistance. It could be thought that the colloidal silica, which is approximately five times smaller than the alumina particles, acts as a “ball bearing” to lubricate the particle-particle contacts. Using Eq. 2.12, the N_{hex} value was calculated to be 140. Hence, to achieve a complete coating of the alumina particle by the smaller silica particles would require a particle number ratio considerably higher than that needed to modify the suspension rheology. Therefore, complete coating of the larger particle is not needed to eliminate the suspension yield stress.

Table 5-2. The particle number ratio at the alumina:silica critical blend ratio when the yield stress of the concentrated particle suspension is eliminated.

	Number ratio	
Al_2O_3:SiO_2 (vol%)	Al_2O_3	SiO_2
32:3	1	15
33:2	1	10

As previously discussed, the suspensions shown in Fig. 5-11 have undergone a two day preparation with the samples placed on a tube roller. Figure 5-11 visually shows evolution of the suspension rheology for two different blended systems at pH 8 and pH 9. For the suspension of 34:1 (alumina:silica) at pH 8, the measured yield stress is approximately 150 Pa. The three images show the suspension on day 0, day 1 and day 2, and clearly a high yield stress is observed with no flow when the sample beaker is upturned. However, for the suspension of 33:2 (alumina:silica) at pH 9, the measured yield stress is 0 Pa. When the sample is prepared (day 0), it is clearly seen that the suspension has a yield stress, with no flow when the sample beaker is tilted. One day later, tilting the sample beaker, the suspension has become more liquid-like and flows slowly; characteristic of a highly viscous liquid. On day 2, the suspension is reexamined and found to flow like water (inverting the sample beaker resulted in all sample flowing onto the beaker lid with little sample adhering to the beaker walls).

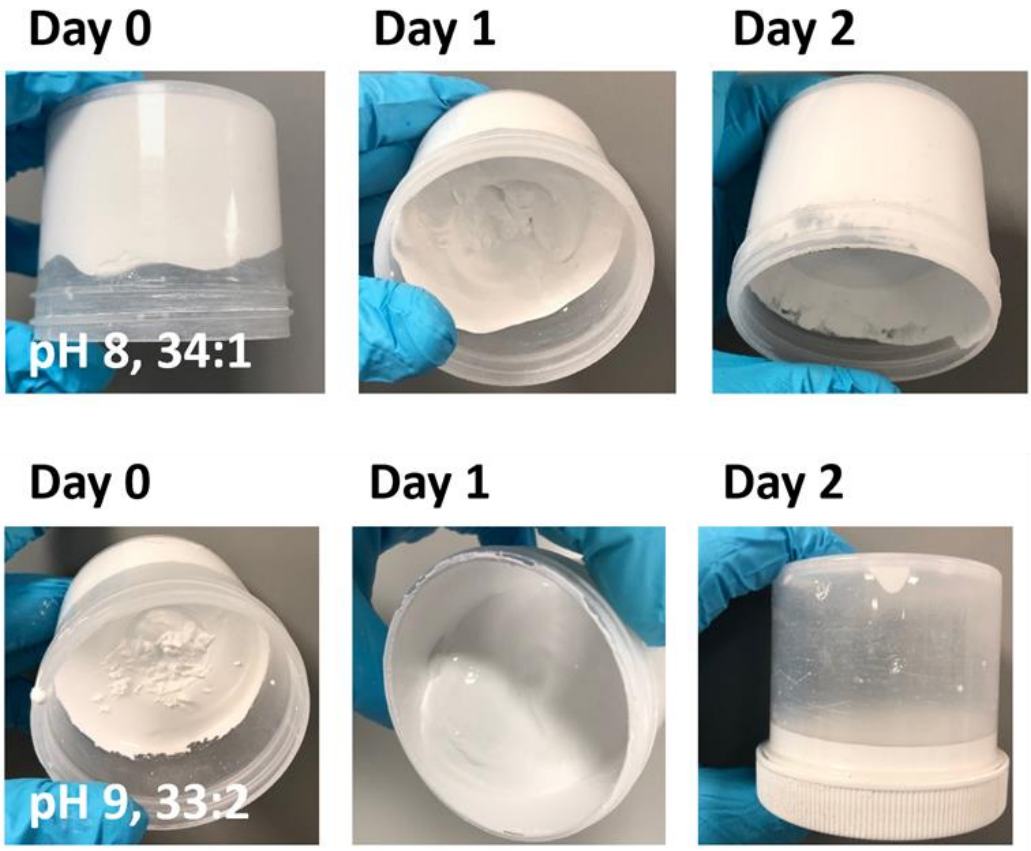

Figure 5-11. Images of the sample preparation protocol showing how the rheology of the concentrated particle suspensions gradually changes over the duration of 2 days. Further images showing the time-dependent behavior are provided in Appendix A6 for pH 8 and pH 9 suspensions of varying alumina-to-silica blend ratios.

Even though the suspension yield stress is eliminated, the images in Fig. 5-11 confirm that the process was time dependent. This may suggest that the performance of the blended system is very much dependent on the distribution of the colloidal silica throughout the alumina particle network. While the suspension is strongly mixed on day 0, a yield stress is still present. The gentle agitation on a tube roller, plus overhead stirrer mixing every 24 hr for 5 min, clearly promotes a change the particle network which leads to the formation of a zero yield stress suspension.

5.3.2 Visualization of the Suspension Internal Structure

To begin to assess the internal structure of the concentrated particle suspensions, a series of cryo-SEM EDX images were collected on several different samples. Figure 5-12 shows typical images collected when studying the suspension of 33:2 (alumina:silica) at pH 9, samples of 32:3 at pH 8, and 32:3 at pH 9 are provided in Appendix A1 and A2. The SEM image (Fig. 5-12a) reveals a circular cross section which results from slicing the sample holder. The dark regions in the SEM image were speculated to be silica due to differences in the electron reflectivity of silica and alumina. This was further confirmed by EDX analysis which clearly showed the contrast between silica and alumina (Fig. 5-12b). These images are quite revealing and show that all of the silica is not dispersed and not uniformly distributed throughout the alumina network. Considering the likely mechanism for flow improvement to be lubrication induced by the colloidal silica particles, such large accumulations of silica particles likely reduces the overall performance of the rheological modifier. While these images represent only a 2D snapshot of the sample, it is reasonable to assume that the scale is also equivalent in the z-direction (vertically). Several of these silica “islands” were observed in many samples, with chord lengths several tens to several hundreds of microns. With the colloidal silica being only 100 nm in diameter, the large scale of these silica “islands” suggests that the number of particles trapped within these large clusters exceeds several tens of thousands.

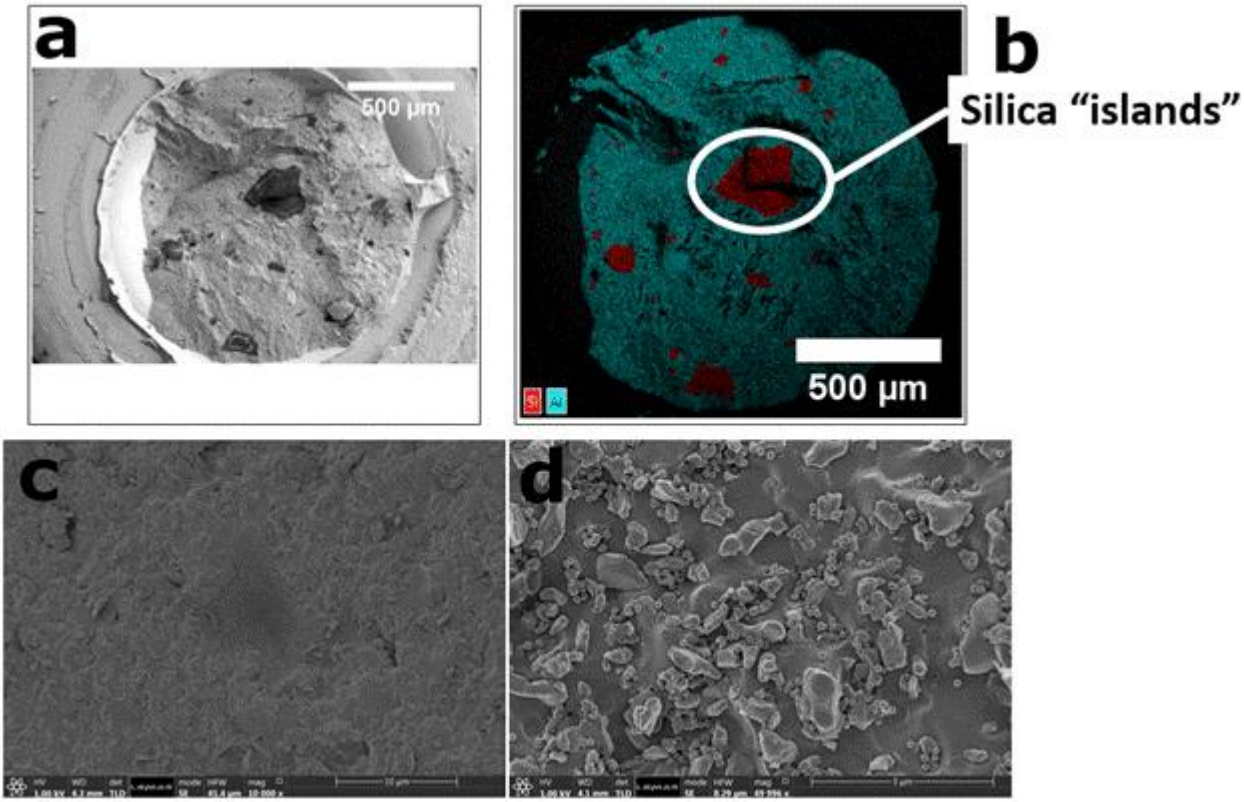

Figure 5-12. Cryo-SEM EDX images of a blended suspension of 33:2 alumina:silica (vol%) in 10^{-3} M NaCl at pH 9. Large clusters of colloidal silica particles were observed throughout the sample and are referred to as silica "islands".

Smaller silica "islands" were also observed in the higher magnification images (Fig. 5-12c) which revealed a somewhat crystalline structure. At the highest magnification of 49,996x, it was possible to visualize individual silica particles dispersed throughout the alumina network (Fig. 5-12d). These silica particles do not coat the larger alumina particles, which might be expected due to the negative surface potentials of both particle species. While this suspension does not have a yield stress, it is clear from the cryo-SEM EDX images that not all of the silica particles contribute to modifying the rheology of the suspension.

To address the issue of poor dispersion of the minor component, a series of tests were undertaken to enhance the dispersion of the colloidal silica. One method considered the use of strong ultrasonication to effectively disperse the colloidal silica prior to blending with the alumina suspension. The silica suspension was prepared as previously described but with ultrasonication for 5min using a sonic dismembrator (Fisher Scientific, Model 120). The suspension was then added to the alumina suspension and the same sample preparation protocol was then followed. It is worth reemphasizing that the initial sample preparation protocol was designed around minimizing the number of intervention steps, such that the protocol could be easily adopted within a large-scale engineering environment.

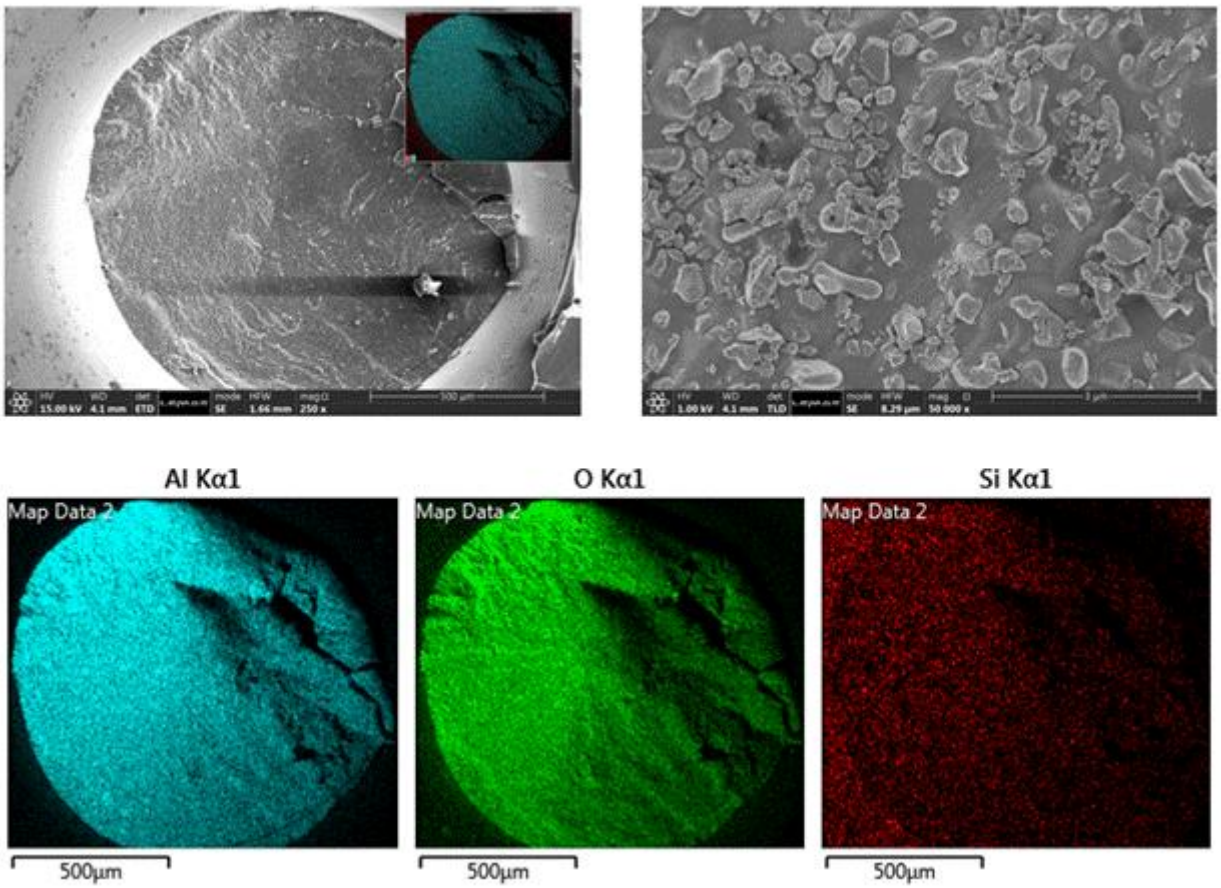

Figure 5-13. Cryo-SEM EDX images of a blended suspension of 34:1 alumina:silica (vol%) in 10^{-3} M NaCl at pH 9. The sample was prepared following the standard protocol except the colloidal silica suspension was ultrasonicated prior to blending with the alumina suspension.

The cryo-SEM EDX images in Fig. 5-13 are for the suspension of 34:1 (alumina:silica) at pH 9 prepared using the ultrasonication method. This suspension was measured to have no yield stress (Fig. 5-14) thus demonstrating a performance improvement by effectively dispersing the minor component. Without sonicating the colloidal silica, the yield stress was eliminated when the blend ratio was 33:2 (alumina:silica, vol%), highlighting the need to include more colloidal silica. Inspection of the SEM images did not reveal large silica “islands” and the EDX map of silica showed a uniform red haze across the observed plane of the sample, supporting the understanding

that the colloidal silica particles were better distributed throughout the concentrated particle suspension.

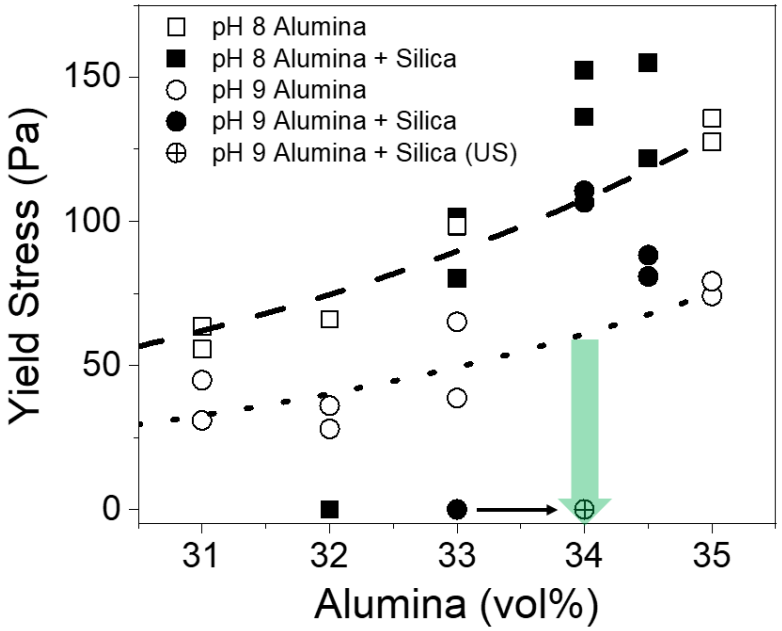

Figure 5-14. A complete summary of all the yield stress data as shown in Fig. 5-10. The new data is shown by the cross-hatched symbol and represents the sample where the colloidal silica is first sonicated prior to blending with the alumina suspension. The dashed lines are exponential fits and represent the typical yield stress values for alumina only. The data indicates that the yield stress can be reduced from approximately 70 Pa to 0 Pa by adding 1 vol% colloidal silica.

5.3.3 Sample Protocol Variation

As shown in Fig. 5-11, the change in the rheology of the prepared suspensions was found to be time dependent, which may suggest there is a correlation between the sample aging time and the effective dispersion of the colloidal silica throughout the alumina network. Figure 5-15 shows the viscoelastic measurement for a suspension of 34:1 (alumina:silica, vol%) at pH 9 measured at two different time intervals. The green symbols represent the

rheology of a sample prepared following the standard test protocol, and the blue symbols represent the rheology of a sample prepared following an extended protocol which included agitation on the tube roller, pH measurement and adjustment every 24 hr up to 5 days. While the Day 2 sample exhibited a yield stress, it is clear from the rheology measurement that the Day 5 sample has no yield stress and the data shows a viscous-dominant behavior. This simple test confirmed that extending the sample preparation protocol and providing more time for the colloidal silica to diffuse throughout the alumina network is advantageous in modifying the rheology of the concentrated particle suspension.

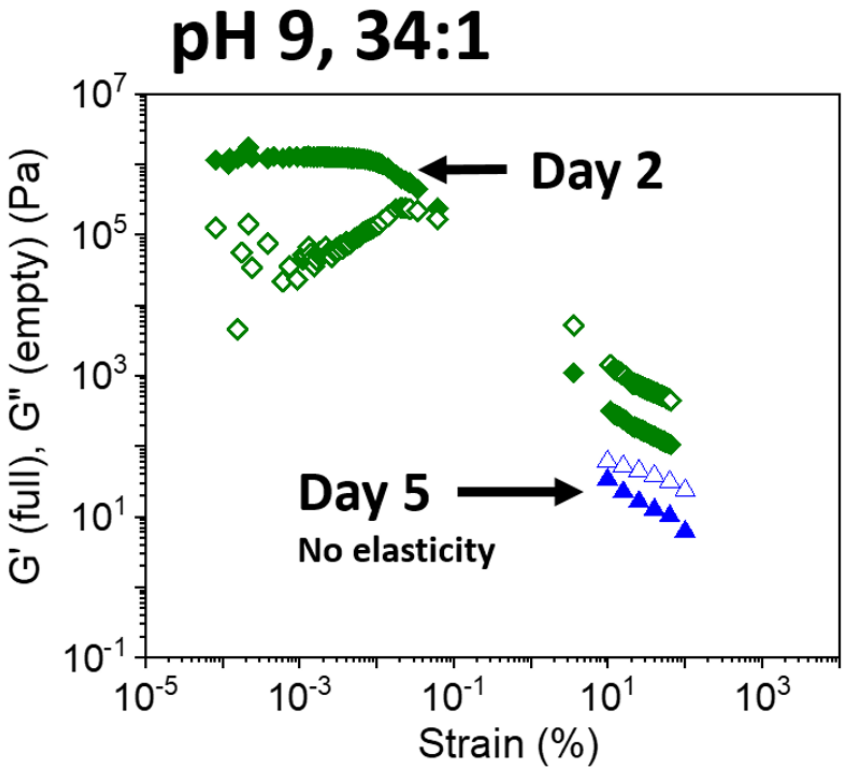

Figure 5-15. Viscoelastic data for two of the same samples prepared following the same sample preparation protocol except one sample was measured after 2 days and the second sample was measured after 5 days.

With the sample preparation protocol influencing the rheology of the concentrated particle suspension, a series of tests were designed to understand the impact of the different steps taken during sample preparation. Table 5-3 summarizes the different samples and the associated preparation protocol. All suspensions were characterized using a constant strain of 10^{-3} % at a constant angular frequency of 50 rad s^{-1}. Sample 7 was measured at the same frequency but at a higher constant strain of 0.1 %.

Table 5-3. Different sample preparation protocols to account for the different steps taken during the standard preparation protocol.

Sample	t = 0	t = 24 hr	t = 48 hr
1	No rollers		
2		No rollers	
3		On rollers	
4		On rollers + stirrer	
5		On rollers + stirrer + adjust pH	
6		On rollers + stirrer + adjust pH + Pre shearing	
7			standard protocol, strain 0.1 %

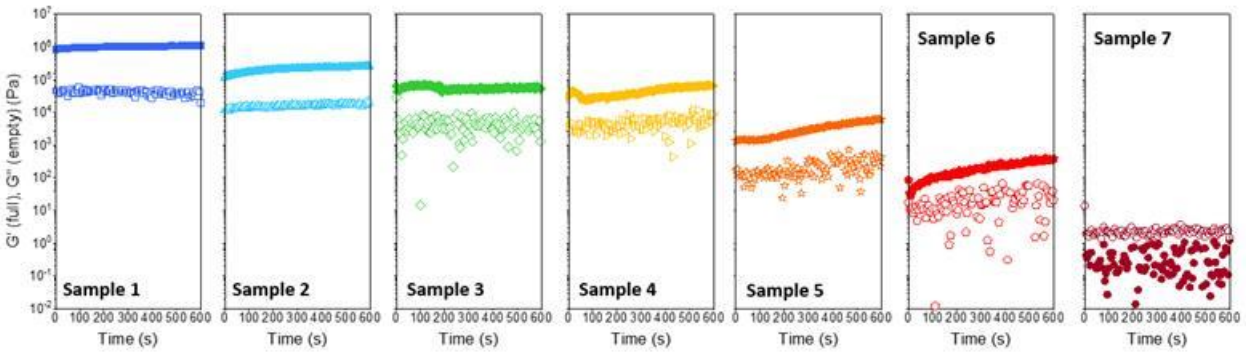

Figure 5-16. Oscillation time sweep of the binary (alumina (31 vol%) and silica (4 vol%)) suspensions in 10^{-3} M NaCl at pH 8, prepared following the standard protocol with preparation variations shown in Table 5-3. Samples 1 – 6: constant angular frequency 50 rad s^{-1} and constant shear strain 10^{-3} %. Sample 7: constant angular frequency 50 rad s^{-1} and constant shear strain 0.1 %. Samples 1 – 7 are shown by symbols: sample 1 (blue squares); sample 2 (cyan triangles); sample 3 (green diamonds), sample 4 (yellow right triangles), sample 5 (orange stars), sample 6 (red pentagons) and sample 7 (dark red circles).

The samples in Fig. 5-16 were prepared using 31:4 (alumina:silica, vol%) at pH 8 in 10^{-3} M NaCl. Following the standard preparation protocol, the suspension exhibited no measurable yield stress, as shown by Sample 7, where the viscous modulus exceeds the elastic modulus. The same sample was measured after different aging times and following different sample preparation protocols. Immediately following sample preparation, Sample 1 shows that the prepared suspension is strongly elastic and will have a yield stress. When the sample is left to age for a further 24 hr without gentle agitation, Sample 2 shows that the magnitude of the viscoelastic moduli slightly reduces, although the sample remains a yield stress suspension. When Sample 1 is aged for 24 hr with gentle agitation, the magnitude of the viscoelastic moduli decreases further. This data suggests that the action of gentle agitation promotes a greater reduction in the viscoelastic moduli

relative to the freshly prepared sample, and the diffusion and/or weakly convective mobility of the colloidal particles is necessary to promote distribution of the colloidal silica throughout the alumina network.

Sample 4 is the same as Sample 3 except some gentle stirring was applied to mimic the stirring when measuring and adjusting the suspension pH. This additional agitation, albeit slightly more intense than the agitation on the tube roller, does not appear to influence the viscoelastic moduli of the suspension. Sample 5 includes a single pH adjustment and shows a reduction in the viscoelastic moduli, but again the suspension remains elastically dominant. This data confirms that the slight acidic drift in the suspension pH appears to maintain a high viscoelastic moduli and similarly a high yield stress of the suspension. While the pH drift will have negligible effect on the zeta potential of the silica particles, the slight reduction in suspension pH would increase the zeta potential of the alumina particles, which would increase the interaction potential between the alumina and silica particles, promoting a higher yield stress suspension, as seen.

Compared to Sample 5, the pre-shearing protocol in the rheometer was applied to Sample 6 and this high intensity agitation reduces the viscoelastic moduli by almost two orders of magnitude. The suspension remains elastically dominant, although the viscoelastic ratio (G'/G") is less than observed in previous samples. Sample 6 clearly indicates that strong agitation weakens the particle network strength, likely as a result of better dispersion of the

colloidal silica throughout the alumina network. This systematic study points to the fact that the colloidal silica is likely lubricating the interactions between the larger alumina particles allowing them to flow more easily, and as the colloidal silica is better distributed throughout the sample, the stronger the lubrication effect. Finally, the standard protocol resulted in a suspension with no yield stress and the sample was prepared over 48 hr, which again underlines the importance of providing sufficient time and agitation to effectively disperse the colloidal silica throughout the alumina network.

5.3.4 Rheology Modification in High Concentration Electrolyte

For the standard sample preparation protocol, suspensions were prepared in 10^{-3} M NaCl and pH adjusted using concentrated HCl or NaOH on Day 0, Day 1 and Day 2. As a result of this pH adjustment, the background electrolyte concentration would increase slightly, and was calculated to possibly increase by one order of magnitude. To determine if a higher electrolyte concentration would have a negative impact on the ability to eliminate the yield stress of a concentrated particle suspension, a simple test was conducted following the same sample preparation protocol but using 10^{-1} M NaCl as the background fluid. Fig. 5-17 compares two suspensions of 33:2 and 32:3 (alumina:silica, vol%) at pH 8. These two suspensions were chosen as they represented the transition between a yield stress and no yield stress suspension following the standard protocol. As shown in Fig. 5-17, an increase in the ionic concentration of the background fluid appeared to have negligible impact on the ability to modify the rheology of the concentrated particle suspensions. The same critical blend ratio was found, and the yield stress of the 33:2

suspension was 55 Pa. This result is encouraging and confirms that in a strongly aggregated network, induced by the high electrolyte concentration, it is possible to add colloidal silica particles at a critical blend ratio to eliminate the suspension yield stress.

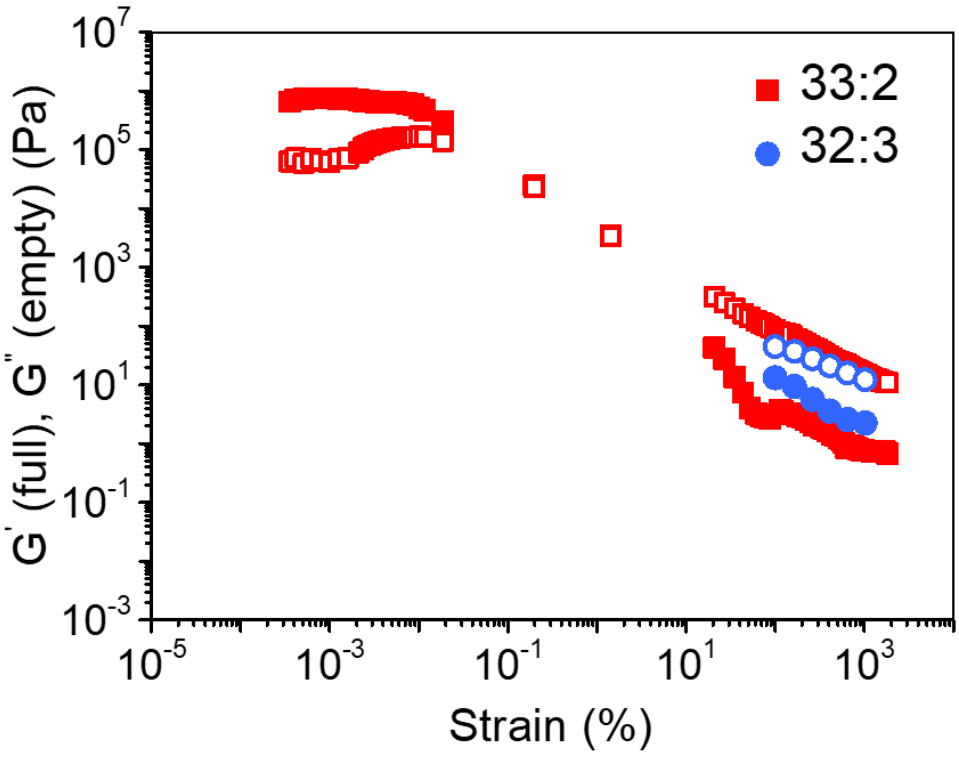

Figure 5-17. Viscoelastic data for two alumina-silica blended suspensions prepared in 10^{-1} M NaCl. The sample pH was fixed at pH 8.

5.3.5 Compressional Resistance of the Blended Suspensions

Considering the potential application of behaviorally modifying suspensions in the nuclear industry, there is a need to understand how such suspensions would behave over long periods of time while in interim or geological storage. Therefore, a test protocol was developed to expose a no yield stress

suspension to compressional consolidation by centrifuging the samples for 15 min at increasing centrifuge speeds, see Fig. 5-18a. The chosen no yield stress suspension was 32:3 (alumina:silica, vol%) in 10^{-3} M NaCl at pH 9. As control samples, suspensions of only alumina were also prepared to 32 vol% (yield stress ca. 30 Pa) and 35 vol% (yield stress ca. 75 Pa) in 10^{-3} M NaCl at pH 9. For the two control samples, the initial centrifuge speed of 750 rpm did not provide sufficient force to begin consolidating the suspension, as seen by a constant solids content (vol%). However, when the centrifuge speed was increased to 1000 rpm, the gelled network began to consolidate and the measured solids content increased. At higher centrifuge speeds the suspension continued to consolidate, with the solids content at the maximum centrifuge speed of 10000 rpm approximately equal to 44.5 vol%. For the no yield stress blended suspension, the initial centrifuge speed of 750 rpm led to significant consolidation of the particle network, with a final solids content of 38.2 vol%. Such behavior contrasts the control samples, but is understandable since the suspension initially exhibits no yield stress, hence the particles are freely mobile. Further gradual increments in the centrifuge speed resulted in a continual increase in the solids content of the blended suspension, with the more significant changes in solid content observed at centrifuge speeds below 5000 rpm. At the highest centrifuge speed, the solids content was approximately equivalent to that of the two control samples.

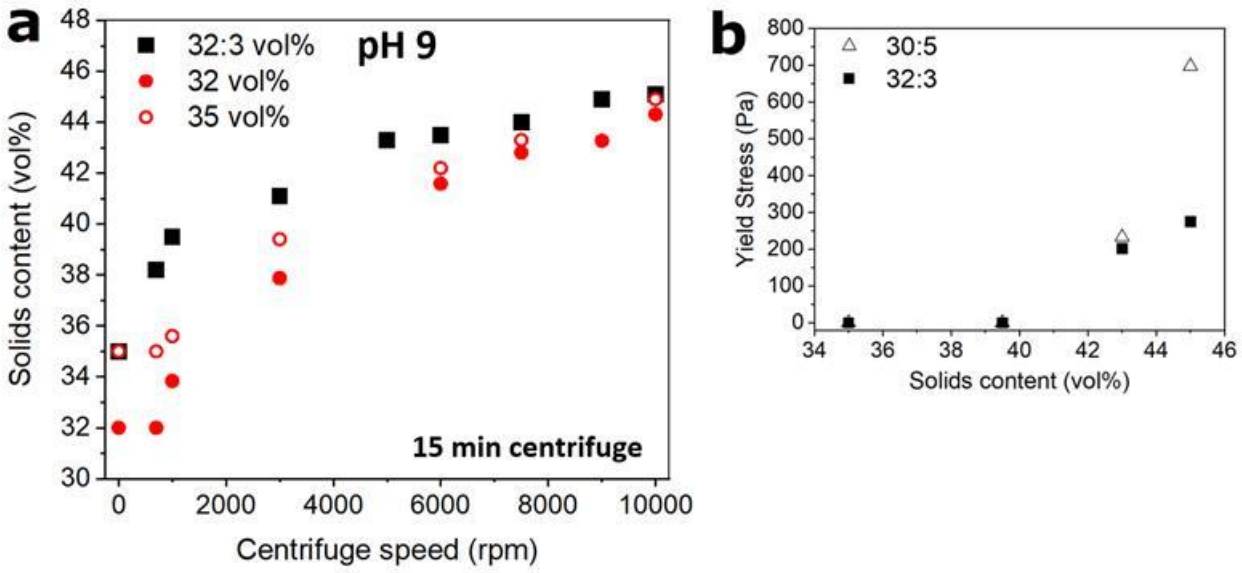

Figure 5-18. The changing solids content (a) and suspension yield stress (b) as suspensions undergo consolidation induced by centrifugal forces. All suspensions were prepared in 10^{-3} M NaCl at pH 9.

The implication of increasing the solids content is that the yield stress of the blended suspension begins to increase with greater consolidation. Two blended suspensions were prepared to 30:5 and 32:3 (alumina:silica, vol%) in 10^{-3} M NaCl at pH 9, with the 30:5 blend doped with an excess of colloidal silica such that the lubricating effect was enhanced. Fig. 5-18b shows that the two blended suspensions can undergo significant solids consolidation before a yield stress begins to develop in the sediment. The critical solid content for the onset of a yield stress was not determined but is greater than 39.5 vol%. Interestingly, the suspension doped with an excess of colloidal silica did not significantly differ from the sample with less silica. The data confirms that while the solid content is sufficiently high, the suspensions are able to consolidate which can lead to an increase in the suspension yield stress. Obviously as a consolidated network begins to form the force required to

induce further consolidation increases, hence a new steady-state would likely be reached in a storage container.

5.4 Conclusions

The yield stress of colloidal particles which are irregular-shaped can increase very rapidly at very low solids concentrations. High yield stress suspensions can cause problems in their processing and handling, thus alternatives to behaviorally modify the rheology of concentrated particle suspensions is desired by the nuclear industry. An approach was adopted whereby spherical colloidal silica particles were blended into a concentrated suspension of larger alumina particles. The size ratio between the two particles is approximately 5:1 (33)for alumina:silica. Two pH conditions were chosen such that the two particle species were weakly attractive and weakly repulsive. A series of alumina:silica blend ratios were studied and it was found that independent of the colloidal interaction (attractive or repulsive), a critical blend ratio could be reached where the yield stress of the concentrated particle suspension was eliminated. Further studies to understand the nature of this flow modification indicated that the colloidal silica is likely acting as a lubricating particle between the larger and irregular-shaped alumina particles. Methods to better disperse the colloidal silica throughout the alumina network led to the critical blend ratio changing, where a suspension with a total solids content of 35 vol% would have no yield stress when 1 vol% silica is added to 34 vol% alumina.

References

1. Hastings, J.J., Rhodes, D., Fellerman, A.S., McKendrick, D. and Dixon, C. New approaches for sludge management in the nuclear industry. *Powder Technology.* 2007, **174**(1), pp.18-24.
2. Jackson, S.F., Monk, S.D. and Riaz, Z. An investigation towards real time dose rate monitoring, and fuel rod detection in a First Generation Magnox Storage Pond (FGMSP). *Applied Radiation and Isotopes.* 2014, **94**, pp.254-259.
3. Gregson, C.R., Goddard, D.T., Sarsfield, M.J. and Taylor, R.J. Combined electron microscopy and vibrational spectroscopy study of corroded Magnox sludge from a legacy spent nuclear fuel storage pond. *Journal of Nuclear Materials.* 2011, **412**(1), pp.145-156.
4. NAO. *The Nuclear Decommissioning Authority: progress with reducing risk at Sellafield.* UK, 2018.
5. Delegard, C.H., Sinkov, S.I., Chenault, J.W., Schmidt, A.J., Welsh, T.L. and Pool, K.N. Determination of uranium metal concentration in irradiated fuel storage basin sludge using selective dissolution. *Journal of Radioanalytical and Nuclear Chemistry.* 2014, **299**(3), pp.1871-1882.
6. Mashal, K., Harsh, J.B., Flury, M., Felmy, A.R. and Zhao, H. Colloid formation in Hanford sediments reacted with simulated tank waste. *Environmental science technology.* 2004, **38**(21), pp.5750-5756.
7. Page, J.S., Reynolds, J.G., Ely, T.M. and Cooke, G.A. Development of a carbonate crust on alkaline nuclear waste sludge at the Hanford site. *Journal of hazardous materials.* 2018, **342**, pp.375-382.
8. Proceeding, I. Management and storage of research reactor spent nuclear fuel. In: *Proceeding of a technical meeting held in Thurso*, 2009.
9. Snow, L.A., Lumetta, G.J., Fiskum, S. and Peterson, R.A. Boehmite actual waste dissolution studies. *Separation Science and Technology.* 2008, **43**(9-10), pp.2900-2916.
10. Einstein, A.J.A.d.P. Eine neue bestimmung der moleküldimensionen. 1906, **324**(2), pp.289-306.

11. Batchelor, G. and Green, J. The determination of the bulk stress in a suspension of spherical particles to order c 2. *Journal of Fluid Mechanics.* 1972, **56**(3), pp.401-427.
12. Batchelor, G. The effect of Brownian motion on the bulk stress in a suspension of spherical particles. *Journal of Fluid Mechanics.* 1977, **83**(1), pp.97-117.
13. Krieger, I.M. and Dougherty, T.J. A mechanism for non-Newtonian flow in suspensions of rigid spheres. *Transactions of The Society of Rheology.* 1959, **3**(1), pp.137-152.
14. Phan-Thien, N. and Graham, A. A new constitutive model for fibre suspensions: flow past a sphere. *Rheologica acta.* 1991, **30**(1), pp.44-57.
15. Shijie, L. and Jacob, H.M. Rheology of Suspensions. In: *Suspensions: Fundamentals and Applications in the Petroleum Industry*. American Chemical Society, 1996, pp.107-176.
16. Daghooghi, M. and Borazjani, I. The effects of irregular shape on the particle stress of dilute suspensions. *Journal of Fluid Mechanics.* 2018, **839**, p.663.
17. Heine, D.R., Petersen, M.K. and Grest, G.S. Effect of particle shape and charge on bulk rheology of nanoparticle suspensions. *The Journal of chemical physics.* 2010, **132**(18), p.184509.
18. Clavaud, C., Bérut, A., Metzger, B. and Forterre, Y. Revealing the frictional transition in shear-thickening suspensions. *Proceedings of the National Academy of Sciences.* 2017, **114**(20), pp.5147-5152.
19. Ten Brinke, A.J., Bailey, L., Lekkerkerker, H.N. and Maitland, G.C. Rheology modification in mixed shape colloidal dispersions. Part I: pure components. *Soft Matter.* 2007, **3**(9), pp.1145-1162.
20. Ten Brinke, A.J., Bailey, L., Lekkerkerker, H.N. and Maitland, G.C. Rheology modification in mixed shape colloidal dispersions. Part II: mixtures. *Soft Matter.* 2008, **4**(2), pp.337-348.
21. Bailey, L., Lekkerkerker, H.N. and Maitland, G.C. Rheology modification of montmorillonite dispersions by colloidal silica. *Rheologica acta.* 2014, **53**(5-6), pp.373-384.

22. Lopez-Lopez, J., Schmitt, A., Moncho-Jorda, A. and Hidalgo-Alvarez, R. Stability of binary colloids: kinetic and structural aspects of heteroaggregation processes. *Soft Matter.* 2006, **2**(12), pp.1025-1042.
23. Islam, A.M., Chowdhry, B.Z. and Snowden, M.J. Heteroaggregation in colloidal dispersions. *Advances in Colloid and Interface Science.* 1995, **62**(2–3), pp.109-136.
24. Raşa, M., Philipse, A. and Meeldijk, J. Heteroaggregation, repeptization and stability in mixtures of oppositely charged colloids. *Journal of Colloid and Interface Science.* 2004, **278**(1), pp.115-125.
25. Yanez, J.A., Shikata, T., Lange, F.F. and Pearson, D.S. Shear Modulus and Yield Stress Measurements of Attractive Alumina Particle Networks in Aqueous Slurries. *Journal of the American Ceramic Society.* 1996, **79**(11), pp.2917-2917.
26. Hondow, N., Brydson, R., Wang, P., Holton, M.D., Brown, M.R., Rees, P., Summers, H.D. and Brown, A. Quantitative characterization of nanoparticle agglomeration within biological media. *Journal of Nanoparticle Research.* 2012, **14**(7), p.977.
27. Yu, K., Zhang, H., Biggs, S., Xu, Z., Cayre, O.J. and Harbottle, D. The rheology of polyvinylpyrrolidone-coated silica nanoparticles positioned at an air-aqueous interface. *Journal of Colloid and Interface Science.* 2018, **527**, pp.346-355.
28. Hogg, R., Healy, T. and Fuerstenau, D. Mutual coagulation of colloidal dispersions. *Transactions of the Faraday Society.* 1966, **62**, pp.1638-1651.
29. Harbottle, D., Chen, Q., Moorthy, K., Wang, L., Xu, S., Liu, Q., Sjoblom, J. and Xu, Z. Problematic stabilizing films in petroleum emulsions: Shear rheological response of viscoelastic asphaltene films and the effect on drop coalescence. *Langmuir.* 2014, **30**(23), pp.6730-6738.
30. Zhang, H., Yu, K., Cayre, O.J. and Harbottle, D. Interfacial particle dynamics: one and two step yielding in colloidal glass. *Langmuir.* 2016, **32**(50), pp.13472-13481.
31. Botha, J., Hunter, T., Johannsmann, D., Austin, D., Hodges, C., Mackay, G., Woodbury, S., Biggs, S. and Harbottle, D. Resonance

properties of quartz crystal microbalance immersed in high solid content suspensions. *Colloids Surfaces A: Physicochemical Engineering Aspects.* 2019, **573**, pp.230-236.

32. Kosmulski, M., Gustafsson, J. and Rosenholm, J.B. Correlation between the zeta potential and rheological properties of anatase dispersions. *Journal of Colloid and Interface Science.* 1999, **209**(1), pp.200-206.

33. Antony, S. and Sciences, E. Link between single-particle properties and macroscopic properties in particulate assemblies: role of structures within structures. *Philosophical Transactions of the Royal Society A: Mathematical, Physical, Engineering Sciences.* 2007, **365**(1861), pp.2879-2891.

Appendix

A1. Cryo-SEM EDX

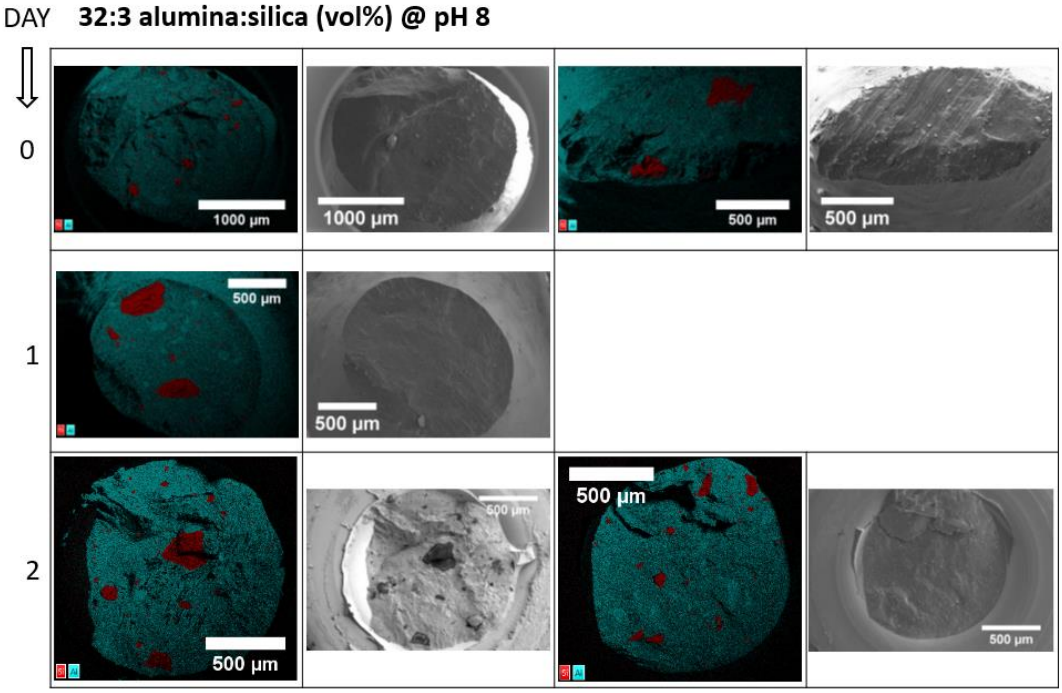

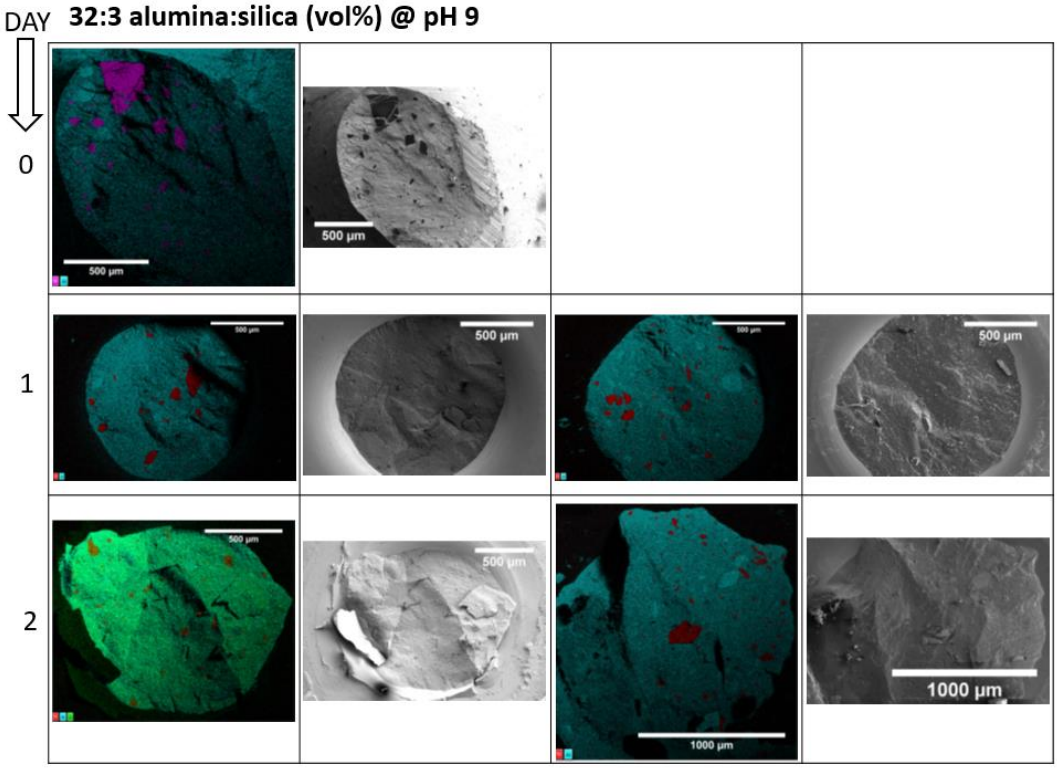

A2. Cryo-SEM

32:3 alumina:silica (vol%) in 10^{-3} M NaCl at pH 8.

Day 0

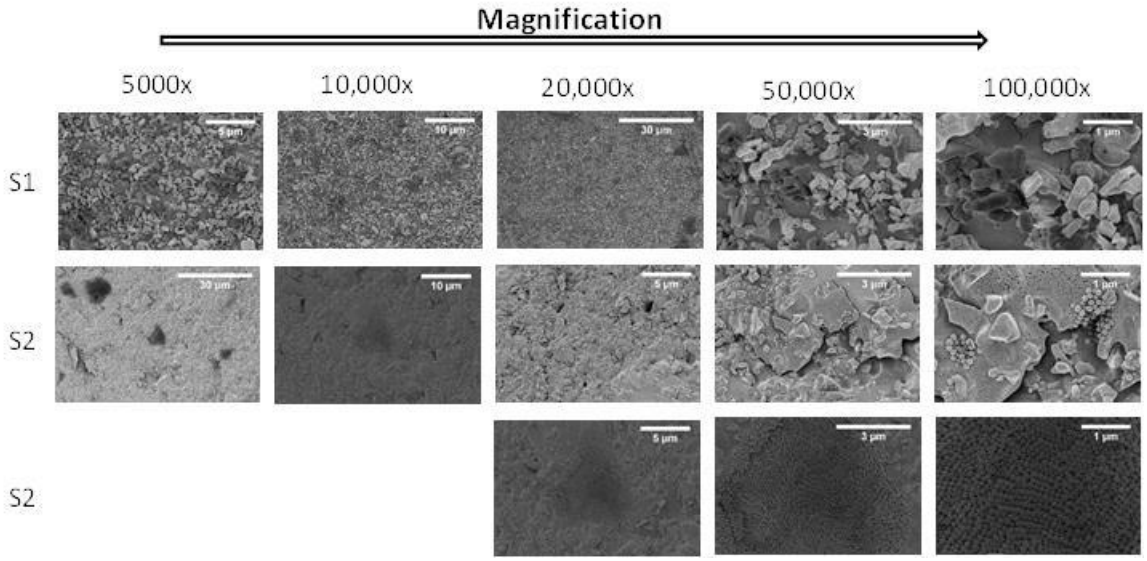

Day 1

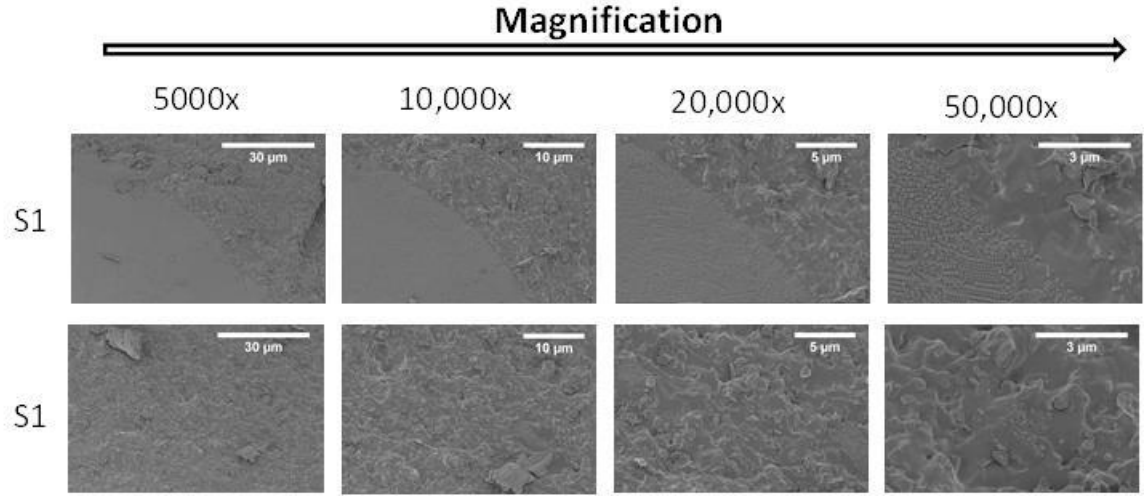

32:3 alumina:silica (vol%) in 10^{-3} M NaCl at pH 9.

Day 0

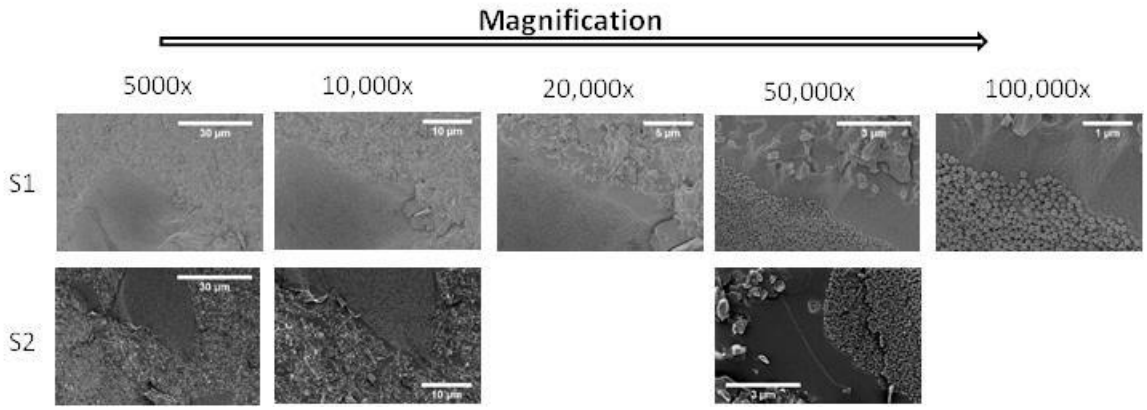

Day 1

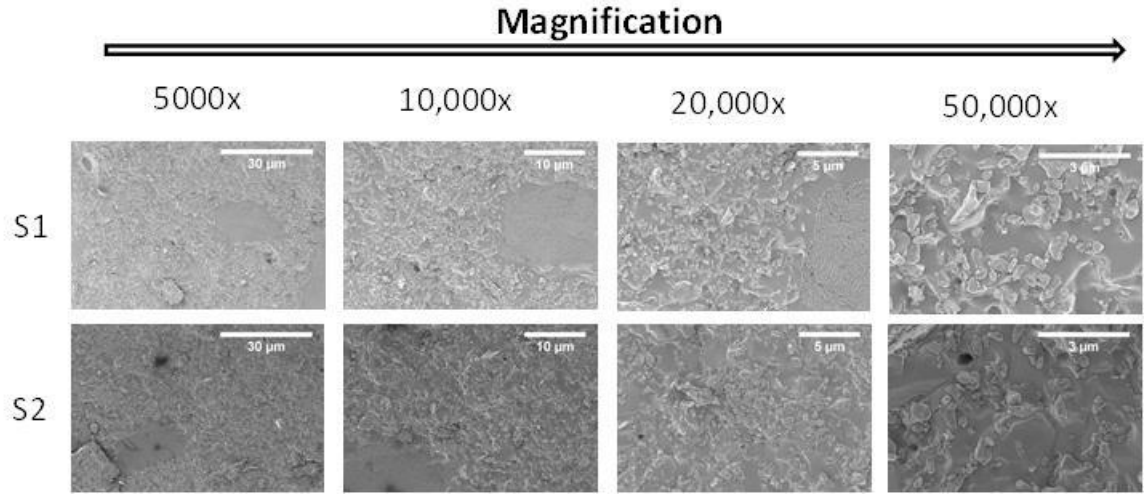

Day 2

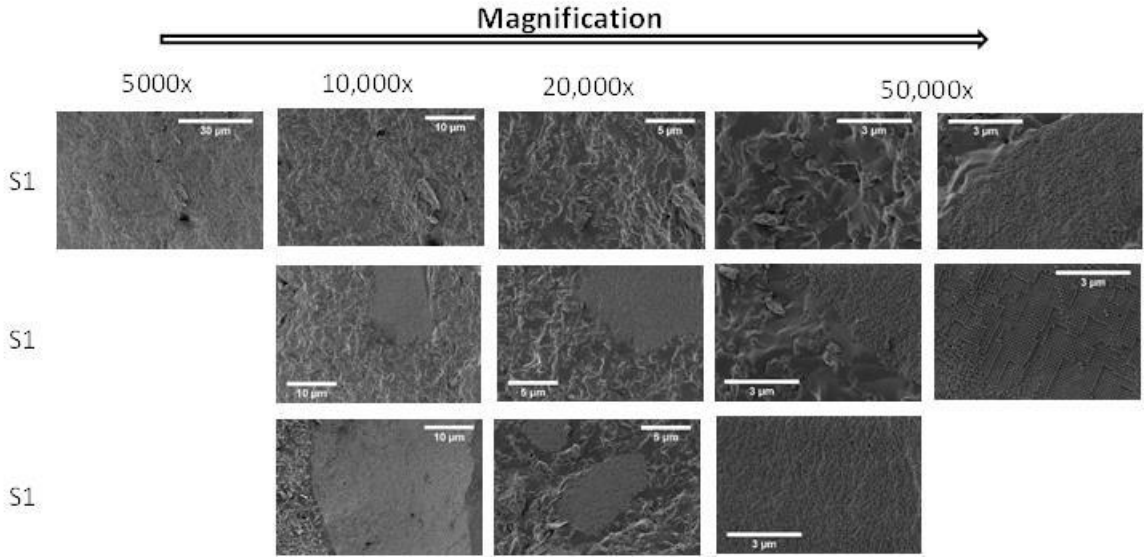

A3. SEM Imaging of Blended Suspensions

Electrolyte = 10^{-3} M NaCl; Suspension concentration = 10000 ppm; Alumina:silica number ratio = 1:1000.

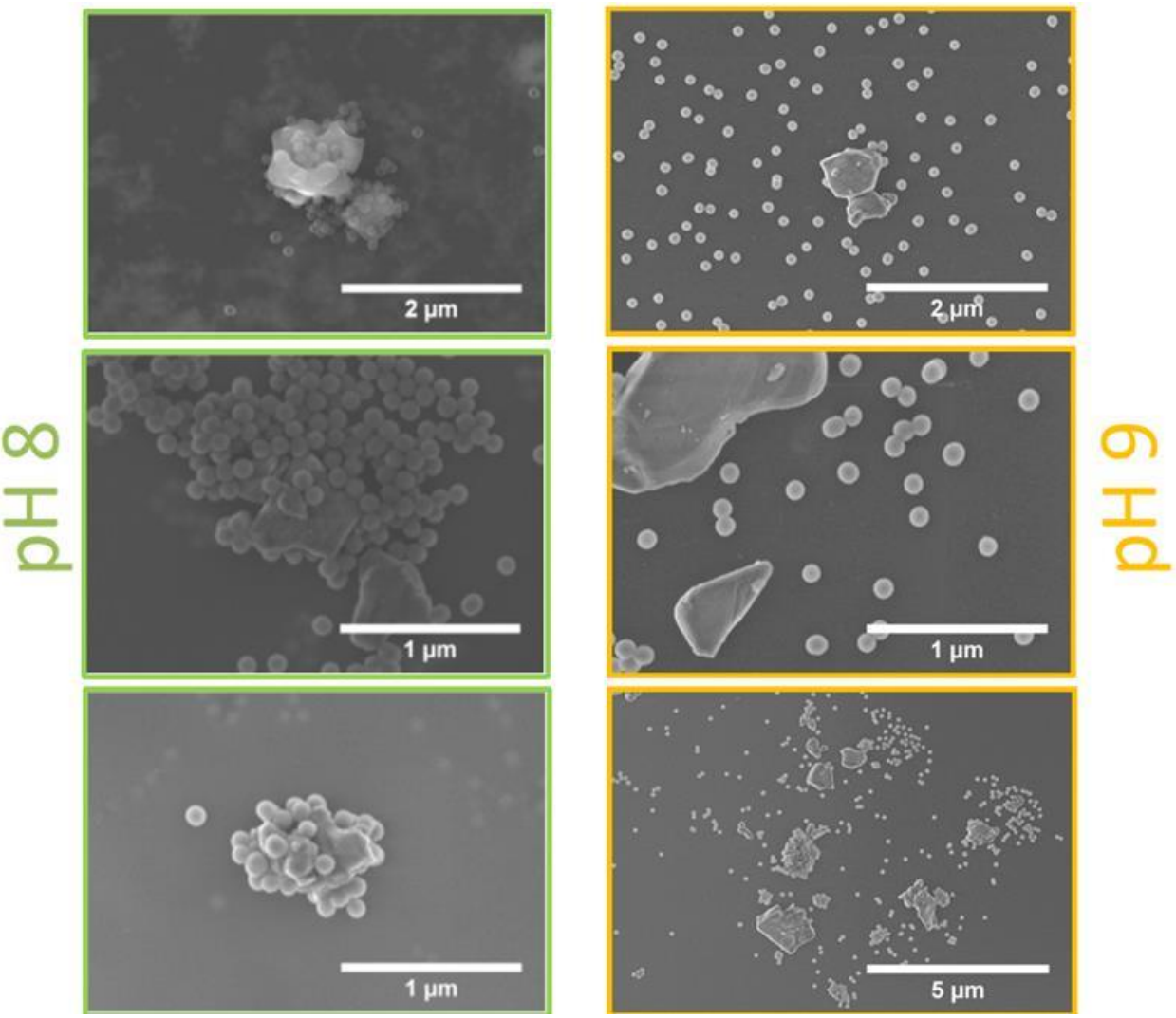

A4. Zeta Potential Curves of Blended Suspensions

Electrolyte = 10^{-3} M NaCl; Suspension concentration = 1000 ppm; Alumina:silica number ratio.

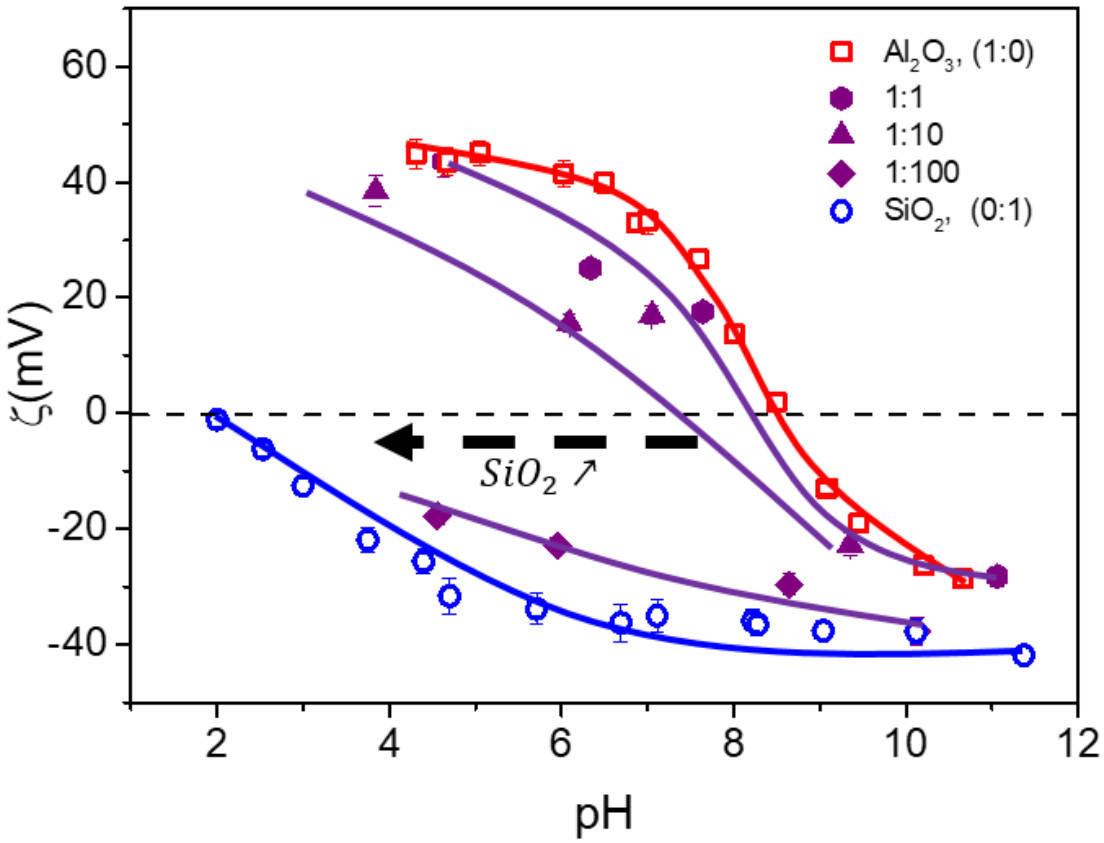

A5. Frequency-dependent Rheology of Concentrated Blended Suspensions

Electrolyte = 10^{-3} M NaCl; Ratio is alumina:silica (vol%).

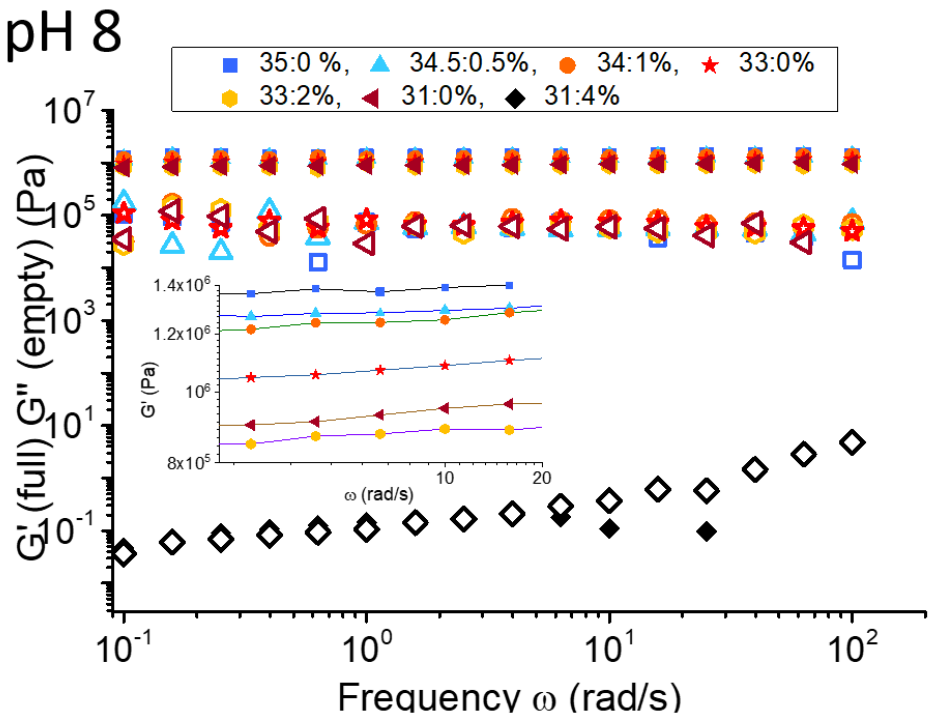

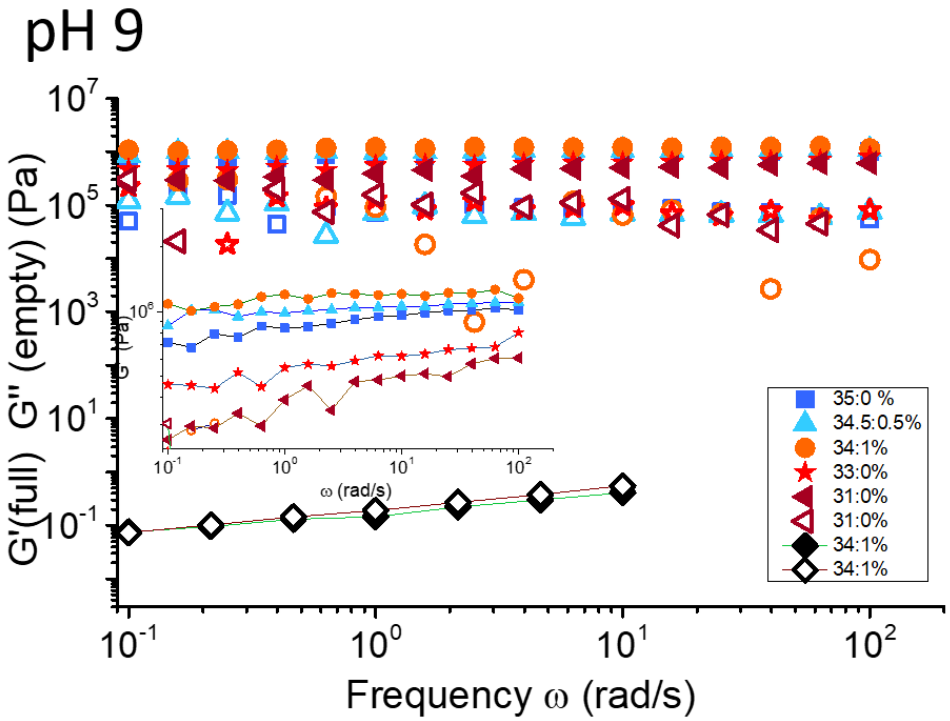

A6. Pictures of the as-prepared Blended Suspensions

Electrolyte = 10^{-3} M NaCl; Ratio is alumina:silica (vol%).

pH8

Ratio	Day 0	Day 1	Day 2
35:0%	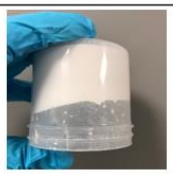	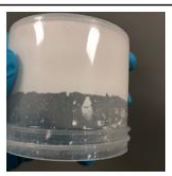	
34.5:0.5%	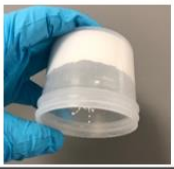	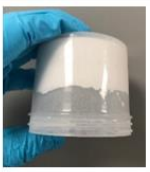	
34:1%		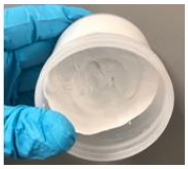	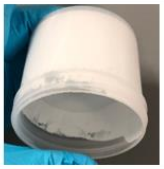
33%	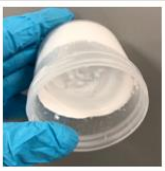	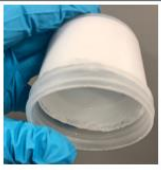	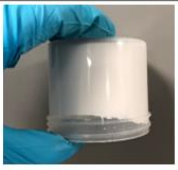

Ratio	Day 0	Day 1	Day 2
33:2%			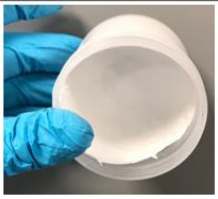
32:3%	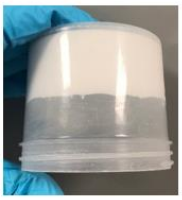		
31%	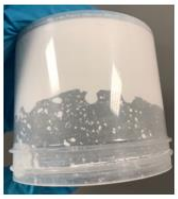		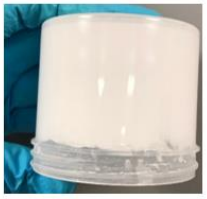

pH 9

Ratio	Day 0	Day 1	Day 2
35:0%	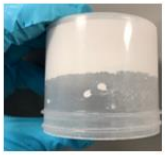	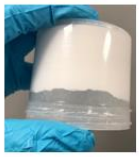	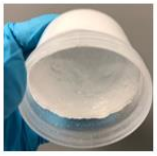
34.5:0.5%	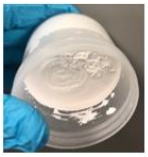	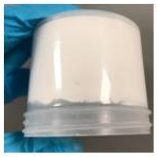	
34:1%	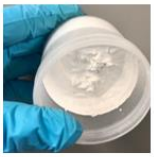	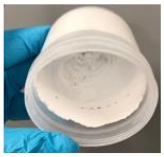	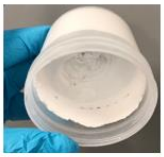
33%	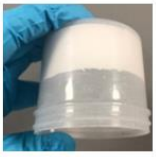		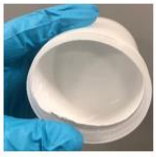

Ratio	Day 0	Day 1	Day 2
33:2%			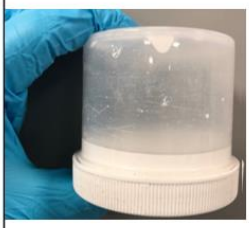
31%	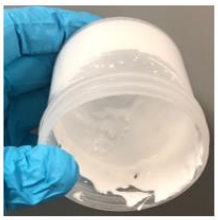	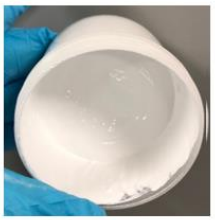	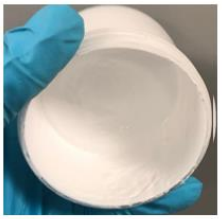

Chapter 6
Weak Gel in a No Yield Stress Blended Suspension

Synopsis

The time effect on the viscoelastic properties of no yield stress suspensions has been considered. The focus of the work was on suspensions with a relatively high silica content, for example, 31:4 (alumina:silica, vol%) in 10^{-3} M NaCl at pH 8. These suspensions were previously shown to exhibit no yield stress, and a yield stress was only observed to develop following significant consolidation of the suspension. Gelling of fumed silica is a widely reported phenomena in the literature, with weak gels observed to form at very dilute silica concentrations. Since the silica component is the minor species (on a volume basis) in the alumina suspension, the potential for gelling to occur has been studied The time effect and the potential for a weak gel to form has industrial significance since the blended suspensions would be considered for long term handling prior to discharge into containers for ultimate disposal.

Introduction

This chapter discusses the phenomena of sample gelation and how it can be eliminated. Gelling would be considered undesirable in many applications as it is a time-dependent stiffening of a suspension. In the current study, the objective was to eliminate yield stress within a concentrated particle suspension. The following reviews provide a comprehensive discussion on suspension gelling (1-4).

6.1 Gels

Colloidal stability has been previously discussed in Chapter 2. Increased electrostatic repulsion increases the stability of a colloidal suspension. This stability can be reduced by increasing the background electrolyte concentration, which increases the attractive van der Waals forces (by weakening the electrostatic force) to form very weak fractal-like open flocs. At a critical solids concentration (vol%), as defined by the gel point, these weak fractal-like flocs begin to interact and form a continuous 3D network, referred to as a gel, when the structure is self-sustained. However, under shear this network and flocs can be destroyed (3-5). The transition at the gel point is often described as a transition from a liquid to a weak solid (6-9).

The rheology of colloidal gels are often difficult to measure. A number of factors such as temperature (10), measurement geometry (11, 12), method of measurement - torque or strain amplitude (13), sample pre-shearing (14), and angular frequency (15) can affect the rheology of a gel significantly.

6.2 Rheometer Geometry Effects

Servais et al. (11) studied the viscoelasticity of a 15 w/w% gelatin at pH 5. A controlled stress (ThermoHaake RS150) rheometer was used at 24°C. A number of different vane diameters were used including, 7, 12, 18, and 22 mm. A bob of 20 mm diameter was also used. A comparison was made between vane (18 mm and 22 mm) and bob geometries. It was shown that the data was not reproducible for vanes of 7 mm and 12 mm diameter due to the "stickiness" nature of the gelatin, which caused the gelation to non-uniformly coat the surface of the geometries, with the issue more widely discussed in literature (16). An oscillation time sweep was used with fixed strain and angular frequency of 3% and 1 Hz (6.28 rad s^{-1}), respectively. Gelatin is a high molecular weight, highly branched biopolymer which at a critical concentration goes through sol-gel transition as the biopolymer chains begin to interpenetrate and entangle with one another. Gelatin is a soft solid and behaves solid-like due to the entanglement of the biopolymer. Servais et al. confirmed that the vane was the best geometry to use for solid-like systems due to minimal or no wall slippage (11).

6.3 Temperature

Servais et al. (11) also studied the temperature effect on a 2 w/w% k-carrageenan gel at pH 7.3 using a 22 mm vane. The rheology was measured during a temperature sweep between 12°C and 30°C with the temperature increasing at 0.4°C/ min. Shear strain and angular frequency were fixed at 3% and 1 Hz, respectively. When increasing the temperature, the viscoelastic

moduli decreased due to disentanglement of the crosslinking gel, a result of increased Brownian motion of the k-carrageenan chains.

Amiri et al. conducted a frequency sweep at fixed strain (0.1%) to study the viscoelasticity of 9 wt% silica (12 nm) suspension in glycerol-water (50/50) at pH 10.5, using 0.1 M NaCl as the background electrolyte (17). Similar to previous observations, an increase in temperature weakened the strength of the gel. With increasing temperature the G' contribution decreased due to increased particle mobility and decreased strength of hydrogen bonds due to the higher thermal energy.

6.4 Pre-shear Protocol

Marunaka and Kawaguchi (14) studied the effect of pre-shear on the viscoelastic behavior of fumed silica in various alkanes such as octane, dodecane and hexadecane. Hydrophobic fumed silica (VP-NKC130) of 16 nm diameter was used. Silica suspensions of 7 vol% were prepared in each alkane. A Paar Physica MCR-300 rheometer with a 50 mm and 1°cone and plate geometry was used. All suspensions were pre-sheared as 1000 s^{-1} for 10 min and allowed to rest for 2 min to provide sufficient time for structure recovery prior to measurement. A number of tests were completed to understand the transient stress behaviour by pre-shearing the suspensions at various shear rates between 0.01 and 1000 s^{-1} (14).

Figure 6-1 shows the shear stress profiles of fumed silica (7 vol%) in three different alkenes: octane, dodecane and hexadecane which are represented

in Figures (a), (b) and (c), respectively. The shear rates applied were 0.1, 1, 10, 100 and 1000 s^{-1} and are shown by the purple circles, blue squares, green diamonds, yellow triangles and red inverted triangles, respectively. Each shear rate was applied for 60 min at 25°C and the shear stress measured, however, the data shown Figure 6-1 is for the first 20 min and beyond that time the rheology remained unchanged. For octane and dodecane, the authors observed structural build-up at shear rates of 10 s^{-1} and less, observing a sigmoidal shear stress profile with increasing time. At shear rates $\geq$ 100 s^{-1}, the shear stress was observed to slightly decrease with time, indicating some slight structural breakdown. Such behaviour was not observed for the hexadecane suspensions. For the hexadecane suspensions, the shear stress increased rapidly at low shear rates. The authors claim that hexadecane can embed into the attached hexadecyl chains (modified fumed silica), whereas octane and dodecane may be squeezed out from the hexadecyl chains. Thus, it can be expected that attractive forces in hexadecane should be greater than that in octane and dodecane due to the molecular penetration of the dispersion medium (14).

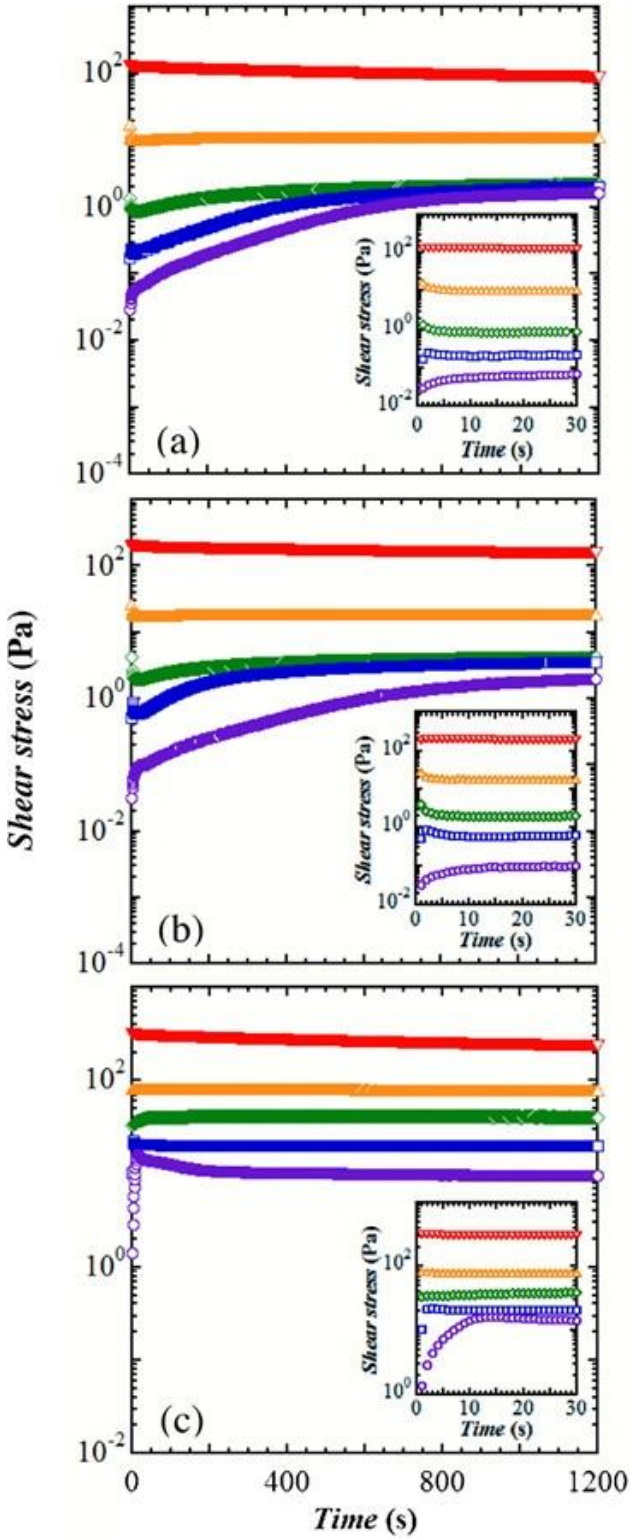

Figure 6-1. Shear stress profiles of hydrophobic fumed silica (7 vol%) in three alkanes (a) octane, (b) dodecane and (c) hexadecane as a function of shear rate at 25°C. Shear rate is shown as 0.1 s^{-1} (purple circles), 1 s^{-1} (blue squares), 10 s^{-1} (green diamonds), 100 s^{-1} (yellow triangles) and 1000 s^{-1} (red inverted triangles). Figure is taken from ref. (14).

6.5 Particle Concentration, Salt and pH Effects

Amiri et al. (18) studied the effects of particle concentration, salt and pH on the stability and viscoelasticity of silica suspensions. Aerosil 200 fumed silica with an average diameter of 12 nm was used to prepare suspensions at 1.3, 1.6, 2 and 2.3 vol% at pH 8.5, with 0.6 M NaCl used as the background electrolyte. A Physica MCR 301 rheometer (Anton Paar) was used with a concentric cylinder geometry. Suspension pre-conditioning at 50 s^{-1} for 2 min was applied to all samples prior to measurement. Time sweeps were conducted at a fixed strain and frequency of 0.05% and 1 rad s^{-1}, respectively.

The time-dependent viscoelastic moduli are shown in Figure 6-2 as a function of the particle concentration. The storage (G') and loss (G") moduli are shown by full and empty symbols, respectively. Amiri et al. (18) showed silica gels can form at solids concentrations as low as 1.3 vol%. It was also observed that increasing the particle concentration increased the strength of the silica gel, which is understandable since more particle contacts would be present in the 3D network. Similar results were reported for higher salt concentrations (2.75 M), with G' increasing as the attractive forces strongly dominant, and the rate of gelation was increased. The authors state that the mechanism for gelling in basic conditions is due to the interaction between associated and dissociated silanol groups (SiO^- and SiOH). As such, the nanoparticles become linked by acid-base interactions between silanol groups on the particle surface, with the interaction occurring through the hydrogen bound water of hydrated cations within the vicinity of the surface.

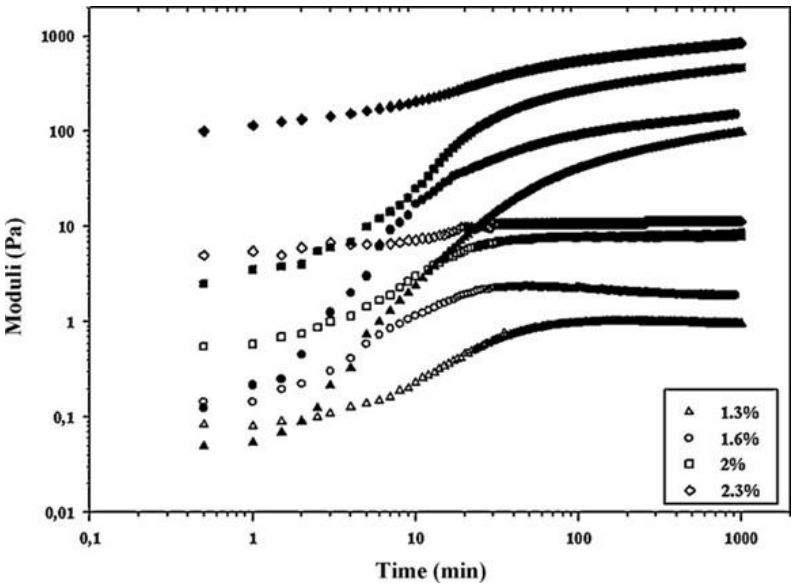

Figure 6-2. Evolution of elastic moduli as a function of silica particle concentration at pH 8.5 and 0.6 M NaCl electrolyte. Shear strain and angular frequency were fixed at 0.05% and 1 rad s^{-1}, respectively. G' and G" are represented by full symbols and empty symbols, respectively. Figure is taken from ref. (18).

6.6 Ageing Study

Derakhshandeh et al. (19) studied the effect of sample ageing on the rheology of nano-crystalline cellulose (NCC) suspensions. A rod shape NCC powder was prepared to 10 wt% in deionized water. The particle size was 270 nm rod length and 20 nm diameter as measured by light scattering. To obtain complete dispersion, each suspension was sonicated for 20 min and then allowed to rest for 30 min prior to sample loading into the rheometer.

A Physica MCR-501 stress controlled rheometer (Anton Paar) was used with a 25 mm parallel-plate for dynamic oscillation and steady-shear flow assessments. All suspensions were pre-conditioned for 1000 s applying a

constant high strain and frequency of 200% and 62.8 rad s^{-1}, respectively. Suspensions were then allowed to rest for 300 s prior to measurement (19).

Figure 6-3a shows the oscillation time sweep for 10 wt% NCC suspensions at 20°C and fixed frequency of 62.8 rad s^{-1} for 1000 s. The shear strain was varied as follows: 3, 10, 15, 20,25, 27, 30, 38 and 50%. All samples showed ageing, with the storage modulus (G') measured to steadily increase with time. At low strain (3%) the ageing of the NCC suspension was more significant than ageing at high strain values. The authors explained such behaviour as a strain dependent shear thickening response (increase in G'), with low strain having negligible impact on the structure generation, while high strain was sufficient to overcome the structure forming potential and reduced the rate of structural development.

Suspensions of NCC were also measured under steady flow conditions (varying shear rate). Figure 6-3b shows the viscosity of NCC suspensions as a function of the applied shear rate. Constant shear rates applied were 0.1s^{-1} (full black circles), 0.3 s^{-1} (empty circles), 0.5 s^{-1} (inverted full triangles), 1s^{-1} (empty full black triangles) and 3 s^{-1} (full black squares). A similar trend was observed as shown in Figure 6-3a. The NCC suspension viscosity increased with time, but is clearly shear rate dependent, and high shear rates were able to depress and at 3 s^{-1} can negate the ageing effect. Hence, hydrodynamic effects are able to exceed Brownian effects (thermal forces). This behavior can be considered in terms of the Peclet number which is a ratio between the

hydrodynamic and diffusion contributions, with the non-dimensionless number given as (20):

$$\boldsymbol{Pe} = \frac{\boldsymbol{6\pi r^3 \dot{\gamma} \eta}}{\boldsymbol{kT}} \qquad \textbf{Eq. 6-1}$$

where r is the particle radius, $\dot{\gamma}$ is the shear rate, η the viscosity of the fluid, *k* the Boltzmann constant and *T* the temperature in Kelvin. When Pe > 1 the hydrodynamic contribution dominates behavior and when Pe < 1 the diffusion (thermal energy) contribution dominates behavior.

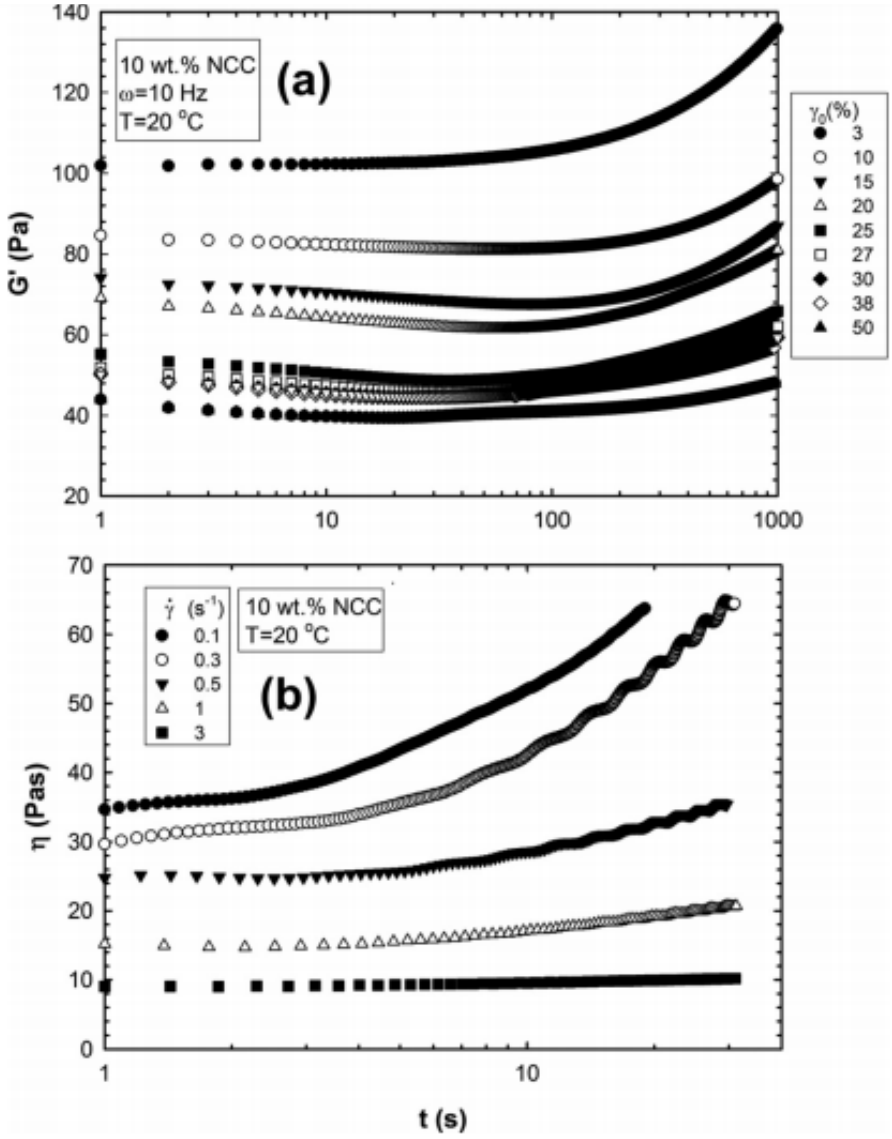

Figure 6-3. Time-dependent rheological properties of 10 wt% nanocrystalline cellulose (NCC) suspensions. a) Suspension storage modulus, G' as a function of time and varying strain. b) Suspension viscosity as a function of time and varying shear rate. All experiments conducted at 20°C. Figure is taken from ref. (19).

6.7 Experimental Method

All the samples of alumina and silica blended suspensions were prepared using the standard protocol for oscillatory measurements, as outlined in Section 4.3.2, Chapter 4. In brief, alumina (520 nm) and silica (100 nm)

nanoparticles were mixed to a total solids concentration of 35 vol% (31 vol% alumina + 4 vol% silica). NaCl was used as the background electrolyte at 10^{-3} M and the pH fixed at pH 8.

Oscillation rheology experiments were conducted using a Discovery HR-2 Rheometer (TA Instruments). Two geometries were used; i) vane geometry (diameter = 15 mm, length = 38 mm), and ii) bob geometry (diameter = 28.02 mm, length = 41.94 mm) with the standard size cup (diameter = 30 mm) used with both geometries. For the Discovery HR-2 rheometer, instrument calibration and geometry calibration, refer to Section 4.3.2.3, Chapter 4.

6.8 Results and Discussion

As previously shown in Chapter 5, above a critical blend ratio (alumina:silica, and dependent on the suspension pH), the concentrated suspension was found to exhibit no yield stress with the yield stress of the concentrated suspension shown to dissipate over 48 h, see Fig. 6-4. However, when the sample was left to rest (no agitation) for several days, it was noticed that the suspension showed some degree of thickening (increased viscosity), with the suspension viscosity reduced again once mixed for 15 min. This led to the thinking that a weak gelling was occurring in the suspension. While the phenomena of gelling has been observed when mixing two oppositely charged particles at low solids concentrations (solids content as low as 1.5 vol%) (21), the phenomena has not been reported for high solids concentration suspensions.

Gelling of fumed silica (high surface area and hydrophilic silica) is widely reported, with hydrogen bonding and electrostatic interactions, as well as the solids concentration governing the gelling rate and gel strength (22). Blends of fumed silica and magnesium oxide (MgO) have been widely reported to form cements of magnesium silicate hydrate (M-S-H) (23) via the reaction $MgO + mSiO_2 + nH_2O \rightarrow MgO{\cdot}mSiO_2{\cdot}nH_2O$, with the reaction possible at room temperature (24). The reaction is driven by using highly reactive silica (fumed silica) with the increase in gel strength to the level of conventional cements occurring over tens of days. In the UK nuclear industry, this method of cementation has been considered as a route to produce a stable waste form for the large volumes of Mg(OH) legacy waste. The Mg(OH) is considered as a precursor to form M-S-H. It should be noted that such reactions to form cements require substantially higher silica concentrations than used in the current study, with typical blend ratios (Mg/Si) in the range of 0.5 – 2.0 (24).

It is also worth noting that a blend of 31 vol% alumina and 4 vol% silica in 10^{-3} M NaCl at pH 8 was left on a bottle shaker for 6 months at ambient conditions and no significant gel strength was observed. However, a rheometer study was designed to quantify the short-time and weak gelling behavior of the alumina and silica blend.

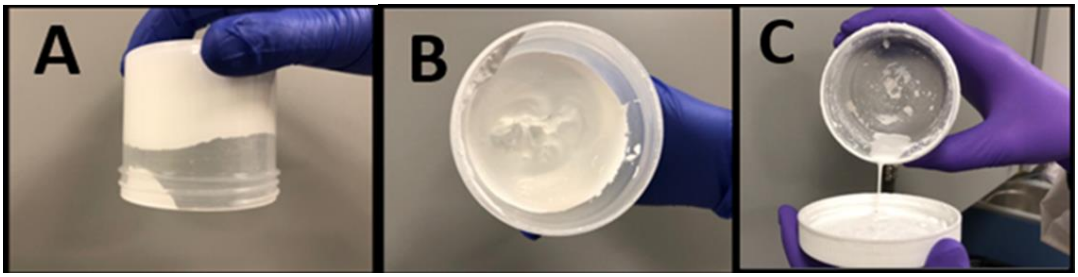

Figure 6-4. Concentrated suspension of 31 vol% alumina and 4 vol% silica in 10^{-3} M NaCl at pH 8. Visual assessment of the suspension yield stress after t = 0 h (A); t = 24 h (B); and t = 48 h (C).

6.8.1 Geometry Assessment

Since the samples of interest exhibit no yield stress and behave like a low viscosity, Newtonian fluid, a preliminary test was conducted to determine which geometry, vane or bob, is most suitable for making rheological measurements of the suspension gelling. The preliminary tests considered the viscoelasticity of water, a Newtonian fluid which has no G' contribution. If geometry inertia influences the viscoelasticity, G' can be measured. As such, an oscillation time sweep was conducted at a frequency of 10 rad s^{-1} and varying shear strain of 0.5%, 1.0% and 10.0%. All measurements were conducted at 25°C. The viscoelastic properties, elastic (G') and viscous (G") are shown by the blue and green symbols, respectively in Figure 6-5.

Figure 6-5a shows the viscoelastic data when using the vane geometry. Clearly at all three strains (%) a G' contribution is measured which exceeds the G" contribution, thus signifying significant contribution from geometry inertia. However, when using the bod geometry (Figure 6-5b), the geometry inertia is substantially less, as such a G' contribution is sporadically measured,

signifying some noise in the measurement, but for a strain of 1% the G' contribution is almost non-existent, with the G" contribution being steady in the region of 2 × 10^{-2} Pa. Using $\eta' = \frac{G''}{\omega}$, the viscosity was determined to be 2 × 10^{-3} Pa.s, which is higher than water but underlines the measurement sensitivity of the rheometer. This data highlights the importance of minimizing instrument inertia when measuring low viscosity fluids. This can be achieved by using the bob geometry (concentric cylinder) and minimizing the strain, as well as ensuring that the strain is within the linear viscoelastic region.

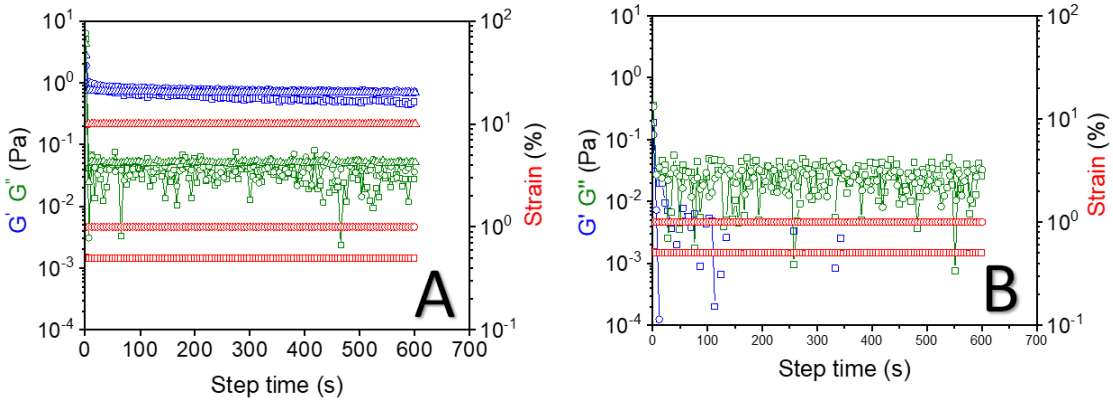

Figure 6-5. Geometry assessment to measure the viscoelastic properties of a Newtonian fluid (water). Figure 6-5A shows the G' and G" contributions when measured using a vane geometry at increasing strains of constant frequency, 10 rad s^{-1}. Figure 6-5B shows data collected using a bob geometry for the same test conditions. All experiments completed at 25°C.

6.8.2 Strain Control

Using the bob geometry, the viscoelastic properties of a 31 vol% alumina and 4 vol% silica suspension at pH 8 was measured, see Figure 6-6 as a function of strain control. The sample was pre-sheared for 180 s at 200 s^{-1}. Since the sample has no initial yield stress, the rest period was set to t = 0 s. An

oscillation time sweep was conducted for 600 s with the frequency constant at 10 rad s^{-1}, and the oscillation strain equal to 0.1 %. The G' and G" contributions are shown by the blue and green symbols, respectively. When applying a low strain (0.1 %), the G' contribution was found to exceed the G" contribution, even though the suspension was initially purely viscous. As shown in Figure 6-6, the oscillation strain achieved a constant value within a few seconds, and under constant oscillation strain, the contributions of G' and G" were shown to increase (rather significantly) after 100 s, likely confirming the onset of suspension gelling.

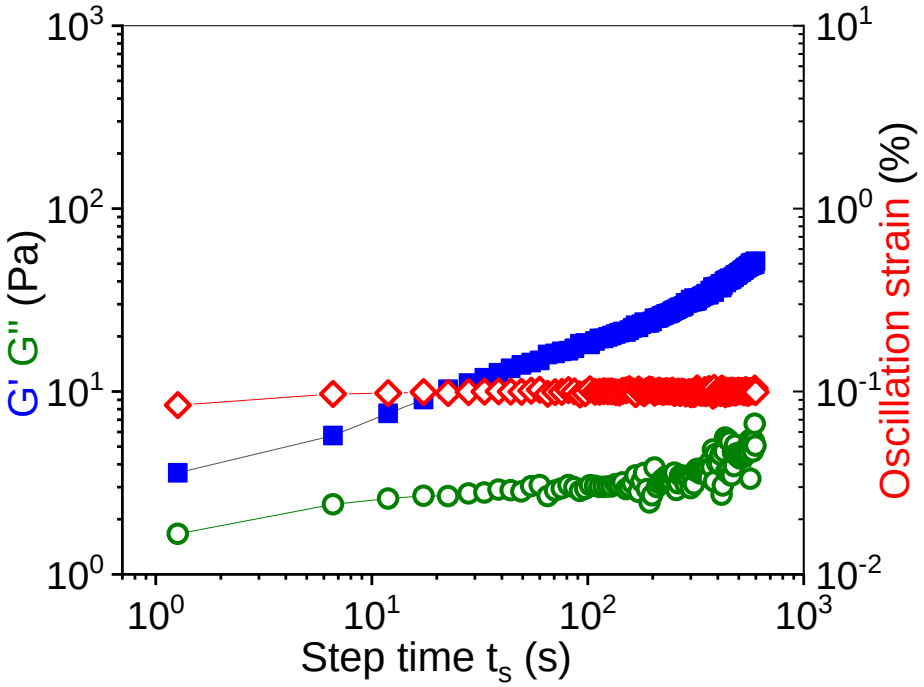

Figure 6-6. Time-dependent viscoelasticity of a 31 vol% alumina and 4 vol% silica suspension in 10^{-3} M NaCl at pH 8. The bob geometry was oscillated at constant frequency 10 rad s^{-1} and constant strain 0.1 %.

6.8.3 Evidence of Gelling

6.8.3.1 Constant Shear Strain

As previously shown, the viscoelastic properties of the liquid-like blended suspension was sensitive to the applied strain. Therefore, the 31 vol% alumina and 4 vol% silica suspension in 10^{-3} M NaCl at pH 8 was subjected to time sweep measurements at different oscillation strains of 0.1 %, 0.5%, 1.0%, 10.0% and 100.0%, which are represented by the □, ○, △, ◇ and ☆ symbols respectively in Figure 6-7. All samples were pre-sheared for 300 s at 200 s^{-1} and no rest time was applied prior to measurement. Measurements were made over 600 s with the bob geometry oscillated at a constant angular frequency of 10 rad s^{-1}.

At all oscillation strains (%), the G' and G" values were found to increase during the measurement. At the lowest strain (0.1 %), the G' contribution was found to exceed the G" contribution at all time steps, likely confirming the presence of a weak gel. As the oscillation strain increased, the G' contribution was shown to consecutively decrease, while the G" values were found to be almost insensitive to the changing strain values. As such, a condition was met when initially the G" value exceeds the G' value (10% strain), and with time the moduli transition and G' value exceeds the G" value, thus signifying a transition from liquid-like to solid-like behaviour, indicating a gelling transition. At 100% strain the suspension was found to be viscous-dominant at all times, and G" exceeded G'. This is likely due to the high strain preventing structure formation. The data underlines the importance of oscillation strain when measuring the gelling time of a concentrated particle suspension.

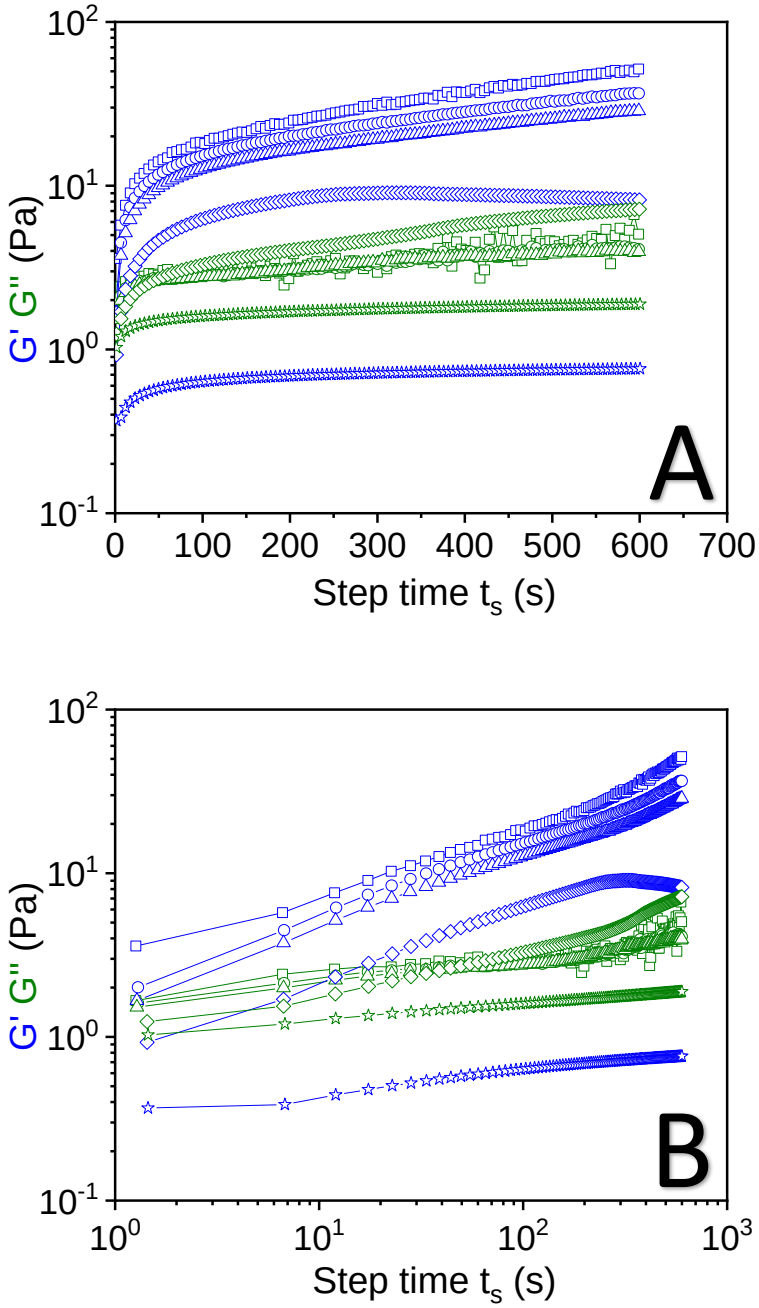

Figure 6-7. A) Time-dependent and strain-dependent viscoelasticity of 31 vol% alumina and 4 vol% silica in 10^{-3} M NaCl and pH 8. The bod geometry was used at constant angular frequency of 10 rad s^{-1}, and varying oscillation strains of 0.1%, 0.5%, 1.0%, 10.0% and 100% as shown by the □, ○, △, ◇ and ☆ symbols respectively. G' and G'' are shown by the blue and green symbols, respectively. Figure B is the same data but plotted on a log-log scale.

6.8.3.2 Constant Shear Rate

The weak gelling in the high solids content blended suspensions can also be studied under constant shear rate, measuring the change in shear stress and thus suspension viscosity. The concentrated suspensions were prepared as previously described, and without any pre-shearing the suspensions were sheared at shear rates of 0.1, 1, 10, 50, 100 and 200 s^{-1}, as shown by the black squares, red circles, blue triangles, green diamonds, violet stars and orange crossed squares, respectively, in Figure 6-8. Measurements were made over 300 s, and the initial 30 s are shown as an inset in Figure 6-8.

An increase in stress signifies increasing resistance to the geometry rotation, and thus an increase in suspension viscosity. Since the particle concentration remains constant, and the water chemistry unchanged, such behavior is consistent with weak gelling of the particle suspension. The effect is clearly shear rate dependent, with the largest change in shear stress measured at 0.1 s^{-1} (black squares), and no change in shear stress at 200 s^{-1} (crossed orange squares). At the lowest shear rate (0.1 s^{-1}), the stress is below the limit of the instrument. However, as the gelling process proceeds, the stress is then measured. Over the 300 s, the gelling process continues, as shown by the increasing viscosity with time. Such characteristic is consistent with the structural build-up in particle suspensions (14). With increasing shear rate, the gelling rate of the concentrated particle suspension is suppressed, with small aging effects observed at 1 and 10 s^{-1}. At higher shear rates there is no dependence on time. Again, this response is consistent with the understanding that gelling is promoted when the applied stress is below a

critical stress for network formation, and beyond the critical stress, the structure build-up is suppressed by the applied stress, likely due to the hydrodynamic effect exceeding the Brownian motion (diffusion) effect.

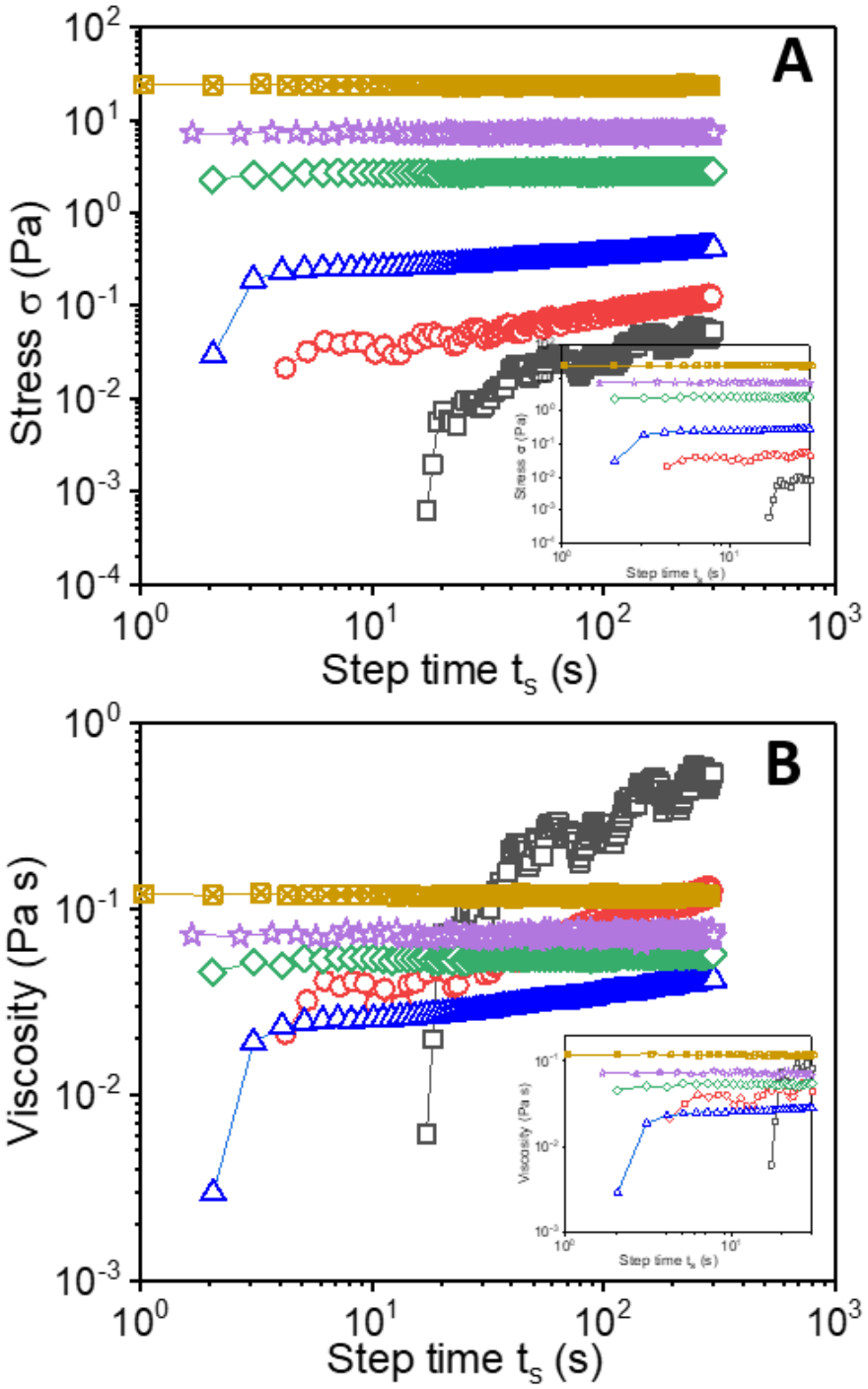

Figure 6-8. Time-dependent shear stress (A) and viscosity (B) of the concentrated suspension (31 vol% alumina and 4 vol% silica in 10^{-3} M NaCl and pH 8) as a function of shear rate: 0.1 s^{-1} (black squares), 1 s^{-1} (red circles), 10 s^{-1} (blue triangles), 50 s^{-1} (green diamonds), 100 s^{-1} (violet stars) and 200 s^{-1} (orange crossed squares). Insets refer to the initial 30 s of the measurement.

Using Eq. 6.1 the Peclet number was calculated for the two particle species based on the viscosity of water (8.9×10^{-4} Pa.s), temperature of 298.15 K, the particle radius as measured and the shear rate as set in the experiment. The Boltzmann constant was, 1.38×10^{-23} m^2 kg/s^2 K.

The Peclet number describes the balance between the hydrodynamic and thermal (Brownian) forces. As shown in Eq. 6-1, the Peclet number is given by: $\frac{6\pi r^3 \dot{\gamma} \eta}{kT}$, hence at a critical shear rate, Pe > 1, and the hydrodynamic forces dominate suspension behavior. While many-particle effects undoubtedly have a quantitative influence on particle self-diffusivity, it is possible to apply the same reasoning for high volume fraction particle suspensions. At higher particle concentrations, the Peclet number is slightly modified to account for the volume fraction and is written in the form $\mathrm{Pe} = \frac{3\pi\eta_\infty(\Phi)\dot{\gamma}r^3}{kT}$ (25). As shown in Table 6-1, the Peclet number for both particle species increases with increasing shear rate, as expected. However, due to the small particle size of the colloidal silica, all Peclet numbers remained < 1, indicating that their behavior in the fluid is dominated by diffusion. The larger alumina particles, which are also the main component of the concentrated particle suspension, shows a transition from diffusion dominated to hydrodynamic dominated as the shear rate > 10 s^{-1}. This finding complements the experimental data and supports the understanding that a weak gel can only form when the diffusion contribution dominates the particle behavior in the suspension.

Table 6-1. Calculated Peclet numbers for alumina and silica particles as a function of the solids concentration and shear rate. The calculated values are based on the high solids concentration equation.

	Peclet Number	
Shear Rate (s^{-1})	**Alumina**	**Silica**
0.1	2.49×10^{-3}	2.29×10^{-6}
1	2.49×10^{-2}	2.29×10^{-5}
10	2.49×10^{-2}	2.29×10^{-4}
50	1.25	1.14×10^{-3}
100	2.49	2.29×10^{-3}
200	4.99	4.58×10^{-3}

6.8.3.3 Varying Strain and Angular Frequency

To determine the influence of oscillation strain and angular frequency on the viscoelastic properties of the concentrated particle suspensions, a series of tests were conducted where the angular frequency was fixed and the sample underwent a series of aging tests with the applied strain varied from 0.1 % to 100 %, see Fig. 6-9. All samples were prepared to 31:4 alumina:silica (vol%) in 10^{-3} M NaCl at pH 8. A pre-shear of 200 s^{-1} was applied for 300 s prior to each strain step. The time dependent viscoelastic properties were then measured for 600 s. Angular frequencies were varied as 0.1, 1, 10, 50, 100 and 300 rad s^{-1} (see Fig. 6-9).

At the lowest angular frequency (0.1 rad s^{-1}), the viscoelastic response of the concentrated particle suspension was observed to change as a function of the oscillation strain. At the highest strain (100 %), the material was observed to be liquid-like as the G" contribution greatly exceeded the G' contribution. As the oscillation strain was reduced, the viscoelastic ratio (G"/G') reduced and at very low strain values the viscoelastic moduli were almost equivalent.

Increasing the angular frequency to 1 rad s^{-1}, the concentrated particle suspension showed an oscillation strain and time dependent response. At the highest oscillation strain the material was once again found to be liquid-like. However, as the strain was reduced, the material demonstrated a clear transition from liquid-like (G" > G') to solid-like (G' > G") behavior at a critical time known as the gelling time. A further increase in the angular frequency (to 10 rad s^{-1}) showed a similar characteristic behavior of the material, although the gel times were found to differ from those observed at lower angular frequencies. The measured response of the material was observed to change dramatically at an angular frequency of $\geq$ 50 rad s^{-1} when the concentrated particle suspension was measured to be liquid-like at all oscillation strains. At even higher angular frequencies (100 and 300 rad s^{-1}), the data showed no characteristic trend and a significant amount of noise was found in most datasets. This response was likely due to the very high angular frequencies approaching the measurement limit of the rheometer, and for the high oscillation strains exceeding the linear viscoelastic region.

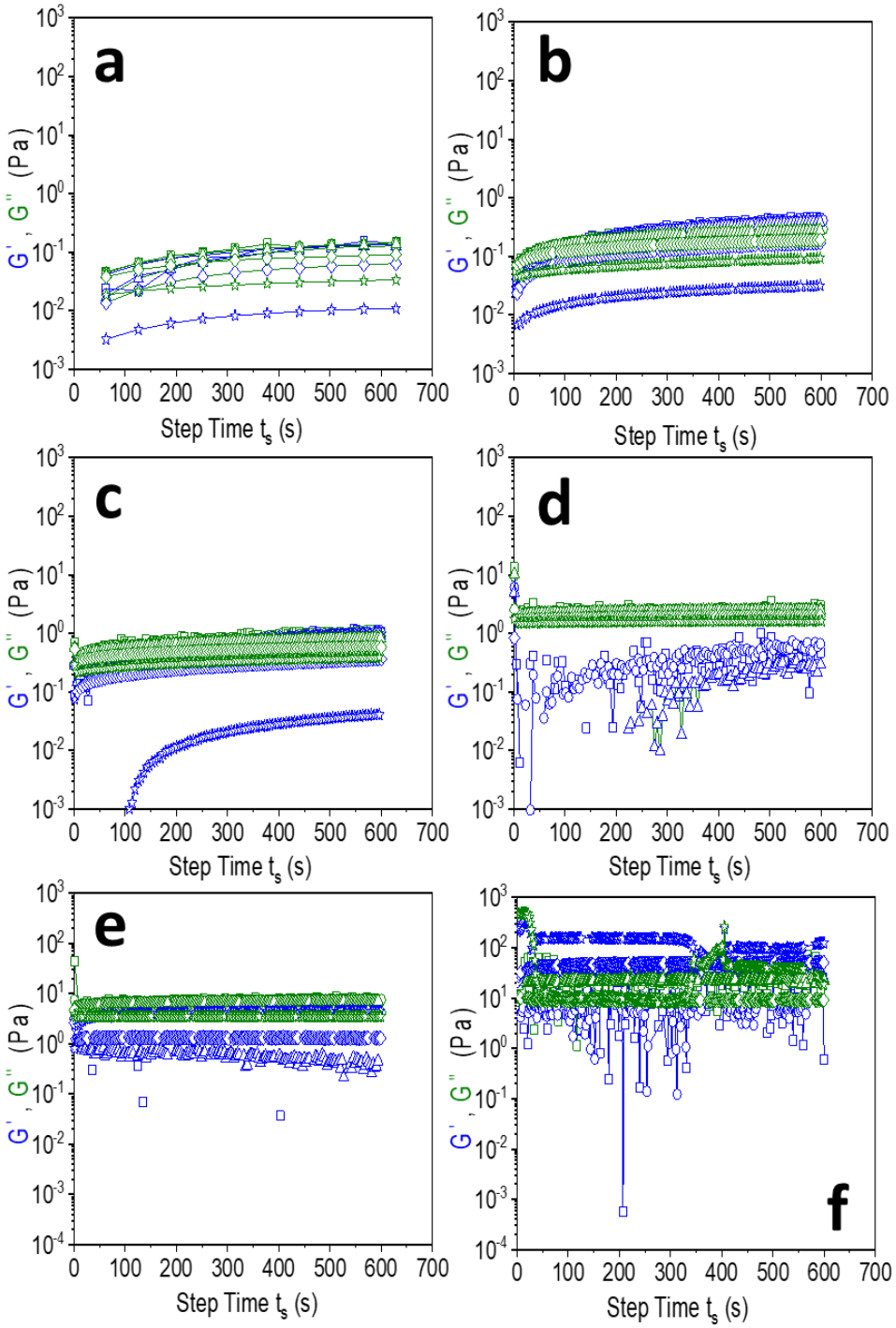

Figure 6-9. Elastic modulus (G') and viscous modulus (G") as a function of various constant strains with time for suspensions of 31:4 alumina:silica (vol%) in 10^{-3} M NaCl at pH 8. G' and G" are displayed as open blue and open green symbols, respectively. 0.1%, 0.5%, 1.0%, 10.0% and 100% of constant oscillation strain were used and displayed as □, ○, △, ◇ and ☆, respectively. A constant angular frequency was applied as (a) 0.1 rad s^{-1}, (b) 1 rad s^{-1}, (c) 10 rad s^{-1}, (d) 50 rad s^{-1} (e) 100 rad s^{-1} and (f) 300 rad s^{-1}.

A summary of the angular frequency and oscillation strain dependence on the G' plateau is shown in Fig. 6-10. The angular frequencies of 0.1, 1, 10, 50, 100 and 300 rad s^{-1} are shown by the orange pentagon, violet stars, blue triangles, green diamonds, black squares and red circles, respectively.

Two characteristic trends were observed as a function of the angular frequency. For angular frequencies $\leq$ 10 rad s^{-1} (blue triangles), the G' plateau was almost independent of strain (%), up to ~1 %, thereafter the G' plateau was found to decrease. At higher angular frequencies the characteristic response changed, and the G' plateau was found to increase slightly with increasing strain (%). Such behavior can be characterized as strain softening (angular frequency $\leq$ 10 rad s^{-1}) and strain hardening observed at higher angular frequency (15).

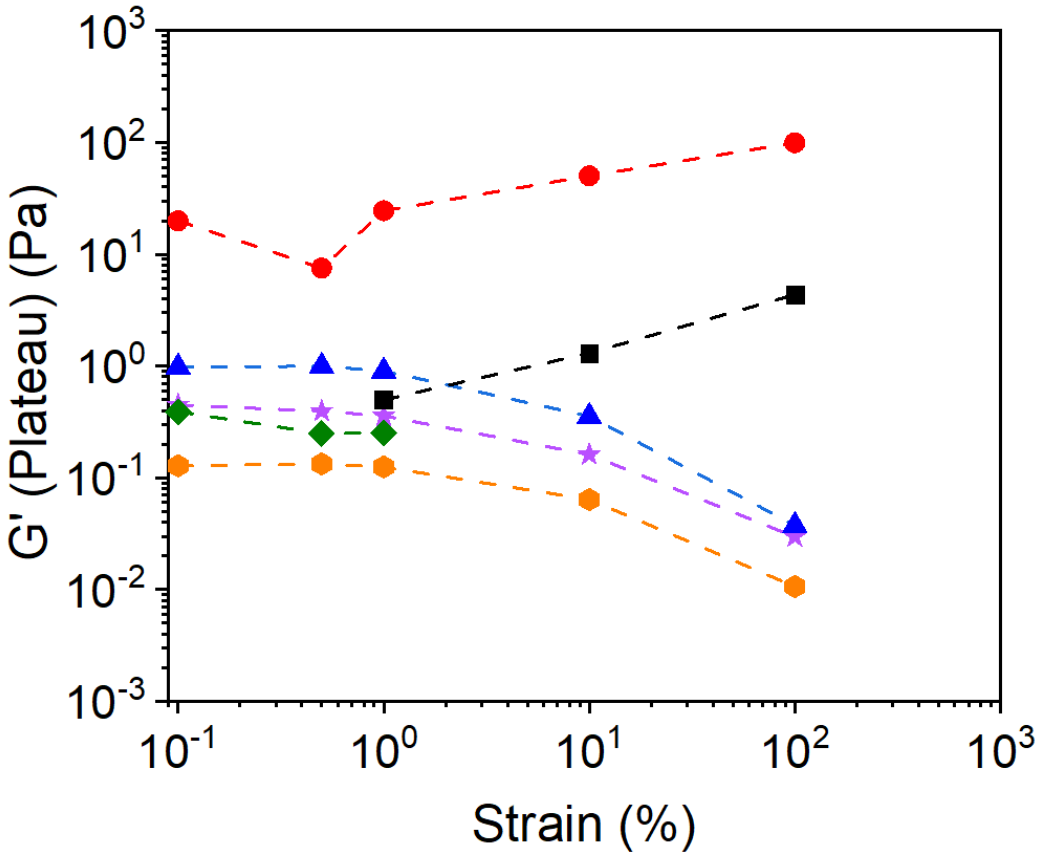

Figure 6-10. G' plateau from Fig. 6-9 for 31:4 alumina:silica (vol%) suspensions in 10^{-3} M NaCl at pH 8. G' plateau as a function of oscillation strain (%) and different angular frequencies: 0.1 rad s^{-1} (orange pentagons); 1 rad s^{-1} (violet stars); 10 rad s^{-1} (blue triangles); 50 rad s^{-1} (green diamonds); 100 rad s^{-1} (black squares); and 300 rad s^{-1} (red circles).

For those suspensions which were shown to form a weak gel, it is possible to compare the gelling time (Fig. 6-11) as a function of the applied oscillation strain. The gelation time was taken to be the critical condition when G' = G". For an angular frequency of 1 rad s^{-1}, the gelling time was found to increase slightly with increasing strain. This response indicates that greater deformation in the particle network inhibits the rate at which weak gel network can form. At an angular frequency of 10 s^{-1} the gelling time is substantially

increased and was not measured at all oscillation strains. Such response is likely a result of wall slip which occurs at large strains in the nonlinear regime (26).

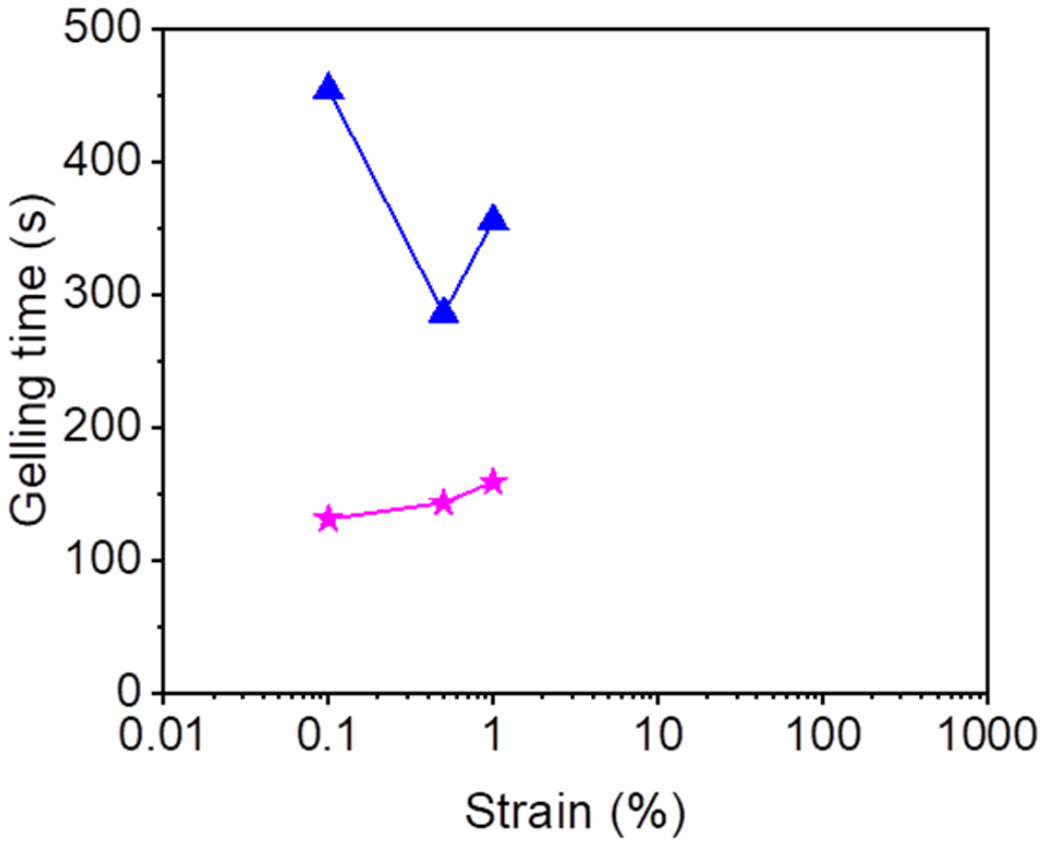

Figure 6-11. Gelation time at G' = G" for 31:4 alumina:silica (vol) in 10^{-3} M NaCl at pH 8. The angular frequencies are 1 rad s^{-1} (violet stars) and 10 rad s^{-1} (blue triangles).

The higher G' plateau at higher angular frequencies (Fig. 6-10) is characteristic of a viscoelastic concentrated colloidal suspension where the suspension appears to stiffen at higher angular frequencies as the material is not able to respond fast enough to the changes in the sinusoidal hydrodynamic motion and thus an apparent stiffening is observed. Such

behavior may be characteristic of a Maxwell fluid (27) where G" $\propto \omega$ and G' $\propto \omega^2$. When the frequency is increased the elastic contribution increases faster than the viscous contribution resulting in a purely elastic response when approaching the high frequency limit. The transition from predominantly viscous to elastic behavior occurs at a characteristic time, known as the relaxation time. This behavior and also be characterized by the Deborah number, *De*, which is defined as the ratio of a characteristic relaxation time of the fluid to the characteristic time of the flow, indicating the relative importance of elasticity (27, 28).

The gradual gelling of the concentrated particle suspensions is evident and dependent upon the hydrodynamic contribution to the system (Fig. 6-8). Several other studies have measured the time dependent rheology of colloidal silica suspensions and observed an increase in the elastic contribution suspension. Fusier et al. (29) studied the elastic modulus as a function of time for silica beads of 1.4 μm and crushed silica particles of 2 μm. All samples were exposed to a pre-shear protocol prior to measuring the elastic modulus as a function of time at a strain of 0.01 % and 1 Hz frequency. The authors observed a rapid increase in the elastic modulus within the first 200 s followed by a gradual increase to a value of 3×10^4 Pa after 20 min. at such low strains the authors claim at the isolation does not induce microstructural rearrangement in the suspension as the oscillation remains in the linear domain, such is the case in the current study, for the low oscillation strains (Fig. 6-9). Fusier et al. state that the measured thixotropy depends on the Brownian motion of the colloidal particles and the interparticle strength. As

previously discussed in Table 6-1, at all applied shear rates to the sample (Fig. 6-8), the behavior of the colloidal silica particles is dominated by their Brownian motion, while for the colloidal alumina particles a critical shear rate is exceeded when the hydrodynamic contribution begins to dominate their behavior. This indicates that the colloidal silica has the potential to reorganize within the structure to a more energetically favorable configuration, potentially promoting weak gelling of the suspension.

For the interparticle strength, the contribution of electrical double layer forces to modifying the yield stress or elastic modulus of a suspension has been considered by several authors. The model by Scales et al. (30) essentially considers the volume fraction, particle size, particle shape factor and the van der Waals and electrostatic repulsive forces, and thus as the total interaction energy is more dominated by the attractive van der Waals forces, the yield stress or elastic modulus will increase. it is difficult to assess if changes in the strength of the colloidal interaction are influencing the observed data in Figs. 6-8 and 6-9. However, data presented in Chapter 5, Fig. 5-15, may have revealed that the particle interaction strength is changing as a function of time. Fig. 5-16 directly compares two samples that were prepared following the same protocol as highlighted in Table 5-3, but Sample 5 was pH adjusted to pH 8 while Sample 4 was not pH adjusted. As previously explained in Chapter 5, the pH of the blended suspension was found to drift ever so slightly to lower pH values of pH 8. If the sample pH was not readjusted (Sample 4), then the viscoelasticity appeared almost independent of the measurement time. However, if the sample pH was readjusted (Sample 5), the magnitude of the

measured viscous and elastic moduli were found to be lower than Sample 4, but also a measurable increase in the G' contribution was seen over 600 s following a pre-shear protocol. This increase in the elastic contribution reduced the difference between the elasticity measured in Sample 4 and Sample 5, hence the suspensions were becoming more alike with time.

The slight reduction in pH is likely due to an impurity from the silica which can be associated to the manufacturing process of silica. Amorphous silica is typically produced by the acidification of solutions of sodium silicate. As previously stated, the particle samples used throughout the study were not pre-treated, and experimental observations were that concentrated alumina suspensions remained stable with no pH drift, which was consistent with blended suspensions with very little silica. However, for this particular suspension of 34:1 alumina:silica (vol%), which was chosen as the suspension exhibited no yield stress, the high silica content caused a slight drift in the pH to a lower value.

From Fig. 5-6 in Chapter 5 the change in the zeta potential of the two particle species can be determined. For silica, the zeta potential of the particle can be considered independent of pH when the suspension pH is greater than pH 6.5 (z.p. = -36 mV). However for alumina, the particle zeta potential increases as the pH decreases from pH 8 (z.p. = 13.5 mV) to pH 7 (z.p. = 33 mV). Referring to the HHF equation (Eq. 5.4, Chapter 5), the increase in the difference between the zeta potentials of the silica (-ve) and alumina (+ve) particles

would strengthen the total interaction potential between the two particles, and increase the elastic modulus of the concentrated particle suspension.

6.9 Conclusions

The weak gel of a blended suspension which exhibited no yield stress was considered. The study focused on the blended suspension of 31:4 alumina:silica (vol%) in 10^{-3} M NaCl at pH 8. A series of tests were conducted in both oscillation and rotational rheometry mode, and independent of the measurement approach a weak gel was observed to form when the oscillation strain or the shear rate was below a critical threshold, indicating that the structure formation can be suppressed by increasing the contribution of the hydrodynamic forces, as described by the Peclet number. The mechanism for gel formation was mostly attributed to the slight reduction in the suspension pH from pH 8. For blended suspensions with a high silica content, a slight reduction in the suspension pH was observed, while this change in pH did not change the zeta potential of the silica particles, it did more than double the positive zeta potential of the alumina particles. As such, the total interaction strength between the negative silica particles and positive alumina particles increased, which would increase the elastic modulus of the concentrated blended suspension. Therefore, the time dependent change in G' resulted from a change in the suspension pH.

References

1. Rahman, I.A. and Padavettan, V. Synthesis of silica nanoparticles by sol-gel: size-dependent properties, surface modification, and applications in silica-polymer nanocomposites—a review. *Journal of Nanomaterials.* 2012, **2012**.
2. Tokita, M., Nishinari, K.J.S. and Science, C. *Gels: structures, properties, and functions.* London New York: Springer Dordrecht Heidelberg 2009.
3. Osada, Y., Kajiwara, K. and Ishida, H. *Gels handbook.* Elsevier, 2001.
4. Brinker, C.J. and Scherer, G.W. *Sol-gel science: the physics and chemistry of sol-gel processing.* Academic press, 2013.
5. Mewis, J. and Wagner, N.J. *Colloidal Suspension Rheology.* Cambridge: Cambridge University Press, 2011.
6. Dzuy, N.Q. and Boger, D.V. Yield Stress Measurement for Concentrated Suspensions. *Journal of Rheology.* 1983, **27**(4), pp.321-349.
7. Goodeve, C.F. A general theory of thixotropy and viscosity. *Transactions of the Faraday Society.* 1939, **35**, pp.342-358.
8. McDowell, C. and Usher, F.L. Viscosity and rigidity in suspensions of fine particles. I–Aqueous suspensions. *Proceedings of the Royal Society of London. Series A, Containing Papers of a Mathematical Physical Character.* 1931, **131**(817), pp.409-427.
9. Botha, J.A. *Application of Quartz Crystal Microbalance to Measure the Rheology of Complex Colloidal Suspensions* Ph.D thesis, University of Leeds, 2018.
10. Keetels, C.J.A.M., van Vliet, T. and Walstra, P. Gelation and retrogradation of concentrated starch systems: 1 Gelation. *Food Hydrocolloids.* 1996, **10**(3), pp.343-353.
11. Servais, C., Ravji, S., Sansonnens, C. and Bauwens, I. Oscillating vane geometry for soft solid gels and foams. *Journal of Texture Studies.* 2002, **33**(6), pp.487-504.
12. Geraghty, R. and Butler, F. Viscosity characterization of a commercial yogurt at 5C using a cup in bob and a vane geometry over a wide shear

rate range (10−5S−1-103s−1). *Journal of Food Process Engineering.* 1999, **22**(1), pp.1-10.

13. Erni, P., Fischer, P., Windhab, E.J., Kusnezov, V., Stettin, H. and Läuger, J. Stress-and strain-controlled measurements of interfacial shear viscosity and viscoelasticity at liquid/liquid and gas/liquid interfaces. *Review of scientific instruments.* 2003, **74**(11), pp.4916-4924.
14. Marunaka, R. and Kawaguchi, M. Rheological behavior of hydrophobic fumed silica suspensions in different alkanes. *Colloids and Surfaces A: Physicochemical and Engineering Aspects.* 2014, **456**, pp.75-82.
15. Raghavan, S.R. and Khan, S.A. Shear-thickening response of fumed silica suspensions under steady and oscillatory shear. *Journal of Colloid and Interface Science.* 1997, **185**(1), pp.57-67.
16. Larson, R.G. *The structure and rheology of complex fluids.* New York: Oxford university press., 1999.
17. Amiri, A., Øye, G. and Sjöblom, J. Temperature and pressure effects on stability and gelation properties of silica suspensions. *Colloids and Surfaces A: Physicochemical and Engineering Aspects.* 2011, **378**(1-3), pp.14-21.
18. Amiri, A., Øye, G. and Sjöblom, J. Influence of pH, high salinity and particle concentration on stability and rheological properties of aqueous suspensions of fumed silica. *Colloids and Surfaces A: Physicochemical and Engineering Aspects.* 2009, **349**(1-3), pp.43-54.
19. Derakhshandeh, B., Petekidis, G., Shafiei Sabet, S., Hamad, W.Y. and Hatzikiriakos, S.G. Ageing, yielding, and rheology of nanocrystalline cellulose suspensions. *Journal of Rheology.* 2013, **57**(1), pp.131-148.
20. Abbott, S. *The Abbott Guide to Rheology.* Ipswich UK: Steven Abbott TCNF Ltd UK, 2019.
21. Weston, J.S., Harwell, J.H. and Grady, B.P. Rheological characterization of yield stress gels formed via electrostatic heteroaggregation of metal oxide nanoparticles. *Soft Matter.* 2017, **13**(38), pp.6743-6755.

22. Patel, A., Mankoč, B., Sintang, M.B., Lesaffer, A. and Dewettinck, K.J.R.A. Fumed silica-based organogels and ‘aqueous-organic’bigels. 2015, **5**(13), pp.9703-9708.
23. Tonelli, M., Martini, F., Calucci, L., Fratini, E., Geppi, M., Ridi, F., Borsacchi, S. and Baglioni, P.J.D.t. Structural characterization of magnesium silicate hydrate: towards the design of eco-sustainable cements. 2016, **45**(8), pp.3294-3304.
24. Walling, S.A. and Provis, J.L.J.C.r. Magnesia-based cements: a journey of 150 years, and cements for the future? 2016, **116**(7), pp.4170-4204.
25. Brady, J.F. and Morris, J.F. Microstructure of strongly sheared suspensions and its impact on rheology and diffusion. *Journal of Fluid Mechanics.* 1997, **348**, pp.103-139.
26. Laurati, M., Egelhaaf, S. and Petekidis, G. Nonlinear rheology of colloidal gels with intermediate volume fraction. *Journal of Rheology.* 2011, **55**(3), pp.673-706.
27. Barnes, H.A. A review of the rheology of filled viscoelastic systems. *Rheology reviews.* 2003, pp.1-36.
28. Del Giudice, F., D’Avino, G., Greco, F., Netti, P.A. and Maffettone, P.L. Effect of fluid rheology on particle migration in a square-shaped microchannel. *Microfluidics and Nanofluidics.* 2015, **19**(1), pp.95-104.
29. Fusier, J., Goyon, J., Chateau, X. and Toussaint, F. Rheology signature of flocculated silica suspensions. *Journal of Rheology.* 2018, **62**(3), pp.753-771.
30. Scales, P.J., Johnson, S.B., Healy, T.W. and Kapur, P.C. Shear yield stress of partially flocculated colloidal suspensions. *AIChE Journal.* 1998, **44**(3), pp.538-544.

Chapter 7

Conclusions

The study considered different methods to accurately measure the shear yield stress of high solids content suspensions. There were many challenges in sample preparation and measurement, and through iteration of the method, an approach was successfully demonstrated to accurately and reproducibly measure the high yield stress values of high solids content alumina suspensions. In rotational mode, the stress ramp proved difficult to generate repeatable data, with consecutive cycles in the stress producing little consistency. In addition, the fitting of a flow curve to a standard yield stress model (for example the Herschel-Bulkley model) proved very challenging with small sensitivities in the fitting parameters strongly influencing the shear yield stress. Operating the rheometer in oscillation mode proved to be more successful and the yield stress was first examined using strain control method. However, because the rheometer is stress controlled, the strain-stress feedback loop created several difficulties in smoothly executing the strain ramp, with the rheometer strain often overshooting the desired strain due to difficulties in ramping up the rheometer stress. To overcome this issue the method was adapted to follow a torque ramp, thus eliminating the need for a feedback, with the torque being directly applied to the sample and the strain determined from the torque applied. This method is used throughout the study as described in the following Chapters.

The yield stress of colloidal particles which are irregular-shaped can increase very rapidly at very low solids concentrations. High yield stress suspensions can cause problems in their processing and handling, thus alternatives to behaviorally modify the rheology of concentrated particle suspensions is desired by the nuclear industry. An approach was adopted whereby spherical colloidal silica particles were blended into a concentrated suspension of larger alumina particles. The size ratio between the two particles is approximately 5:1 for alumina:silica. Two pH conditions were chosen such that the two particle species were weakly attractive and weakly repulsive. A series of alumina:silica blend ratios were studied and it was found that independent of the colloidal interaction (attractive or repulsive), a critical blend ratio could be reached where the yield stress of the concentrated particle suspension was eliminated. Further studies to understand the nature of this flow modification indicated that the colloidal silica is likely acting as a lubricating particle between the larger and irregular-shaped alumina particles. Methods to better disperse the colloidal silica throughout the alumina network led to the critical blend ratio changing, where a suspension with a total solids content of 35 vol% would have no yield stress when 1 vol% silica is added to 34 vol% alumina.

The weak gel of a blended suspension which exhibited no yield stress was considered. The study focused on the blended suspension of 31:4 alumina:silica (vol%) in 10^{-3} M NaCl at pH 8. A series of tests were conducted in both oscillation and rotational rheometry mode, and independent of the measurement approach a weak gel was observed to form when the oscillation

strain or the shear rate was below a critical threshold, indicating that the structure formation can be suppressed by increasing the contribution of the hydrodynamic forces, as described by the Peclet number. The mechanism for gel formation was mostly attributed to the slight reduction in the suspension pH from pH 8. For blended suspensions with a high silica content, a slight reduction in the suspension pH was observed, while this change in pH did not change the zeta potential of the silica particles, it did more than double the positive zeta potential of the alumina particles. As such, the total interaction strength between the negative silica particles and positive alumina particles increased, which would increase the elastic modulus of the concentrated blended suspension. Therefore, the time dependent change in G' resulted from a change in the suspension pH.

Future Work

The study has conclusively shown that the rheology (yield stress) can be significantly modified when blending colloidal silica into a concentrated alumina particle suspension. The work has met the original research hypothesis yet has introduced more research questions as the work developed. The sections below introduce areas which require further investigation in order to test the robustness of the system studied.

7.1 Magnesium Hydroxide Suspensions

The current study focused on alumina suspensions and their modification through the addition of colloidal silica. While alumina is very relevant to the US nuclear industry, in the UK the predominant particle species is magnesium hydroxide ($Mg(OH)_2$). The basis for choosing alumina was that the strength of the colloidal interaction between the major and minor particle species could be accurately controlled by adjusting the suspension pH. This is due to the fact that alumina has an iso-electric point in the region of pH 8.5, and shows strong positive potentials below this pH and strong negative potentials above this pH. With silica being negatively charged across a wide pH range, the nature of the interaction between the alumina and silica could be adjusted from weakly attractive to weakly repulsive. In the current study, it was proven that the yield stress of the suspension could be eliminated regardless of the system being weakly attractive and weakly repulsive. This demonstrates the robustness of the suspension rheology modification.

Figure 7.1 shows the zeta potential curves for micron- and nano-sized $Mg(OH)_2$. The iso-electric point for the two particle species is in the range of pH 10 – 11, with the surface potentials being weakly negative and positive at pHs greater than and less than the iso-electric point, with a limited operational window (pH range). This limited pH range is due to the conversion of $Mg(OH)_2$ to other species at lower pH values, such as hydromagnesite ($Mg_5(CO_3)_4(OH)_2{\cdot}4H_2O$) (1). In addition, the nuclear industry stores its liquid waste at approximately pH 11 as this provides a more suitable environment to prevent the bloom of organic species within the storage ponds. As such, the suspensions of interest to the UK nuclear industry would be at the isoelectric point of the $Mg(OH)_2$. This may introduce some challenges in the sample preparation protocol ensuring that the colloidal silica is homogeneously distributed throughout a network that is strongly aggregated. However, if the colloidal silica can be successfully distributed throughout the $Mg(OH)_2$ network, the current study has confirmed that the yield stress can be eliminated even if the colloidal interaction between the major and minor particle species is either weakly attractive or weakly repulsive. Hence, yield stress elimination should also be possible for a $Mg(OH)_2$ suspension.

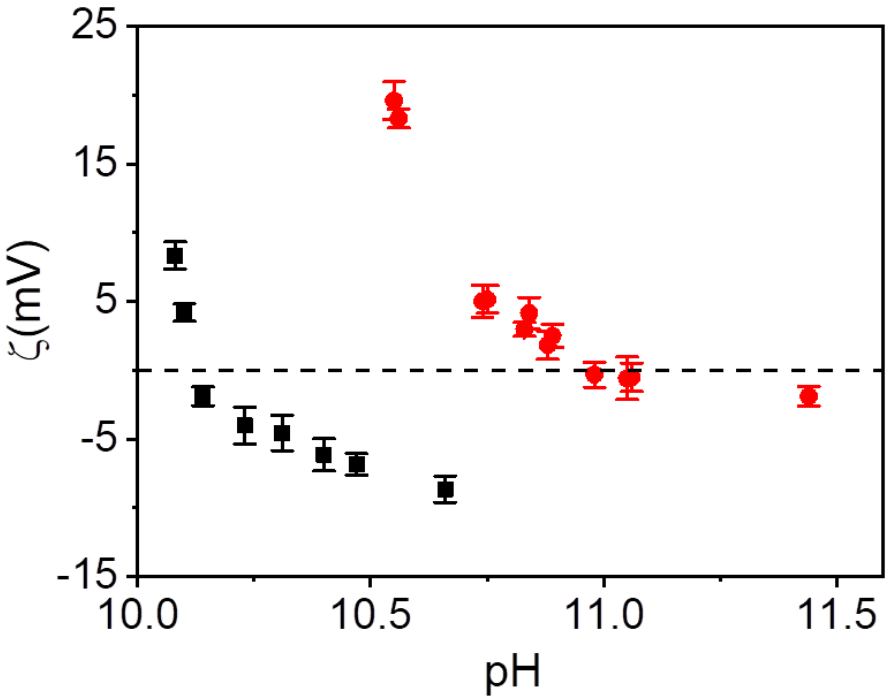

Figure 7-1. Zeta potential of nano-sized and micron-sized $Mg(OH)_2$. The black and red symbols represent the 1 μm and 15 nm Mg(OH)2 respectively.

7.2 Particle Size Ratio

The current study focused on two particle species of the major component being alumina of ca. 500 nm and the minor component being spherical silica of ca. 100 nm. Blending these two particles was able to eliminate the yield stress of high solids content suspensions. However, the broader interest is to understand the mechanism by which this yield stress modification occurs in order to better optimize the system such that a minimal amount of the minor component has to be added to eliminate the yield stress. The work presented in Chapter 5 highlighted issues around dispersion of the colloidal silica throughout the alumina particle network, with large silica “islands” being

observed, and thus confirming that a significant number of silica particles are non-contributing to modifying the suspension rheology. It is hypothesized that an optimum dosage of the minor component, i.e. minimizing the amount of silica added, can be achieved if all silica particles were dispersed.

Preliminary research with silica particles of different sizes confirmed that there is likely to be an optimum size ratio between the major and minor particle species in order to achieve the optimal lubrication effect. Studies using larger silica particles of 0.8 μm (Fig. 7-2 a and b) proved that even with a blend ratio of 30:5 alumina:silica (vol%), the blended sample, which was prepared following the same standard protocol, did not modify the yield stress of the suspension. On further analysis, the number ratio for this blend ratio was calculated to be 22:1 alumina:silica, hence on a number basis there were very few silica particles in the alumina suspension to promote lubrication. Noting that the particle number ratio is likely important, a smaller particle of 80 nm was also considered. However, this particle size was found to be difficult to disperse and required significant high strength ultrasonication to disperse the particles to the primary particle size (Fig. 7-2 c and d). This ultimately led to poor dispersion of the silica throughout the alumina network and did not significantly modify the rheology of the high solids content suspension. Further work to understand the critical size ratio is needed.

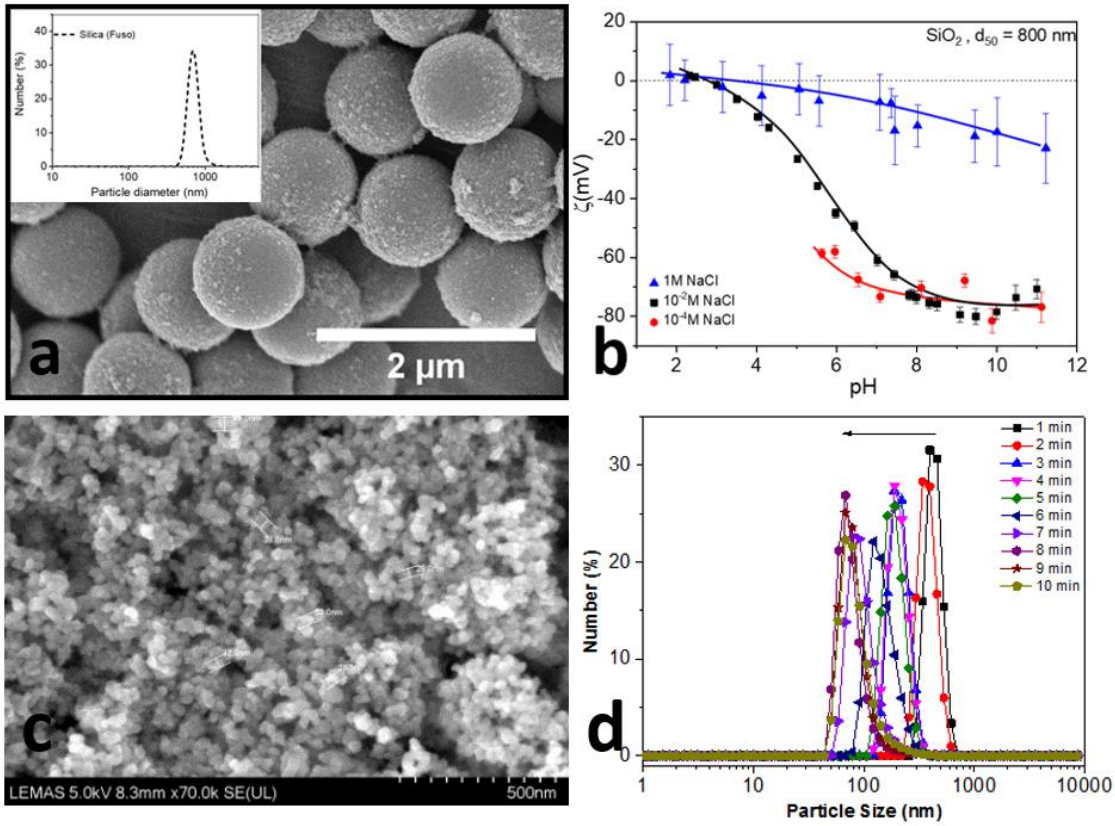

Figure 7-2. a) SEM and particle size distribution of larger colloidal silica (FUSO). b) Zeta potential curves of FUSO silica as a function of pH and electrolyte concentration. The zeta potential curves were similar to that measured for the silica used throughout the study. c) SEM images of the smaller, 80 nm, nano-sized silica. d) Particle size distribution of the nano-sized silica at 1 min time intervals following intensive sonication using a dismembrator.

7.3 Long Term Ageing Effects

The intended application of this system is to modify the rheology of legacy nuclear waste which will go into interim storage in the UK, potentially up to anything between 50 and 100 years, prior to ultimate disposal in the geological disposal facility which is still yet to be identified in the UK. An area of further research interest would be to understand the long-term aging effects on the rheology of the blended suspensions. It has already been discussed in

Chapter 5, but when working with magnesium oxide and silica there is potential to form magnesium silicate hydrate (M-S-H) which can increase the gel strength of the suspension. This has already been discussed to depend on the silica:magnesium oxide ratio (vol %), and initial thoughts suggest that the blend ratio required to eliminate the suspension yield stress would be below the critical ratio that initiates the reaction to cause significant strengthening of the particle network.

Another ageing characteristic which would require further investigation is the potential time-dependent consolidation of the high solids content blended suspension. While some preliminary work has been shown in Chapter 5, and highlighted the potential for yield stress to redevelop beyond a critical vol %, it is possible to look at the consolidation process more sophistically using a stability analyzer, such as the LUMiSizer. This will then allow a direct comparison between the force applied and the consolidation/compression of the particle network. Some preliminary data is shown in Fig. 7-3 for different blend ratios of alumina:silica (vol%).

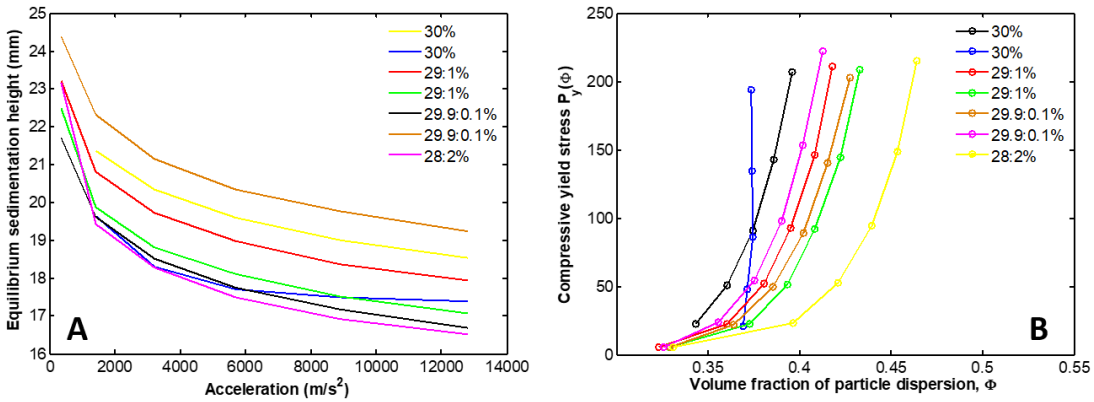

Figure 7-3 Consolidation behavior of alumina:silica (vol%) blended suspensions prepared in 10^{-3} M NaCl at pH 8.

With increasing rotational speed of the LUMiSizer, the high solids content blended suspension consolidates and attains a new equilibrium sediment height (a result of the force balance between the compressive force and the strength of the formed particle network), as determined from light transmission profiles through the sample cell. This data can be further processed to determine the compressive yield stress as a function of the solids volume fraction, following the method outlined by Yow and Biggs (2). The preliminary data shows the relationship between compressive yield stress and solid volume fraction depends on the blend ratio, with blended suspensions showing a modest increase in the compressive yield stress as the solid volume fraction starts increasing. Such behavior is in good agreement with the shear yield stress data reported in Chapter 5. This is likely to be favorable for the long term storage of these blended suspensions, and through further investigation it would be interesting to use Cryo-SEM to visualize the alumina:silica content with sample height, to determine if the silica

preferentially sediments in the alumina network, thus diminishing the lubrication effect.

References

1. Zhang, L., Mishra, D., Zhang, K., Perdicakis, B., Pernitsky, D. and Lu, Q. Electrokinetic study of calcium carbonate and magnesium hydroxide particles in lime softening. *Water Research.* 2020, **186**, p.116415.
2. Yow, H.N. and Biggs, S. Probing the stability of sterically stabilized polystyrene particles by centrifugal sedimentation. *Soft Matter.* 2013, **9**(42), pp.10031-10041.